WARWICK

'Advances in Ultrasonic Capacitive Transducer Technology'

By

Toby James Gray Robertson B.Eng. (Hons) M.Res.

Submitted for the degree of
Ph.D. in Engineering
to the
University of Warwick
describing research conducted in the
School of Engineering

Submitted August 2001

Table of contents

List of figures

Chapter 1

Chapter 2

Chapter 3

Chapter 4

Chapter 5

Chapter 6

Chapter 7

List of Tables

Acknowledgements

Firstly, I would like to thank Professor David Hutchins for his excellent supervision, endless guidance, and support. I would also like to express thanks to Dr. Duncan Billson, and Dr. David Schindel, for sharing their extensive knowledge and advice on the subject area, and to Russell Noble at the Defence Evaluation Research Agency (DERA), Malvern, for his support, encouragement, and continual supply of micromachined transducers. Thanks are also due to C. McIntyre, D. Choi, and T.H. Gan, fellow Ph.D. students, for their companionship and helpful suggestions.

I would like to thank all the staff in the School of Engineering who have given their assistance, and apologies for not naming them individually. Additional thanks are due to Frank Courtney for his help with the photolithography, and Steve Wallace and all the technicians in the engineering workshops for manufacturing the various casings and components used in the construction of transducers described in this thesis.

I would like to thank my family, all my friends, and of course Lucy, for their encouragement and patience. Finally, I would like to thank members, and ex-members, of the Warwick University Sailing Club for allowing me to get away from work occasionally.

Toby Robertson August 2001

Declaration

The work described in this thesis was conducted by the author, except where stated otherwise, in the School of Engineering, University of Warwick between the dates of October 1997 and July 2001. No part of this work has been previously submitted to the University of Warwick or any other academic institution for admission to a higher degree. All publications to date arising from this thesis are listed after the bibliography.

T.J.G. Robertson, 8th August 2001.

Summary

This thesis describes the development and characterisation of a variety of novel capacitive ultrasonic transducers for use in air-coupled and immersion applications. The first sections of this thesis examine the fabrication and initial characterisation of novel fully micromachined transducers. These devices, produced using a silicon surface micromachining process, consisted of a large laterally dimensioned (up to 5mm square), silicon nitride membrane, typically 0.5-2μm in thickness, above a nominal 2μm air gap. Typical operation in air was observed in the MHz region. The effects of membrane thickness and size were studied, as well as the effect of applied bias voltage. Differences between batches of devices were investigated. Their dynamic membrane displacements were measured using interferometric techniques. When driven with transient voltages typical displacements of a few nm were observed. Their radiated fields were also investigated, and compared to plane piston approximations, calculated with a Matlab™ program. Good agreement was found.

This thesis also describes the development and characterisation of three novel air-coupled focusing transducers. Two of these devices utilised shaped backplates, one being cylindrically concave, and the other conically concave, to produce lines of focus. The third device utilised an off-axis parabolic mirror to produce a point of focus. The development and characterisation of each is described. Their frequency responses were measured, and found to be comparable with similar planar transducers. Experiments were devised to measure their vertical and lateral resolutions, the latter typically being found to be approximately a wavelength of their centre operating frequency (~500kHz). Their radiated peak sound pressure fields were measured, and for the cylindrical and conical device compared to theoretical plane piston approximations calculated with a Matlab™ program, with good agreement of form being found. Finally, all three transducers were used to create 3-D images of a two pence coin, using amplitude and time of arrival data. Reasonable images resulted.

The final section, examines the development of an immersion transducer. This was characterised as both source and receiver, showing increases in both bandwidth and frequency response than when used in air. The effects of backplate surface properties on the characteristics of the device were studied, using a range of roughened, polished, and photolithographic metallic backplates. In addition, the effect of applied bias was also investigated. Sound pressure fields were measured, using both broadband and narrowband tone burst excitations, and compared to theoretical predictions from plane piston theory. These were calculated using a Matlab™ program, with good agreement found. The transducer was then used to produce pulse-echo C-scan images of artificially induced machined defects in Perspex and aluminium plates. Excellent images resulted.

1 Introduction

1.1 Introduction

Sound is the coordinated oscillation of molecules, which can travel through solids, liquids, and gases. The word sound can also be used to describe the auditory sensation produced by the human ear due to the detection of the vibration of these molecules. Sound is also an important mechanism through which humans, and the majority of the animal kingdom, communicate, taking the form of a set pattern of noises, or frequencies. The frequency of vibration of the molecules, f, hence that of the sound, is related to the speed of propagation of the wave in the medium, c, and the wavelength of the oscillation, λ by the following:

$$f = c/\lambda . \tag{1.1}$$

The acoustic signal is said to be ultrasonic if its frequency of oscillation is in excess of approximately 20 kHz, and infrasonic if it is below 20 Hz. These figures relate to the range of hearing of an average young person, whose ears would interpret a vibrational disturbance in the range 20 Hz – 20 kHz as a sound. Hence, ultrasound is a vibrational movement of molecules at frequencies above the audible range of humans. However, other animals such as bats, porpoise, whales, and dolphins have all found ultrasound useful for probing places where light is unavailable. This technique has been replicated by humans in SONAR (SOund Navigation and Ranging) systems for location of submerged objects.

Ultrasound is also very useful as a measurement tool for applications such as position, thickness, distance, and flow measurement. It can also be used for the non-destructive evaluation (NDE) of materials to detect defects such as cracks, voids, delaminations, and in the medical profession, for diagnosis, imaging and therapeutic applications.

This chapter begins with a brief history of ultrasonics. This is then followed by an overview of the basic properties of ultrasound such as transmission mechanisms through a medium, atmospheric absorption, and the radiation patterns from a source transducer. The final section gives an overview of the remaining chapters of this thesis.

1.2 Ultrasound – A brief history

One of the first pioneers to report producing ultrasound was Ruldolph Koenig, in around 1850. He constructed a number of devices, such as organ pipes, and tuning forks to produce sound from about 4kHz to 90kHz, to determine the upper frequency range of human hearing. Approximately 30 years later, in 1883, P. Galton developed an ultrasonic whistle, again for investigation of the upper limit of human hearing. This was in improvement over Koenings instruments, because its frequency could be continuously altered by changing the size of a resonant cavity within the device. During this period, in 1877, Lord Rayleigh published his famous book 'The theory of sound' [1].

The big breakthrough for ultrasound technology came in 1880, when French physicists Pierre Curie and his brother Jacques Curie discovered the piezoelectric effect [2]. This discovery revealed that if pressure were exerted on a quartz crystal, an electric charge would appear on its faces (hence its name from Greek, piezo = to press). Conversely, if the crystal were placed in an alternating electric field, it would deform and oscillate. However, the importance of this discovery in ultrasound generation and reception was not realised until approximately 30 years later, in 1912, after the sinking of the Titanic. This tragic accident triggered new thought into underwater object detection systems. Such a system was proposed soon after the catastrophe by Sir Hiram S. Maxim, an American engineer and inventor in an interview with Scientific American. This, together with the outbreak of World War I, dramatically increased research in this area.

By 1918, a high power SONAR system was developed by M.C. Chilowski, a Russian engineer and Paul Langevin, a French physicist to detect submerged German

submarines [3]. They demonstrated that higher acoustic intensities could be achieved by using piezoelectric transducers operating at resonance.

After the war, in the 1920's, Sokolov, a Russian scientist working at the Electrotechnical Institute of Leningrad, was one of the first to propose that ultrasound could be used as a non-destructive evaluation (NDE) technique to detect flaws within solid objects. Over the following two decades, a number of systems were developed for this task. One worthy of note here was called the M1, and was one of the first pulse-echo systems, developed by Messers Kelin and Huges in England. It wasn't until the early 1940's when ultrasound was first applied in medical diagnosis. In 1942 Karl Dussik, who is generally regarded as the first person to use ultrasound as a diagnostic tool, along with his brother, Friederich, published a paper describing a technique to locate tumours within the brain [4].

The outbreak of World War II triggered technological developments in radar, which were soon adapted for use in improved SONAR systems. After the war, in 1949, Josef and Herbert Krautkrämer produced the first German version of a pulse-echo flaw detector. The late 1940's and 50's saw new developments in valve technology, that lead to increased frequencies, shortened pulse lengths, and improved sensitivity of these instruments. There use in medical diagnosis was now becoming increasingly widespread with the introduction of a number of commercial instruments. The 1960's and 70's, saw the introduction of the transistor into commercial equipment, further improving the performance of such systems.

Up until now, piezoelectric transducers were the only type of ultrasonic transducer in common use. Materials were generally tested using either a contact method, where the transducer(s) were held against the sample usually with some form of a coupling gel, or while in immersion, using water (or some other suitable liquid) as the coupling medium. However, in the 1980's, the advantages of non-contact inspection methods were being realised; removing the need for the expensive couplant gels, or the immersion tank, which could be impractical in some cases. These new

systems required transducers capable of transmitting and receiving high frequency, broadband ultrasound in air. Even with the high power amplifiers and high gain receivers, piezoelectric materials were found generally unsuitable, due to their large impedance mismatch with air. Various techniques were (and still are) being tried to improve their performance (this is discussed further in Chapter 2). Capacitive (or electrostatic) transducers, however, were found to be a good alternative, offering high sensitivities, and bandwidths over their piezoelectric counterparts. It is the development of these capacitive transducers, for air and immersion applications, that is the focus of this thesis.

1.3 Basic properties of ultrasound

1.3.1 Introduction

This section contains an overview of the basics of the properties of ultrasound (equally applicable to sound as well). The purpose is to introduce the theory relevant to the work described in later chapters.

1.3.2 The propagation of ultrasound through a medium

As stated earlier, ultrasonic radiation is the propagation of a vibration through a medium at frequencies in excess of that audible to humans (approximately >20kHz). It is a wave phenomenon, in that each particle of the medium vibrates in some way and passes its energy onto its neighbours, while remaining near its original position (except in the special case of fluid streaming).

In gases, and the majority of liquids, this movement of the particles is always parallel to the direction of travel and is known as a longitudinal wave. However, in solids, (and a very few viscous liquids), a so-called shear (or transverse) wave can also exist, where motion of the particles is perpendicular to the direction of the wave.

Schematic diagrams illustrating the mechanisms of the longitudinal and shear wave are shown in Figure 1.1(a & b).

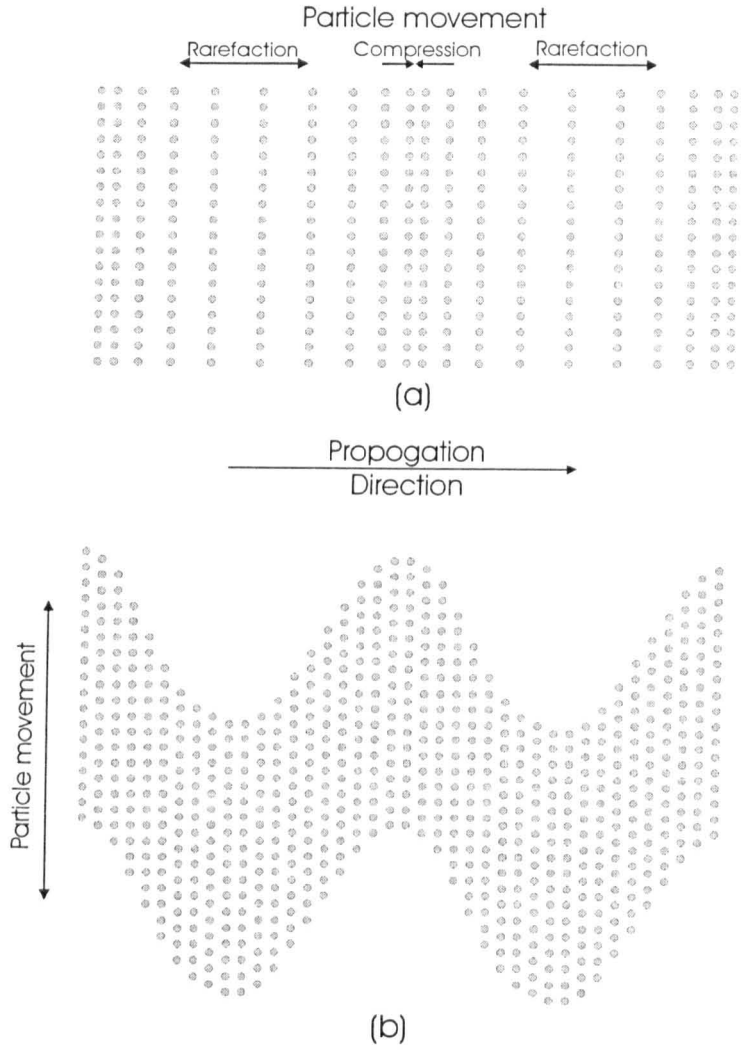

Figure 1.1: *Schematic diagram showing the particle movement in, (a) a longitudinal wave, (b) a shear wave.*

The velocity of propagation of a longitudinal wave, c_L, is dependent on the material properties, and for a solid is given by:

$$c_L = \sqrt{\frac{E(1-\sigma)}{\rho(1+\sigma)(1-2\sigma)}} \tag{1.2}$$

where, σ is the Poisson's ration, ρ is the density, and E is the Young's modulus of the material. In addition, for the shear wave, the velocity of propagation can be calculated from:

$$c_S = \sqrt{\frac{E}{2\rho(1+\sigma)}} \tag{1.3}$$

where, again, σ is the Poisson's ration, ρ is the density, and E is the Young's modulus.

For dry air, at 0°C, and at standard pressure (101.325 kPa), a number of exact values have been proposed for velocity of wave propagation, c. These have ranged from 331.29 ms^{-1} [5] to 331.46 ms^{-1} [6]. The actual value has been the subject of some debate [7,8], but it is now regarded as being between 331.44ms^{-1} and 331.46 ms^{-1}. For the work presented in this thesis, it was assumed to be 331.44ms^{-1}.

This velocity depends on a number of factors, namely, temperature, pressure, humidity, and frequency [9, 10]. However, for an approximate calculation, the effects of pressure, humidity, and frequency can be neglected, and can be calculated by the following equation:

$$c = 331.44\sqrt{T/273.16} \tag{1.4}$$

where, T is the air temperature in degrees Kelvin. So, at 20°C (293.16°K), the velocity of sound is approximately 343.4 ms^{-1}.

The passage of sound waves through a medium causes an acoustic pressure, p, to be created. This can be calculated from:

$$p = zv \tag{1.5}$$

where, v is velocity of the motion of the particles, and is called the acoustic particle velocity, (not to be confused with c, the wave propagation velocity), and z the specific acoustic impedance of the medium. This impedance is generally a complex quantity, due to the possible phase shift between the acoustic velocity and pressure. The real part of z is known as the characteristic impedance, Z, or acoustic resistance (the electrical analogy being electrical resistance), and is related to the density of the medium, ρ, and the velocity of wave propagation in that medium, c, by:

$$Z = \rho c \tag{1.6}$$

The intensity of an ultrasonic wave is the average rate of flow of energy through an area normal to the direction of wave propagation [11]. This can be either calculated from the pressure:

$$I = \frac{p^2}{2\rho c} = \frac{p^2}{2Z} \tag{1.7}$$

or, from the particle velocity, v, by substitution of equation 1.5 into 1.7:

$$I = \frac{\rho c v^2}{2} = \frac{Z v^2}{2} \tag{1.8}$$

Shear and longitudinal waves are not the only modes of ultrasonic wave supported in a medium. Other, more complex waves can exist. In a solid, surface waves (or Rayleigh waves) [1,12], can be generated, where the particles on the surface of the solid move in an elliptical motion, changing to a circular motion further in from the surface. Similar waves can also exist between the interface of two solid materials (Stonely waves [13]), and within thin layers coated onto a solid (Love waves [14]). Thin plates can support waves called Lamb waves (or plate waves) [12,15]. There are two fundamental types of Lamb wave, namely symmetric (stress), and asymmetric (bending) waves. As detailed knowledge of these is not required for this thesis, they will not be described further.

1.3.3 Propagation of ultrasound through an interface

When ultrasound strikes an interface between two media (with differing acoustic impedances), reflected waves arise, and for angles of oblique incidence, refracted waves also exist (as in optics). In the latter case, so-called mode conversion may also take place, where, for example, longitudinal waves in air may be converted to shear or surface

waves in a solid (or vice-versa). This phenomenon is of considerable importance for NDE applications. The ratio of the intensity of the reflected wave to the transmitted wave is called the reflection coefficient, and likewise, the ratio of the transmitted wave to the reflected wave, the transmission coefficient. For the case when the impinging ultrasound is perpendicular to the interface between two media, A and B, with impedances of Z_A and Z_B (see Figure 1.2), the transmission, T, and reflection, R, (power) coefficients can be calculated from:

$$R = \left(\frac{Z_B - Z_A}{Z_A + Z_B} \right)^2 \tag{1.9}$$

$$T = 4 \cdot \frac{Z_A \cdot Z_B}{(Z_A + Z_B)^2} \tag{1.10}$$

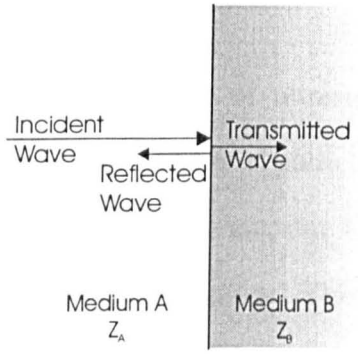

Figure 1.2: *Transmission and reflection of a perpendicular incident ultrasonic wave on the boundary between two media.*

When the impinging ultrasound is at oblique incidence to the interface, at an angle α_i to the normal of the boundary (Figure 1.3), then the directions of the reflected and transmitted waves are determined by Snell's law of refraction (primarily used for optics but applicable to any wave propagation phenomenon) given by:

$$\frac{\sin \alpha_i}{\sin \alpha_t} = \frac{c_A}{c_B} \tag{1.11}$$

where, c_A and c_B are the acoustic velocities in materials A and B respectively, α_i is the angle of the incident wave, and α_t the angle of the transmitted wave to the to the normal of the boundary.

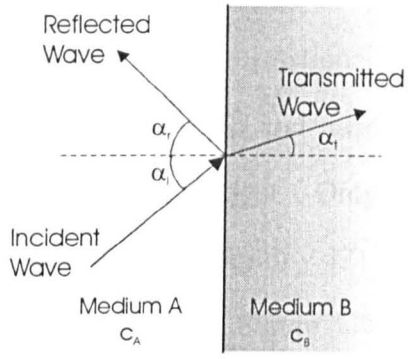

Figure 1.3: *Reflection and refraction of an incident plane wave at an interface between two media.*

1.3.4 Ultrasonic absorption

The mechanism of the transmission of ultrasound through a material can be described as the elastic deformation of individual particles of that medium. This transfer of energy between particles is not 100% efficient, due to effects such as internal friction (i.e. viscosity in liquids) and thermal conductivity. This results in a finite amount of the oscillation energy being converted to thermal energy; hence, the ultrasonic signal is attenuated (or absorbed) as it propagates through that medium.

Accurate calculation of this absorption can be complex due to the various energy dissipation mechanisms (as many as 24 in air [16]). Air is especially problematical because of its nature as a variable mixture of gases, making an accurate calculation of ultrasonic absorption difficult [17]. However, there have been a number of studies [18-20] that found there are only two main mechanisms of absorption. The first is known as classical absorption, and is due to the aforementioned case of the internal friction between the molecules of the gas and its thermal conductivity, while the second is known as relaxation loss. This is caused when the translation energy (of the ultrasonic wave) is

absorbed into the gas molecules themselves, as internal rotational and vibrational energy states. Hence, the overall absorption loss in air is given by:

$$a = a_{cl} + a_{rot} + a_{vib,O} + a_{vib,N} \tag{1.12}$$

where, a_{cl} is the classical absorption, α_{rot} the rotational relaxation loss, $a_{vib,O}$ and $a_{vib,N}$ the vibrational relaxation loss due to oxygen and nitrogen respectively. All of these terms are frequency and temperature dependent. Only the vibrational relaxation loss terms, $a_{vib,O}$ and $a_{vib,N}$, are dependent on humidity [21]. Data for dry air at standard temperature and pressure (STP) is given in Figure 1.4, (from ANSI standard (S1.26) [21]). Note that the classical absorption and rotational relaxation loss has been lumped together as a rotational plus classical term, a_{cr}. It can be seen from Figure 1.4, that at frequencies in excess of 300kHz this term becomes the dominant mechanism in the absorption of the acoustic wave. Hence, as the relaxation loss terms can be neglected at higher frequencies, humidity has no effect on the overall absorption.

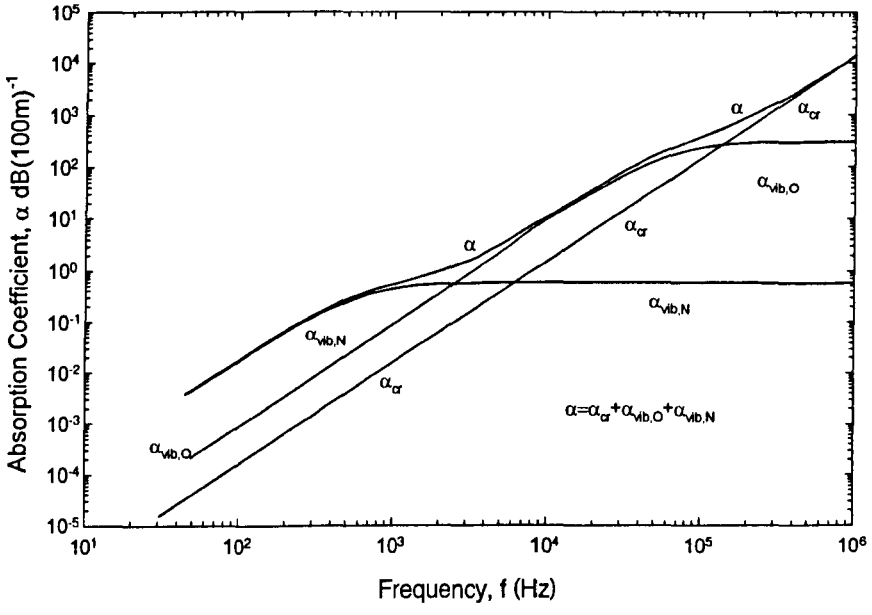

Figure 1.4: *Absorption coefficient for acoustic waves in air at 293.15 K (20 °C), 101.325kPa and 70% relative humidity (after ANSI S1.26-1978 [21]).*

Bass et al [17] evaluated a relationship between the classical plus rotational absorption term, temperature, and pressure, from experimental data. This was as follows:

$$a_{cr} = 15.895 \times 10^{-11} \cdot \frac{\left(T/T_o\right)^{1/2} \cdot f^2}{\left(P/P_o\right)} \tag{1.13}$$

where, a_{cr} is the absorption due to classical plus rotational mechanisms (dB/m), T the measured temperature, T_o the reference temperature (293.15 K), P the measured pressure, P_o the reference pressure (101.325 kPa), and f the frequency of the ultrasonic wave. This equation is valid for air at a temperature between 0-40°C, and with pressure below about 2 atmospheres (~200 kPa). It should also be noted that the attenuation is proportional to the square of the frequency.

Figure 1.5 shows an example of absorption in air, and shows the effect on an infinitely broadband signal (with an arbitrary initial amplitude of unity) after passing through 20mm of air, at STP. It can be seen that the air has a low-pass filtering effect on the ultrasonic signal, with a –6dB cut-off at approximately 1.4MHz. This demonstrates that for a practical air-coupled ultrasonic system the upper frequencies are limited to around 2MHz, over which excessive absorption occurs.

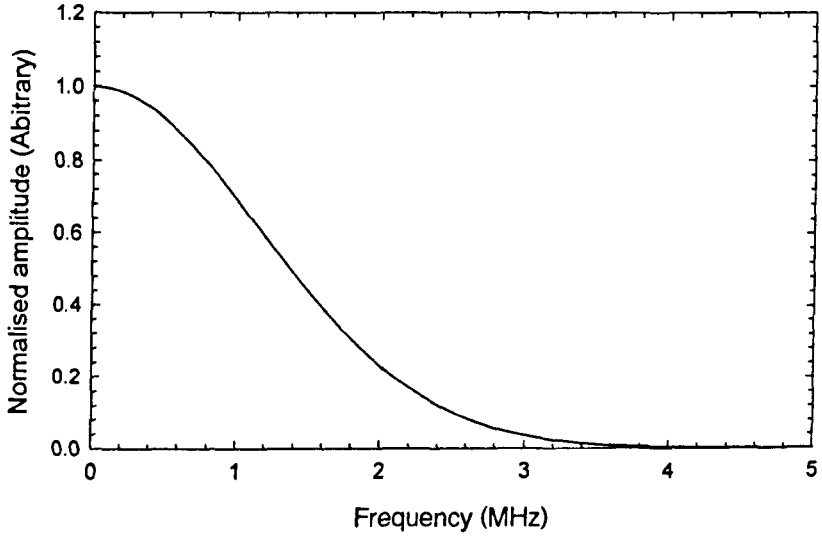

Figure 1.5: *Theoretical amplitude of an infinitely broadband signal attenuated by transmission through 20mm of air at STP.*

1.3.5 Radiation beam pattern from a source

For the development of an ultrasonic measurements system, some knowledge of the sound field emanating from its source(s) is important. Systems may require transducers with narrow beams, while others may require wider fields of view. The angle of divergence (see Figure 1.6) of the transmitted beam is controlled mainly by diffraction, and can generally be determined by the ratio of the size of the transmitting source to the wavelength, λ, of the produced ultrasound [22]. For a transducer with a circular aperture of diameter, D, the divergence angle, θ, of the beam can be approximated by:

$$\sin\theta \approx 1.22\frac{\lambda}{D} \tag{1.14}$$

Hence, with a fixed wavelength a larger diameter transducer would produce a less divergent beam. Likewise, for the same diameter transducer, a shorter wavelength (hence higher frequency) signal would also have the same effect.

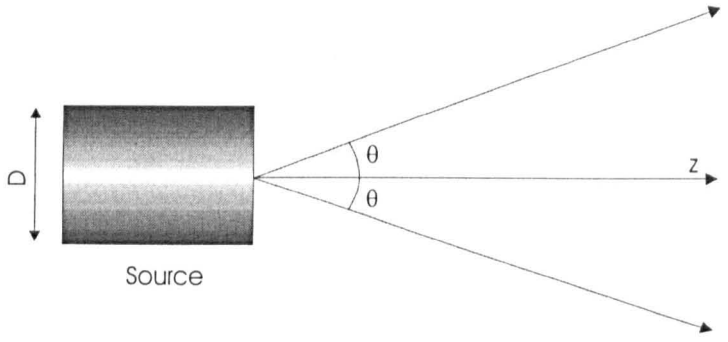

Figure 1.6: *Angle of divergence, θ, of the sound field emanating from a cylindrical transducer due to diffraction.*

For the theoretical prediction of the sound field emanating from a source, a planar piston in an infinite ridged planar baffle solution is commonly used. In this instance, it is assumed that the transducer resembles a uniform vibrating piston held within an infinitely large 'wall', or ridged planar baffle. The purpose of the baffle is to prevent acoustic signals travelling from the rear of the piston around to the front. The arrangement is shown schematically in Figure 1.7, along with the geometric system

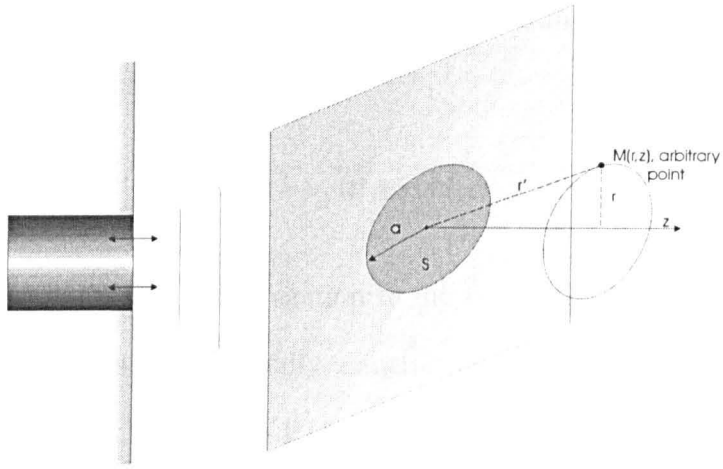

Figure 1.7: *Schematic and geometry of the circular plane piston in an infinite planar baffle approximation.*

used. Huygens' principal (primarily used in optics) [23], can then be applied, where the surface of the piston is imagined as being comprised of an infinite number of point sources, each producing a hemispherical wave. A surface integral can then be performed, summing the contributions of each of these individual elements to give the velocity potential ϕ at a point, ***M(r,z)***. This method was first demonstrated by Lord Rayleigh [1], and is hence known as the Rayleigh integral:

$$\phi(\boldsymbol{M},t)=\frac{1}{2\pi}\int_{S}\frac{v_o\,(t-r'/c)}{r'}dS \qquad \textbf{(1.15)}$$

where, r′ is the distance between the observation point, ***M***, and the elementary points dS on the surface of the piston, and $v_o(t)$ the normal particle velocity at the front of the source. The pressure, $p(\boldsymbol{M},t)$ at point ***M*** can be obtained from the velocity potential by:

$$p(\boldsymbol{M},t)=\rho\frac{d\phi}{dt}(\boldsymbol{M},t) \qquad \textbf{(1.16)}$$

where, ρ is the density of the medium.

Later work by Oberhettinger [24] and Stephanishen [25] treated the problem using an impulse response method. This essentially defined the velocity potential as a

convolution of the instantaneous particle velocity $v_o(t)$ with a function, $h(r,t)$, known as the velocity impulse response:

$$\phi(M,t) = v_o(t) * h(M,t) \tag{1.17}$$

where, * represents a convolution operation in the time domain. The velocity impulse response function $h(r,t)$ is fundamentally a spatial integration and is given by replacing the particle velocity, $v_o(t)$, in equation 1.15, with a Dirac delta (or impulse) function $\delta(t)$:

$$h(M,t) = \frac{1}{2\pi}\int_S \frac{\delta(t-r'/c)}{r'}dS \tag{1.18}$$

For the case of the circular piston source, Oberhettinger [24] was one of the first to report a numerical solution for the velocity impulse response. This is as follows; for the case $r<a$, where a is the radius of the source, and r the radial position of the observation point (i.e. the observation point, M, is directly in front of the piston source) the impulse response is given by:

$$\begin{aligned} h(M,t) = &\quad 0, && t < t_1, \\ = &\quad c, && t_1 < t < t_2, \\ = &\quad \frac{c}{\pi}\cos^{-1}\left[\frac{c^2t^2 - z^2 + r^2 - a^2}{2r(c^2t^2 - z^2)^{1/2}}\right], && t_2 < t < t_3, \\ = &\quad 0, && t_3 < t. \end{aligned} \tag{1.19}$$

and, for the case $r>a$ (i.e. the observation point is beyond the edge of the piston source):

$$\begin{aligned} h(M,t) = &\quad 0, && t < t_2, \\ = &\quad \frac{c}{\pi}\cos^{-1}\left[\frac{c^2t^2 - z^2 + r^2 - a^2}{2r(c^2t^2 - z^2)^{1/2}}\right], && t_2 < t < t_3, \\ = &\quad 0, && t_3 < t \end{aligned} \tag{1.20}$$

and, for the case where $r=a$ (i.e. the observation point is on the boundary between the piston and the baffle:

$$
\begin{aligned}
h(M,t) = \quad & c/2, && t < t_2, \\
= \quad & \frac{c}{\pi}\cos^{-1}\left[\frac{c^2t^2 - z^2 + r^2 - a^2}{2r(c^2t^2 - z^2)^{1/2}}\right], && t_2 < t < t_3, \\
= \quad & 0, && t_3 < t
\end{aligned}
\tag{1.21}
$$

where, the times, t_1, t_2, t_3 are defined as:

$$
\begin{aligned}
t_1 &= \frac{z}{c}, \\
t_2 &= \frac{\left\{z^2 + (r-a)^2\right\}^{1/2}}{c}, \\
t_3 &= \frac{\left\{z^2 + (r+a)^2\right\}^{1/2}}{c}.
\end{aligned}
\tag{1.22}
$$

These represent the transit times for the plane wave from the centre of the transducer, t_1, and the times for waves from the nearest edge, t_2, and the furthest edge, t_3 (known as edge waves). These are illustrated in Figure 1.8. This demonstrates that the impulse response at point *M*, is a combination of the plane and edge wave components. This is shown more clearly if equation (1.19) is re-written as:

$$
\begin{aligned}
h(\mathrm{M},t) &= cH(t-t_1) + \left(\frac{c}{2\pi}\right)\cos^{-1}\left[\frac{c^2t^2 - z^2 + r^2 - a^2}{2r(c^2t^2 - z^2)^{1/2}}\right]H(t-t_2)H(t_3-t) \\
&= (\text{Plane wave component}) \quad + \quad (\text{Edge wave component})
\end{aligned}
\tag{1.23}
$$

where, *H(t)* is the Heaviside step function, which is defined as unity for $t>0$ and zero for all other cases.

It should be noted, from equations (1.20) – (1.22), that when the observation point, *M*, is beyond the edge of the piston, (i.e. $r>a$) there is no contribution by the plane wave to the impulse response, and in the special case when *M* is on the edge of the piston (i.e. $r=a$) the plane wave contribution is $c/2$.

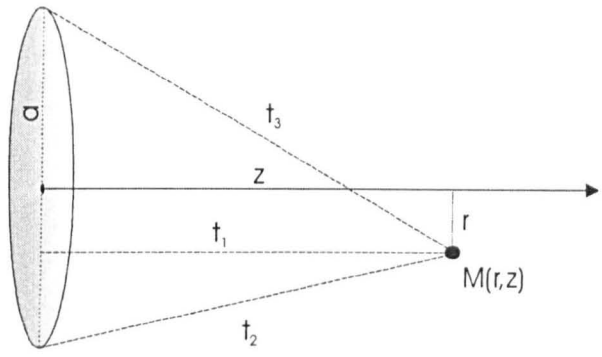

Figure 1.8: *Plane and edge wave transit times to point M.*

The aforementioned impulse response method is ideally suited to fast computation of the sound pressure fields. This was first proposed by Lockwood and Willette [26] who computed three-dimensional theoretical pressure plots for a circular source. The advantage of this method is that once the impulse response field for a transducer has been calculated, the velocity potential and, hence, the resultant pressure field, can be easily and efficiently computed for a variety of piston surface velocities.

A numerical example is shown in Figure 1.9, as a pressure field plot for a 10mm diameter circular piston driven by (a) a 500kHz, 10 cycle tone burst, and (b) a broadband transient (centre frequency 500kHz) piston surface velocity. The two plots show a characteristic shape, consisting of two distinct regions. The first, in close proximity to the source, is known as the near field region, where constructive and destructive interference occurs. The area further away from the source, where the pressure amplitude eventually decays away to zero, is known as the far field region.. These areas are more clearly shown in Figure 1.10(a & b), which shows the on-axis pressure (i.e. r=0) for the 10mm source with the same driving conditions as before. The differences between the broadband transient, and the more narrow tone burst plot are most evident in the near field region, with greater variations in pressure present in the latter case. Side lobes are also evident in the tone burst case (Figure 1.9(a)) while not for the broadband transient case (Figure 1.9(b)). The reduced interference in the broadband case is simply due to the lower number of drive cycles over time, hence there being less time

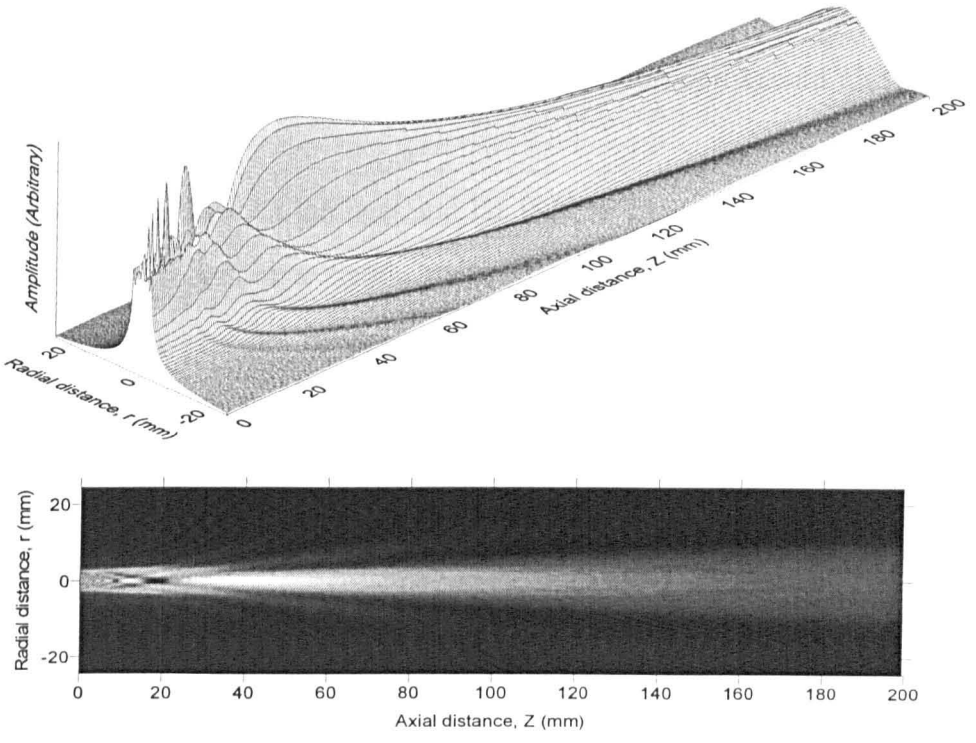

(a)

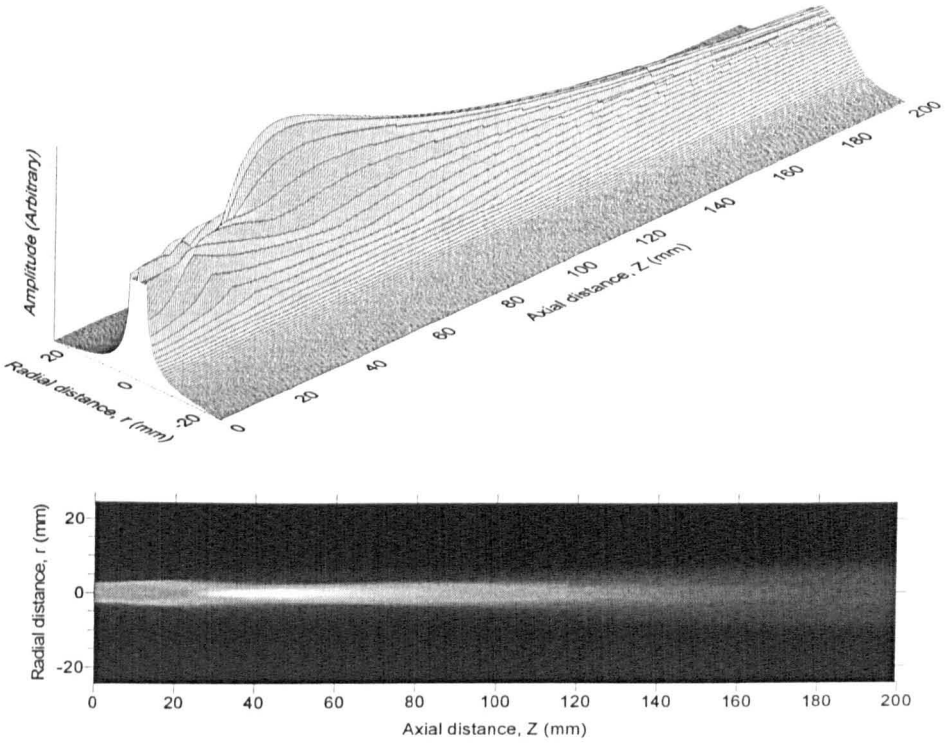

Figure 1.9: *Theoretical sound pressure filed plots (in air) for a 10mm diameter circular piston source driven by (a) 10 cycle 500kHz tone burst, (b) broadband transient (centre 500kHz)*

for interference to occur. In addition, shorter pulses cannot completely cancel each other, where longer or continuous waves can. It should also be noted that for an accurate theoretical sound pressure field plot, atmospheric absorption should also be taken into consideration.

The region between the near and far field is known as the far field / near field boundary. This occurs at a certain distance from the source transducer, at the last maxima before the pressure decays to zero. This distance, N, is approximated by the following equation:

$$N \approx \frac{a^2}{\lambda} \tag{1.24}$$

where, a is the radius of the transducer, and λ the wavelength of the emitted ultrasound. Thus, for the above example, a=5mm and λ=0.68mm (in air), so N≈36.76mm, comparing favourably with Figure 1.10(a & b).

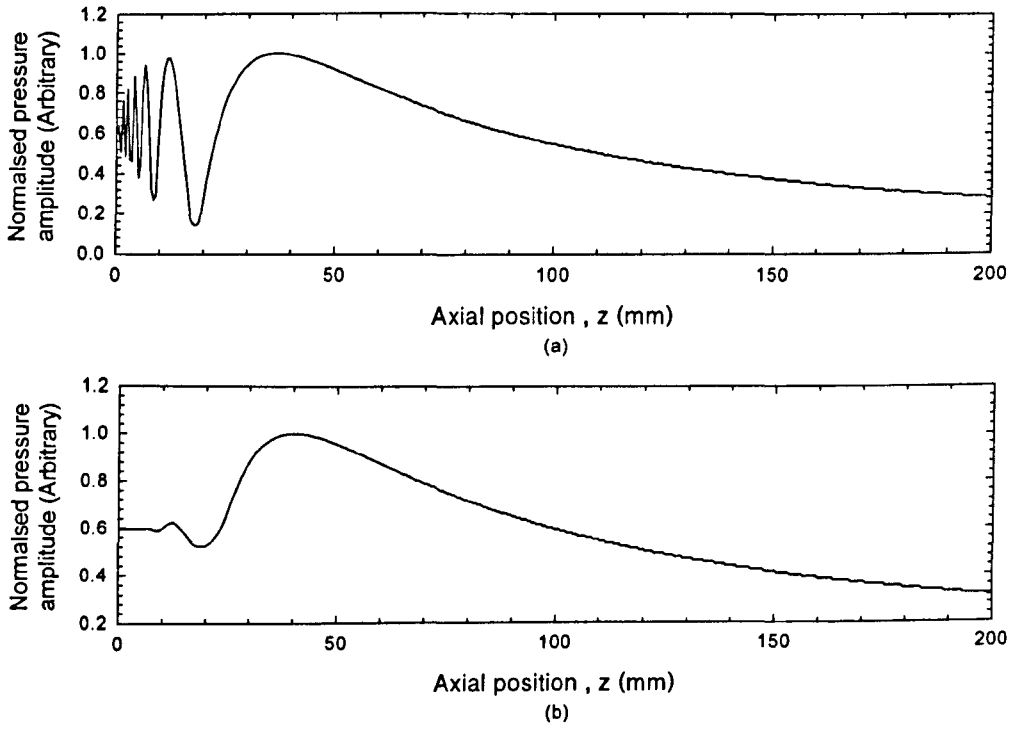

Figure 1.10: *On axis theoretical pressure field plots (in air) for a 10mm diameter circular piston source with, (a) 500kHz 10 cycle tone burst, and (b) broadband (centre 500kHz) transient surface velocities.*

As stated previously, the above solution is for a transducer with a circular aperture. However, work discussed in later chapters required a solution for a source with a rectangular aperture. Derivation of the pressure field in this case is slightly more complex, due to the non-circular symmetry of the transducer.

This problem was examined explicitly by Freedman [27] in 1960. His approach was to use phase approximations to calculate the resultant pressure field. However, these approximations had a limited (spatial) range over which these were valid. Later work (1972) by Lockwood and Willette [26] derived a closed form solution for the impulse response of a rectangular piston source, using the aforementioned impulse response method. This was an extension to the work done previously by Stephanishen [25]. More recently, however, there have been more developments [28-32], spurred on by the ever-increasing use of imaging and phased array structures usually consisting of rectangular shaped elements. These methods have mainly focused on producing faster, more efficient, methods of computing the resultant pressure field [31].

For the work described in later chapters, the theoretical method proposed by Emeterio and Ullate [29,30] was used. This method gives an exact expression for the velocity impulse response, $h(t)$. As in the case of the circular source, the analytical expression used depends on the geometrical position of the observation point, $\boldsymbol{M}$, and the time interval, t. Figure 1.11 shows a schematic of the piston, and the geometrical

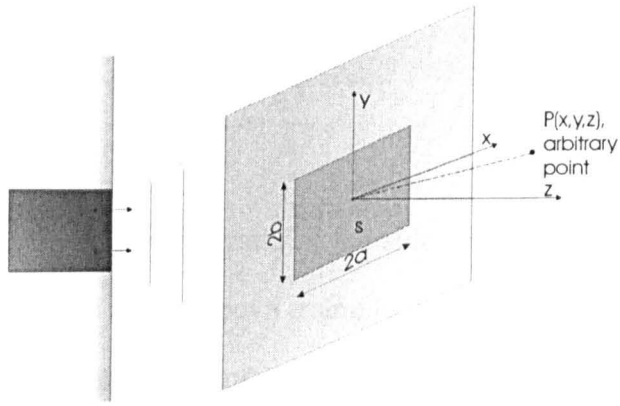

Figure 1.11: *Schematic and geometry system of the rectangular plane piston in an infinite planar baffle approximation.*

system used. The larger side length of the rectangle is defined as 2a and the shorter as 2b. The theory defines four geometrical regions; I: $x \geq a$, $y \geq b$; II: $x \leq a$, $y \geq b$; III: $x \geq a$, $y \leq b$: IV: $x \leq a$, $y \leq b$. There are also four time intervals, each corresponding to the times of the edge waves from the four sides of the rectangle. For a complete description, please refer to the literature.

Figure 1.12 shows a numerical example, as a computed sound pressure field plot from a 10mm square piston oscillator driven by (a) 10 cycle 500kHz tone burst, and (b) a broadband transient (with centre frequency of 500kHz) surface velocity. The pressure fields again contain two distinct regions, with the far field / near filed boundary clearly visible in both instances. However, examination of the near field region (for the tone burst case) shows fewer variations in the sound pressure than for that produced by the circular source (Figure 1.9(a)). Figure 1.13(a & b) illustrates this more clearly as an on-axis plot of pressure for both cases of drive condition. This less pronounced interference (compared to the circular transducer) is due to the non-circular symmetry of the square transducer, and hence differing time intervals for the arrival of the edge waves. As in the field plot for the circular transducer, the broadband signal produces less variation in the pressure field than that of the tone burst drive for the reasons described previously.

Comparison of the on-axis pressure plots for the circular and square sources (Figure 1.10 & Figure 1.13), reveals that the position of the far field / near field boundary, N, has changed. The boundary distance, N, for a rectangular transducer is given by:

$$N \approx h \cdot \frac{a^2}{\lambda} \tag{1.25}$$

where, h, is a factor that depends on the ratio of the side lengths of the transducer (b/a) and is given in Table 1.1. Thus for the above example, a=5mm, λ=0.68mm, h=1.37 (b/a =1), so $N \approx$50.4mm. This compares favourably with Figure 1.13(a & b).

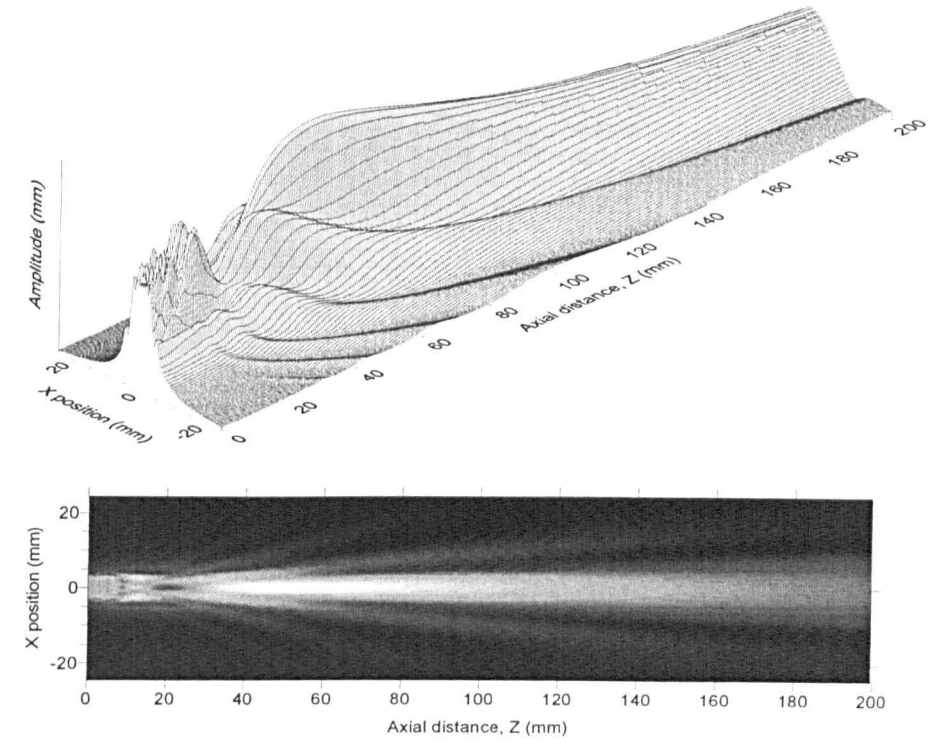

(a)

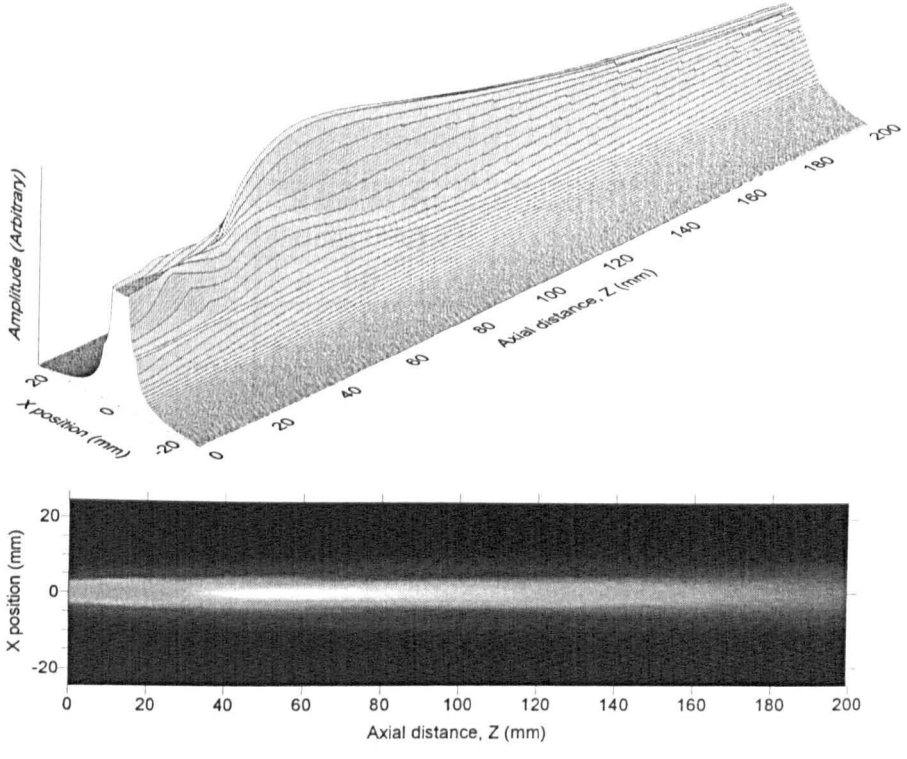

(b)

Figure 1.12: *Theoretical sound pressure field plots from a 10mm square piston source driven by (a) 500kHz 10 cycle tone burst, (b) broadband transient (centre 500kHz)*

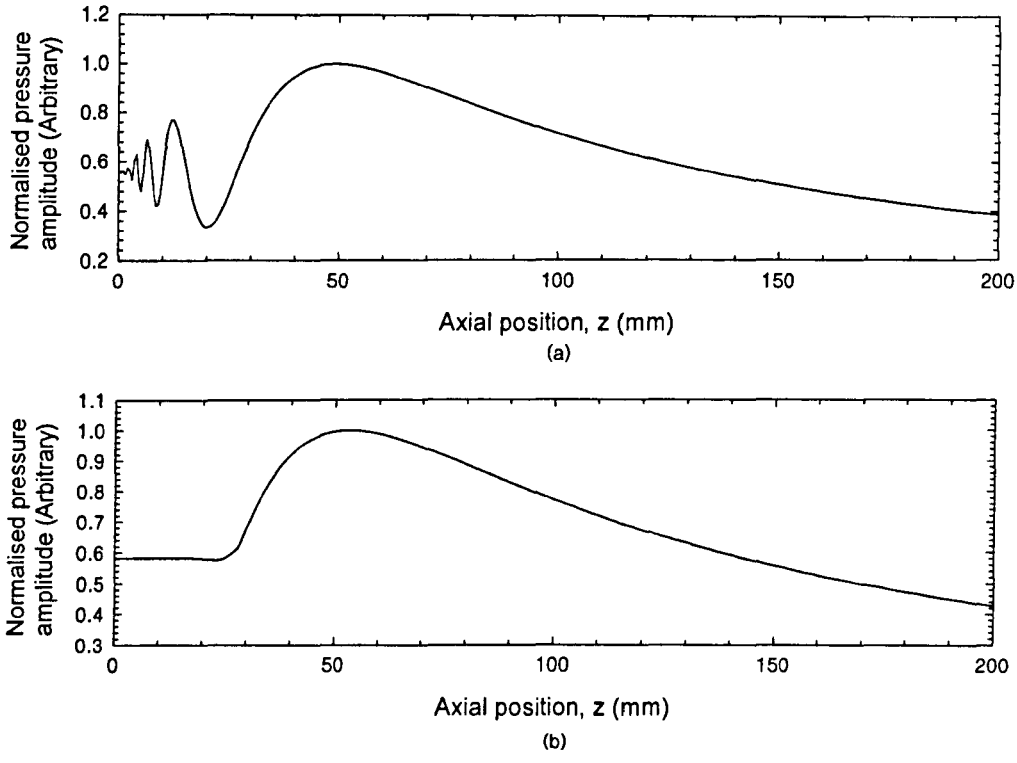

Figure 1.13: *On axis theoretical pressure field plots (in air) for a 10mm square piston source with, (a) 500kHz 10 cycle tone burst, and (b) broadband (centre 500kHz) transient surface velocities.*

Ratio of the sides (*b/a*)	*h*
1.0	1.37
0.9	1.25
0.8	1.15
0.7	1.09
0.6	1.04
0.5	1.01
0.4	1.0
0.3	0.99
0.2	0.99
0.1	0.99

Table 1.1: *Factor h values for the calculation of the far field / near field boundary distance, N, for rectangular piston oscillators (after Krautkrämer, Krautkrämer [22])*

1.3.6 Focusing of ultrasound

It is often necessary to focus ultrasound, for applications such as imaging [33], or creating regions of high intensity, such as for studying the cavitation of liquids [34]. A transducer is usually defined as focusing if the width of its beam is reduced to a size less than the diameter of the transducer. There are various methods used to achieve this focusing, such as acoustic lenses, reflection off curved mirrors, etc. Another method is to shape the front face of the device. For a transducer of radius a, with a spherically concave face, of radius of curvature, r, the on-axis pressure, at position z, is given by (from [35]):

$$p = p_o \left| \frac{2}{1 - \frac{z}{r}} \right| \sin\left[\frac{\pi}{\lambda} \left(\sqrt{(z-h)^2 + a^2} - z \right) \right] \qquad (1.26)$$

where, z is the axial position (m), a is the radius of the source, and h is given by the following:

$$h = r - \sqrt{r^2 - a^2} \qquad (1.27)$$

A plot of the on axis absolute pressure, calculated using Equation (1.26) and (1.27), is shown in Figure 1.14 for a spherically concave plane piston source. Two plots are shown, one with the radius of curvature, r=60mm and the other r=20mm. The positions of these geometrical points of focus are also shown on the plot as grey lines. It can be seen that the for the plot with r=20mm, the position of maximum pressure is approximately equal to r, but for r=60mm it is approximately 15mm closer than expected, due to the diffraction effects of the source transducer. Hence, for a strongly focusing device, the focal point is approximately equal to r, the geometrical point of focus. However, as this geometrical focus moves towards the far field / near field boundary, the actual position deviates further from that of the geometric focus. The focal

distance can also never be larger than the far field / near field boundary for that size of plane piston transducer.

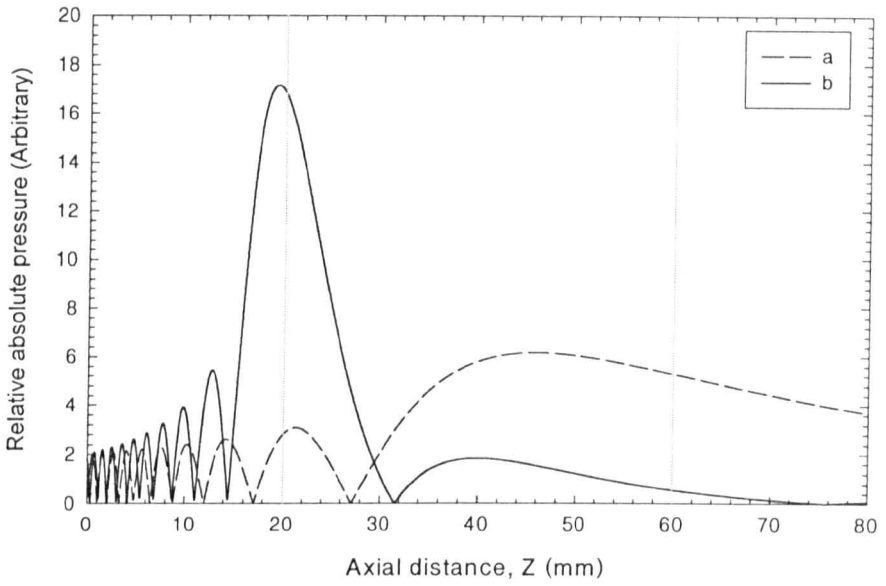

Figure 1.14: *On axis absolute sound pressure from a plane piston source (a=10mm), with a spherically concave front face with a radius of (a) 60mm (b) 20mm. (Calculated from 1.26 with λ=1 and P_o =1)*

1.4 Thesis outline

The thesis describes the work conducted on the development and characterisation of a number of capacitive transducers for air-coupled and immersion applications. New designs of transducers are examined, including fully micromachined silicon transducers, three types of focusing device and, an immersion transducer. A brief summary of the work in each of the remaining chapters is described below.

Chapter 2 gives an overview of capacitive transducer technology, beginning with a brief historical review of the capacitive transducer. This is followed with a review of techniques used in the manufacture of such devices, and its implication on transducer performance. Finally, alternatives to the capacitive transducer, for air-coupled applications, are described.

Chapter 3 contains details of the fabrication and initial characterisation of new novel fully micromachined silicon capacitive transducers. These devices comprise of a surface micromachined silicon nitride membrane (typically 1mm^2), above a nominal

2μm air gap. Studies on the effects of membrane thickness, size and bias voltage are conducted. In addition, comparisons between different batches of devices are made. Initial immersion operation results are also described.

Chapter 4 continues with the characterisation of the surface micromachined silicon devices, with firstly interferometric measurements of dynamic membrane displacements and then measurements of their radiated sound pressure fields. Comparison of these with theoretical plane piston sound field approximations are then made.

Chapter 5 investigates two novel designs of line focusing air-coupled transducer. These utilised shaped backplates, one cylindrically concave and the other conically concave, to create lines of focus. Firstly, their design and construction is discussed, from their design stage through to assembly. Then the devices are characterised to determine their frequency response. Their radiated sound pressure fields are also measured and compared to theoretical fields, calculated using plane piston theory. Their lateral and vertical resolutions were also determined experimentally. Finally, an application of surface imaging using both devices was examined.

Chapter 6 continues the study of focusing transducers, with the examination of a novel fully focusing device. This air-coupled transducer utilises reflection from an off-axis parabolic mirror to create a point of focus. Similar experiments to those in the previous chapter are performed, to determine its frequency response and resolution. Surface imaging is also examined, and comparisons made to the two line focused devices described in Chapter 5.

In Chapter 7, a capacitive transducer for immersion applications was investigated. A purpose built transducer was manufactured, based on a typical air-transducer design with the addition of O-ring seals and waterproof connections. The characteristics of this device, while in immersion, were examined. Further investigations into the effects of backplate surface topography on the frequency and sensitivity characteristics of the device were also made, with random (roughened/polished) and machined backplates.

Imaging of defects in Perspex and aluminium plates, using the capacitive immersion device is also described.

1.5 References

[1] J.W.S. Rayleigh, "The theory of Sound", (Dover, New York), 1945 (reprint).

[2] J. Curie, P. Curie, "Développement par pression de l'é'lectricite polaire dans les cristaux hémièdres à faces inclinées", C.R. Acad. Sci (Paris) 91:294, 1880.

[3] C.M. Chilowsky, M.P. Langévin,"Procídés et appareil pour production de sous-marins dirigés et pour la localsation à distances d'obstacles sons-marins", French patent no. 502913, 1916.

[4] K.T. Dussik, "On the possibility of using ultrasound waves as a diagnostic aid", Neurol Psychat., pp. 153-174, 1942.

[5] G.S.K. Wong, "Speed of sound in standard air", *J. Acoust. Soc. Am.,* vol. 79, pp. 1359-1365, 1986.

[6] O. Cramer, "The variation of the specific heat ratio and the speed of sound in air with temperature, pressure, humidity and CO_2 concentration", *J. Acoust. Soc. Am.,* vol. 93, no. 5, pp. 2510-2516, 1993.

[7] M. Geenspan, "Comments on 'Speed of sound in standard air' (J. Acoust. Soc. Am. 79, 1359-1366 (1986))", *J. Acoust. Soc. Am.,* vol.82, no.1, pp.370-372, 1987.

[8] G.S.K. Wong, "Response to 'Comments on 'Speed of sound in standard air' (J. Acoust. Soc. Am. 82, 370-372 (1987))", *J. Acoust Soc. Am.,* vol.82, no.1, pp.373-374, 1987.

[9] C.L. Morfey, G.P. Howell, "Speed of sound in air as a function of frequency and humidity", *J. Acoust. Soc. Am.,* vol.68, no.5, pp.1525-1527, 1980.

[10] G. P. Howell, C.L. Morfey, "Frequency dependence of the speed of sound in air.", *J. Acous. Soc. Am.,* vol.82, no.1, pp.375-376, 1987.

[11] J.F.Frederick, "Ultrasonic Engineering", John Wiley & Sons, Inc.,1965.

[12] I.A. Viktorov, "Rayleigh and Lamb waves – Physical theory and Applications", *Plenum Press, New York,* 1967.

[13] R. Stoneley, "Elastic waves at the surface of separation of two solids", *Proc. R. Soc. London.,* Series A, vol.116, pp. 416-428, 1924.

[14] M. Hirao, Y. Sotani, K. Takami, H. Fukuoka, "Love waves propagation in a solid with a coldworked surface layer", *J. Non Destr. Eval.*, vol. 2, pp. 51-55, 1981.

[15] H. Lamb, "On waves in an elastic plate", *Proc. R. Soc. London,* Series A, vol. 93, pp. 114-128, 1917.

[16] L.J. Bond, C-H. Chiang, C.M. Fortunko, "Absorption of ultrasonic waves in air at high frequencies (10-20MHz)", *J. Acoust. Soc. Am.,* vol. 92, no. 4, pt. 1, pp. 2006-2015, 1992.

[17] H.E. Bass, L.C. Sutherland, J.E. Piercy, L.B. Evans, "Absorption of Sound by the Atmosphere", in *Physical Acoustics*, vol. XVII, pp. 145-233, Academic press, New York, 1984.

[18] H.E. Bass, F.D. Shields, "Absorption of sound in air: High frequency measurements", *J. Acoust. Soc. Am.,* vol.62, no.3, pp.571-576,1977.

[19] H.E. Bass, H-J. Bauer "Atmospheric absorption of sound: Analytical expressions", *J. Acoust. Soc. of Am.,*, vol.52, no.3, pt.2, pp.821-825, 1972.

[20] B.D. Lawrence, J.A. Simmons, "Measurements of atmospheric attenuation at ultrasonic frequencies and the significance for echolocation by bats", *J. Acoust. Soc. Am.,* vol.71, no.3, pp.585-590,1982.

[21] ANSI S1.26 –1978 ASA 23-78, "Method for the calculation of the absorption of sound by the atmosphere", *American National Standards Institute, New York*, 1978.

[22] J. Krautkrämer, H. Krautkrämer, "Ultrasonic testing of materials", 4th edition, Springer-Verlag, New York 1990.

[23] F. A. Jenkins, H. E. White, "Fundamentals of Optics", (McGraw-Hill Book Company),3rd edition, 1956.

[24] F. Oberhettinger, "On transient Solutions of the Baffled Piston Problem", *J. Res. Natl. Bur. Stand*, vol. 65, pp. 1- , 1961.

[25] P.R. Stepanishen, "Transient Radiation from Pistons in an Infinite Planar Baffle", *J. Acoust. Soc. Am.*, vol. 49, no. 5, pp.1629-1638, 1970.

[26] J.C. Lockwood, J.G. Willette, "High-speed method for computing the exact solution for the pressure variations in the nearfield of a baffled piston", *J. Acoust. Soc. Am.,* vol. 53, no. 3, pp. 735-741. 1973.

[27] A. Freedman, "Sound Field of a Rectangular Piston", *J. Acoust. Soc. Am.,* vol. 32, no. 2, pp. 197-208, 1960.

[28] A. Sahin, A.C. Baker, "Ultrasonic pressure fields due to rectangular apertures", *J. Acoust. Soc. Am.*, vol. 96, no. 1, pp. 552-556, 1994.

[29] L.G. Ullate, J.L.S Emeterio, "Diffraction impulse response of rectangular transducers", *Acout. Soc. Am.,* vol. 92, no. 2, pp. 651-662, 1992.

[30] L.G. Ullate, J.L.S. Emeterio, "A new algorithm to calculate the transient near-field of ultrasonic phased arrays", *IEEE Trans. Ultrason. Ferroelec. Freq. Ctrl.,* vol. 39, no. 6, pp. 745-753, 1992.

[31] Tat-Jin Teo, "An improved Approximation for the Spatial Impulse Response of a Rectangular Transducer", *IEEE Trans. Ultrason. Ferroelec. Freq. Ctrl.*, vol. 45, no. 1, pp. 76-83. 1998.

[32] H. Masuyama, K. Nagai, K.Mizutani, "Quadratic-curve approximation of impulse responses to calculate radiated fields from rectangular transducers", *Japn. J. Applied. Physics.,* vol. 39, no. 5B, pp. 3144-3149, 2000.

[33] A.J. Hayman, P.D. Hanstead,. "Developments in direct ultrasonic visualization of defects", *Ultrasonics,* vol.17, no.3, pp.105-12, 1979.

[34] C.X. Deng, Xu. Qihong, R.E. Apfel, C.K. Holland. "Inertial cavitation produced by pulsed ultrasound in controlled host media", *J. Acoust. Soc. Am.,* vol.100, no. 2, pt.1, pp.1199-1208, 1996.

[35] H.T. O'Neil, "Theory of focusing radiators", *J. Acoust. Soc. Am.,* vol. 21, no. 5, pp. 516-526, 1949.

2 Review of Capacitive Ultrasonic Transducer Technology

2.1 Summary

This purpose of this chapter is to give an overview of capacitive (or electrostatic) transducer technology to date, from the basic condenser microphone to fully micromachined devices. Operation and construction methods are described, together with theories on the predicted frequency response of such transducers. Alternatives to the capacitance transducer are also examined.

2.2 The capacitive transducer

2.2.1 Background

The capacitive, (or electrostatic) ultrasonic transducer is primarily used for the transduction of ultrasound into air (or gas). This is due to its inherent low acoustic impedance (see below). Operation has also been demonstrated in liquids [1] (discussed further in Chapter 7). The device is similar in form to the condenser microphone [2], and is essentially a variable capacitor, consisting of a thin flexible membrane fixed over a ridged conducting backplate. The earliest known reference to such a device was by Wente in 1917 [3]. This utilised a thin metallic membrane (or diaphragm) separated from a back electrode by a 25μm air gap. It was demonstrated that this device had an undamped resonant frequency of approximately 17kHz. Later improvements to the design widened its bandwidth by increasing air damping, with the addition of grooves, or holes, in the backplate [4-6]. Further work reported by McLachlan [7] incorporated a solid dielectric layer between the backplate and front electrode to improve performance. However, these devices only had a useful bandwidth within the audio frequency range. Three years later, in 1937, Sell [8] reported a similar device with increased centre

frequency and bandwidth, incorporating concentric grooves in the backplate. However, in 1954 Kuhl et al [9] produced transducers capable of operation in the 50-100kHz range. His basic design, using a conducting contoured backplate and a thin (~10μm) metallised polymer film for the membrane, and was the basis for the more modern capacitive transducer designs. Further work shortly ensued, namely by Matsuzawa [10,11] who studied the effects of membrane thickness and backplate surface properties on the characteristics of the transducer.

2.2.2 Transducer construction

The construction of the polymer-based capacitive transducer, as described by Kuhl et al [9], consists of a thin flexible polymer membrane, metallised on one side and fixed with its insulating surface against a ridged contoured conducting backplate, as illustrated in Figure 2.1. During operation, a DC biasing voltage is usually applied between the backplate and the membrane, electrostatically attracting it to the backplate, trapping tiny air pockets. As a detector, an impinging ultrasonic wave causes the membrane to deflect, changing the capacitance of the device. Due to the applied DC bias voltage, this change in capacitance can be observed as a movement of charge on and off the 'plates' of the device, and amplified with a charge amplifier. For a source of ultrasound, the membrane can also be deflected, electrostatically, with the application of

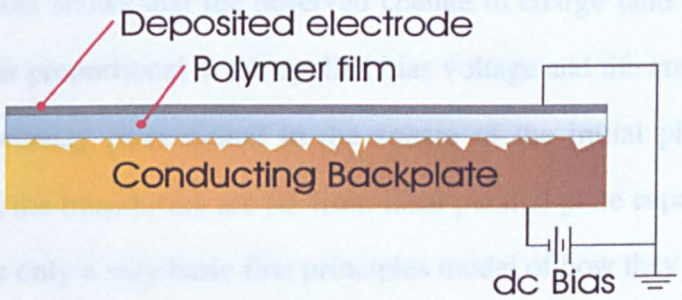

Figure 2.1: *Schematic diagram of the basic random backplate capacitive transducer*

pulsed voltages, often superimposed into a DC bias voltage to improve bandwidth. Due to the relatively low acoustic impedance of the membrane/air pocket system, the capacitance transducer is ideally suited for the transduction of ultrasound into air. Various studies have shown that the performance (centre frequency, bandwidth, and sensitivity) of a capacitive transducer is mainly controlled by the surface topology of the backplate [12].

Assuming a basic parallel plate capacitor model, with air as the dielectric, the capacitance, C, of the device would be given by the following:

$$C = \frac{A \cdot \varepsilon_o}{x} \tag{2.1}$$

where, A is the area of one of the plates, ε_o is the relative permittivity of free space, and x the plate separation. Hence, changes in the plate separation, Δx, cause changes in the capacitance of the device, ΔC. This is given by differentiation of equation (2.1):

$$\Delta C = -\frac{A \cdot \varepsilon_o}{x^2} \cdot \Delta x . \tag{2.2}$$

Assuming a constant biasing voltage, V_p, the observed change in charge, ΔQ, on the plates, due to this change in capacitance, ΔC, is given by:

$$\Delta Q = \Delta C \cdot V_p = -\frac{A \cdot \varepsilon_o}{x^2} \cdot \Delta x \cdot V_p . \tag{2.3}$$

Hence, this basic model shows that the observed change in charge (and thus the signal from the transducer) is proportional to the applied bias voltage and the area of one of the plates. It is also inversely proportional to the square of the initial plate separation. However, in practice, the transducers are far from ideal parallel plate capacitors, and the above calculations are only a very basic first principles model of how they operate.

2.2.3 Transducer manufacture techniques

As mentioned above, the characteristics of the polymer-based capacitive transducer have been found to be mainly dependent on the surface properties of the backplate. Thus, over the past few decades, this has been the focus of transducer design, with many different manufacturing techniques reported. However, these methods can all be generally classified into three main groups. The first utilises metallic backplates with random surface features that have either been mechanically roughened using grinding/polishing techniques, by shot peening, or other similar methods [13,14]. Devices constructed in this way were generally found to operate up to a few hundred kHz, for rough backplates, or up to 3MHz, for backplates with highly polished surfaces.

The second grouping utilise backplates with more controlled surface profiles, and hence more predictable responses. The majority of the studies in this group used polished backplates with 'V-grooves' machined into their surface [15-19]. These have generally been found to operate, predictably, up to a few hundred kHz. Other methods used to produce 'controlled' contoured backplates have included introducing pits into, or features onto, their surface, using photolithography [20], laser ablation [1,21], or silk screen printing [22].

The advent of silicon micromachining technology provided another means of producing accurate surface profiles. Work by Suzuki et al [23] described the fabrication of a transducer with a polished silicon backplate containing an array of etched square pits (typically $10\mu m^2$ to $50\mu m^2$). This was shown to have improved bandwidth over all previous designs. Further work by Schindel et al [24] reported that a similar device demonstrated a –6dB bandwidth extending from <100kHz to 2.3MHz. Figure 2.2 illustrates a schematic diagram of such a device (from [25]). The increased bandwidth of these devices, over its predecessors, can be explained as follows; the areas of membrane over the un-etched polished sections of the silicon wafer (i.e. in contact) tend to

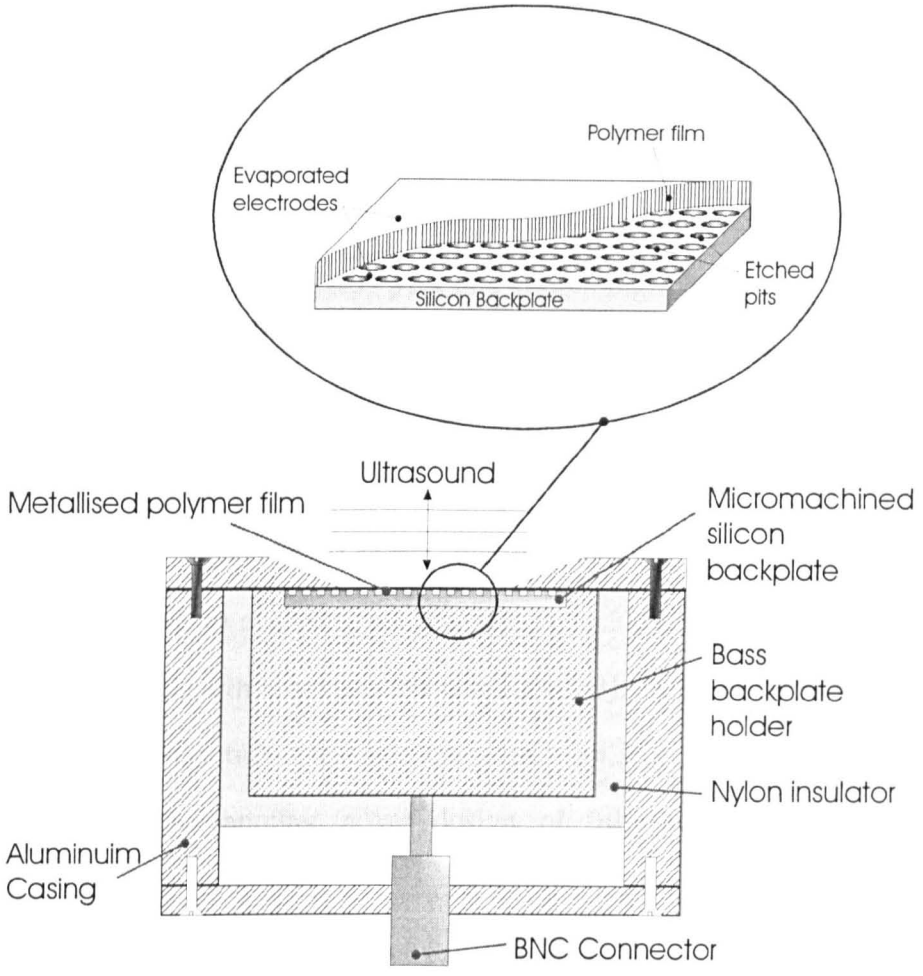

Figure 2.2: *Schematic diagram of a micromachined capacitive transducer.*

generate/receive the higher frequency signal components, while the areas over the etched parts (i.e. holes) tend to damp the membrane, and produce a lower frequency response.

The third, and most recent group of capacitive transducers, contains the so-called fully micromachined devices. These differ from the other types described above because the whole device, including the membrane, is fabricated using micromachining techniques. These transducers offer many advantages over those described previously, namely good reproducibility, ability to incorporate on-chip electronics, potential low-cost (when mass produced), and the ability to create arrays of separate elements. One of the fist device to be produced in this way was a silicon-based microphone, described by Hohm [26]. This was shortly followed by many other similar designs. Kuhnel and Hess [27] described a fully micromachined silicon device with a silicon nitride membrane and a structured silicon backplate. Another such device was described by Bergqvist et al

[28,29] which utilised a suspended surface micromachined metallic backplate above a membrane formed by bulk micromachining the back of the silicon substrate.

More recently, fully micromachined devices operating above 100kHz have been realised. The first of these is based on the lower frequency microphone design, constructed from two silicon wafers, with one containing the membrane, and the other performing as a backplate. It was demonstrated to have a flat frequency response up to 180kHz [30]. An alternative approach uses surface micromachining to produce a silicon nitride membrane supported above a silicon substrate [31-33]. In this design, the membrane is typically supported at 50μm intervals, creating a hexagonal cell structure. The devices were found to operate from 1.6MHz to 11.5MHz (depending on fabrication parameters), with bandwidths between 5% and 20% [33]. A similar design, but utilising a polysilicon membrane, has also been presented [34,35]. During this research, the author has investigated another novel design of fully micromachined transducer, consisting of a surface micromachined silicon nitride membrane, typically 1-2μm thick, and 50μm-5mm square in size, differing to previous ultrasonic transducer designs in that it is completely unsupported (i.e. one continuous membrane), over a 2μm deep air cavity [36]. This work is discussed later in Chapters 3 and 4.

2.3 Theoretical frequency response of the capacitive transducer

There have been a number of approaches used to attempt to model the behaviour of capacitive transducers, mostly with limited success. The first simple model assumes that the membrane acts as a frictionless piston above an air pocket acting as a spring. The frequency at which such a system would resonate can be calculated from [19]:

$$f = \frac{1}{2 \cdot \pi} \sqrt{\frac{\gamma \cdot P_a}{\rho \cdot d_a \cdot d_f}} \qquad (2.4)$$

where, γ is the adiabatic constant for air, P_a the atmospheric pressure, ρ the density of the film, and d_f *and* d_a the thickness and depth of the membrane and air gap respectively.

For a condenser microphone that contains a well-defined air gap, Equation (2.4) is easy to evaluate. However, for the case of a high frequency transducer with a thin membrane lying on top of a randomly rough backplate, the air gap, d_a, is much more difficult to predict accurately. The average gap can be estimated from either the measured nominal capacitance of the device, the surface roughness parameter, R_a, of the backplate, or a combination of them both. In the case of machined backplates, the air gap calculation is much easier as it is defined by the depth of the groove or hole. Using these methods, Equation (2.1) has been used to predict, with limited success, the frequencies of a number of devices (with random and machined backplates) operating up to approximately 600kHz [37].

An alternative model, used by several authors [9, 14, 23, 31-32, 37], assumes the transducer is a uniform circular membrane fixed around its periphery (i.e. a drum skin), with its fundamental resonant frequency given by [38]:

$$f = \frac{2.4048}{\pi \cdot D}\sqrt{\frac{T}{\rho_f}} \qquad (2.5)$$

where, T is the tension, ρ_f the density, and D the diameter of the membrane. With the early devices, consisting of a membrane over a defined air gap, this model showed some promise. However, for the more modern design devices, with the membrane in contact with the backplate, less success has been achieved. Work with these devices (random and machined backplate designs) showed that the tension in the membrane had marginal affect on the overall response of the transducer [23,24], hence implying the frequency response depended more on the interaction between the membrane and the air layer beneath it. Yet, with the latest fully-micromachined devices, with well-defined air gaps and tensioned membranes, this model has been used again, with reasonable success

[31,32]. However, it still neglects the effect of membrane stiffness and the air gap beneath it.

The next model [39] was developed exclusively for grooved backplate transducers. It assumes the transducer resembles an array of separate resonator like elements [40]. Each of these elements can then be described with a Helmholtz resonator model, with a resonant frequency given by:

$$f = \frac{c}{\pi}\sqrt{\frac{\rho_o}{2 \cdot \sigma \cdot h}} \tag{2.6}$$

where, h is the depth of the groove, ρ_o the density of the air, c sound velocity in air, and σ the mass per unit area of the membrane. It can be seen that this has similar form to Equation (2.4).

More recently, Anderson et al [20] proposed a more complex model, where the electrical and mechanical characteristics of the device were lumped together (known as a lumped parameter model). In the mechanical half of the model, the diaphragm is treated as a stressed plate, rather than a membrane, hence including bending stiffness effects (unlike the models outlined above). Membrane tension, density, electrostatic pressure, external acoustic pressure, and pressure within the air gap were also taken into account. The electrical section of the model uses a simple parallel plate theory, defining the instantaneous capacitance of the device, in terms of its nominal plate separation (air gap) and average deflection. These two 'halves' of the model are then lumped together, and a resultant equivalent circuit is developed.

Improvements to this model have since been made by Sun et al [41], who corrected a mistake made in the calculation of the equivalent circuit. The model was also modified, by effectively combining two separate models, one for the region over the cavities, and the other for that over the backplate surface. This improved the agreement between theoretical predictions and experimentally obtained data.

The models outlined above demonstrate that the operation of capacitive transducer is very complex, with many factors affecting its characteristics. The lumped

parameter model is by far the most accurate. However, it is also very complex requiring many parameters whose derivations are still (as yet) unpublished.

2.4 Alternatives to the capacitive transducer

2.4.1 Piezoelectric transducers

It was noted in the previous chapter, that piezoelectric based devices were (and still are) by far the most widely used means of detecting and creating ultrasound. This is mainly because piezoelectric transducers are generally inexpensive, rugged, compact, hence well suited to an industrial environment. They have been successfully developed for use in solids (contact transducers) and liquids (immersion transducers). However, for air-coupled applications a problem arises, due to the high acoustic impedance mismatch of the piezoelectric material, and that of air. This leads to very poor transduction for air-coupled applications.

This impedance mismatch is illustrated by Table 2.1, which contains the parameters of some significant materials commonly used in the construction of piezoelectric transducers. The transmission coefficients for the different materials into air and water are also shown. These were calculated using Equation (1.10) from Chapter 1.

From Table 2.1, it can be seen that for coupling into air, the majority of the acoustic energy is reflected back into the piezoelectric material, and only a small fraction is actually transmitted. There have been various solutions to this problem. The first, which had limited success, was to use a high power drive along with high gain amplifiers [42,43]. An alternative to this method is to reduce the effective acoustic impedance of the piezoelectric element, hence improving the transmission efficiency of the transducer. A variety of solutions have been proposed, such as the use of a metallic [44] or polymer [45] membrane driven by a piezoelectric element, or by a conical shell, again driven by

Material	Density ρ (kg·m^{-3})	Velocity of propagation c_L (m·s^{-1})	Acoustic impedance Z (kg·m^{-2}·s^{-1})	T_{air}	T_{water}
Quartz SiO_2	2650	5760	15.3×10^{6}	10.8×10^{-5}	0.325
Zirconate Piezoceramics PZT-5A	7750	3880	30×10^{6}	5.5×10^{-5}	0.181
Lead-niobate piezoceramics $PbNb_2O_6$	5800	2800	16×10^{6}	10.3×10^{-5}	0.313
Piezopolymer PVDF	1880	2260	4.6×10^{6}	35.9×10^{-5}	0.742
Air @ 20°C	1000	1483	1.5×10^{6}	1.0	110.3×10^{-5}
Water 20°C	1.2	344	413.8	110.3×10^{-5}	1.0

Table 2.1: *Acoustical properties of piezoelectric materials (from [46]), with their calculated transmission coefficients into air and water.*

a piezoelectric element, that produces Lamb waves across its surface which 'leak' into the air [47].

Another alternative is to use a matching layer (of $\lambda/4$ thickness) so that:

$$Z_m^{\,2} = Z_A \cdot Z_B \qquad (2.7)$$

where, Z_A and Z_B are the impedances of the two media A and B, and Z_m is that of the matching layer. If this equation is satisfied, all the energy is coupled from medium A to medium B. This would, at first glance, seem ideal, however there are disadvantages; the first is the frequency dependence of the required thickness of the matching layer ($\lambda/4$), therefore reducing the bandwidth of the device. Secondly, is the problem of finding a suitable material for the matching layer. To satisfy Equation (2.4), Z_m needs to be approximately 0.1×10^{6} Kgm^{-3}s^{-1} (0.1 MRayl). Unfortunately, there are very few suitable materials with such an impedance. However, there have been various attempts at finding a suitable material, such as balsa wood [48], cork [49], aerogels (compacted hollow glass spheres) [50], and silicone rubber [51]. Multiple matching layers have also tried with some success [52]. However, generally, the matching layer approach improves sensitivity at the expense of bandwidth. Another method is to use piezoelectric materials

that have lower acoustic impedance. Polyvinylidene difluoride (PVDF) is one such material, and has shown some promise when used in air [53].

An alternative to the approaches outlined above, is to reduce the effective impedance of the piezoelectric element itself. This can be achieved with piezocomposite structures, where parts of the piezoelectric material, usually a piezoceramic, are removed and replaced with a filler material, usually epoxy resin. This reduces the density and acoustic velocity of the material, and hence its acoustic impedance. There are various types of piezocomposite structure, and they are defined in terms of the mechanical connectivity of the two different materials. For air-coupled work, the 1-3 connectivity piezocomposite has shown the most promise [54-56]. In this configuration, the piezoceramic is formed into vertical square pillars with a filler material between, as illustrated in Figure 2.3. This is usually achieved by machining a series of slots into single block of piezoceramic, and then filling with epoxy. A matching layer is then usually then placed on top of the device covering one end of the pillars, while a backing layer is fixed to the other. For operation as a source, the piezoceramic pillars are usually excited in their thickness resonance mode. The bandwidth of such devices is heavily dependant on the backing layer, with higher damping resulting in broader bandwidth. However, this increased damping reduces the sensitivity of the device. Recently, improvements in sensitivity have been made by coupling the thickness resonance, with the first lateral resonance of the device, enabling increased bandwidths, of approximately 1.5MHz, centred at 1.2MHz being reported, with reasonable sensitivities [57].

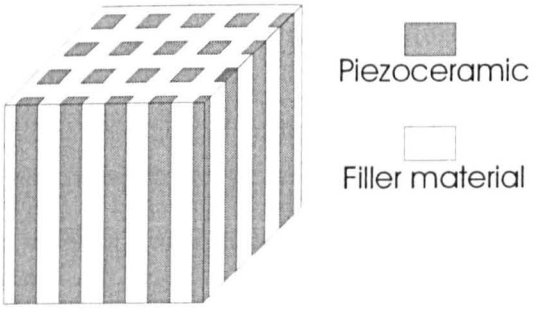

Figure 2.3: *Schematic diagram of a 1-3 connectivity piezocomposite structure.*

Disadvantages of these devices are firstly, their inherent complexity of construction, and due to this complexity, various unwanted internal modes of resonance. Their sensitivity has also been demonstrated to be less than capacitive transducers [57]. However, they are still a viable alternative for the transduction of ultrasound into air.

2.4.2 Other alternatives

There are also various other methods with which ultrasound can be generated and/or detected using non-contact methods in air. Those worthy of mention here are laser systems [58,59], spark discharge, magnetostrictive materials, and the electromagnetic ribbon transducer [60].

2.5 Conclusion

This chapter has described the development of the capacitive transducer, from its original form as the condenser microphone, to fully micromachined devices. Modelling techniques commonly used for such devices have also been discussed. Alternatives to the capacitive transducer, for the transudation of ultrasound into air have also been described.

2.6 References

[1] A.G. Bashford, D.W. Schindel, D.A. Hutchins, "Micromachined ultrasonic capacitance transducers for immersion applications", *IEEE Trans. Ultrason. Ferroelect. Freq. Control,* vol. 45, no.2, pp. 367-375, 1988.

[2] G.S.K. Wong, A.F.W. Embleton, "AIP Handbook of condenser microphones-Teory, calibration and measurements", AIP Press, New York, 1995.

[3] E. C. Wente, "A condenser transmitter as a uniformly sensitive instrument for the absolute measurement of sound intensity", *Phys. Review*, vol. 10, pp. 39-63, 1917.

[4] I.B. Crandall, "Air-damped vibrating system – theoretical calibration of the condenser transmitter", *Phys. Rev.,* vol. 11, pp. 449-460, 1918.

[5] E.C. Wente, "The thermophone", *Phys. Rev.,* vol. 19, pp. 333-345, 1922.

[6] E.C. Wente, "Sensitivity and precision of the electrostatic transmitter for measuring sound intensities", *Phys. Rev.,* vol. 19, pp. 498-503, 1922.

[7] N.W. McLachlan, "Loudspeakers", (Clarendon Press, Oxford), 1934.

[8] H. Sell, "Eine neue Methode zur Umwandlung mechanischer Schwingungen in elektrische und umgekehrt", *Z. Techn. Phys.,* vol. 18, 1937.

[9] W. Kuhl, G.R. Schröder, F.K. Schröder, "Condenser transmitters and microphones with solid dielectric for airborne ultrasonics", *Acoustica,* vol. 4, no. 5, pp. 519-532, 1954.

[10] K. Matsuzawa, "Condenser microphones with plastic diaphragms for airborne ultrasonics I", *J. Phys. Soc. Japan,* vol. 13, 1533-1543, 1958.

[11] K. Matsuzawa, "Condenser microphones with plastic diaphragms for airborne ultrasonics II", *J. Phys. Soc. Japan,* vol. 15, 167-174, 1960.

[12] H. Carr, W.S.H. Munro, M. Rafiq, C. Wykes, "Developments in capacitive transducers", *Non-destruc. Test. Eval.,* vol. 10, no. 1, pp. 3-13, 1992.

[13] F. Messa, "Ultrasonic transducers for use in air", *Proc. IEEE,* vol. 53, no. 10, pp. 1363-1371, 1965.

[14] J. Merhaunt, "A contribution to the theory of electrostatic transducers based on the electrostatic principals", *Acustica,* vol. 17, pp. 283-293, 1967.

[15] J. Hietanen, P. Mattila, J. Stor-Pellin, F. Tsuzuki, H. Väätäjä, K. Sasaki, M. Luukkala, "Factors affecting the sensitivity of electrostatic ultrasonic transducers", *Measur. Sci. & Tech.,* vol. 4, pp 1138-1142, 1993.

[16] J. Hietanen, J. Stor-Pellinen, M. Luukkala, "A model for an electrostatic ultrasonic transducer with a grooved backplate", *Meas. Sci. Technol.,* vol. 3, pp. 1095-1097, 1992.

[17] P. Mattila, J. Hietanen, "Bandwidth control of an electrostatic ultrasonic transducer", *Sensors Actuators A,* vol. 45, pp. 203-208, 1994.

[18] G.J. Brown, D. Reilly, "Ultrasonic tomographic imaging of solid objects in air using an array of fan-shaped-beam electrostatic transducers", *Ultrasonics,* vol. 34, no. 2-5, pp. 111-115, 1996.

[19] M. Rafiq, C. Wykes, "The performance of capacitive ultrasonic transducers using v-grooved backplates", *Meas. Sci. Technol.,* vol. 2, pp. 168-174, 1991.

[20] M.J. Anderson, J.A. Hill, C.M. Fortunko, N.S. Dogan, R.D. Moore, "Broadband electrostatic transducers: modelling and experiments", *J. Acoust. Soc. Am.,* vol. 97, no. 1, pp. 262-272, 1995.

[21] D.W. Schindel, D.A. Hutchins, "Capacitance devices for the controlled generation of ultrasonic fields in liquids", *IEEE Ultrasonics Symposium Proceedings, Florida, USA,* vol. 1, pp. 301-304, 1991.

[22] W.S.H. Munro, C. Wykes, "Arrays for airbourne 100kHz ultrasound", *Ultrasonics,* vol. 32, no. 1, pp. 57-64, 1993.

[23] K. Suzuki, K. Higuchi, H. Tanigawa, "A silicon electrostatic ultrasonic transducer", *IEEE Trans. Ultrason. Ferroelect. Freq. Control,* vol. 36, pp. 620-627, 1989.

[24] D.W. Schindel, D.A. Hutchins, L. Zou and M Sayer, "The design and characterisation of micromachined air-coupled capacitance transducers", *IEEE Trans. Ultrason. Ferroelect. Freq. Control,* vol. 42, pp. 42-51, 1995.

[25] D.W. Schindel, D.A. Hutchins, "Air-coupled ultrasonic transducer", *US Patent,* 5 287 331, Feb. 1994.

[26] D. Holm, "A subminiature condenser microphone with silicon nitride membrane and silicon back plate", *J. Acoust. Soc. Am,* vol. 85, no. 1, pp. 476-480, 1989.

[27] W. Kuhnel, G. Hess, "Micromachined subminiature condenser microphones in silicon", *Sensors & Actuators A,* vol. 32, no. 1-3, pp. 560-564, 1992.

[28] J. Bergqvist, J. Gorbet, "Capacitive microphone with a surface micromachined backplate using electroplating technology", *J. Microelectromechanical Sys.,* vol. 3, no. 2, pp. 69-75, 1994.

[29] G.M. Sessler, "Silicon microphones", *J. Audio Eng. Soc.,* vol. 44, no. 1-2, pp. 16-22, 1996.

[30] C. Thielemann, G.M. Sessler, "Capacitive silicon sensors for ultrasound", *Acoustica,* vol. 83, no. 4, pp. 715-720, 1997.

[31] M.I. Haller, B.T. Khuri-Yakub, "A surface micromachined electrostatic ultrasonic air transducer", *IEEE Trans. Ultrason. Ferroelec. Freq. Control,* vol. 43, pp. 1-6, 1996.

[32] I. Ladabaum, X. Jin, H.T. Soh, A. Atalar, B.T. Khuri-Yakub, "Surface micromachined capacitive ultrasonic transducers", *IEEE Trans. Ultrason, Ferroelec, Freq. Control,* vol. 45, no.3, pp. 678-690, 1998.

[33] I. Ladabaum, B.T. Khuri-Yakub, D. Spoliansky, "Micromachined ultrasonic transducers: 11.4MHz transmission in air and more", *Applied Phys. Lett.* , vol. 68, no. 1, pp. 7-9, 1996.

[34] P.-C. Eccardt, K. Niederer, T. Scheiter, C. Hierold, "Surface micromachined ultrasound transducers in CMOS technology", *Proc. IEEE Ultrasonics Symposium,* pp. 959-926, 1996.

[35] P.-C. Eccardt, K. Niederer, "Micromachined ultrasonic transducers with improved coupling factors from a CMOS compatible process", *Ultrasonics,* vol. 38, pp. 774-780, 2000.

[36] R.A. Noble, A.D.R. Jones, T.J. Robertson, D.A. Hutchins, D.R. Billson, "Novel wide-bandwidth micromachined ultrasonic transducers", *IEEE Trans. Ultrason. Ferroelec. Freq Control.,* (accepted for publication, in press), 2001.

[37] H.Carr, C. Wykes, "Diagnostic measurements in capacitive transducers", *Ultrasonics,* vol. 31, pp. 13-20, 1993.

[38] L.E. Kinsler, A.R. Frey, A.B. Coppens, J.V. Sanders, "Fundamentals of acoustics", (Wiley, New York.) 3rd edition, 1982.

[39] J. Hietanen, J. Stor-Pellinen, M. Luukkala, P. Mattile, F. Tsuzuki, K. Sasaki, "A Helmholtz resonator model for an electrostatic ultrasonic air transducer with a V-grooved backplate", *Sensors Actuators A,* vol. 39, pp. 129-132, 1993.

[40] J. Hietanen, J. Stor-Pellinen, M. Luukkala, "Amodel for an electrostatic ultrasonic transducer with a grooved backplate", *Meas. Sci. Technol.,* vol. 3, pp. 1095-1097, 1992.

[41] L. Sun, M. Sayer, D.W. Schindel, L. Zou, "Modeling and Optimisation of Micromachined Air-Coupled Capacitance Transducers", *IEEE Proc. Ultrasonics Sympositum,* vol. 2, pp. 979-982, 1997.

[42] D.E. Chimenti, C.M. Fortunko, "Characterisation of composite prepeg with gas-coupled ultrasonics", *Ultrasonics,* vol. 32, pp. 261-264, 1994.

[43] A.J. Rogovosky, "Development and application of ultrasonic dry-contact and air-contact C-scan systems for non-destructive evaluation of aerospace composites", *Mat. Eval.,* vol. 49, pp. 1491-1497, 1991.

[44] M. Babic, "A 200kHz Ultrasonic transducer coupled to the air with a radiating membrane", *IEEE Trans. Ultrason. Ferroelec. Freq. Control.,* vol. 38, no. 3, pp. 252-255, 1991.

[45] L. Durris, L. Goujon, A. Pelourson, P. Gonnard, M. Brissaud, C. Richard, "Airborne Ultrasonic Transducer", *Ultrasonics*, vol. 34, pp. 153-158, 1996.

[46] S. Kočiš Z. Figura, "Ultrasonic measurements and technologies", (Chapman & Hall, London). First Edition, 1996.

[47] H. Dabirikhah, C.W. Turner, "Leaky plate wave air borne ultrasonic transducer", *Electronic Letters,* vol. 30, no. 8, 1549-1550, 1994.

[48] J. Stor-Pellinen, M. Oksanen, R. Vuohelainen, J. Rantala, J. Hartikainen, M. Luukkala, "Photoacoustic inspection of matching layers of ultrasonic air-coupled transducers", *Proc. IEEE Ultrason. Symp.,* vol. 1, pp. 665-668, 1989.

[49] S. Schiller, C.-K. Hsieh, C.-H. Chou, B.T. Khuri-Yakub, "Novel high frequency air transducers", *Rev. Prog. Quant. NonDestr. Eval.,* vol. 9, pp. 795-798, 1990.

[50] O. Krauß, R. Gerlach, J. Fricke, "Experimental and theoretical investigations of SiO_2-aerogel matched piezo-transducers", *Ultrasonics,* vol. 32, pp. 217-222, 1994.

[51] J.D. Fox, B.T. Khuri-Yakub, G.S. Kino, "High frequency acoustic wave measurements in air", *Proc. IEEE Ultrason. Sympos.,* vol. 1, pp. 581-584, 1993.

[52] W. Pajewski, M. Szalewski, "Ultrasonic transducers radiating into the air in the frequency range 50-250kHz", *Archives of Acoustics*, vol. 17, no. 4, 511-523, 1992.

[53] L. Capineri, S.A. Fiorillo, L. Masotti, S. Rocchi, "Array of PVDF sensors for ultrasonic imaging in air", *Proc. IEEE Ultrason. Sympos.,* vol. 1, pp. 487-490, 1994.

[54] T.R. Gururaja, W.A. Schultze, L.E. Cross, R.E. Newnham, B.A. Auld, Y.J. Wang, "Piezoelectric composite materials for ultrasonic transducer applications Part I: Resonant modes of vibration of PZT rod-polymer composites", *IEEE Trans, Son, Ultrason,* vol. 32, pp. 481-498, 1985.

[55] T.R. Gururaja, W.A. Schultze, L.E. Cross, R.E. Newnham, "Piezoelectric composite materials for ultrasonic transducer applications. Part II: Evaluation of ultrasonic medical applications", *IEEE Trans. Son. Ultrason.,* vol. 32, pp. 499-513, 1985.

[56] J.A. Hossack, G. Hayward, "Finite-element analysis of 1-3 composite transducers", *IEEE Trans. Ultrason. Ferroelec. Freq. Control,* vol. 38, pp. 618-629, 1991.

[57] A. Gachagan, G. Hayward, "Improving the bandwidth of 1-3 connectivity composite receivers using mode coupling", *J. Acoust. Soc. Am.,* vol. 103, no. 6, pp. 3344-3352, 1998.

[58] D.A. Hutchins, "Ultrasonic generation by pulsed lasers", *in Physical Acoustics – principals and methods,* ed. W.P. Mason & R.N. Thurston, vol. XVIII, Academic press, New York, pp. 21-123, 1998.

[59] R.J. Dewhurst, Q. Shan, "Optical remote measurement of ultrasound", *Meas. Sci. Technol,* vol. 10, pp. 139-168, 1999.

[60] C.S. M^{c}Intyre, "The development of air-coupled ultrasonic transducers", *Ph.D. Thesis,* University of Warwick, 1999.

3 *Surface Micromachined Silicon Transducers- Fabrication and Characterisation*

3.1 Summary

This chapter examines the characterisation and development of a novel type of silicon surface micromachined ultrasonic transducer. These transducers differ from other similar devices in that they consist of a thin single silicon nitride membrane, with large lateral dimensions, over an air cavity, whereas devices reported elsewhere utilise a cell geometry, with a single transducer consisting of many (1000's) of individual membranes and cavities.

The first section outlines the fabrication procedure used to produce these devices. This is followed by examination of their static characteristics, in terms of their membrane deflections with an applied d.c. bias, and capacitance-voltage characteristics to aid in the understanding of their operation.

The second section outlines initial characterisation experiments performed to examine their dynamic ultrasonics characteristics in air; with their frequency response and sensitivity measured using a variety of techniques. Experiments are performed to study the effects of membrane thickness, membrane size, and applied bias on the transducers characteristics. This work reported in this chapter has been the subject of several publications [1-3].

The final section describes preliminary experiments performed to examine the characteristics of these devices when immersed in liquids.

3.2 Introduction

Recently there has been increased interest in the development of capacitive ultrasonic transducers that are fully fabricated by micromachining processes. Such

devices have inherent advantages over their polymer film / ridged backplate predecessors. These are, namely, reproducibility, ease of manufacture, high controllability, realisation of arrays of discrete elements, incorporation of on chip drive/receive electronics, and potential low-cost when mass-produced.

These high frequency ultrasonic devices have evolved from earlier work with audio frequency silicon-based microphones [4-9], one of the first of which was produced by Holm et al [4], consisting of a silicon nitride membrane, and a silicon backplate. Kuhnel and Hess [7] also described a similar silicon microphone, fabricated using micromachining to produce a silicon nitride membrane and structured silicon backplate. Other novel fabrication techniques have included a surface micromachined, electroplated metallic backplate suspended above a bulk micromachined silicon membrane [8]. However, it is only relatively recently that devices for use above 100kHz have been studied. Such a device was described by Thielemann et al [10], which was based on the lower frequency microphone design, constructed from two bonded silicon wafers, one containing a back etched membrane, with the other acting as a backplate. This was demonstrated to exhibit a flat frequency response up to 180kHz. Transducers for operation in the MHz region require thinner membranes than those employed in the construction of the lower frequency microphones. Work with transducers fitted with polymer membranes has shown that membrane thicknesses below 5μm are typically required for efficient operation in excess of 1MHz [11]. Hence, fully micromachined high frequency transducers generally utilise membranes below 2μm in thickness.

Work with these high frequency transducers has been reported by a variety of authors, with a number of different design approaches. The first to be described here are produced by Stanford University [12-17]. Their transducer design utilises a Low Pressure Chemical Vapour Deposition (LPCVD) silicon nitride membrane above a silicon substrate containing a lower electrode on its surface. This membrane is typically supported at 50μm intervals, creating a hexagonal cell structure. Each transducer consists of a large number of cells (typically 1000's), the sidewalls of which support the

membrane. Such devices have been reported to operate in air from 1.6MHz to 11.5MHz (dependent on fabrication parameters), with bandwidths of between 5% and 20% [13]. Generally, each hexagonal cell is highly resonant, and the overall bandwidth of a transducer is controlled by careful sizing (and hence in this case its resonant frequency) of its individual cells. Operation has also been demonstrated in liquids with increased bandwidth due to higher damping and improved impedance match of the membrane with the liquid medium [15].

The second design approach has been developed by Siemens AG, Germany [18, 19]. This again utilises the cell approach. However, this time the device fabrication is integrated into a standard BiCMOS process, using only industry standard layers to construct the device. The membrane itself is fabricated from a 400nm thick capacitor polysilicon layer of the process, with a field oxide (600nm thick) acting a sacrificial layer, hence resulting in a 600nm air cavity under the membrane. The use of the BiCMOS process to fabricate the transducer has advantages as it allows the incorporation of on-chip electronics, and production at standard IC foundries. However, it also has disadvantages, as the BiCMOS process is fixed, and the materials deposited during the fabrication are optimised for their electrical characteristics, and cannot be altered. Hence, membrane properties, such as thickness and stresses, and depth of air gap, cannot be easily controlled.

This chapter describes the development and characterisation of an alternative type of fully micromachined capacitive transducer. These devices consist of a single large silicon nitride membrane up to 5mm wide, self supported around its periphery above an air cavity. This differs to the aforementioned devices as with these a single complete transducer consists of a large number of cells (1000's), each of only ~40μm or so in diameter.

The first section of this chapter describes the fabrication process used to produce the transducers. This is followed by a section examining membrane dynamics by measurement of their static membrane displacements and capacitance-voltage

characteristics. Their dynamic characteristics are then examined, in terms of their sensitivity and frequency response in air. In the final section a set of preliminary measurements are performed with the transducers used in immersion.

3.3 Device Fabrication

These devices were fabricated in collaboration with the Defence Evaluation Research Agency (DERA), Malvern, UK, using their in-house silicon micro-fabrication facility. The fabrication procedure used a low temperature, CMOS compatible, surface micromachining process. An advantage of this facility is that the post-processing of devices onto a silicon substrate after the fabrication of CMOS signal processing electronics would be possible as the maximum temperature used in this process is approximately 400°C.

A scanning electron microscope (SEM) micrograph of a typical 1mm square device is shown in Figure 3.1. The transducer consists of a thin silicon nitride (Si_3N_4) membrane, typically 0.5μm to 2μm in thickness. This is positioned at a controlled distance from a fixed lower electrode formed on the silicon substrate. The air gap between the moveable membrane and fixed electrode is nominally 2μm.

Figure 3.2 shows the fabrication process for these transducers. Firstly, a 4-inch [100], silicon wafer was insulated with a 500nm layer of thermally grown silicon oxide. The lower, fixed, electrode was then formed by sputtering a 200nm layer of aluminium silicon (AlSi), and defined using optical lithography and dry reactive-ion etching (RIE), based on chlorine chemistry (BCL_3 as the primary gas), see (a). The sacrificial layer was then defined by spin-coating a layer of polyimide onto the substrate and curing in a nitrogen atmosphere at 370°C. This was then subsequently etched, again using optical lithography and chlorine based RIE, to leave islands of sacrificial polyimide (b). Note that the thickness of this layer defines the air gap between the lower (fixed) and upper (movable) electrodes, and was typically 2μm.

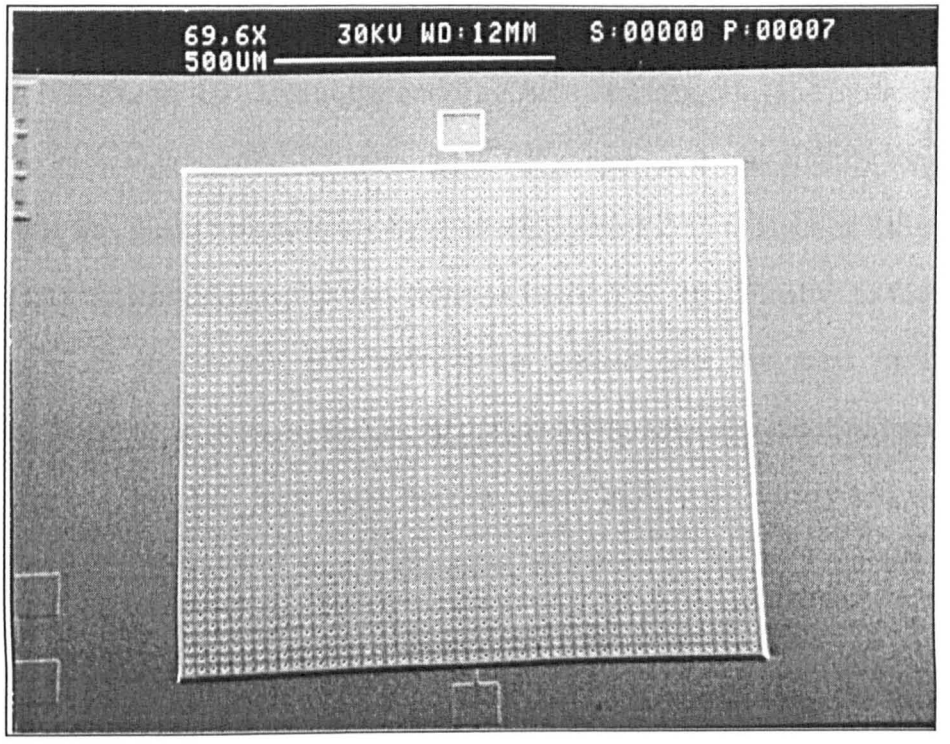

Figure 3.1: *SEM micrograph of a typical 1mm square device.*

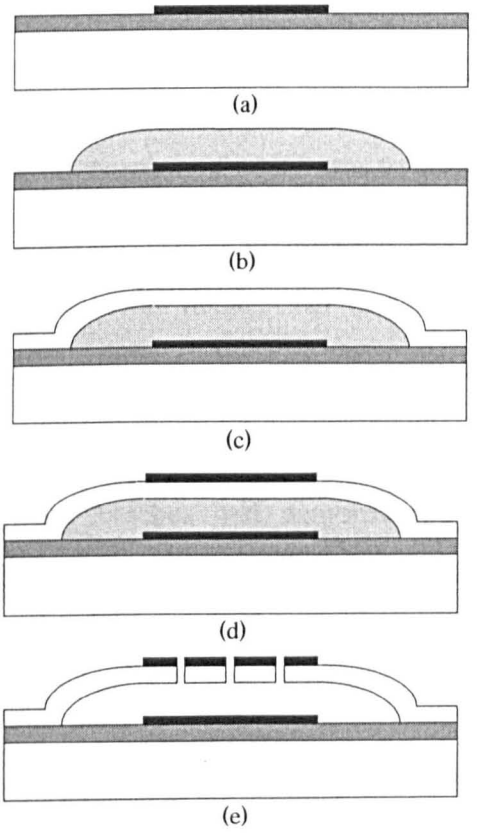

Figure 3.2: *Process flow for the fabrication of the transducers (Note, curvature of membrane sides is exaggerated).*

The membrane was formed using a plasma enhanced vapour deposition (PECVD) of Si_3N_4 at 400°C, over the entire substrate surface (c). The intrinsic stress of this membrane was controlled by varying the RF power, so it was slightly tensile. The top electrode was then formed, firstly by sputtering with a 200nm layer of AlSi, and then defined using optical lithography and chlorine based RIE (d). Finally, to form the air cavity under the membrane, etch holes were defined over the areas of sacrificial polyimide. These holes were created using optical lithography and chlorine based RIE to etch through the top AlSi layer, and fluorine based RIE to etch the Si_3N_4 membrane layer. These were typically of 3μm in diameter, on a pitch of 20μm. The removal of the sacrificial polyimide layer, and hence the release of the membrane, was then performed using a dry etch process with oxygen plasma RIE, for approximately four minutes (e). This process has advantages over traditional wet techniques, where stiction problems could occur, hampering the release of the membrane from the substrate.

Over the period of this study, a number of devices from three different batches have been supplied by DERA. These consisted of two preliminary test batches, (numbers 97204 and 97223), the purpose of which was to tailor the fabrication process to optimise their membrane properties (such as intrinsic stress). After these, a larger optimised batch (number 98163) was made. All these batches consisted of devices fabricated with 1μm and 2μm nominal thickness membranes. In addition, the optimised 98163 batch, was also fabricated with nominal 0.5μm thick membranes, as initial testing with the two preliminary test batches had demonstrated that improved frequency response resulted with the thinner membraned devices (as will be shown later). The physical size of transducers produced also varied with the batches. The first two preliminary runs had devices ranging from 20μm to 1mm square. However, initial testing with these had shown the sensitivity of the smallest devices to be relatively low (due to their size), hence, after discussions with DERA, the optimised batch (98163) consisted of devices ranging from 1mm to 5mm square. The fabrication process also differed slightly with this batch as a re-flow stage was added after the definition of the

polyimide sacrificial layer to smooth the edges of the sacrificial islands. This resulted in devices whose membranes had slightly rounded corners, hence slightly altering the geometry of the membrane support mechanism. This was done to alleviate problems encountered with the edges of the membrane being etched during the definition of the etch holes, due to the photoresist not covering the 'sharp' corners sufficiently. The properties of these device batches, including the relevant wafer numbers, are summarised in Table 3.1.

The transducers were supplied mounted in 24-pin DIL prototype packages. To allow electrical connections to these, a test fixture was constructed with a 24-pin DIL socket connected to a number of BNC terminals. This was housed in a shielded die-cast aluminium box to reduce electrical noise. Provision was also made for an optical rod mount on the box, to enable accurate alignment during the characterisation procedures. A photograph of a selection of packaged devices is shown in Figure 3.3(a) along with a photograph of the test fixture box (b).

Batch No.	Wafer No(s).	Nominal membrane Thickness	Nominal air gap	Device sizes
97204	A3	1μm	2μm	20μm, 50μm, 250μm, 500μm, 1mm Square
97204	A8	2μm	2μm	"
97223	A2	1μm	2μm	"
97223	A7	2μm	2μm	"
98163	A7/A8	0.5μm	2μm	1mm, 2mm 3mm, 5mm Square, 1mm Circular
98163	A9/A10	1μm	2μm	"
98163	A12/A13	2μm	2μm	"

Table 3.1: *Summary of the properties of the different batches of device supplied by DERA (Malvern).*

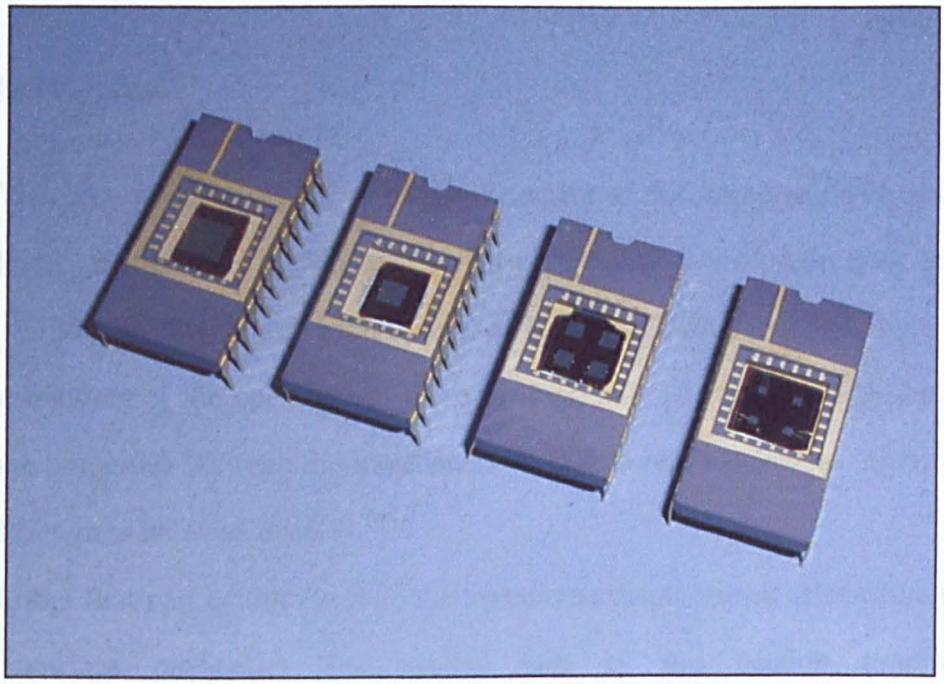

(a)

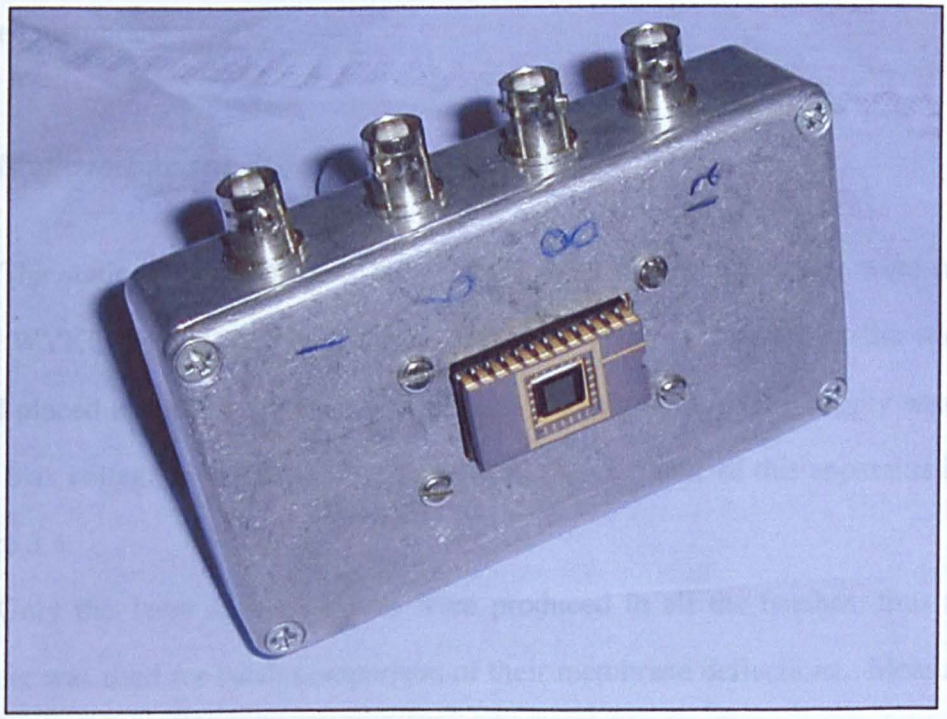

(b)

Figure 3.3: *Photographs of (a) a selection of micromachined transducers mounted in 24-pin DIL packages, and (b) one of the test fixture boxes used to allow electrical connections to the devices via BNC leads.*

3.4 Static Testing

3.4.1 Background

This section examines the static displacement of the membrane with applied d.c. bias voltage. It illustrates the differences between the first two preliminary batches of devices (97204 and 97223), and the optimised batch (98163). This was done to aid in the understanding of the operation of these devices, and examine the differences in the membrane properties between the transducers from different batches, as initial tests had shown differences between them.

In the first part of this section, the membrane displacement is measured using a WYKO surface profiler. The second part of this section examines the capacitance/voltage (CV) characteristics of the devices. These are then compared to the measured membrane displacements.

3.4.2 Static membrane deflection measurements

The static membrane deflections for all three batches of device were measured using a WYKO optical surface profiler. The devices were mounted in the test fixture box and placed under the profiler microscope. A variable dc power supply was used to apply a bias voltage to the transducer under test. A schematic of this apparatus is shown in Figure 3.4.

Only the 1mm square devices were produced in all the batches, thus this size transducer was used for batch comparison of their membrane deflections. Measurements were taken of the 1μm and 2μm thick membranes from the 97204 and 97223 batches, and 0.5μm, 1μm and 2μm membranes from the 98163 batch. The applied bias voltage was varied from 0V to 30V in 2V increments, with a surface profile dataset taken at each interval. Figure 3.5(a-c) show a selection of the images and cross-sections for bias

voltages of 0V, 16V, and 30V, for each of the 2μm thick membrane devices measured. It can be seen that there were large variations in the maximum membrane deflections between the different batches. The initial trial batches (97204 and 97223) were found to exhibit reasonably large deflections, with the membrane moving by up to 110% of the air gap (note that in this case the membrane was domed at 0V bias, hence the overall deflection is greater than the air gap). The optimised 98163 batch, however, showed much lower deflections, typically only about 15%-20% of the air gap at 30V bias. Hence, this would indicate they had a higher intrinsic stress than the previous batches.

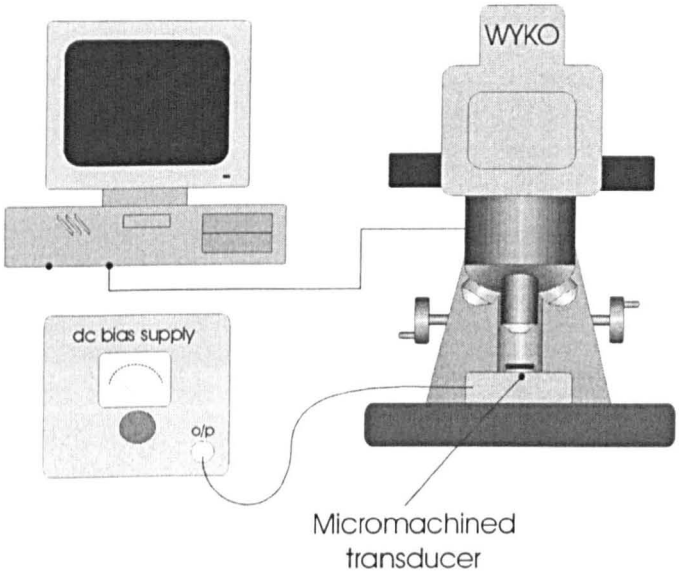

Figure 3.4: *Membrane deflection measurement apparatus.*

Generally, the deflection of the membrane was found to be only uniform at low bias voltages (<15V) above which, the membranes began to buckle. This buckling is evident in the 16V and 30V cross-section plots, and is more prominent in the thinner (0.5μm and 1μm) membranes. The reasons for this buckling are not entirely understood but could be due to localised differences in the crystalline structure of the silicon nitride membrane itself. Further examination of the devices, using a SEM revealed that the surface of the lower metallised electrodes was irregular. This could also be a contributing factor to the buckling, as uneven charge distributions across the membrane /

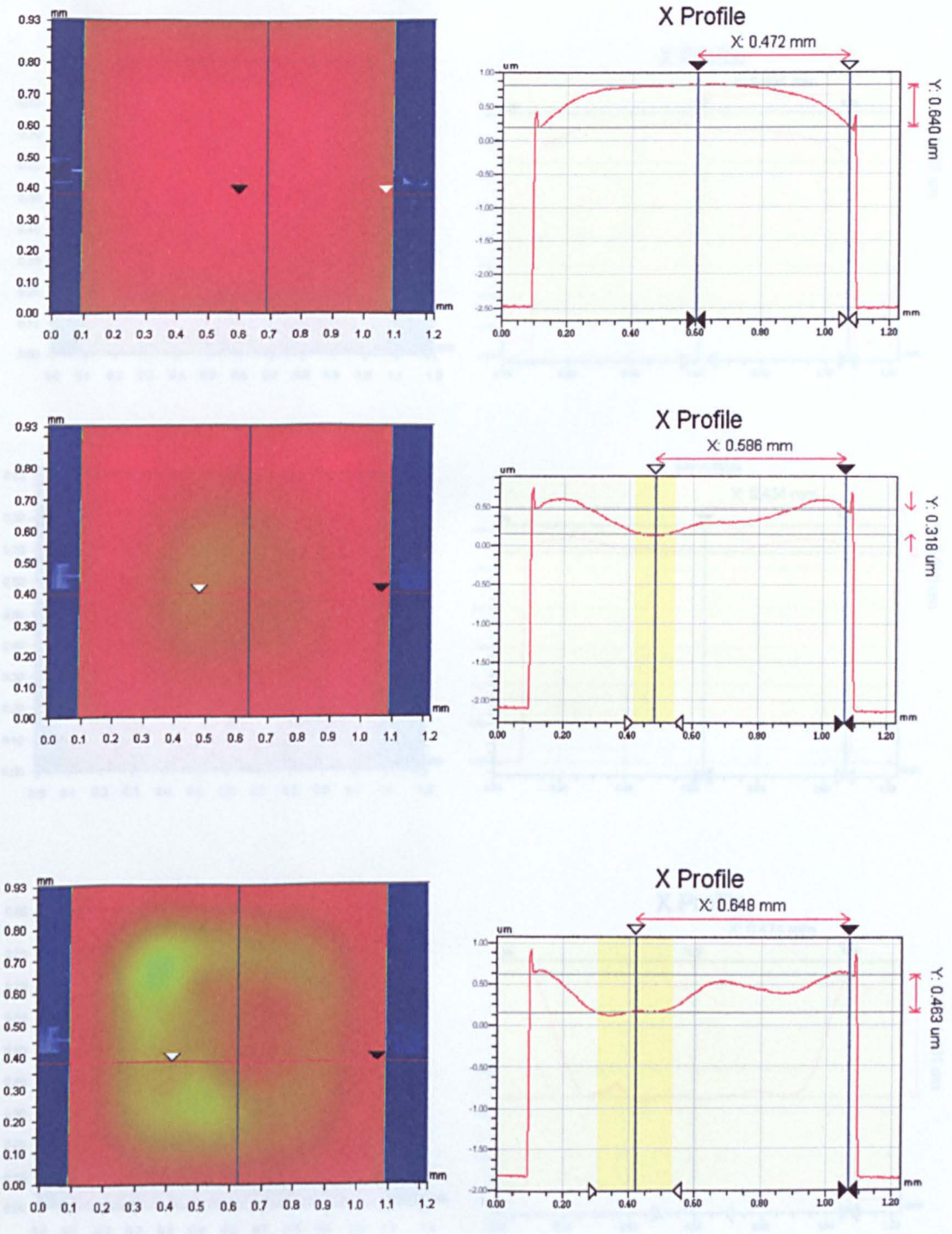

Figure 3.5(a): *WYKO images and profile cross-sections of a 1mm square device with a 2μm thick membrane (wafer A8) from batch 97204 with applied bias of 0V (top), 16V (middle), 30V (bottom).*

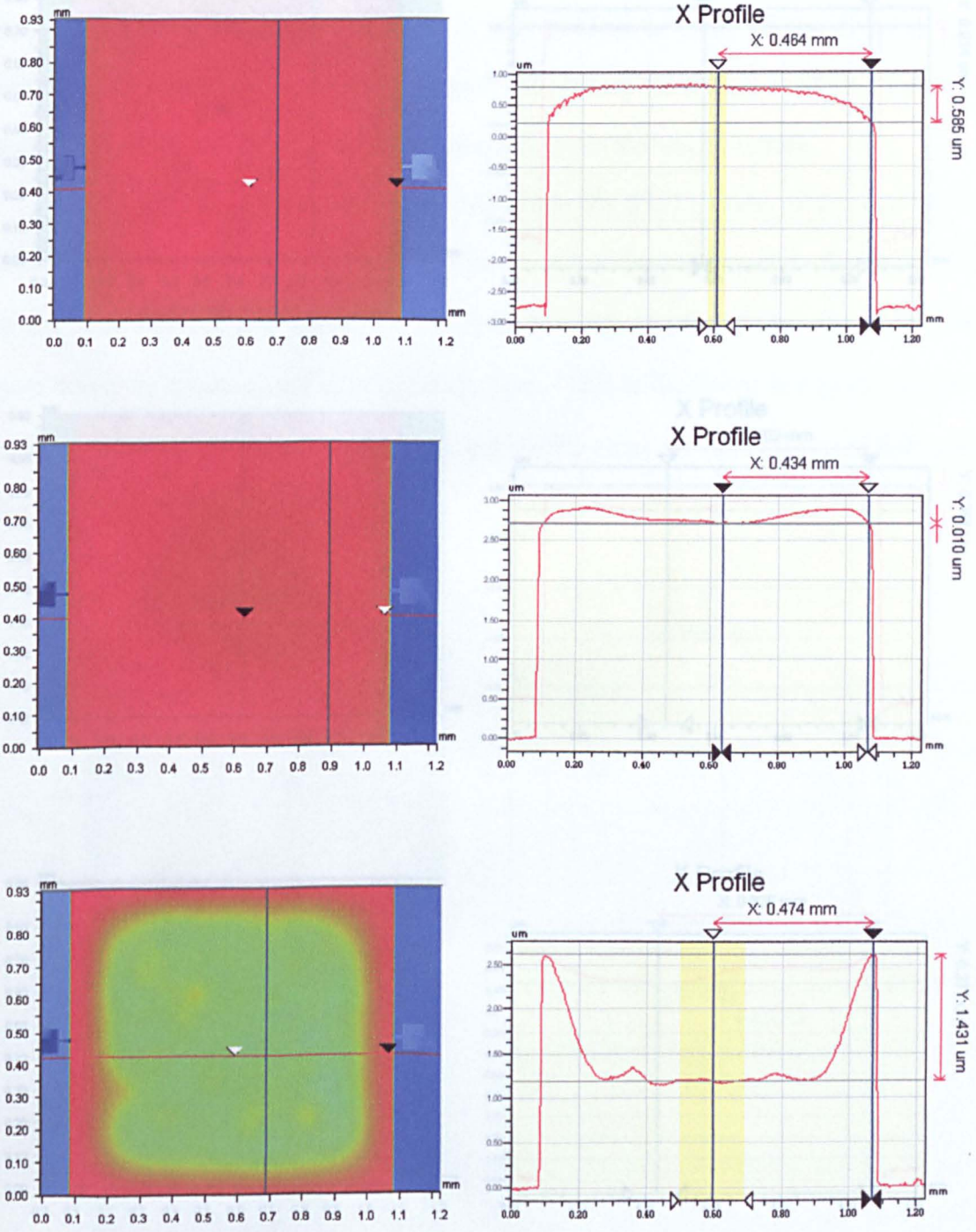

Figure 3.5(b): *WYKO images and profile cross-sections of a 1mm square device with a 2μm thick membrane (wafer A7) from batch 97223 with applied bias of 0V (top), 16V (middle), 30V (bottom).*

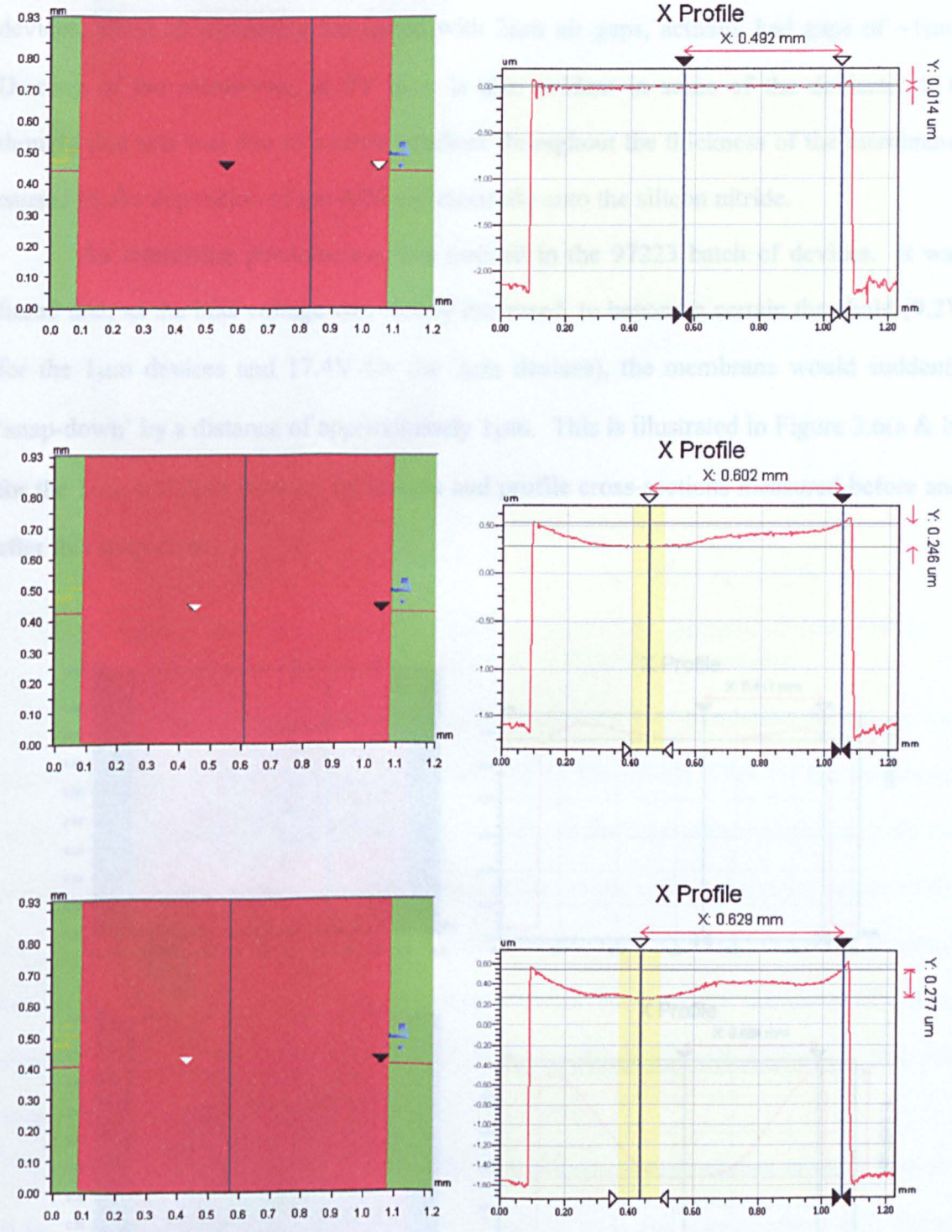

Figure 3.5(c): *WYKO images and profile cross-sections of a 1mm square device with a 2μm thick membrane (wafer A11) from batch 98163 with applied bias of 0V (top), 16V (middle), 30V (bottom).*

backplate would result. This study also revealed that the optimised 98163 batch of devices, although nominally fabricated with 2μm air gaps, actually had gaps of ~1μm. Doming of the membrane, at 0V bias, is also evident in some of the devices. It is thought that this was due to a stress gradient throughout the thickness of the membrane, caused by the deposition of the AlSi top electrode onto the silicon nitride.

An interesting phenomenon was noticed in the 97223 batch of devices. It was found that, as the bias voltage was slowly increased, to beyond a certain threshold (9.2V for the 1μm devices and 17.4V for the 2μm devices), the membrane would suddenly 'snap-down' by a distance of approximately 1μm. This is illustrated in Figure 3.6(a & b) for the 1μm and 2μm devices, by images and profile cross-sections measured before and after this snap-down.

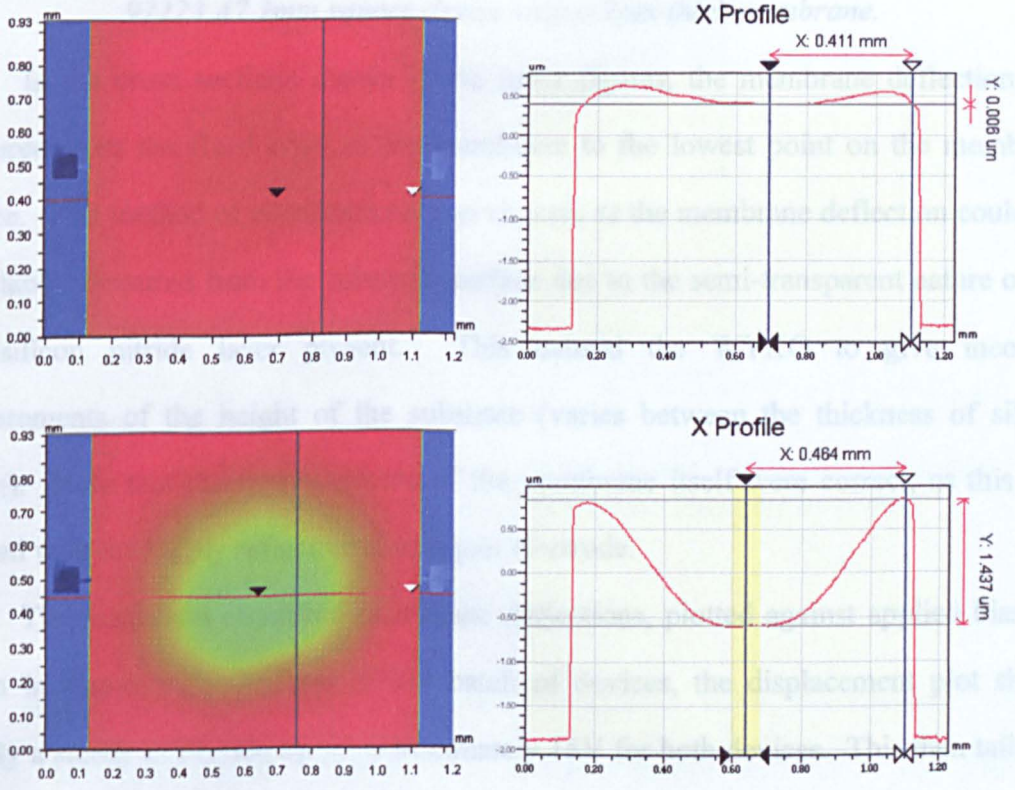

Figure 3.6(a): *Snap effect between 8.1V (top) and 8.2V (bottom) observed in the 97223 A2 1mm square device with a 1μm thick membrane.*

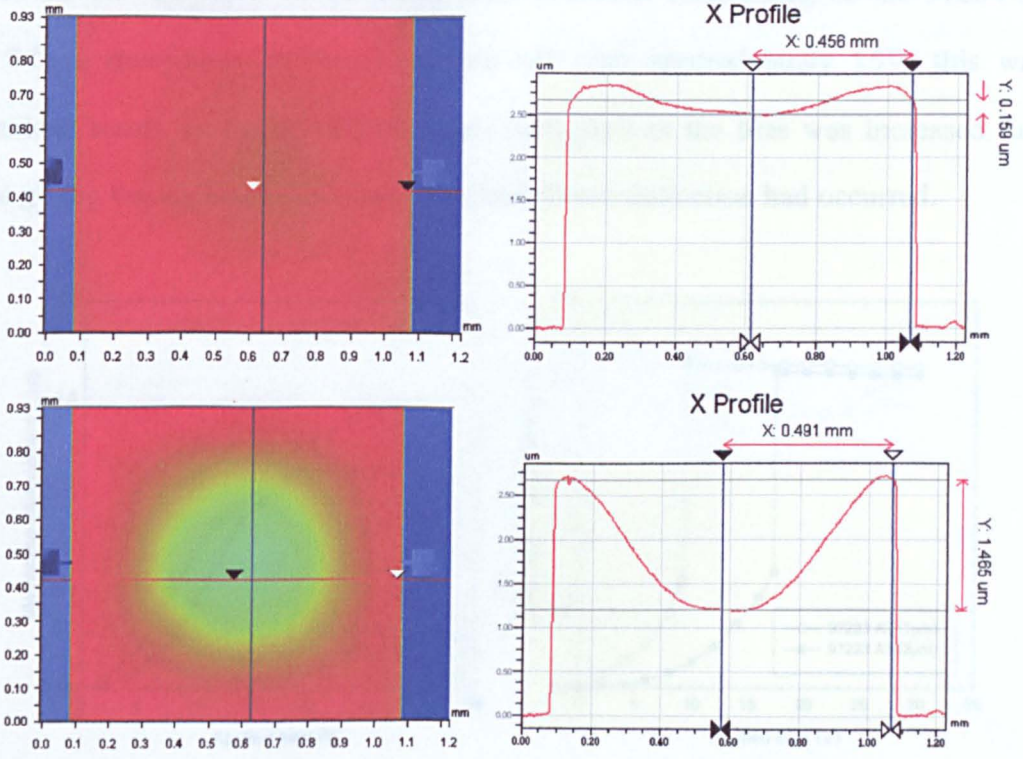

Figure 3.6(b): *Snap effect between 17.3V (top) and 17.4V (bottom) observed in the 97223 A7 1mm square device with a 2μm thick membrane.*

In the cross sections shown in the latter figures, the membrane deflection was measured from the fixed edge of the membrane to the lowest point on the membrane surface. This method of measurement was chosen, as the membrane deflection could not be reliably measured from the substrate surface due to the semi-transparent nature of the thin silicon nitride layer present. This caused the WYKO to give incorrect measurements of the height of the substrate (varies between the thickness of silicon nitride). Note that the measurements of the membrane itself were correct, as this was covered with the highly reflective aluminium electrode.

The maximum measured membrane deflections, plotted against applied bias are shown in Figure 3.7. For the 97204 batch of devices, the displacement plot shows initially a steady deflection up to approximately 15V for both devices. This then tails off to a maximum of approximately 1.2μm for the 2μm thick device, and 1.5μm for the thinner 1μm device. In the 97223 batch plots, the snap down effect is clearly visible occurring at approximately 9V and 17V for the 1μm and 2μm devices respectively. The

curves for the optimised 98163 batch show a similar relationship to the 97204 batch. The 0.5μm membrane appears to flatten off after approximately 15V; this was an anomalous result, as the membrane edges collapsed as the bias was increased further, hence giving the appearance that no more membrane deflection had occurred.

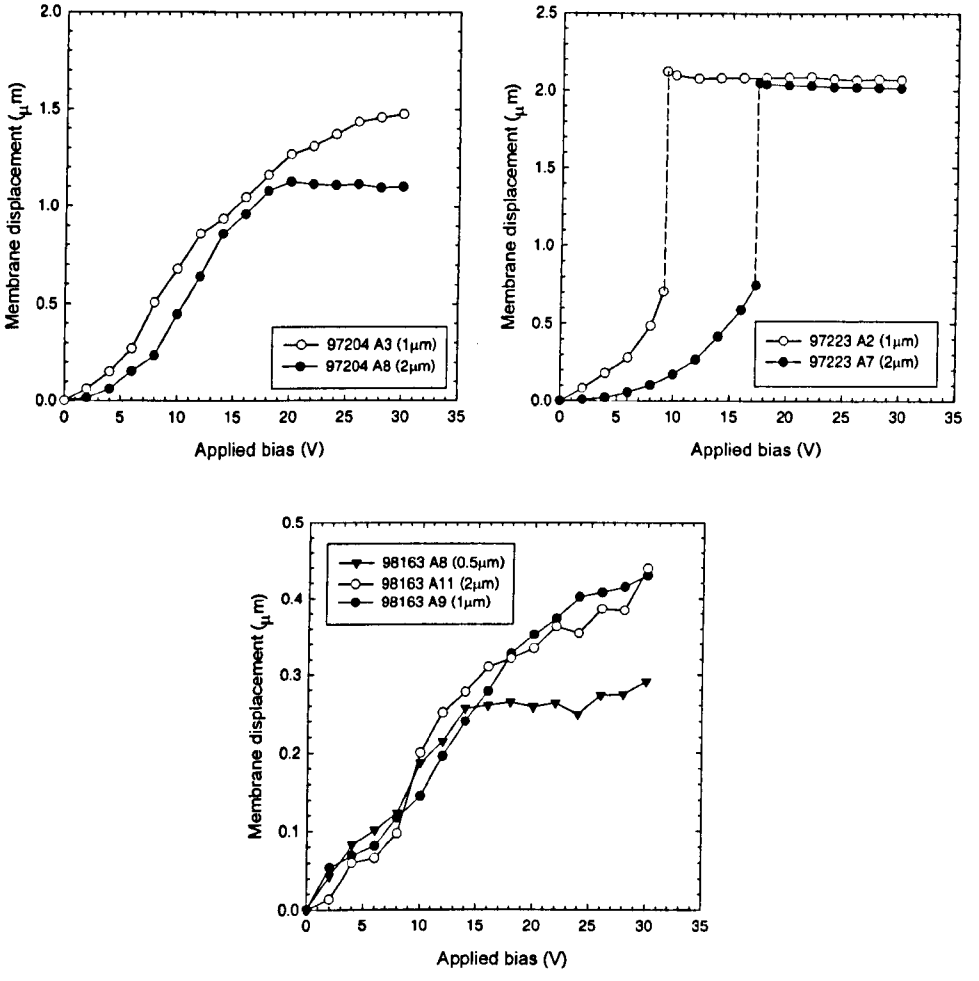

Figure 3.7: *Measured maximum membrane displacements, plotted against applied bias voltage, device batch number and membrane thickness as shown.*

3.4.3 Capacitance-Voltage characteristics

This section examines the capacitance-voltage (CV) characteristics of the devices, using an Agilent precision LCR analyser (model 42849A). The measured capacitances, plotted against applied bias are shown in Figure 3.8. Note they are plotted on the same scale axis for comparison. These, as would be expected, are similar in form to the measured displacements above. The snap down effect is again evident in the

97204 batch of devices, occurring between the same applied bias voltages as above. The optimised 98163 batch shows relatively linear relationship with applied bias, with higher capacitances than the 97204 batch due to their smaller air gaps. Note in each case, the devices with thinner membranes were found to exhibit higher capacitances, as would be expected.

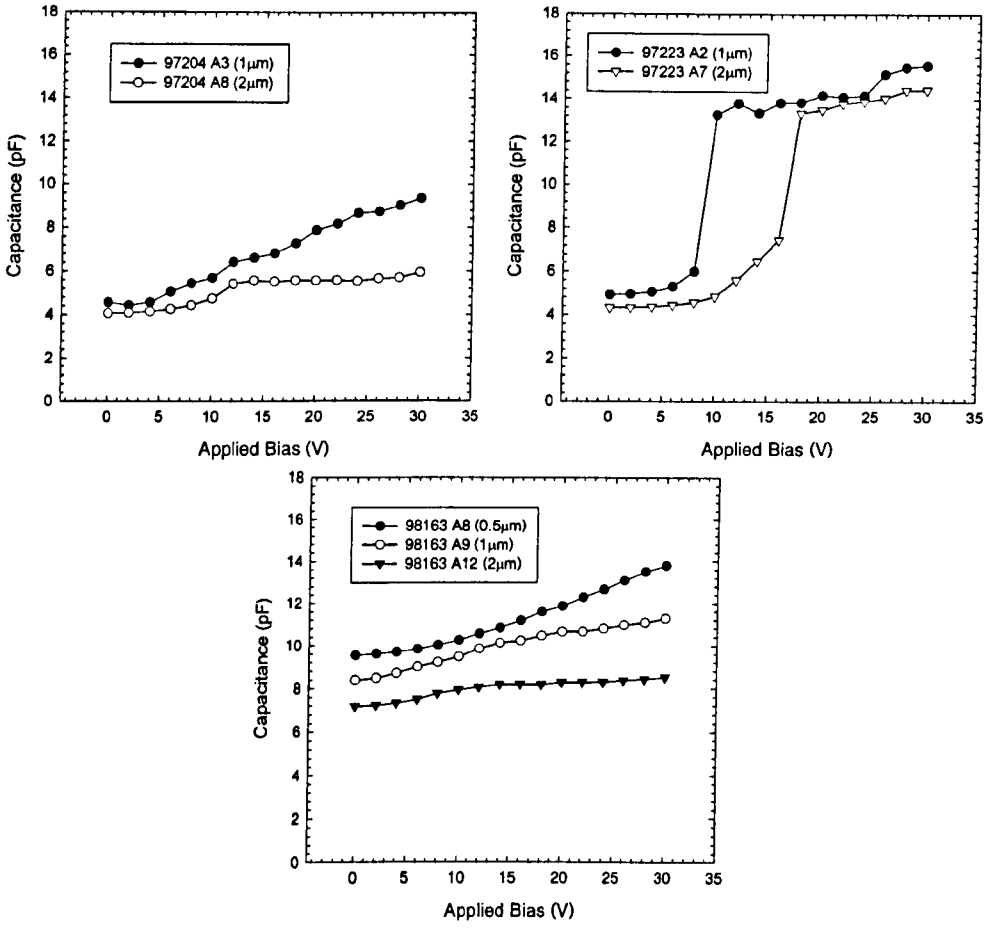

Figure 3.8: *Measured capacitance, plotted against applied bias voltage for the 1mm square micromachined devices, batch and membrane thickness as shown (measurements taken at 1kHz).*

3.5 Initial dynamic testing in air

3.5.1 Introduction

This section describes a set of initial experiments performed to examine the dynamic characteristics of the transducers, in terms of their ultrasonic properties. Throughout the following work, the 1mm square transducers, with 1μm thick membranes

from the optimised 98163 batch became the 'benchmark' device, and hence the majority of the characterisation work was done using these transducers. The first part of this section examines the characteristics of these devices using a variety of techniques. These include pulse-echo, a source detector pair (pitch-catch), and using other types of source and detector transducers. Such techniques have been previously described as typical methods in which transducers can be characterised in terms of their frequency response and sensitivity [20]. The influence of the 'snap down' effect, observed in the 98223 batch of devices is then studied. This is followed by a comparison of the characteristics of the 1mm devices from the two preliminary batches, and the optimised batch.

3.5.2 Pulse echo operation

A 1mm square device with a 1μm thick membrane (98163 A9 batch) was positioned 5mm (±0.5mm) from a flat optical mirror. The device was connected to a Panametrics pulser/receiver unit (model 5055PR), via a capacitive de-coupling circuit (see Figure 3.9) to allow the application of a 20V dc bias. A diplexer unit was also connected between the pulse unit and the de-coupling box to enable a Cooknell charge amplifier (model CA6/C) to be used as the receiver amplifier, instead of the integral receiver in the Panametrics unit. Note that this amplifier was used in preference to the Panametrics receiver as it provided higher sensitivity and improved signal to noise

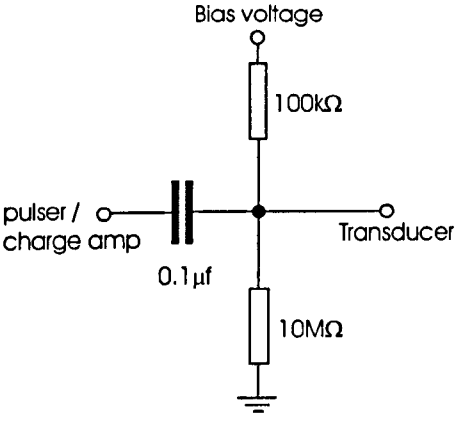

Figure 3.9: *Schematic diagram of the capacitive de-coupling circuit.*

performance, which was required due to the relative small signals from the transducer (due to its size). The function of the diplexer was to isolate the charge amplifier from the high voltage drive signal produced by the pulser unit, while allowing the echo signal to be received.

The pulser unit (used on its lowest energy, and highest damping settings) provided a wide bandwidth transient signal. A typical drive waveform, measured across an attached 1mm square micromachined transducer, with an oscilloscope probe, is shown in Figure 3.10(a), along with its corresponding calculated frequency spectrum (b). This shows that it produced a relatively flat voltage excitation over the region of interest (0-15MHz). Hence, an impulse response measurement would be approximated with this drive signal. A Tektronix TDS430A oscilloscope, with an integral disk drive, was used to observe and store waveforms for later analysis. This arrangement is shown in Figure 3.11.

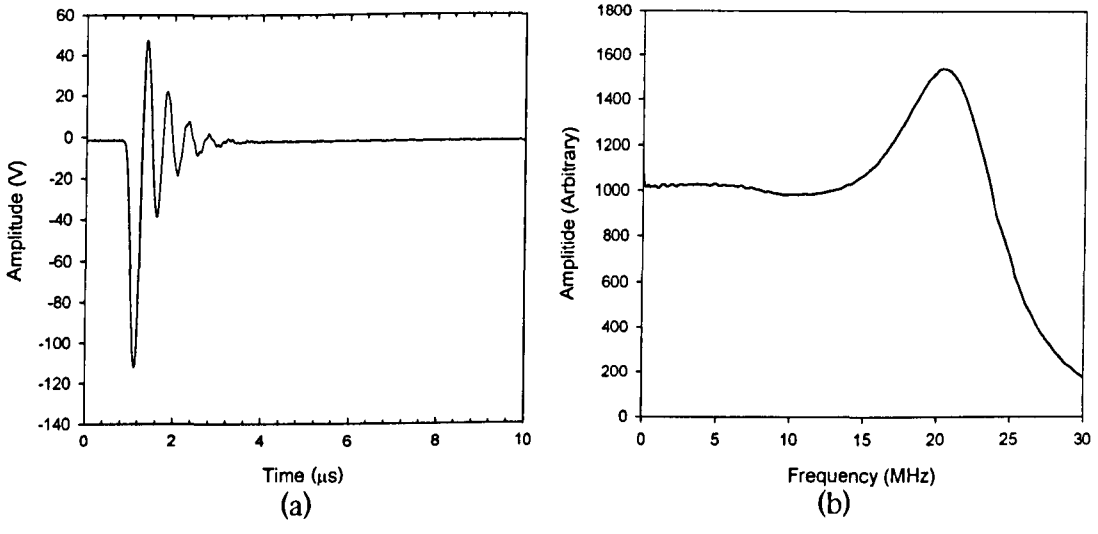

Figure 3.10: *(a) Typical measured transient drive signal from the Panametrics pulser unit, and (b) corresponding frequency spectrum.*

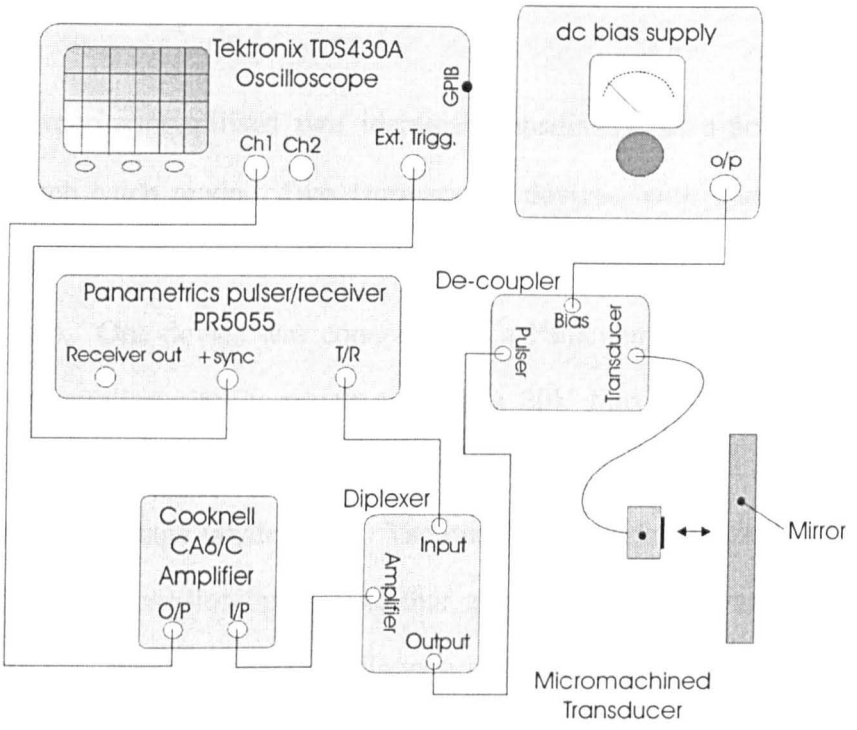

Figure 3.11: *Schematic diagram of the pulse-echo characterisation equipment.*

Figure 3.12(a) shows the typical received pulse-echo waveform, together with its corresponding frequency spectrum (b). This shows a relatively well-damped wide bandwidth signal, with a peak frequency and (-6dB) bandwidth of approximately 1.2MHz, and 700kHz (52%) respectively. Note that over the propagation gap used here, the attenuative effect of air can be ignored.

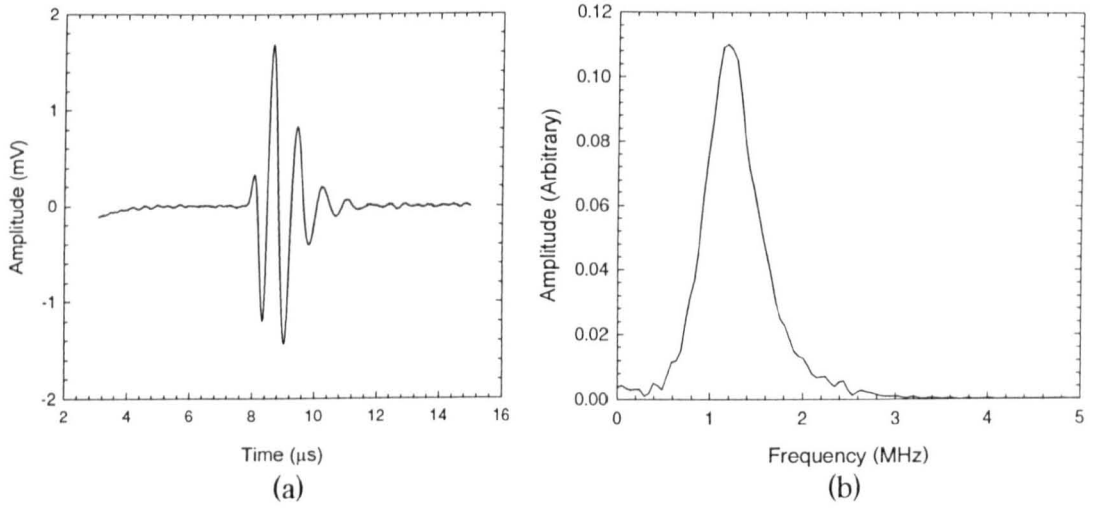

Figure 3.12: *(a) Pulse-echo waveform from a 1mm square 1μm membrane (98163 A9) device, and (b) corresponding frequency spectra.*

3.5.3 Source-detector pair (pitch-catch)

This experiment utilised two identical transducers, as a source detector pair, operated in pitch catch mode. Two 1mm square devices, with 1μm thick membranes (98163 batch) were axially positioned facing each other with a 10mm (±1mm) air propagation gap. One device was connected to a Panametrics (model 5055PR) pulser unit, via a de-coupling circuit, which allowed a 20V bias to be applied. The other transducer was coupled to a Cooknell charge amplifier (model CA6/C), which also supplied a biasing voltage (again 20V). The output of the charge amplifier was fed to a Tektronix TDS430A oscilloscope. Note that all the equipment was the same as used above. Figure 3.13 shows a schematic diagram of this arrangement.

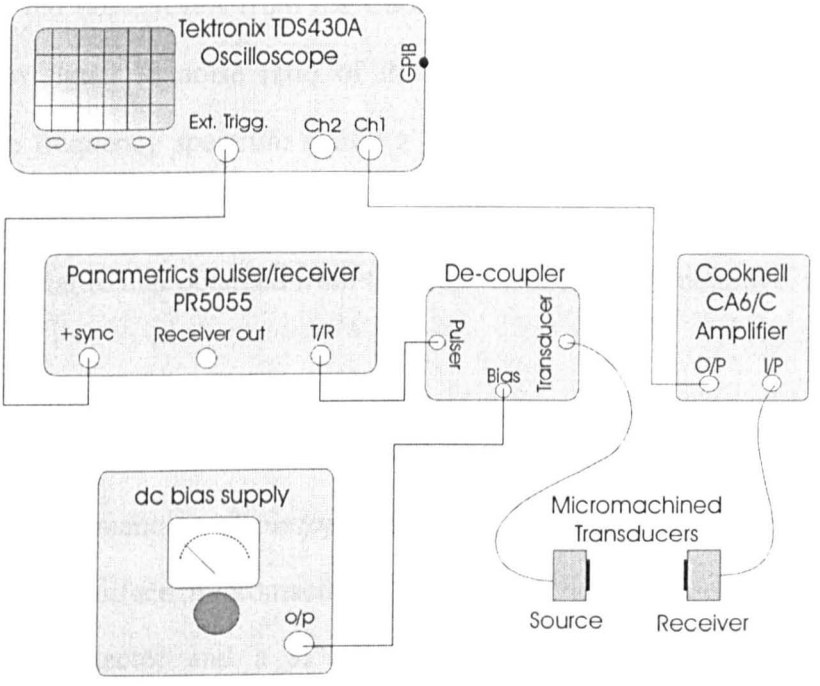

Figure 3.13: *Source-detector pair apparatus.*

Figure 3.14(a) shows the received time waveform, along with its corresponding frequency spectrum (b). It can be seen that a relatively well-damped wide bandwidth signal, with an amplitude of 27mV pk-pk has resulted. Note that this waveform (as well as others in this chapter unless otherwise stated) was signal-averaged to reduce noise.

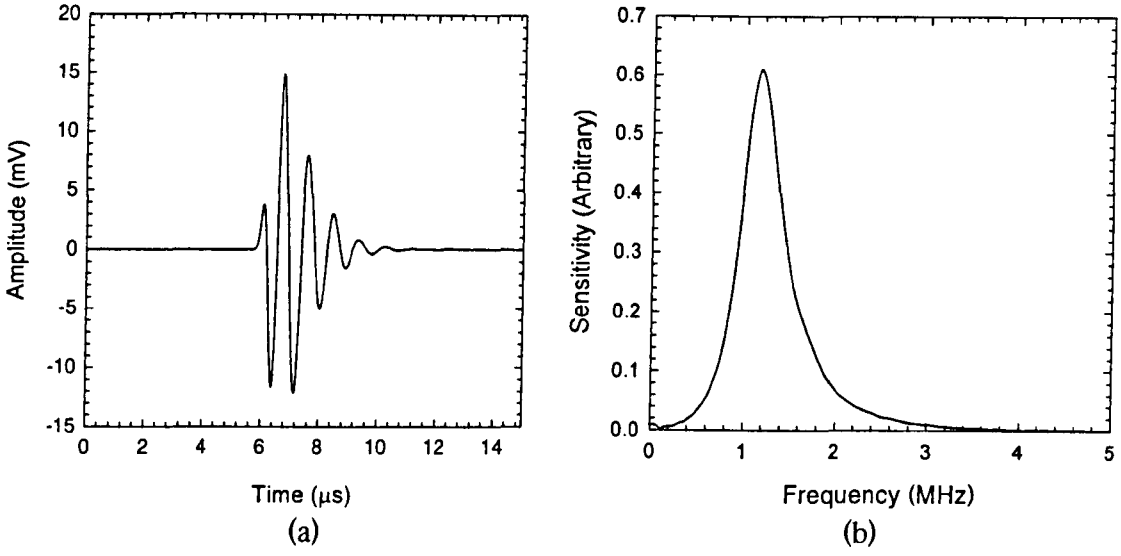

Figure 3.14: *(a) Waveform received by a 1mm square micromachined transducer with a 1μm thick membrane (98163 A9) positioned 10mm (±1mm) from a similar source transducer, (b) corresponding frequency spectrum.*

Typical measured noise levels from the Cooknell charge amplifier were ~1.2mV pk-pk, and hence the signal to noise ratio of the whole system was approximately 22.5:1 (~27dB). The frequency spectrum shows a peak frequency of approximately 1.2MHz, with a bandwidth of ~650kHz, ranging from 900kHz to 550kHz. This, as would be expected, is similar to that obtained from the pulse echo experiment above.

3.5.4 Characterisation using other types of transducer

These experiments used piezoelectric and polymer-based capacitive transducers to investigate the surface micromachined devices. The first used a micromachined transducer as a detector and a ½" diameter Panametrics 10MHz nominal centre frequency piezoelectric immersion transducer as a source. This transducer was chosen, as its frequency response in the region of interest, 0-3MHz, was relatively flat, being well below its nominal resonant frequency. As this transducer was designed for immersion applications, its impedance match with air was poor, hence producing low signal levels. However, it was still possible to obtain reasonable signals when using the micromachined transducers as detectors. In addition, for comparison a capacitive air

transducer, with a micromachined backplate and polymer membrane [21], whose construction was described in Chapter 2 was also tried as a source.

The piezoelectric source was connected directly to a Panametrics pulser/receiver unit, and axially aligned with a 1mm square micromachined detector (1μm membrane, 98163 A9). A 10mm (±1mm) air propagation gap was used. The micromachined detector was connected to a Cooknell charge amplifier, and a bias of 20V was applied. A Tektronix TDS430A oscilloscope was used to observe the received waveforms. The source transducer was then substituted for the capacitive polymer device (together with the de-coupling unit to allow the application of a 100V bias), and the measurement repeated. This arrangement is shown in Figure 3.15.

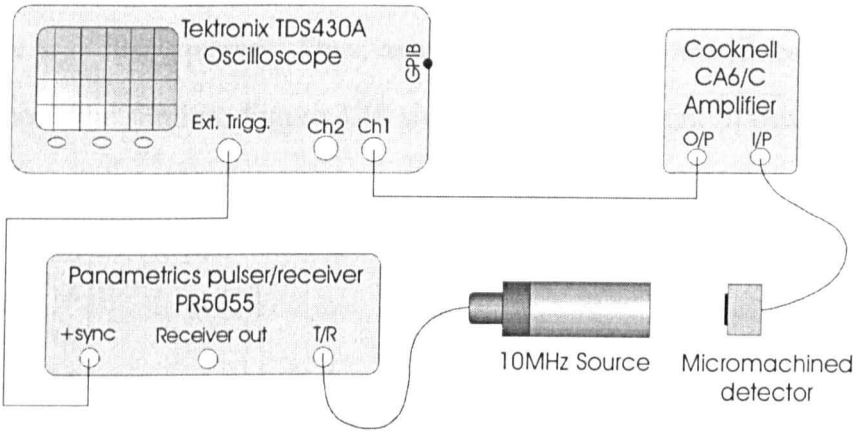

Figure 3.15: *Transducer characterisation set-up using a 10MHz piezoelectric source transducer and a micromachined detector.*

Figure 3.16 shows the measured waveforms from (a) the 10MHz piezoelectric source, and (b) the capacitive polymer device. In both cases, a wide bandwidth well-damped signal is evident. Comparison of the signals reveals that the capacitive source transducer has produced signals approximately an order greater in amplitude than the piezoelectric device. Figure 3.17 shows the frequency spectra of these two waveforms, plotted (a) with relative sensitivity, and (b) normalised sensitivity. The relative sensitivity plot again illustrates the sensitivity difference between the capacitive and piezoelectric sources, with the capacitive source providing a much higher amplitude

signal. From the normalised plots, the limited bandwidth of the capacitive polymer source is evident as an overall reduction in the measured frequency response. Hence, such a device would be unsuitable as a source for characterising a micromachined receiver, as it does not possess sufficient bandwidth. The frequency spectrum of the signal from the piezoelectric source, however, showed a peak frequency response at ~1.2MHz, and a bandwidth (-6dB) of ~900kHz, ranging from 700kHz, to 1.6MHz. This is comparable to that observed for pulse-echo and receiver/detector pair experiments described above. Note that in these cases, the resultant frequency response contains both the receive/transmit characteristics (two-way characteristic) of the micromachined transducer, whereas the detector test (performed here) only includes the receiver response (one-way characteristic). So to compare these spectra, the one-way characteristic was first squared. Thus, assuming a reversible transducer, the frequency responses should be similar. Figure 3.18 shows this comparison. It can be seen that the

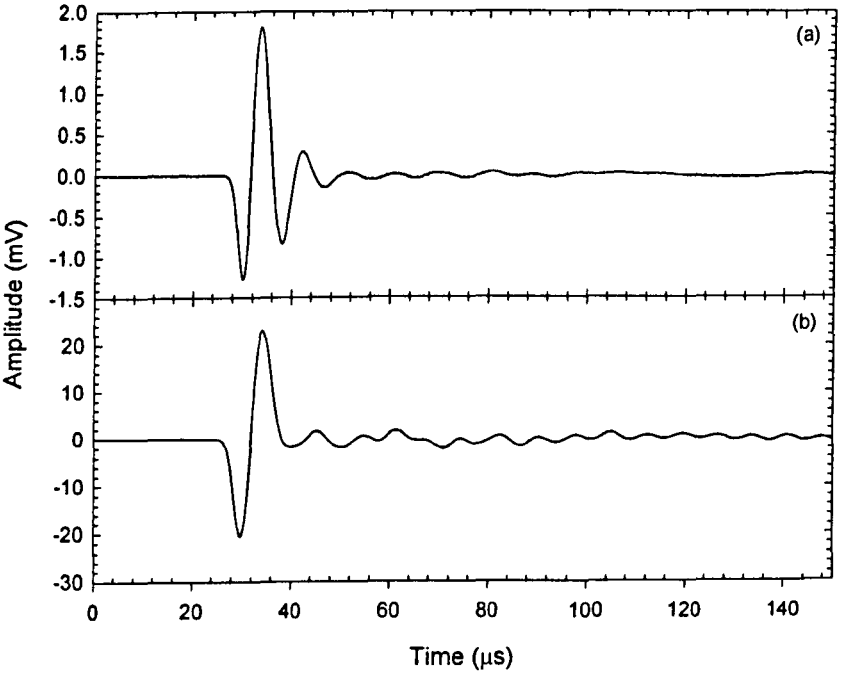

Figure 3.16: *Time waveforms of the signal received by a 1mm square micromachined detector 10mm from, (a) 10MHz piezoelectric source, (b) capacitive polymer source.*

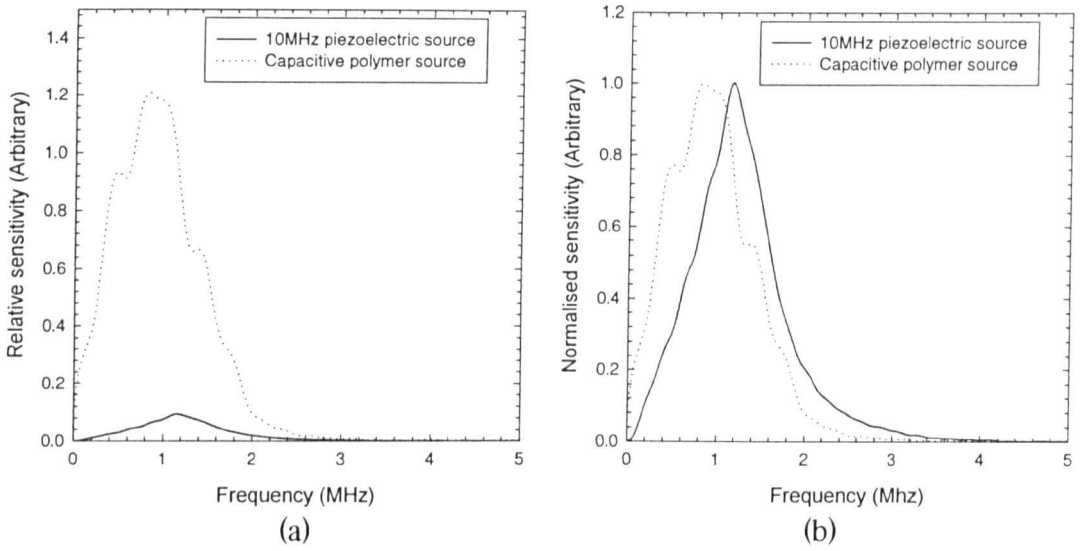

Figure 3.17: *Frequency spectra of the signal received by a 1mm square micromachined detector 10mm from a 10MHz piezoelectric source, and a capacitive polymer source. Plotted with (a) relative sensitivity (b) normalised sensitivity.*

spectra are indeed similar. Hence, for characterisation of the micromachined transducers as receivers, it would appear that the 10MHz piezoelectric source transducer has sufficient bandwidth and sensitivity, and thus will be used for the remainder of the characterisation experiments in this chapter. This also suggests that the transducer has reversible characteristics, exhibiting the same characteristics as a source as when used as a detector.

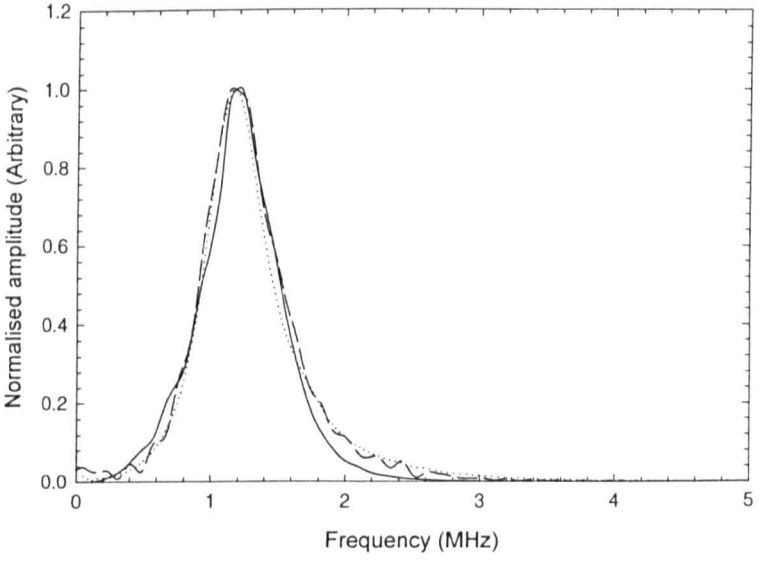

Figure 3.18: *Comparison of the square of the frequency spectrum (solid line) measured with a 10MHz piezoelectric source, the source detector pair frequency spectrum (dotted line), and the pulse-echo frequency spectrum (dashed line).*

A final experiment examined the characteristics of the micromachined transducer as a source to confirm that it is similar to its receiver characteristics, as indicated by the previous experiment. A 1mm square device with a 1μm thick membrane (98163 A9) was positioned 10mm (±1mm) from a 10MHz Panametrics immersion transducer (this time used as a receiver). The micromachined transducer was connected to a Panametrics pulser unit, via a de-coupling circuit to allow the application of a biasing voltage (20V bias was used). The piezoelectric receiver was connected to a Cooknell charge amplifier, with a Tektronix TDS430A oscilloscope used to examine the received waveforms. This arrangement is shown in Figure 3.19.

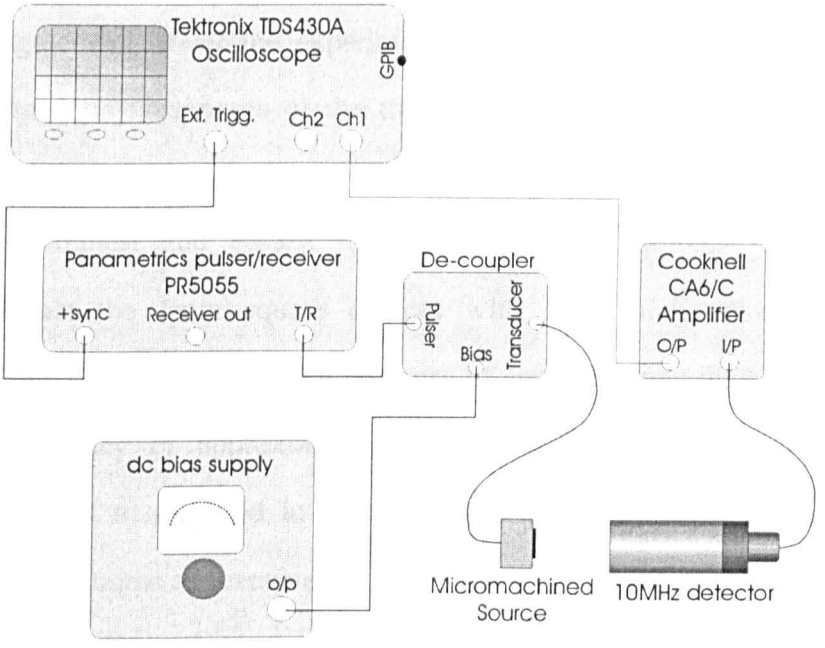

Figure 3.19: *Apparatus used for the micromachined source, piezoelectric detector experiment.*

Figure 3.20(a) shows the received waveform along with its corresponding frequency spectrum (b). As expected, these are very similar to the waveform obtained with the micromachined transducer as a detector, and the piezoelectric transducer as a source. A comparison of their frequency spectra shows they are very similar, with peak frequencies of ~1.2MHz, and bandwidths of ~900kHz, ranging from ~700kHz to 1.6MHz. Hence demonstrating the transducers frequency characteristics are similar during the reception and generation of ultrasound.

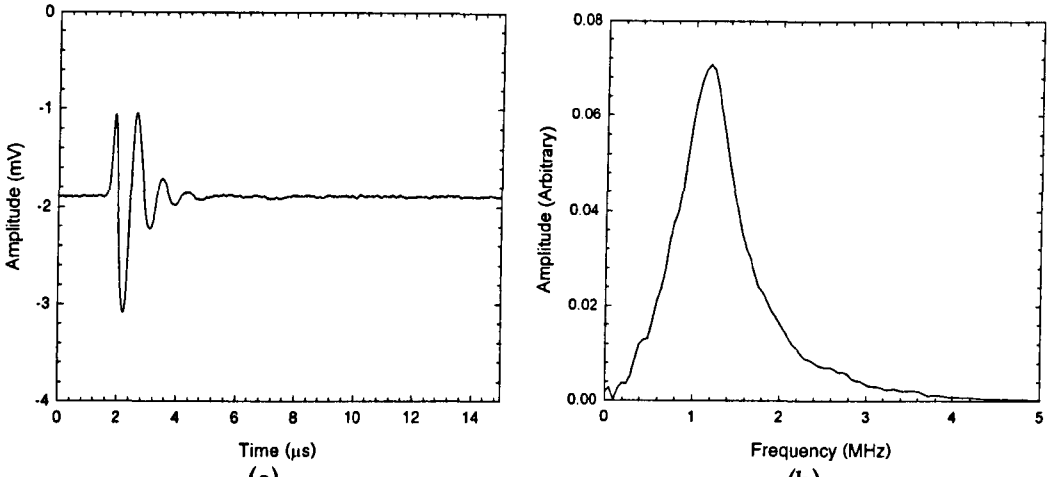

Figure 3.20: *(a) Waveform received by a 10MHz piezoelectric transducer positioned 10mm from a 1mm square micromachined transducer with a 1μm membrane, (b) corresponding frequency spectrum.*

The agreement of all the experiments above demonstrated that they all gave comparable frequency responses of the transducer. Hence, for the remainder of this chapter, the third method, using the 10MHz piezoelectric source was adopted, as this provided the simplest and easiest method of characterisation. The experiments demonstrated that the 1mm square devices with 1μm thick membranes typically exhibited a wide bandwidth frequency response of approximately 900kHz (-6dB) with a peak/centre frequency of approximately 1.2MHz. Also established was that the transducer appeared to operated in a reversible way, exhibiting the same frequency characteristics as a source and receiver.

The above characterisation study was performed using the same devices in each experiment. Due to the high degree of control and repeatability of the micromachining process, it was assumed that this would be representative of all the devices in the batch. To confirm this, an experiment was performed to compare the characteristics of a number of 'identical' transducers. Four 1mm square devices with 1μm thick membranes were tested; all from the 98163 batch, two of which were from wafer A9 and two from wafer A10 (hence also studying repeatability across wafers). They were each tested as a detector, using a 20V bias, and the 10MHz Panametrics piezoelectric transducer as a source. A 10mm propagation distance was used.

Figure 3.21 shows a comparison of the received waveforms (a), and their calculated frequency spectra (b). It can be seen that they are in good agreement, with relatively small differences (being within 6% of each other at the peak frequency).

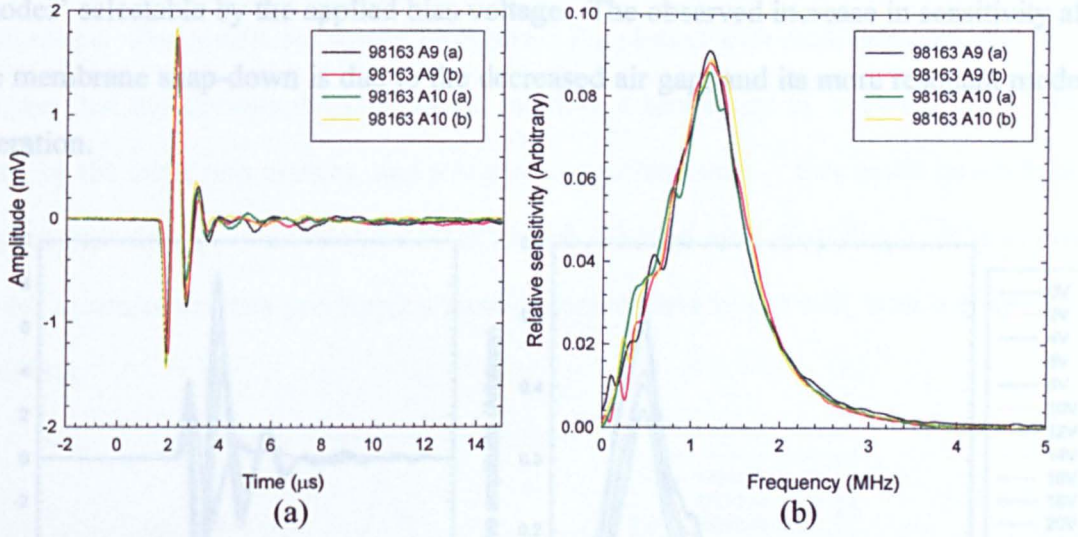

Figure 3.21: *Comparison of (a) the waveforms, and (b) their corresponding frequency spectra, received by four 'identical' 1mm square 1μm thick membrane devices positioned 10mm from a 10MHz piezoelectric source.*

3.5.5 The effect of the 'snap down' observed in the 97204 devices.

The WYKO membrane displacement, and the C-V measurements performed above found that a 'snap down' effect occurred in the preliminary 97223 batch of devices, at approximately 9V and 17V for the 1μm and 2μm thickness membranes respectively. It was thought interesting to investigate the effect of this on the ultrasonic properties of the device. To achieve this, an experiment was performed using a pair of 1mm square transducers with 2μm thick membranes (both 97223 A7). The bias was varied on the source transducer, while a fixed bias of 30V was applied to the receiver. The experimental set-up was the same as used above in Figure 3.13.

The results are shown in Figure 3.22. The time waveforms (a) show a definite change in the transducers characteristics as the bias is increased. The signal has both increased in amplitude, as well as frequency. This is more clearly seen in the plot of relative frequency spectra (Figure 3.22 (b)). It appears that as the bias is increased past the membrane 'snap-down' voltage, its peak frequency response increases from

approximately 900kHz to 1.1MHz. Its bandwidth (-6dB), however, decreases from approximately 1MHz (200kHz to 1.2MHz) to 700kHz (600kHz to 1.3MHz), as the device becomes more resonant. Hence, it appears that this device can be operated in two 'modes' selectable by the applied bias voltage. The observed increase in sensitivity after the membrane snap-down is due to the decreased air gap, and its more resonant mode of operation.

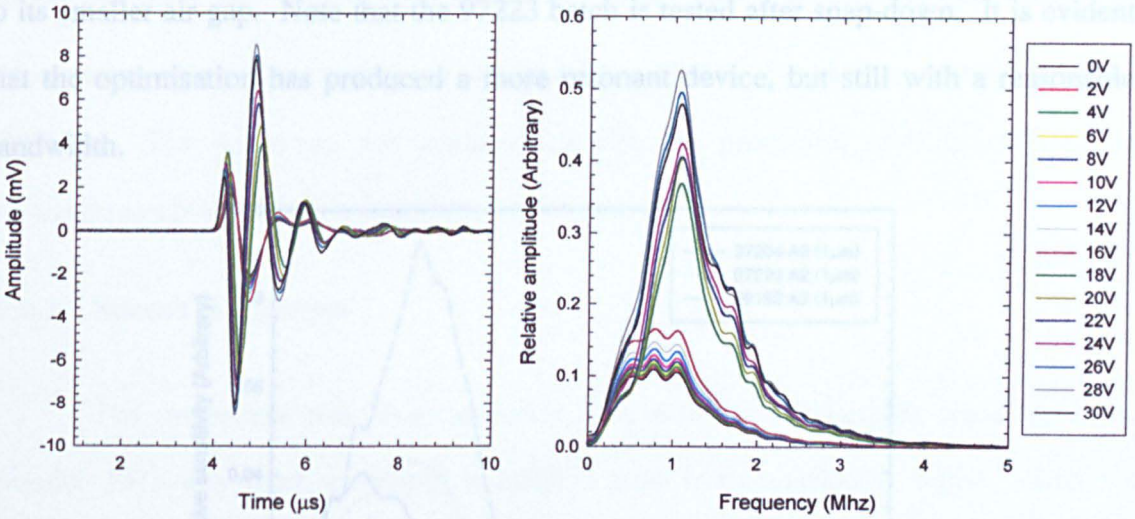

(a) (b)

Figure 3.22: *(a) Time waveforms showing the 'snap-down' effect as the source bias is increased, and (b) their corresponding frequency spectra.*

3.5.6 Examination of the characteristics of different device batches

The static membrane deflection measurements and C-V analysis performed above indicated that there were differences in the membrane properties between the different device batches. This experiment was performed to examine the differences in the ultrasonic characteristics between the different device batches. As discussed above, the first trial batches (97204 and 97223), consisted of devices ranging in size from 10µm square up to 1mm square. However, the latest optimised fabrication run (batch 98163) had device sizes ranging from 1mm to 5mm square. Thus, for a cross-comparison of the differences between the batches, an experiment was performed using the 1mm square devices.

Measurements were taken, comparing the 1μm thickness membrane devices. They were all used as detectors, with a 20V applied bias, and positioned, in turn, 10mm from the 10MHz piezoelectric source transducer. The device under test was coupled to a Cooknell charge amplifier, and waveforms were taken using a Tektronix TDS430A oscilloscope. The results are shown in Figure 3.23, plotted with relative sensitivity. This indicates that the optimised 98163 batch, exhibits a sensitivity of more than twice that shown by the other two devices, and a higher centre frequency. This could be attributed to its smaller air gap. Note that the 97223 batch is tested after snap-down. It is evident that the optimisation has produced a more resonant device, but still with a reasonable bandwidth.

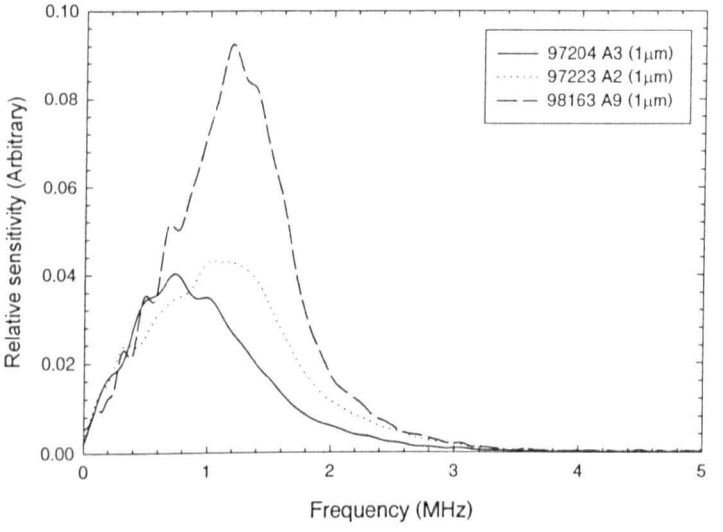

Figure 3.23: *Comparison of typical relative frequency spectra of the signals received from 1mm square devices with 1μm membranes from different batches (20V applied bias), positioned 10mm from a 10MHz piezoelectric source.*

3.5.7 Discussion of preliminary characterisation

The above experiments have shown that the devices exhibited wide-bandwidth response, with typical centre frequencies of the order of 1MHz. The 'benchmark' 1mm square devices with 1μm thick membranes from the optimised 98163 batch were found to exhibit peak frequency response at ~1.2MHz and a bandwidth of approximately 900kHz (75%). The reasons for this wide-bandwidth behaviour will be discussed below.

They have also been demonstrated to operate as reversible transducers, exhibiting the same frequency characteristics as sources and detectors.

3.6 Transducer sensitivity calibration

This section examines the absolute transmit / receive sensitivity of the 1mm square device with a 1μm membrane (98163 A9). To achieve this a calibrated 1/8" Brüel and Kjær microphone (type 4138) was used. This was supplied with a calibrated frequency response extending up to 200kHz. Hence, the device was calibrated at 200kHz. The following sub-sections describe the procedure used to calibrate the device(s) to obtain its source and receiver sensitivity.

3.6.1 Source calibration

The transducer was first calibrated as a source. A Wavetek signal generator (model 191) was used to supply a 200kHz tone burst excitation signal. This was connected to the transducer via a capacitive de-coupling box, to allow the application of a d.c. biasing voltage. The Brüel and Kjær microphone was aligned axially with the micromachined transducer, and placed at a distance of 10mm (±1mm) from it. The microphone was attached to a preamplifier (type 2670), and a measurement amplifier (type 2606), the output of which was fed to a Tektronix 430A oscilloscope. The schematic diagram in Figure 3.24 shows this arrangement.

Before the measurement was performed, the microphone/amplifier system was first calibrated using a piston phone (type 4231). This device gave a calibrated 1kHz (±0.1%) audio signal at a selectable sound pressure level (SPL) of 94dB ±0.2dB (1 Pa), and 114dB ±0.3dB (10 Pa). Note that the SPL levels stated here are relative to 20μPa. The microphone was placed in the aperture of the piston phone, and the amplitude of the signal measured. This was 190mV pk-to-pk and 1.88V pk-to-pk for the high and low

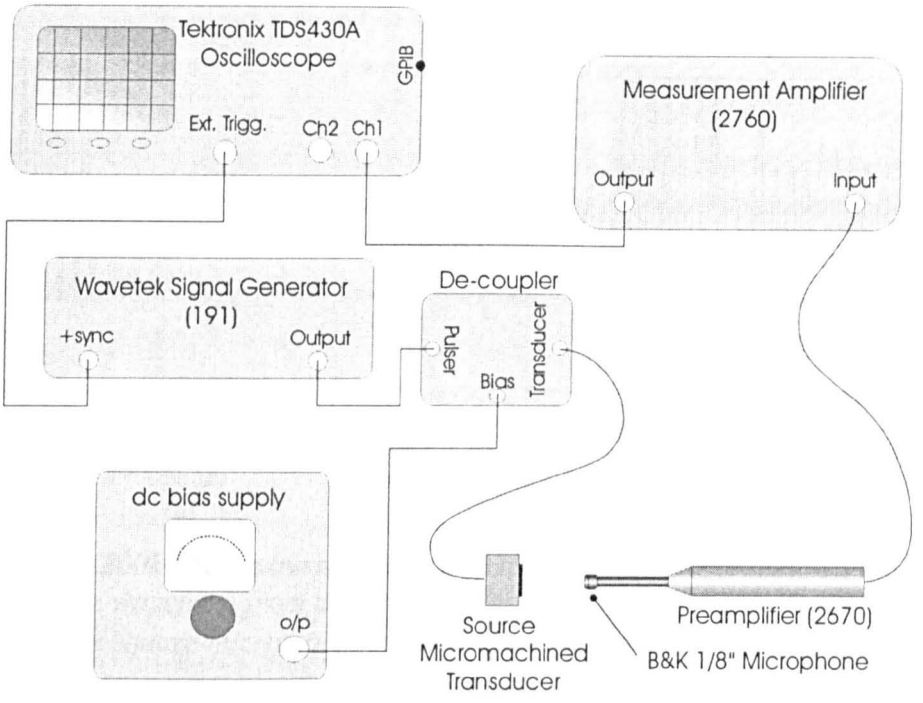

Figure 3.24: *Schematic diagram of the apparatus used to calibrate the micromachined transducer as a source.*

output settings respectively. Hence, the sensitivity of receiver/amplifier system was calculated as ~189 mV/Pa (@1kHz). The calibrated frequency response chart supplied with the microphone was then used to obtain its sensitivity at 200kHz. From the supplied chart, the sensitivity of the microphone was 11.5dB ±0.2dB less than that at 1kHz. Hence, the sensitivity of the system at 200kHz was 50.3mV/Pa ±1mV/Pa.

The micromachined device was driven with a 20V pk-to-pk 200kHz tone burst, with a 20V bias. This was measured using an oscilloscope probe, across the terminals of the transducer, and is shown in Figure 3.25(a). The signal received by the Brüel and Kjær microphone is shown in Figure 3.25(b). This shows the main tone burst, followed by a lower amplitude bust caused by the secondary reflection between the device and the microphone. The average amplitude of the main sine wave signal is ~20.2mV. Hence, this relates to a sound pressure of ~0.4 Pa (~86dB), at an axial position of 10mm when driven by a 20V pk-pk 200kHz signal with 20V bias. Thus, the source sensitivity is approximately 20mPa/V (at an axial position of 10mm, @200kHz and 20V bias).

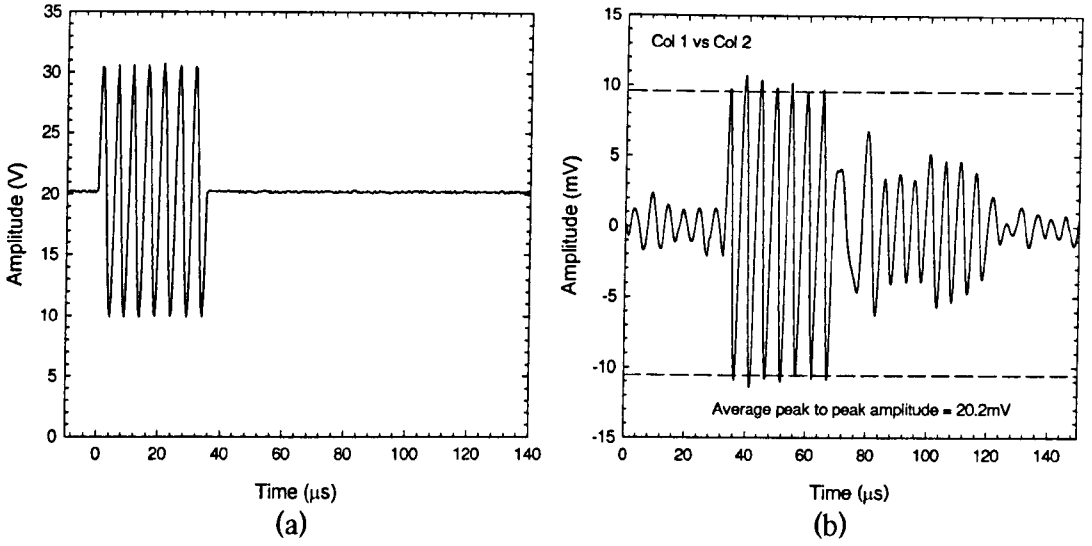

Figure 3.25: *(a) 200kHz tone burst signal used to drive the micromachined transducer. (b) Received time waveform from a Brüel and Kæjr 1/8" microphone, positioned 10mm from a 1mm square micromachined transducer with a 1μm thick membrane.*

3.6.2 Receiver Calibration

The transducer was also calibrated as a detector. This was achieved using a replacement technique, where firstly the calibrated Brüel and Kjær microphone was positioned in the radiated field from a source transducer. The acoustic pressure at this position was then measured. The microphone was then replaced with the micromachined device, and the received signal recorded. The sensitivity of the micromachined transducer could then be calculated.

A micromachined silicon backplate / polymer membrane capacitive transducer [21], with a 10mm aperture was utilised for the source. This was driven using a Wavetek signal generator (model 151) coupled to an ENI RF power amplifier (model A-300). This provided a 200kHz 100V pk-to-pk tone burst signal. A 150V bias was also applied. The 1/8" Brüel and Kjær microphone was aligned axially with the source transducer, and positioned 20mm from its front radiating face. This distance was chosen as it is within the far field region of the source transducer when driven at 200kHz (the far field / near field boundary occurs at approximately 14.6mm). Before the measurement was taken, the microphone \ amplifier system was again calibrated using the same procedure as

discussed above. This time, the sensitivity of the receiver system was calculated to be 195mV/Pa ±2mV/Pa (@200kHz). Note that this was a different sensitivity to the previous measurement, as a higher sensitivity was selected on the receiver amplifier.

A measurement was then taken of the signal from the polymer filmed transducer. The received waveform is shown in Figure 3.26(a). The average amplitude of this signal (ignoring the first two larger cycles) is ~23.6V. This relates to an acoustic pressure of 121Pa (135.6dB). The Brüel and Kjær microphone was then replaced with the micromachined device. This was connected to a Cooknell charge amplifier, which also supplied a 20V bias. Another measurement was taken with this device, and is shown in Figure 3.26(b). This exhibited and average amplitude of ~24.8mV. Hence the sensitivity of the micromachined transducer / Cooknell amplifier system, with 20V applied bias, was ~0.2mV/Pa (-73.9dB re 1V/Pa), at 200kHz. As the Cooknell charge amplifier has a specified sensitivity of 250mV/pC, the sensitivity of the micromachined detector can also be specified as 0.8fC/Pa, at 200kHZ.

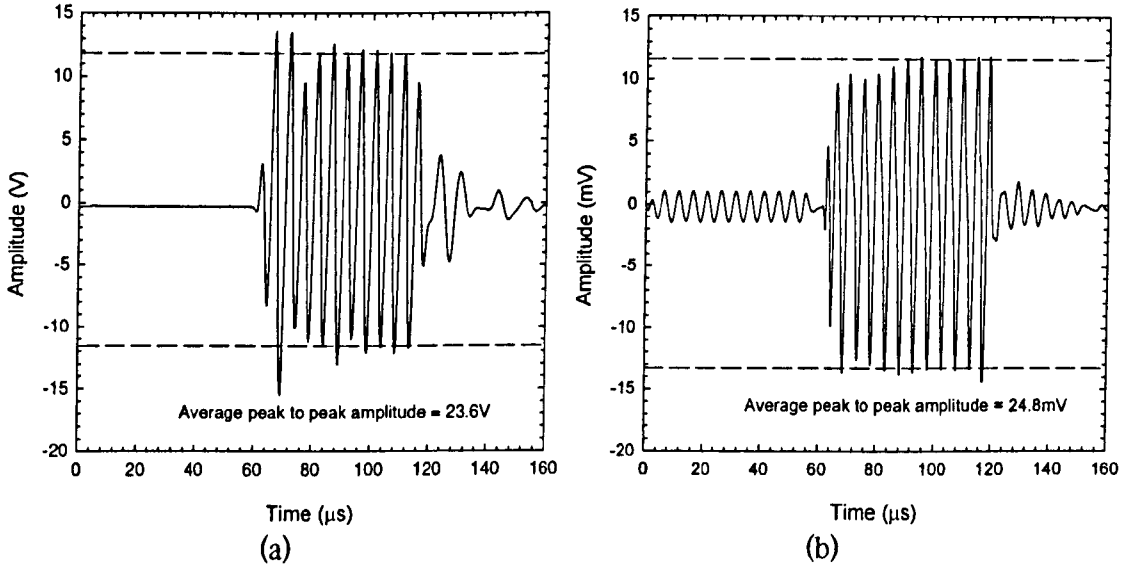

Figure 3.26: *Time waveform from, (a) a calibrated Brüel and Kjær 1/8" microphone, and (b) a 1mm square micromachined detector with a 1μm thick membrane placed 20mm away from a 10mm diameter polymer filmed capacitive source driven by a 200kHz tone burst signal.*

3.6.3 Discussion of sensitivity calibration measurements

The experiments above were conducted at a frequency of 200kHz, as this was the upper limit of the frequency response of the Brüel and Kjær microphone. Examination of the frequency characteristics obtained above for the 1mm square \ 1μm membrane micromachined transducer (98163 batch), shows that its response at 200kHz is approximately nine times less than its response at its peak frequency of 1.2MHz. Hence, its sensitivity, as a receiver, at 1.2MHz would be of the order of 1.8mV/Pa, and as a source, 180mPa/V.

3.7 Effect of membrane geometries

This section examines the effect of membrane thickness, and membrane size on the sensitivity and frequency characteristics of the optimised 98163 batch of transducers.

3.7.1 Membrane thickness

This experiment examined the effect of membrane thickness, on the characteristics of the transducer. A selection of 1mm square devices were used, with membranes of 0.5μm, 1μm and 2μm in thickness (wafers A8, A9 and A12 respectively). These were each used as receivers, in turn, with the 10MHz Panametrics piezoelectric immersion transducer as a source. The experimental set-up was the same as that used previously (see Figure 3.15), with the micromachined transducer under test connected to the Cooknell charge amplifier, and the piezoelectric source connected to the Panametrics pulser unit. A 10mm propagation distance was used. Waveforms were recorded for each transducer, with applied bias voltages of 5V, 10V, 15V, 20V, 25V, and 30V.

Figure 3.27(a) shows a comparison of the waveforms received by the transducers, with 20V applied bias. Their corresponding frequency spectra are also shown, plotted with (b) relative amplitude, and (c) normalised amplitude. The three time waveforms

show well-damped wide bandwidth signals, with the transducers with thinner membranes clearly exhibiting higher amplitude signals. The comparison of their frequency spectra also shows this increase in sensitivity, with the 0.5μm device exhibiting approximately three times more sensitivity than the 2μm device. An increase in frequency response for the devices with thinner membranes is also evident from the normalised frequency spectra, with peak frequencies of approximately 0.8MHz, 1.2MHz, and 1.4MHz for the 2μm, 1μm and 0.5μm devices respectively.

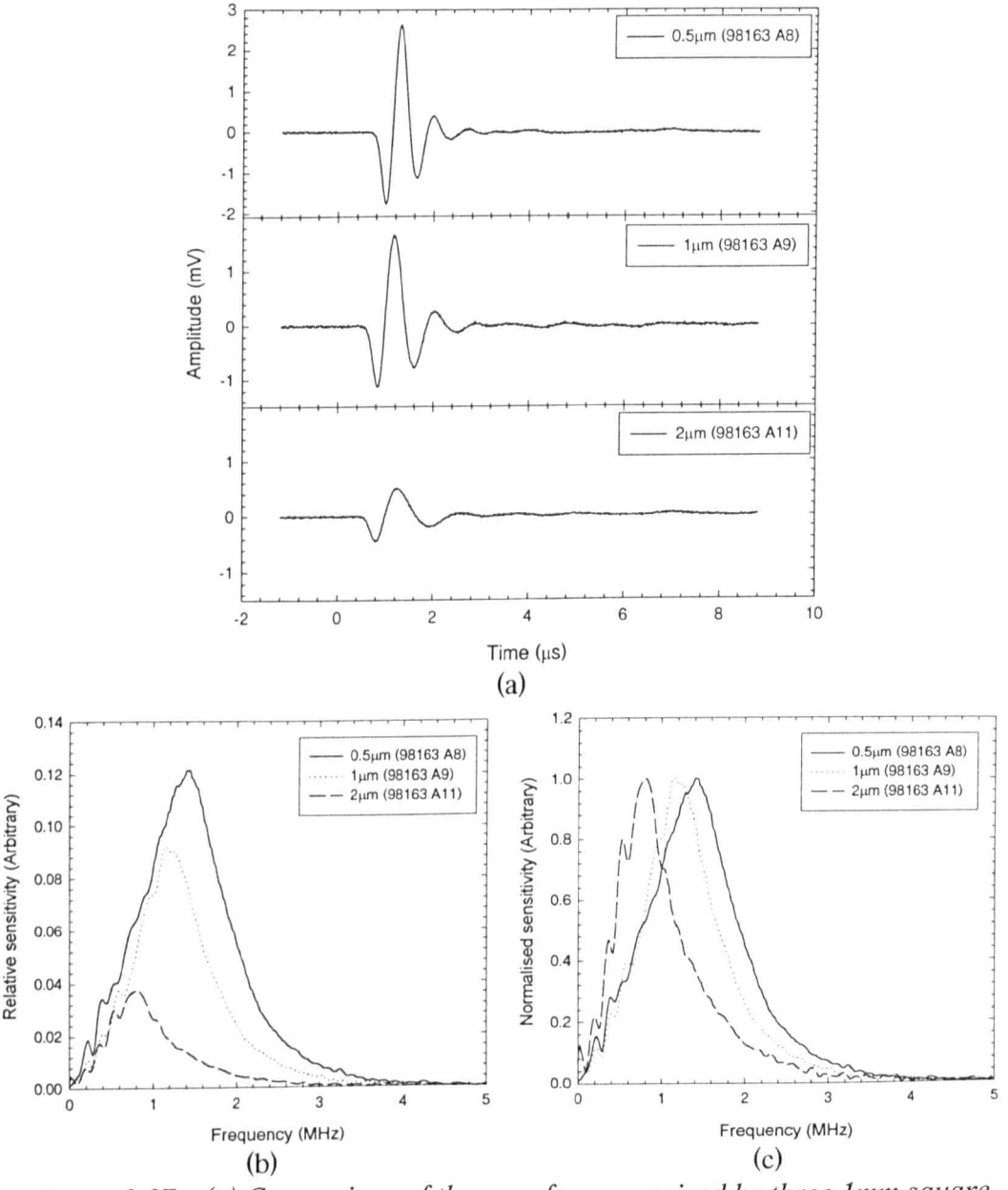

Figure 3.27: *(a) Comparison of the waveforms received by three 1mm square transducers with 0.5μm, 1μm and 2μm thick membranes (20V bias), and their corresponding frequency spectra, plotted with (b) relative amplitude, and (c) normalised amplitude.*

Figure 3.28 shows the peak sensitivities for the three devices, taken from their calculated frequency spectra, plotted against applied bias voltage. It can be seen that these values are approximately consistent with a linear relationship. Neglecting the displacement of the membrane, and hence the change in air gap, this could be expected, as the change in charge (converted to voltage by the charge amplifier) is proportional to applied bias voltage. However, the application of this bias voltage also deflects the membrane, decreasing the air gap. In Chapter 2, it was shown that the sensitivity of a capacitive transducer was proportional to the square of the air gap (assuming a basic parallel plate capacitor model). Thus, a decrease in the air gap would lead to an increase in sensitivity of the device.

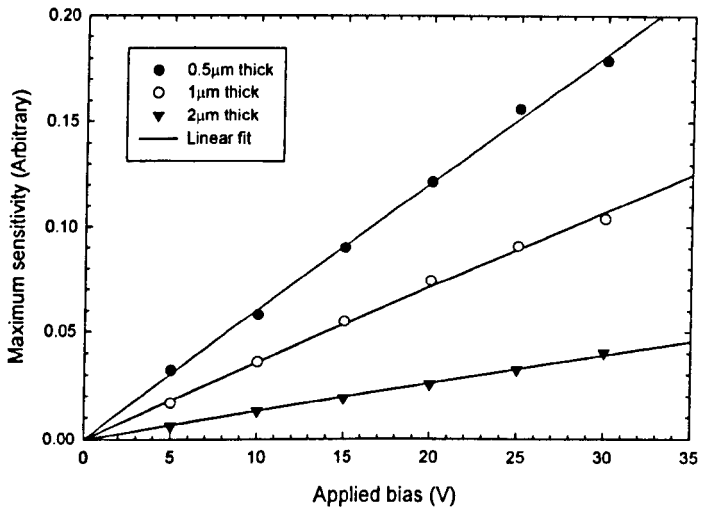

Figure 3.28: *Comparison of peak sensitivity of transducers with 0.5μm, 1μm and 2μm thick membranes.*

Thus for higher bias voltages, an additional increase in sensitivity should also be observed. Referring back to the static displacement measurements, the observed maximum deflection of the membrane at 30V bias (for the 98163 A9 (1μm) device) was approximately 400nm. The nominal air gap plus the membrane thickness is approximately 3μm, hence the change in sensitivity due to this displacement (ignoring the dielectric properties of the membrane) should increase by a factor of approximately 1.3. Hence, the increase in sensitivity due to the deflection change is minimal compared to that due to the increase in applied bias, thus a linear relationship was observed.

Figure 3.29(a) shows the peak, -6dB upper and lower cut off frequencies, and (b) the –6dB bandwidths, for each of the transducers plotted against applied bias. For all three thickness membranes, an increase in their upper, lower and centre frequencies can be observed as the applied bias voltage increases, while the bandwidth remains approximately constant. Also, note that the change in the frequency response between the devices is less for the thicker 2μm membrane.

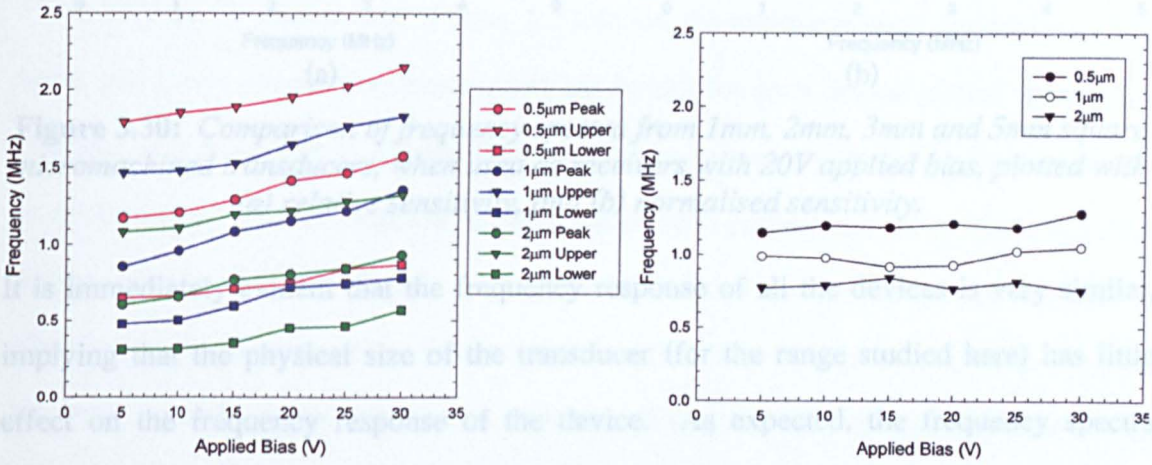

Figure 3.29: *Comparison of the (a) peak frequency response, -6dB lower and upper cut-off frequencies and, (b) -6dB bandwidths of 1mm square receivers with 0.5μm, 1μm and 2μm membranes (98163 A8, A9, A11).*

3.7.2 Membrane lateral dimensions

This experiment examined the effect of the transducers lateral dimensions on its characteristics. Four devices were tested, they were 1mm, 2mm, 3mm, and 5mm square in size, each with membranes of 1μm thickness (all 98163 A9 batch). They were used as detectors, with the 10MHz Panametrics piezoelectric immersion transducer as a source. A 10mm (±1mm) propagation distance was used. The experimental set-up was the same as used previously. Waveforms were first taken with an applied bias voltages of 20V for each of the transducers.

The frequency spectra of the measured waveforms, taken with 20V bias, are shown in Figure 3.30, plotted with relative sensitivity (a), and normalised sensitivity (b).

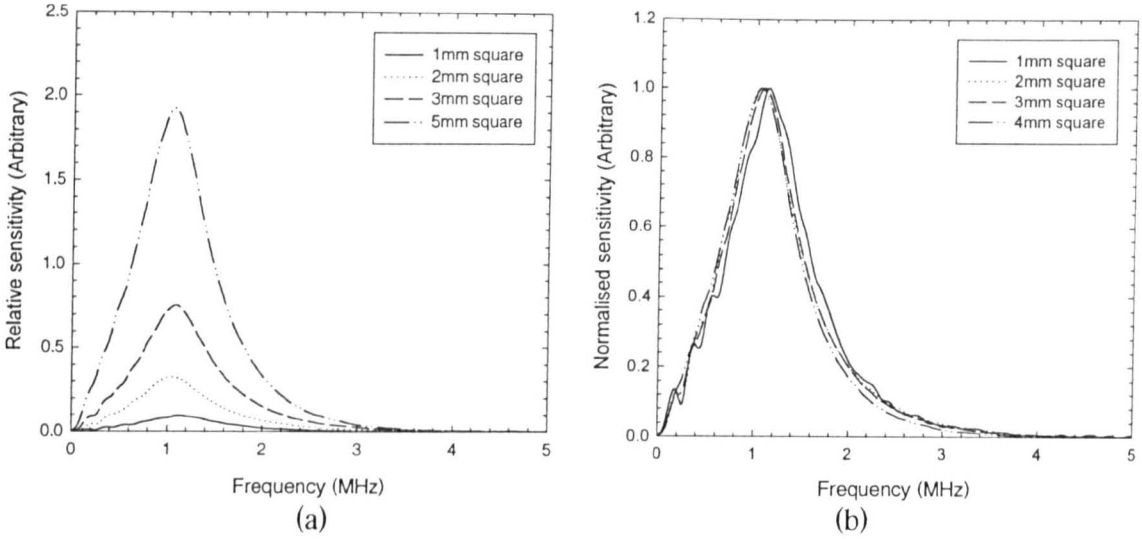

Figure 3.30: *Comparison of frequency spectra from 1mm, 2mm, 3mm and 5mm square micromachined transducers, when used as receivers with 20V applied bias, plotted with (a) relative sensitivity, and (b) normalised sensitivity.*

It is immediately evident that the frequency response of all the devices is very similar, implying that the physical size of the transducer (for the range studied here) has little effect on the frequency response of the device. As expected, the frequency spectra plotted with relative amplitude show large differences in sensitivity between the devices, due to their different active areas. To examine this further, Figure 3.31 shows a comparison of their peak sensitivities. Also plotted in the figure is the predicted

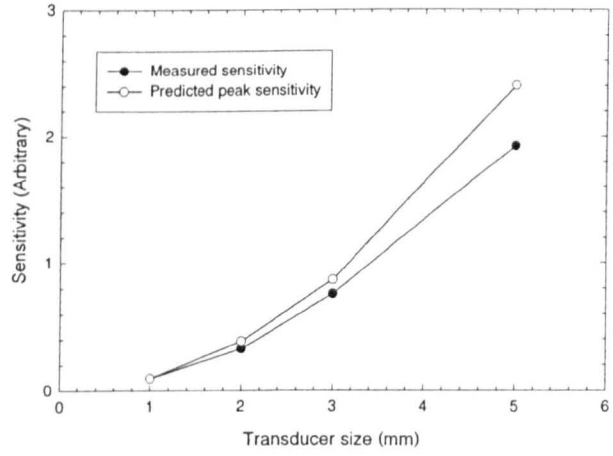

Figure 3.31: *Comparison of the measured peak sensitivity of transducers of size 1mm, 2mm, 3mm, and 5mm square. Predicted sensitivity also shown.*

sensitivity, calculated simply from the difference ratios of the active areas of the transducers. (i.e. the predicted sensitivity of the 5mm square device is simply 25 times the measured sensitivity of the 1mm device). It can be seen that these predicted sensitivities are slightly higher than those measured. This is probably due to diffraction losses from the source transducer; hence, there would not be equal acoustic pressure over the surface of the larger device.

The experiment was then repeated, this time for a variety of bias voltages, from 5V to 30V in 5V increments. Figure 3.32 shows the measured peak sensitivity, (-3dB) upper and lower cut-off frequencies, and bandwidth for each device plotted against bias voltage. It is immediately evident that there again appears to be is very little difference in the frequency characteristics of all the devices, with perhaps the exception of the 1mm square device exhibiting slightly higher characteristics than the others. In addition, as observed in the previous experiment, as the applied bias voltage is increased, the peak frequency, and the upper and lower (-3dB) cut-off frequencies increase, while the overall bandwidth remains approximately constant.

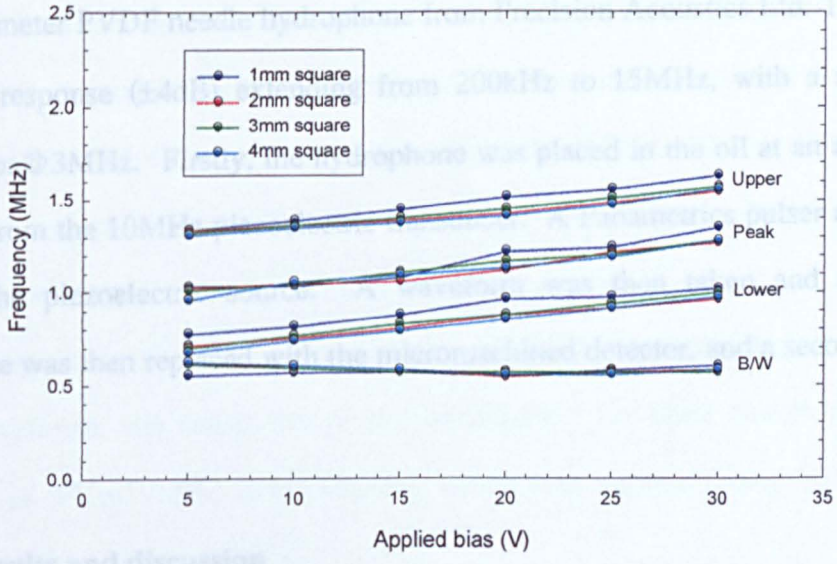

Figure 3.32: *Comparison of peak frequency, -3dB upper and lower cut-off frequencies, and –3dB bandwidth, for a range of different size micromachined transducers (1 μm membrane, 98163 A9).*

3.8 Preliminary experiments in liquids

The experiments described above have all been conducted in air as the transducers were primarily designed for air-coupled work. However, during this study some preliminary experiments were also conducted with the transducers used in immersion. The following sections describe these measurements.

3.8.1 Experimental Technique

The design of these transducers, with the etch holes through the membrane, meant that immersion in water was not possible as it would soon ingress into the device. Hence, for these measurements a low conductivity; low viscosity oil was used instead. This preliminary measurement was performed to study the characteristics of the micromachined devices in liquids. This utilised a 10MHz piezoelectric immersion transducer as a source. A 1mm square transducer with a 1μm thick membrane was used as a detector. A calibration of detection characteristics was performed by comparison to a 1mm diameter PVDF needle hydrophone from Precision Acoustics Ltd. This had a flat frequency response (±4dB) extending from 200kHz to 15MHz, with a sensitivity of 970mV/Mpa@3MHz. Firstly, the hydrophone was placed in the oil at an axial distance of 20mm from the 10MHz piezoelectric transducer. A Panametrics pulser unit was used to drive the piezoelectric source. A waveform was then taken and stored. The hydrophone was then replaced with the micromachined detector, and a second waveform was taken.

3.8.2 Results and discussion

The waveforms and their corresponding frequency spectra are shown in Figure 3.33(a&b) for the hydrophone and micromachined detector respectively. It is

immediately evident that the waveform is well damped, and its frequency has increased markedly beyond that measured in air for the same device. There are several factors that may explain this extended bandwidth. Firstly, the membrane is more highly damped by the liquid than air, and immersion in the liquid pushes the membrane closer to the fixed electrode. Attenuation of higher frequencies in the liquid is also lower than that in air. A final factor is that the acoustic impedance of the membrane itself will be much better matched to the liquid than air, increasing the efficiency of the device.

Examination of the waveform shows an oscillation that, from the frequency spectrum, has a centre frequency of approximately 8MHz. This corresponds to a thickness resonance of the 0.5mm thick silicon substrate upon which the device was fabricated. This resonance has also been found in devices produced by Stanford University, and is a contributing factor in the cross-coupling between elements in array structures [22-24]. Note that here, a simple method to remove this problem would be to thin the silicon wafer sufficiently to move the resonance above the upper frequency cut-off of the device.

Note that the waveform from the micromachined transducer is monopolar, whereas the hydrophone output is bipolar. Interestingly, differentiation of Figure 3.33(b) gives a waveform and frequency spectrum that is very similar to that of the hydrophone (with the addition of the resonance at approximately 8MHz). This is shown in Figure 3.34. This perhaps indicates that the micromachined detector is responding more to particle displacement than pressure when in liquids.

Comparison of the pk-pk amplitudes of the hydrophone and micromachined device waveforms, the sensitivity of the transducer / Cooknell charge amplifier was calculated as 551mV/MPa (±30mV/MPa) which was approximately half that of the PVDF hydrophone (970mV/MPa).

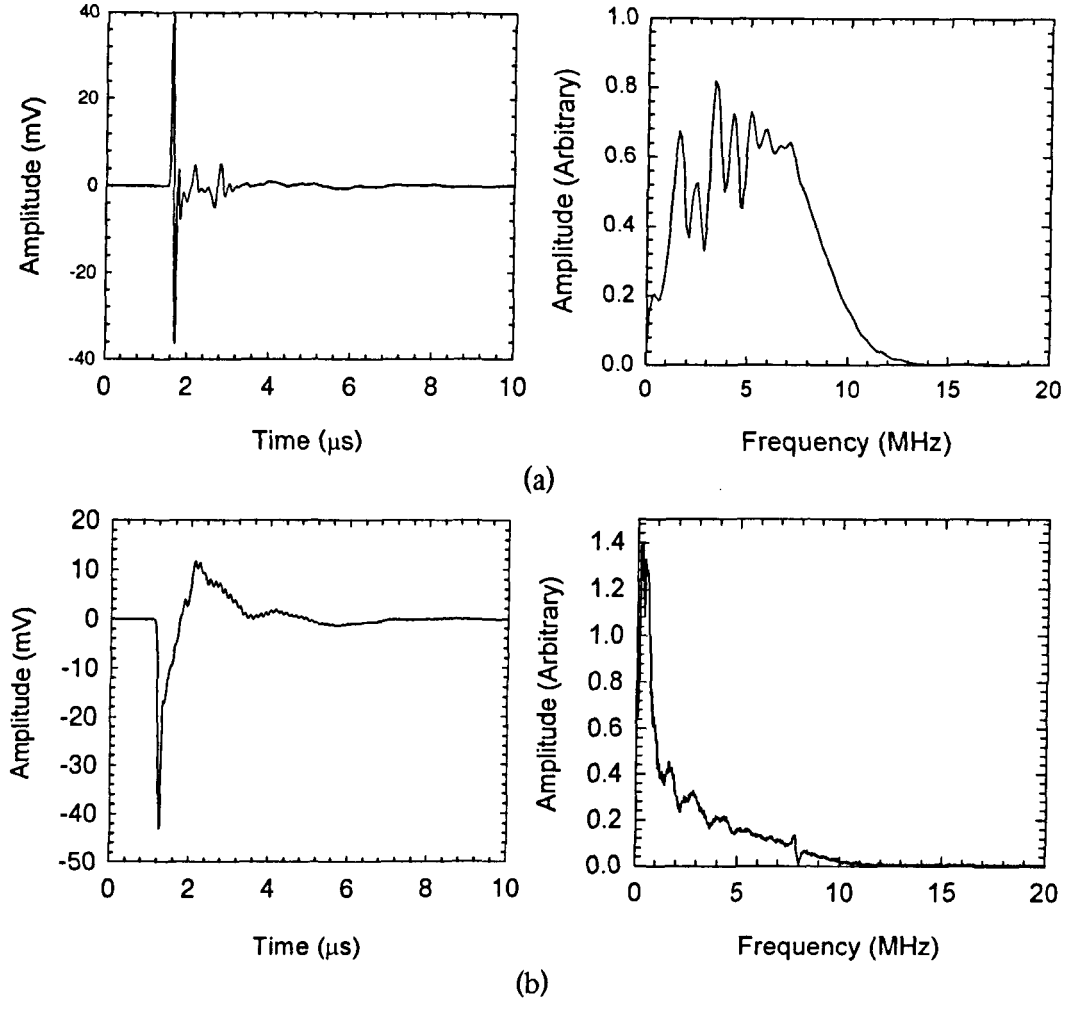

Figure 3.33: *Time waveform (left) and corresponding frequency spectrum (right) received by (a) 1mm diameter PVDF hydrophone and (b) a 1mm square transducer with a 1μm thick membrane positioned 20mm from a 10MHz piezoelectric immersion source in oil.*

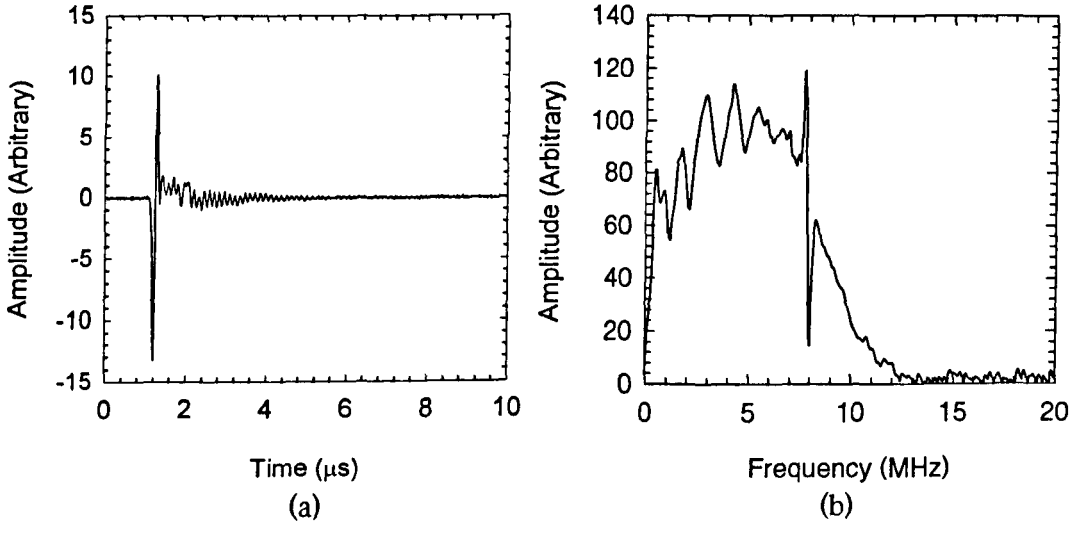

Figure 3.34: (a) *Differentiated waveform, and (b) corresponding frequency spectra received by a 1mm square transducer with a 1μm membrane positioned 20mm from a 10MHz piezoelectric source.*

3.9 Discussion

The initial characterisation experiments demonstrated that in air all the devices examined exhibited wide-bandwidth response, with typical centre frequencies of the order of 1MHz. The 'benchmark' 1mm square devices with 1μm thick membranes from the optimised 98163 batch were found to exhibit a peak frequency response at ~1.2MHz and a bandwidth of approximately 900kHz (75%). Note that this is far greater than that reported in devices produced by the Stanford group, which were typically 5% to 20% [13]. As mentioned previously, the latter devices used a cellular structure where each transducer was constructed from thousands of parallel elements, each of typically 50μm in diameter. These have been successfully modelled using a simple membrane and resonant cavity technique [14]. Each individual cell is generally highly resonant, thus to produce a wide bandwidth device a selection of different size elements (hence with slightly different resonant frequencies) is used. However, conversely, trends in the devices studied here, with far greater lateral dimensions, have indicated that their frequency response is independent of membrane size. This perhaps implies that the mode of operation observed in these devices is more akin to the polymer membrane transducers with ridged backplates, than that seen in the Stanford and Siemens devices.

The WYKO surface profile measurements perhaps give an indication to the wide-bandwidth behaviour observed. Under high bias conditions, all the devices showed signs of uneven height variations (buckling) in the surface profiles. These perhaps indicate inconsistencies in the silicon nitride membrane material itself. It is thought that these random variations play an important part in device operation. Such randomness is observed in similar capacitive polymer devices, as tiny air pockets trapped between the membrane and backplate, and has been suggested that this results in the wide bandwidth behaviour of such devices.

The trends observed with applied bias demonstrated a small shift in the centre frequency response (typically by 20% between 0V and 30V). However very little change

in the overall bandwidth of the device was observed. This could be expected, as when bias voltage is increased, the membrane is deflected more, and hence membrane tension increases and thus its resultant frequency response.

The preliminary immersion work described above demonstrated increases in sensitivity and frequency response when in liquids. Similar trends were seen with the polymer membrane device studied in the previous chapter. This work also highlighted problems caused by the holes in the membrane, when used in liquids, due to the slow ingress of oil into the air cavity resulting in reduced sensitivity. This typically occurred after a few minutes of immersion. A method of refilling the holes after etching of the sacrificial layer has been found and future batches of devices may use this to enable them to be used successfully in immersion.

Generally, the mechanisms involved in the operation of these devices are very complex and hence very difficult to model. Membrane dynamics depend on a large number of factors such as, position of edge anchor points, membrane material properties, and the position and size of etch holes in the membrane. Hence, thorough analysis of the dynamic operation of these devices would require finite element modelling (FEM) of such a structure. Such work is outside the scope of this initial study performed here, and would form the basis of work required for further study of these devices.

3.10 Conclusions

This chapter has described the fabrication and characterisation of a new and novel type of fully micromachined silicon transducer. These differed from other similar devices reported in the literature as they consisted of a single thin large lateral dimensioned membrane, whereas the former generally consist of a cellular structure of smaller membranes and resonant air cavities.

The static membrane deflections of transducers from two preliminary batches, and a further optimised batch of devices have been measured. A 'Snap-down' effect was

observed in the 97223 batch of devices with the bias voltage at which this occurred depending on the thickness of the membrane. Their C-V characteristics have also been measured, and found to be in relatively good agreement with their displacements.

In air, a variety of characterisation experiments have been performed. These demonstrated that the transducers were reversible, with typical peak frequency response at approximately 1.2MHz, and bandwidths (-6dB) of approximately 900kHz (75%). This is much greater than that reported for similar micromachined devices. The effect of 'snap down' observed in the 97223 batch of transducers on its ultrasonic characteristics was also studied and it was found that they effectively operated in two modes, one with lower sensitivity and wider bandwidth, the other with greater sensitivity but with reduced bandwidth. Repeatability between devices from the same batch was found to be excellent.

The effect of membrane width has been examined, with little change in the frequency response between the devices (1mm to 5mm square) observed. Hence, it was concluded that the transducer's frequency response is relatively independent of the physical size of the transducer. The effect of membrane thickness was also investigated, and trends showed that thinner membranes resulted in greater bandwidth and sensitivity and higher centre frequency response.

The effect of bias voltage on the transducers characteristics has also been studied. It was found that increasing the bias tended to increase the peak/centre frequency response of the transducer, while its bandwidth remained approximately constant.

3.11 References

[1] R.A.Noble, R.J.Bozeat, T. J. Robertson, D. R. Billson and D. A. Hutchins, "Novel silicon nitride micromachined wide bandwidth ultrasonic transducers", 1998 IEEE Ultrasonics Symposium - Proceedings, Vol. 2, Ch.422, pp.1081-1084, 1998.

[2] R. A. Noble, A.R.D. Jones, T. J. Robertson, D.A. Hutchins, D.R. Billson, "Novel Wide-Bandwidth Micromachined Ultrasonic Transducers", *IEEE Trans. Ultrason. Ferroelec. Freq.Control,* (accepted for publication in IEEE Trans. UFFC, in press).

[3] R. A. Noble, T.J. Robertson, J.S. McIntosh, D.R. Billson, D.A. Hutchins, "Miniature Silicon Micromachined Ultrasonic Point Detectors for Measurement of airborne Radiated Fields", 2000 IEEE Ultrasonics symposium proceedings, San Juan, Puerto Rico, vol. 1, pp. 955-958, 2000.

[4] D. Holm, "A subminiature condenser microphone with silicon nitride membrane and silicon back plate", *J. Acoust. Soc. Am,* vol. 85, no. 1, pp. 476-480, 1989.

[5] P.R. Scheeper, A.G.H. van der Donk, W. Olthuis and P. Bergveld, "Fabrication of Silicon Condenser Microphones using Single Wafer Technology", *J. Microelectromech. Syst.*, vol. 1, no. 3, pp. 147-154, 1992.

[6] Q. Zou, Z. Li, and L. Liu, "Design and Fabrication of Silicon Condenser Microphone Using Corrugated Diaphragm Technique", *J. of Microelectromech. Syst.*, vol. 5, No. 3, 1996.

[7] W. Kuhnel and G. Hess, "Micromachined subminiature Condenser Microphones in Silicon", *Sensors and Actuators A*, vol. 31, pp. 149-152, 1992.

[8] J. Bergqvist, J. Gorbet, "Capacitive microphone with a surface micromachined backplate using electroplating technology", *J. Microelectromechanical Sys.,* vol. 3, no. 2, pp. 69-75, 1994.

[9] G. M. Sessler, "Silicon Microphones", *J. of the Audio Engineering Soc.,* no. 44, no. 1-2, pp. 16-22, 1996.

[10] C. Thielemann, G. M. Sessler, "Capacitive silicon sensors for ultrasound", *Acta Acustica,* vol. 83, no. 4, pp. 715-720, 1997.

[11] H. Carr, C. Wykes, "Diagnostic measurements in capacitance transducers", *Ultrasonics*, vol. 31, no. 1, pp. 13-20, 1993.

[12] M.I. Haller and B.T. Khuri-Yakub, "A surface micromachined electrostatic ultrasonic air transducer", *IEEE Trans. Ultras. Ferr. Freq. Contr.*, vol. 43, pp. 1-6, 1996.

[13] I. Ladabaum, B.T. Khuri-Yakub, D. Spoliansky, "Micromachined ultrasonic transducers: 11.4MHz transmission in air and more", *Applied Phys. Lett.* , vol. 68, no. 1, pp. 7-9, 1996.

[14] I. Ladabaum, X. Jin, H. T. Soh, A. Atalar, B. T. Khuri-Yakub, "Surface micromachined capacitive ultrasonic transducers", *IEEE Trans. Ultrason., Ferroelect. Freq. Contr.*, vol. 45, no. 3, pp. 678-690, 1998.

[15] X.C. Jin, I. Ladabaum, F.L. Degertekin, S. Calmes, "Fabrication and characterisation of surface micromachined capacitive ultrasonic immersion transducers", *J. Microelectromech. Sys.*, vol. 8, no. 1, pp. 100-114, 1999.

[16] X.C. Jin, I. Ladabaum, F. L. Degertekin, S. Calmes, B. T. Khuri-Yakub, "Fabrication and characterisation of surface micromachined capacitive ultrasonic transducers", *IEEE J. Microelectromech. Syt.*, vol. 8, no. 1, pp. 100-114, 1999.

[17] G.G. Yaralioglu, M.H. Badi, A.S. Ergun, C.H. Cheng, B.T. Khuri-Yakub, F. L. Degertekin, "Lamb wave devices using capacitive micromachined ultrasonic transducers", *Appl. Phys. Letters.*, vol. 78, no. 1, pp. 111-113, 2001.

[18] P.-C. Eccardt, K. Niederer, T. Scheiter and C. Hierold, "Surface micromachined ultrasound transducers in CMOS technology", *Proc. IEEE Ultrasonics Symp.*, pp. 959-962, 1996.

[19] P.C. Eccardt, K. Niederer, "Micromachined ultrasonic transducers with improved coupling factors from a CMOS compatable process", *Ultrasonics,* vol. 38, pp. 774-780, 2000.

[20] A. Gachagan, G. Hayward, S. P. Kelly, W. Galbraith, "Characterization of Air-Coupled Transducers", *IEEE Trans. Ultrason, Ferroelec. Freq. Control,* vol. 43, no. 4, 1996.

[21] D.W. Schindel, D.A. Hutchins, L. Zou and M Sayer, "The design and characterisation of micromachined air-coupled capacitance transducers", *IEEE Trans. Ultrason. Ferroelect. Freq. Control,* vol. 42, pp. 42-51, 1995.

[22] I. Ladabaum, P. Wagner, C. Zanelli, J. Mould, P. Reynolds, G. Wojcik, "Silicon substrate ringing in microfabricated ultrasonic transducers", *IEEE Ultrasonics Symposium, Puerto Rico, USA,* (in press), Oct. 2000.

[23] G. Wojcik, J. Mould, P. Reynolds, "Time –Domain Models of MUT Array Cross-Talk in Silicon Substrates", *IEEE Ultrasonics Symposium, Puerto Rico, USA,* (in press), Oct 2000.

[24] J. Xuecheng, Ö. Oralkan, F.L. Degertekin, B.T. Khuri-Yakub, "Characterization of One-Dimentional Capacitive Micromachined Ultrasonic Immersion Transducer Arrays", *IEEE Trans. Ultrason. Ferroelec. Freq. Control,* vol. 48, no. 3, 2001.

4 Radiated Fields of Surface Micromachined Transducers

4.1 Summary

This chapter continues with the characterisation of the surface micromachined silicon transducers, whose fabrication and initial characterisation were described in the previous chapter. The first section investigates their dynamic membrane displacements, when driven by a broadband transient excitation, using optical interferometry. This is followed by measurement of the radiated fields from 2mm, 3mm, and 5mm square transducers using both broadband transient, and narrowband tone burst excitation signals. The theoretical sound pressure fields from 2mm, 3mm, and 5mm square plane piston sources are calculated and compared to those obtained experimentally.

4.2 Introduction

The previous chapter described the fabrication and initial characterisation of the silicon surface micromachined transducers. This chapter continues their characterisation, firstly by an examination of the dynamic movement of their membranes using an optical technique, and then by investigating their sound pressure fields. Knowledge of these radiated sound pressure fields is important for NDE applications such as through-transmission and lamb wave systems [1,2], to allow accurate retrieval of information from the medium under test. No previous work on the study of fields from fully micromachined transducers seems to have been published.

As discussed in Chapter 2, the main alternatives to the capacitive air-coupled transducer are piezoelectric based devices, with the nearest equivalent in terms of comparable bandwidth and sensitivity being the 1-3 connectivity piezocomposite transducer [3]. Work with the latter, however, has shown that they exhibit very complex

phase changes across their front aperture due to their composite construction of pillars of piezoceramic and filler material [4]. This results in complicated sound pressure fields that are difficult to calculate. Hence, transducers with well-behaved sound pressure fields that can be approximated by plane piston approximations are desirable.

The first section in this chapter examines the dynamic movement of the micromachined transducers membrane, using an optical approach, to measure the surface velocity of the transducer when driven with a broadband transient voltage signal. This information is then used in the second section for calculation of the theoretical broadband sound pressure fields. A comparison of the measured and theoretical fields is then made.

4.3 Optical measurement of surface velocity

4.3.1 Background

The use of optical methods to measure the movement of surfaces has been popular for many years [5]. Such systems generally utilise a laser as a light source, and a photo detector as a receiver. They can be used to directly detect ultrasound in solids, where contact transducers may be problematical, by directly measuring the movement of their surface [6-9]. There are several common techniques of achieving this, including interferometers and knife-edge beam detection. Two of the most common types of interferometer are the Michelson and Confocal Fabry-Pérot [8], although there are also many other derivatives available. They have several advantageous characteristics, such as being non-contact in nature, and exhibiting very flat frequency responses (over a finite range). However, many designs are expensive due to the high precision optics required in their construction Here, a Michelson type interferometer is used to directly measure the dynamic membrane displacement of a 1mm square transducer, with a 1μm thick membrane (98163 batch) when driven with a broadband transient voltage excitation signal. The measurements were taken by the author in the laboratories of Professor R.J.

Dewhurst at the Department of Instrumentation and Analytical Science (DIAS) at UMIST.

A schematic diagram of the Michelson interferometer system is shown in Figure 4.1. It consisted of a HeNe laser source whose beam passed thorough a beam splitter. One of these beams was reflected off a reference mirror, and back to a photo detector. This is known as the reference beam. The other was focused onto the (moving) reflective transducer membrane, and reflected back to the same photo detector. This beam is called the target beam. When the beams are recombined interference occurs between the reference and target beam. Hence, movement of the membrane surface can be measured, either as a change in intensity (phase change) for small displacements, or a number of fringes for greater target motion. The membrane needs to displace by $\lambda/4$ to cause the intensity measured by the photo detector to go between minimum and maximum (i.e. one fringe). This is 158nm, as λ=632nm for HeNe lasers. The interferometer was operated in the region where the rate of change of intensity with deflection of the membrane was greatest (i.e. half way between the minimum and maximum peak intensity). To keep the interferometer in this state, an electronic stabilisation system was used. This utilised a piezoelectric-drive attached to the

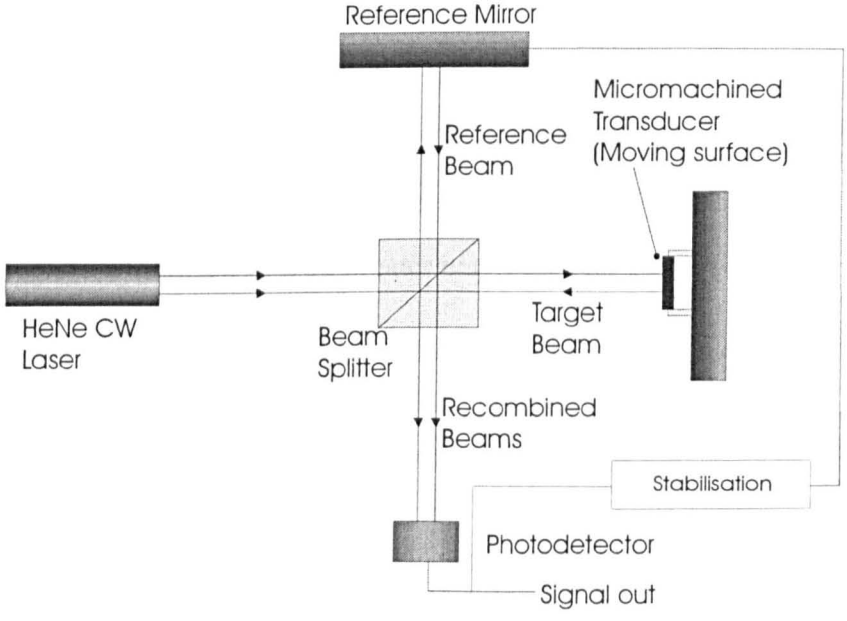

Figure 4.1: *The Michelson interferometer.*

reference mirror, with feed back from the photo detector, effectively adjusting the path length of the reference beam. This feedback system is generally a low-pass filter with an upper cut-off frequency of approximately 1kHz, thus stabilising the system against low frequency vibrations.

A 1mm square device with a 1μm membrane (98163 A9) was positioned so that the incident beam from the beam splitter was at its centre. Note the spot size was approximately 1mm in diameter; hence the average surface displacement was being measured. The transducer was then carefully aligned so the target beam was reflected back to the beam splitter, and onto the photo detector. The transducer was driven by an Avtec pulser unit (model AVRH-1-C), which supplied a 0.1μm, 75V square transient pulse. This was connected to the transducer via a capacitive de-coupling box, to allow the application of a d.c. bias voltage. The output of the photo-detector in the Michelson interferometer was connected to a digital oscilloscope, which in turn was connected to a PC via a GPIB bus to allow the storage of waveforms. Surface displacement measurements were then taken, for applied bias voltages of 0V to 30V in 5V increments.

Figure 4.2(a – f) shows the results of these measurements, plotted as displacement-time waveforms. It is can be seen that the waveforms show well-damped responses, similar in form to those presented in Chapter 3, with typical displacements of the order of a few nm. Also interesting to note is the effect of the applied bias on the membrane displacement. At low bias voltages (0V to 15V), a 'tail off' is evident after the initial pulse, as the membrane returns to its equilibrium position. It appears that this tail reduces with increasing applied bias. This could be expected, as the membrane restoring forces would increase, with greater bias voltages.

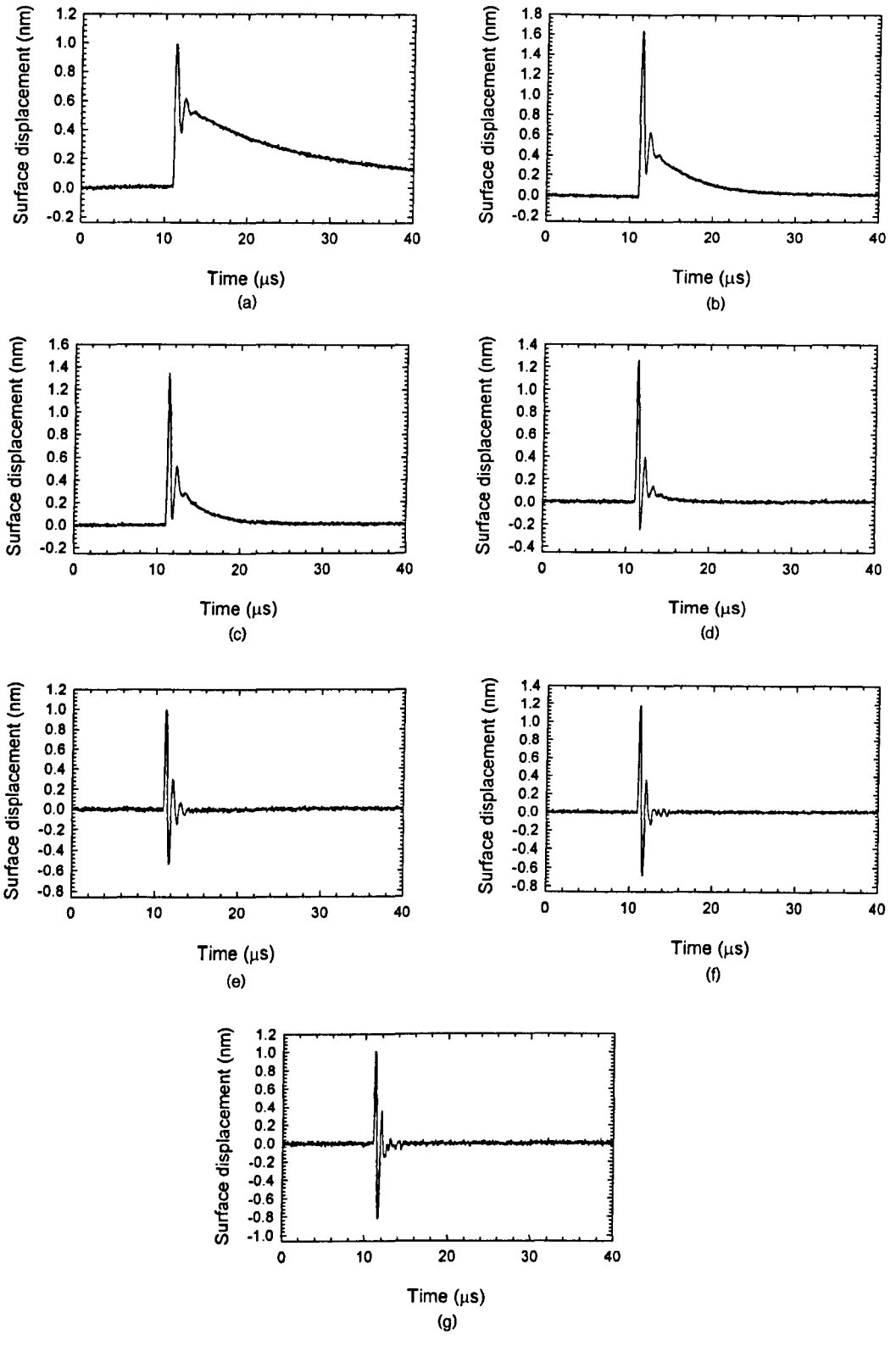

Figure 4.2: Time displacement measurements of a 1mm square transducer with a 1μm thick membrane, driven by a 75V 0.1 μs transient pulse, with an applied bias of (a) 0V, (b) 5V, (c) 10V, (d) 15V, (e) 20V, (f) 25V, and (g) 30V.

The theory for radiated pressure fields from transducers requires knowledge of the velocity waveform of the transducer surface, and not the displacement. These were obtained by differentiation, and are shown together with their corresponding frequency spectra in Figure 4.3. Note that this differentiation operation has increased the noise present in the waveforms. With 20V applied bias (the same bias used in the characterisation experiments above), the waveform and its frequency spectrum are in good agreement with those previously obtained ultrasonically, (see Figure 4.19). The peak frequency response is approximately 1.2MHz, with a bandwidth of approximately 900kHz, ranging from 800kHz to 1.7MHz. The increase in peak frequency response, as observed in the last chapter, with applied bias, is also evident here.

4.4 Radiated sound pressure fields

4.4.1 Background

Previous work, examining the radiated sound pressure fields from capacitive transducers with metallised polymer membranes, has shown they can be modelled using a planar piston in a ridged baffle approximation [10]. This model was described in Chapter 1, and assumes the transducer resembles a plane piston, vibrating with a uniform surface velocity, held within and infinitely large wall. This section examines the radiated pressure fields from the fully micromachined transducers (size 2mm to 5mm square), by first measuring them, and then comparing to pressure fields predicted using the aforementioned theory.

4.4.2 Radiated field measurements

The radiated fields were measured by scanning with a miniature detector, and storing waveforms as a function of position. The miniature detector used was a 500μm square micromachined transducer with a 1μm thick membrane (from batch 97204). This

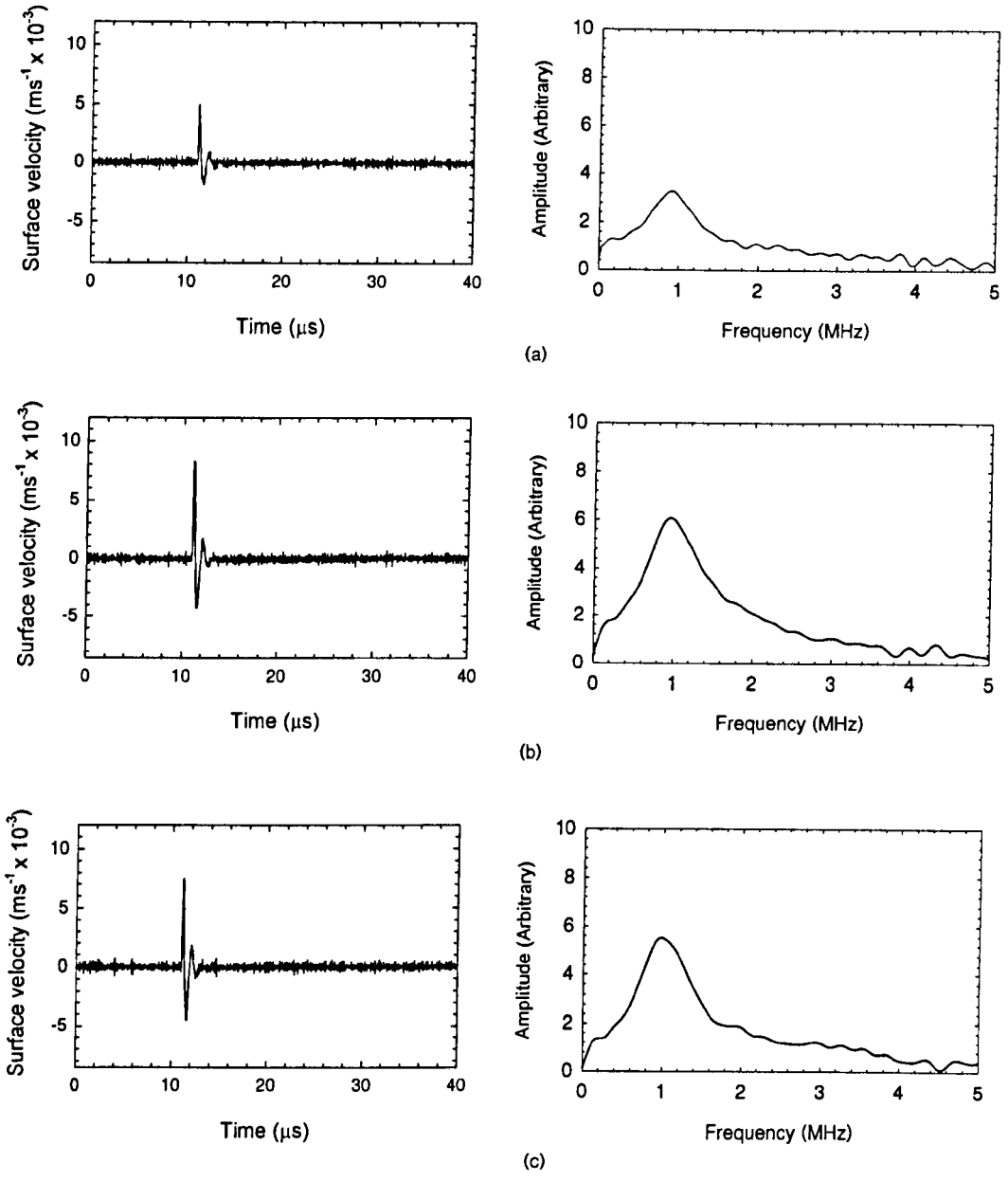

Figure 4.3: *Calculated surface velocity, and corresponding frequency spectra, of a 1mm square transducer with a 1μm thick membrane, driven by a 75V 0.1μs transient pulse, with an applied bias of (a) 0V, (b) 5V, (c) 10V, (d) 15V, (e) 20V, (f) 25V, and (g) 30V.*

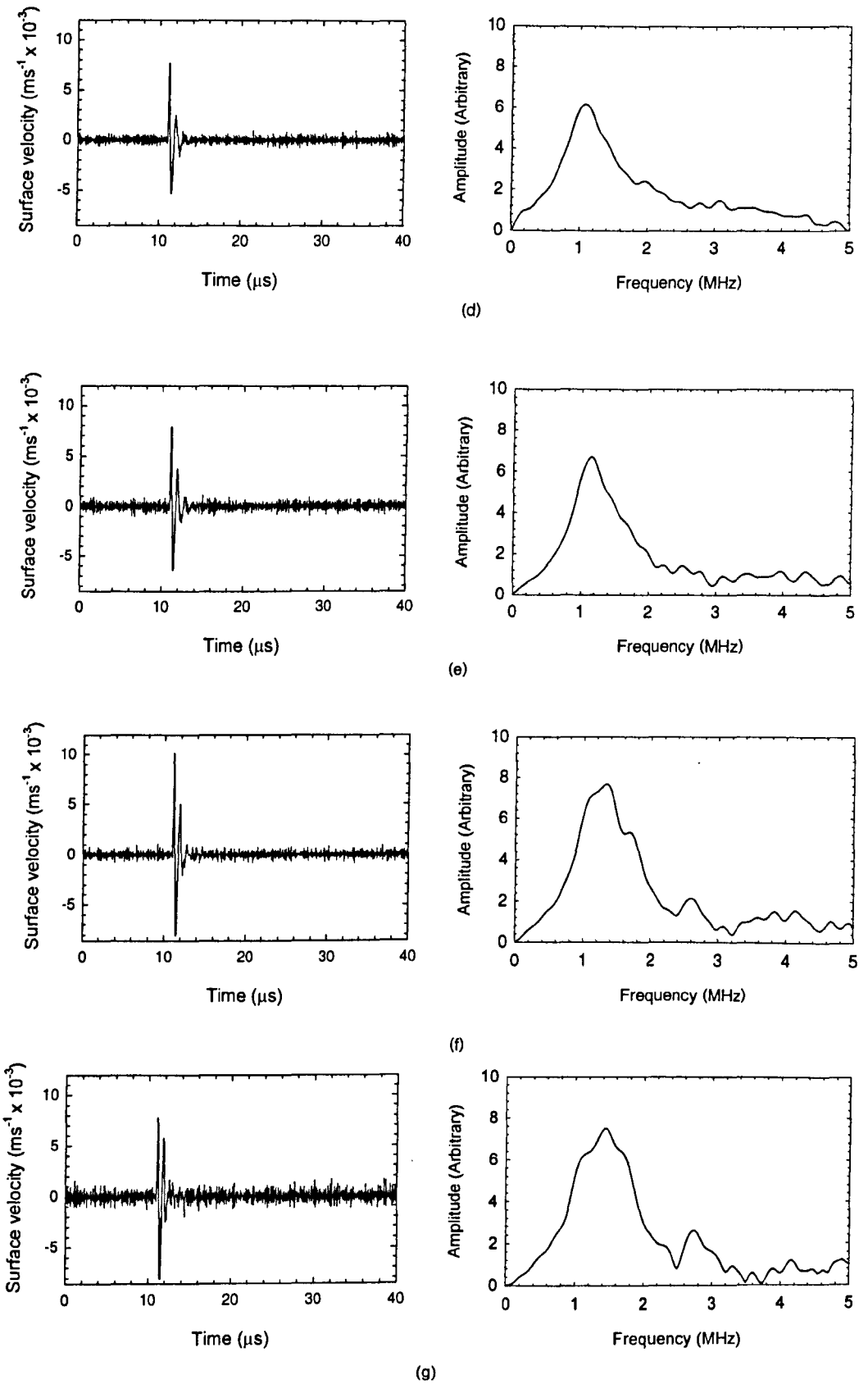

Figure 4.3: (Continued) *Calculated surface velocity, and corresponding frequency spectra, of a 1mm square transducer with a 1μm thick membrane, driven by a 75V 0.1μs transient pulse, with an applied bias of (a) 0V, (b) 5V, (c) 10V, (d) 15V, (e) 20V, (f) 25V, and (g) 30V.*

was mounted on a purpose built probe. A photograph of this is shown in Figure 4.4. Ideally, this detector should be less than a wavelength in diameter at the frequency of interest to prevent directivity problems. However, for sufficient sensitivity, a 500μm detector was required. This 500μm square device was approximately two wavelengths in size at the maximum frequencies studied here (1.5MHz). Its directivity characteristics were examined by scanning a source transducer in a radial motion around it in 0.25° increments. A capacitive transducer, with a 10mm aperture, fitted with a polymer membrane was utilised as a source, and was driven with a 1MHz tone burst signal. The 500μm detector was positioned well into its far field at an axial position of approximately 200mm. The directivity plot obtained is shown in Figure 4.5. It is evident that at this frequency, the detector cannot be considered omni-directional at 1MHz, and this would have some influence on the measured pressure fields, by being less sensitive to signal paths at angles away from the axis.

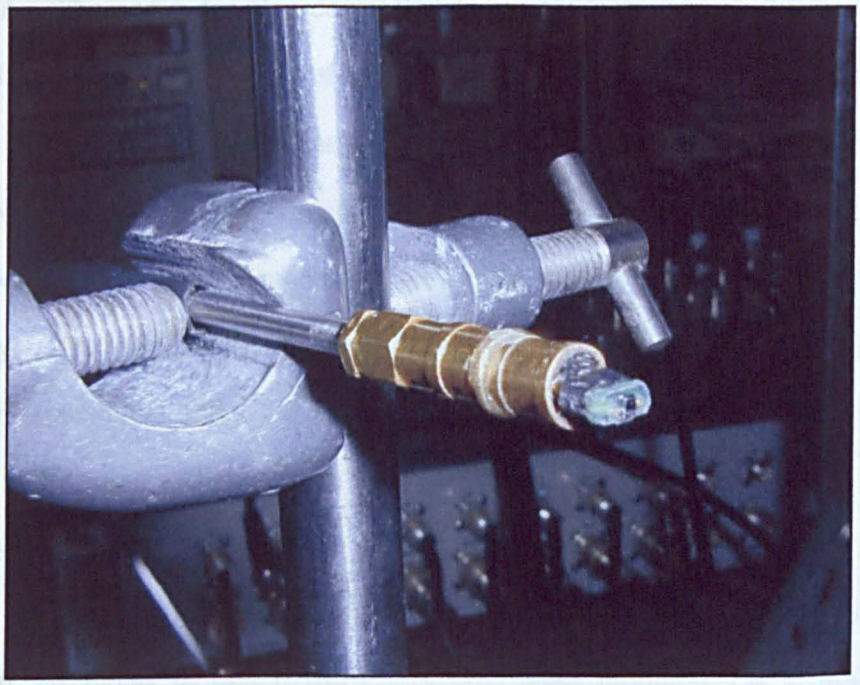

Figure 4.4: *Photograph of the 500μm square micromachined detector miniature probe used to measure the radiated sound pressure fields.*

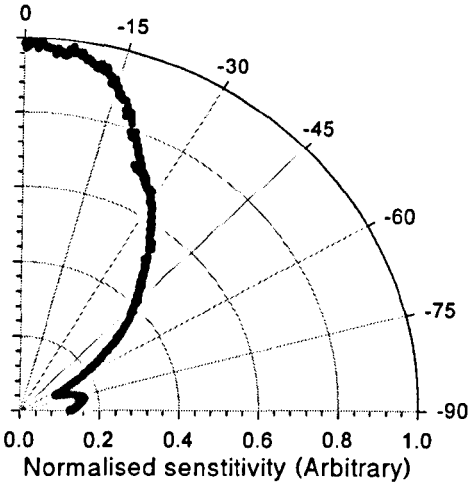

Figure 4.5: *Directivity plot of a 500μm square micromachined detector, measured using a 1MHz tone burst signal.*

A schematic diagram of the complete scanning system is shown in Figure 4.6. A 2-axis linear scanning stage fitted with stepper motors was attached to a custom-built stepper motor controller. This was interfaced to a PC, via a serial link, to allow full *x-y* computer control of the stage. The specifications of the scanning stages are given in Appendix A. The computer also controlled a Tektronix TDS430A digital oscilloscope via a GPIB bus, thus enabling waveforms to be taken and stored. A LabVIEW™ virtual instrument (VI), was written to scan the *x-y* stage in a raster fashion, while taking and storing waveform data from the oscilloscope as a function of position. The transducer under test was placed in the fixture box, and positioned so its sound field was radiating horizontally. The miniature detector was mounted onto the *x-y* stage and positioned axially to the transducer under test. A photograph of this arrangement is shown in Figure 4.7.

The field scans were initiated 2mm (±0.5mm) from the front active face of the transducer. This distance was required to allow clearance between the miniature detector and the DIL packages in which the transducers were mounted. A spatial frequency period of 200μm was used in all scans, over an area measuring 15mm by 30mm in the *x* and *z* directions respectively. Note that, as all the transducers scanned here were square,

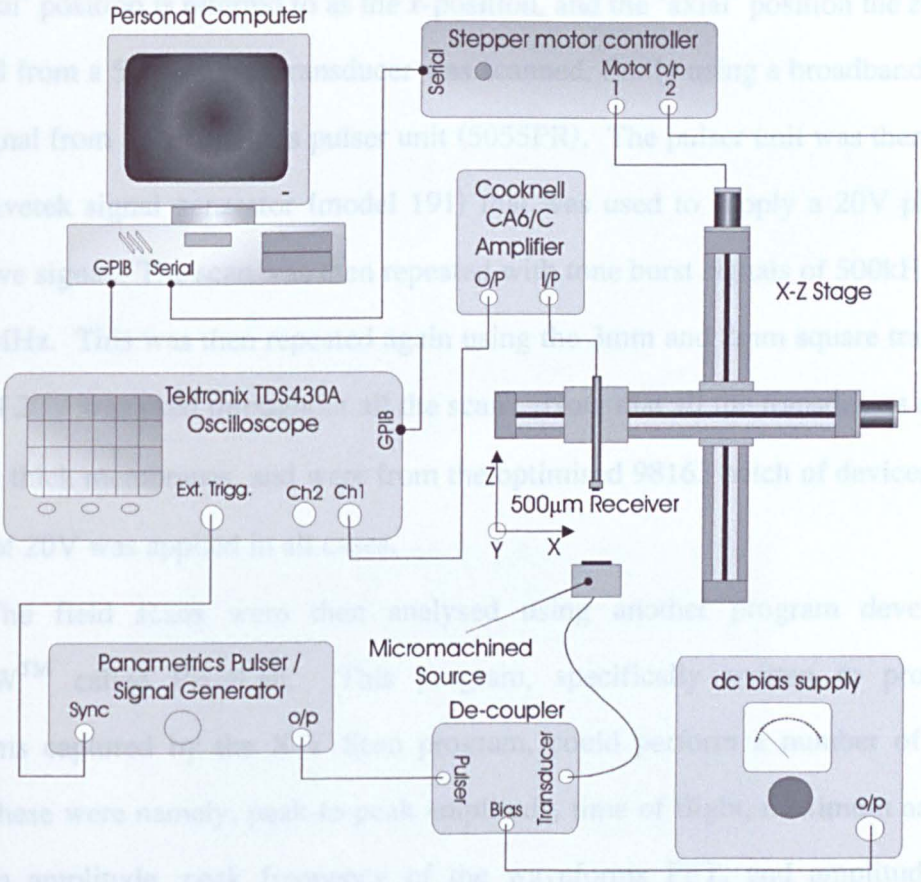

Figure 4.6: *Experimental apparatus used to scan the radiated field from the micromachined transducers.*

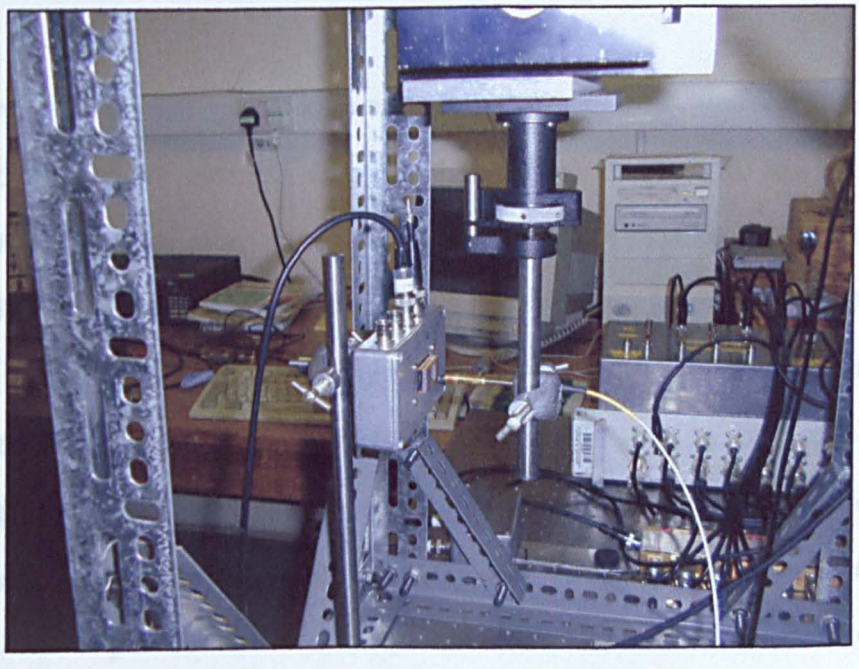

Figure 4.7: *Photograph of the scanning arrangement.*

the 'radial' position is referred to as the x-position, and the 'axial' position the z-position. The field from a 5mm square transducer was scanned, firstly using a broadband transient drive signal from a Panametrics pulser unit (5055PR). The pulser unit was then replaced by a Wavetek signal generator (model 191) that was used to supply a 20V pk-pk tone burst drive signal. The scan was then repeated with tone burst signals of 500kHz, 1MHz, and 1.5MHz. This was then repeated again using the 3mm and 2mm square transducers. A bias of 20V was used throughout all the scans. Note that all the transducers examined had 1μm thick membranes, and were from the optimised 98163 batch of devices. A bias voltage of 20V was applied in all cases.

The field scans were then analysed using another program developed in LabVIEW™ called PixieLab. This program, specifically written to process the waveforms captured by the X-Y Scan program, could perform a number of analysis tasks. These were namely, peak-to-peak amplitude, time of flight, maximum amplitude, minimum amplitude, peak frequency of the waveforms FFT, and amplitude of the waveform FFT at a specified frequency. All of these could be applied either to the whole waveform, or to a selected portion of the waveform with the use of a selectable 'analysis window'.

Here, the program was used to extract the peak-to-peak amplitude and positional data from the stored waveforms. This was then plotted to create 3D images of the peak sound pressure fields for each of the devices. The plots obtained are shown in Figure 4.8 to Figure 4.10 for the 5mm, 3mm and 2mm square devices respectively. These figures each show the broadband plot, displayed both as a wire frame mesh plot and greyscale image, where lighter shading represents higher amplitude, and the three tone burst plots, plotted as greyscale images. As expected, in each case, the narrow band tone bust plots show far more complex variations within the near field than the broadband transient plots. The shift in position of the near field / far field boundary can also be clearly seen between the tone burst plots, moving closer to the source transducer as the frequency decreases. Side lobes are also evident in the far field regions.

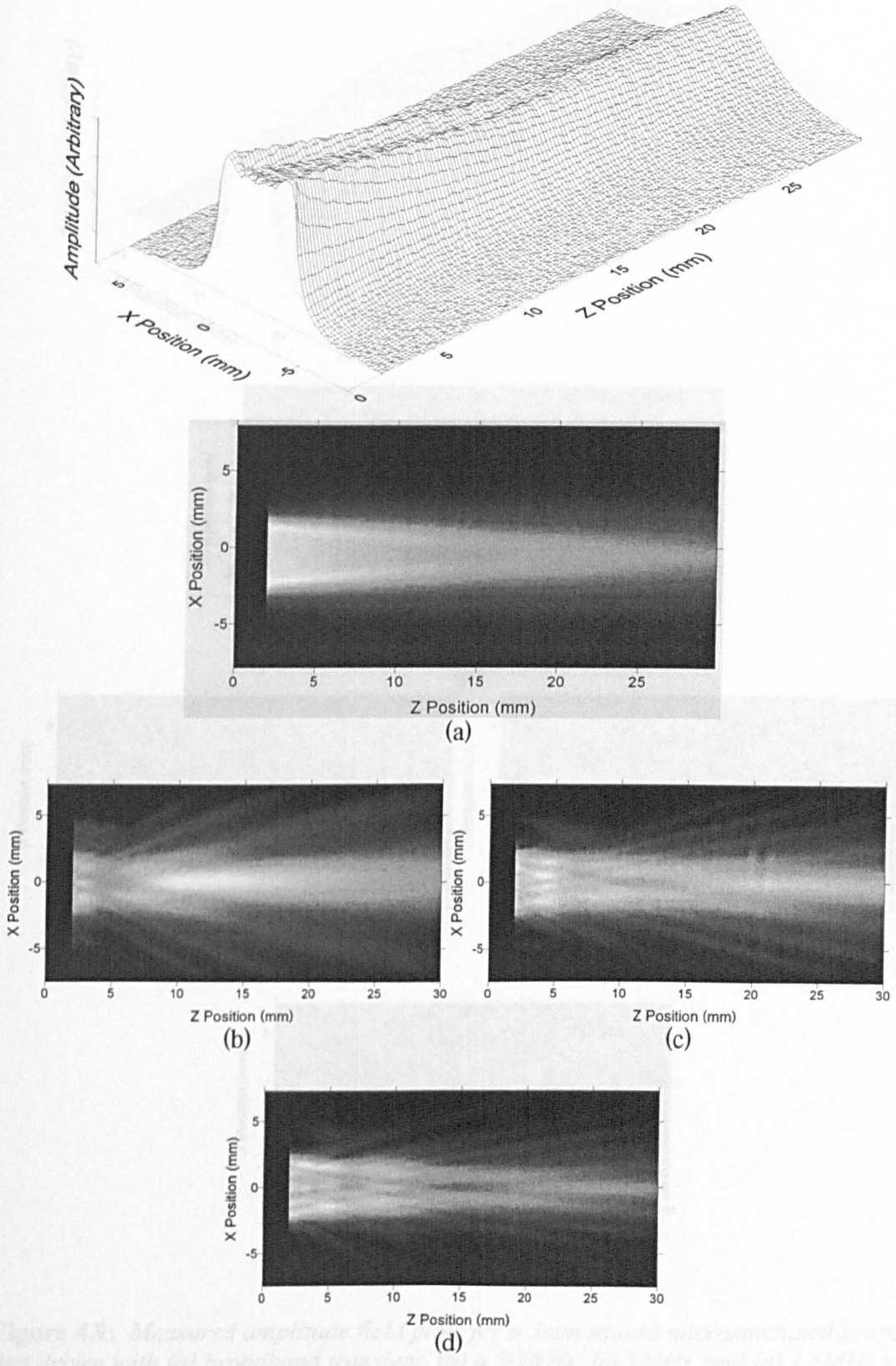

Figure 4.8: *Measured amplitude field plots for a 5mm square micromachined source when driven with (a) broadband transient, (b) a 500kHz, (c) 1MHz, and (d) 1.5MHz tone bursts.*

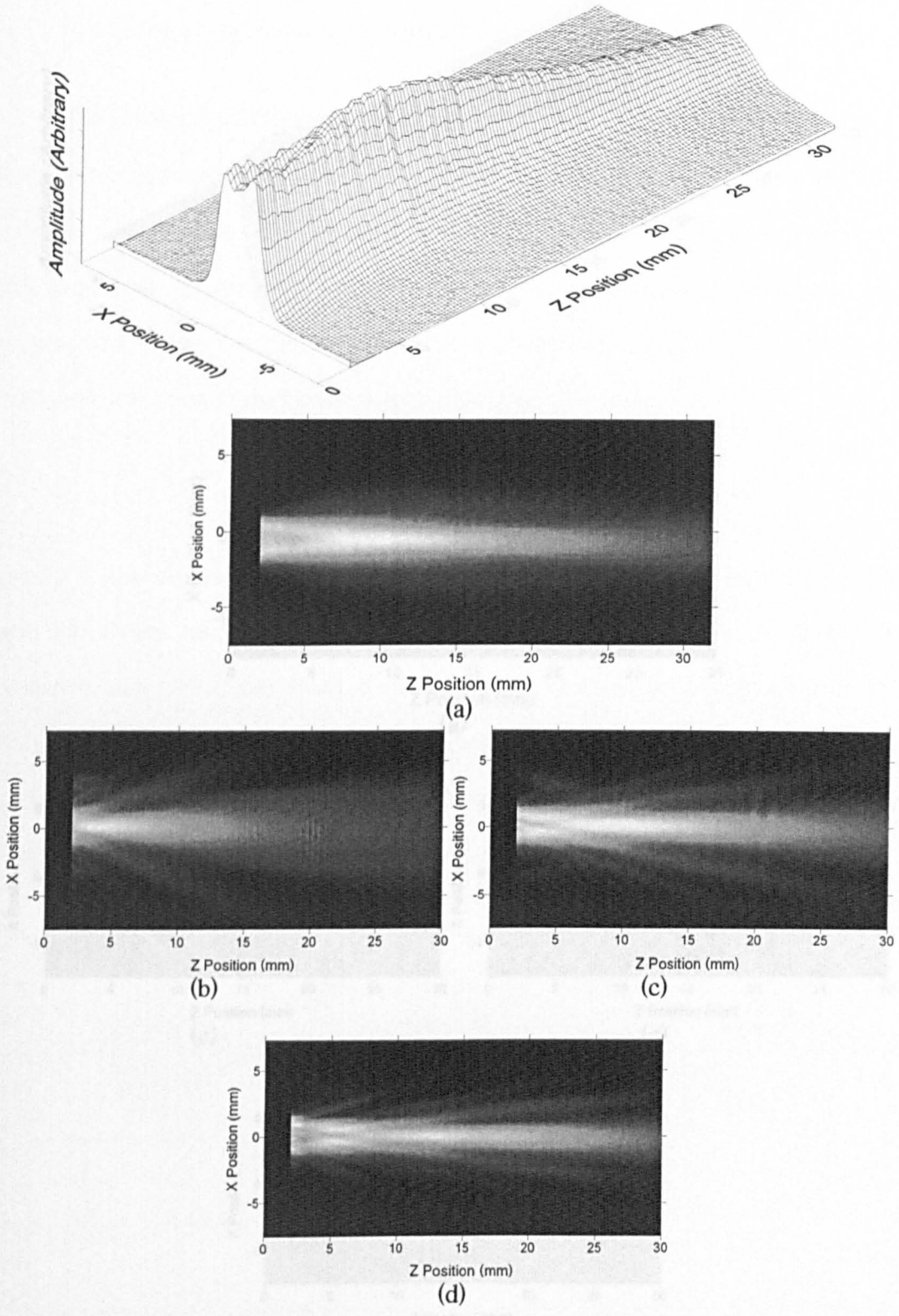

Figure 4.9: *Measured amplitude field plots for a 3mm square micromachined source when driven with (a) broadband transient, (b) a 500kHz, (c) 1MHz, and (d) 1.5MHz tone bursts.*

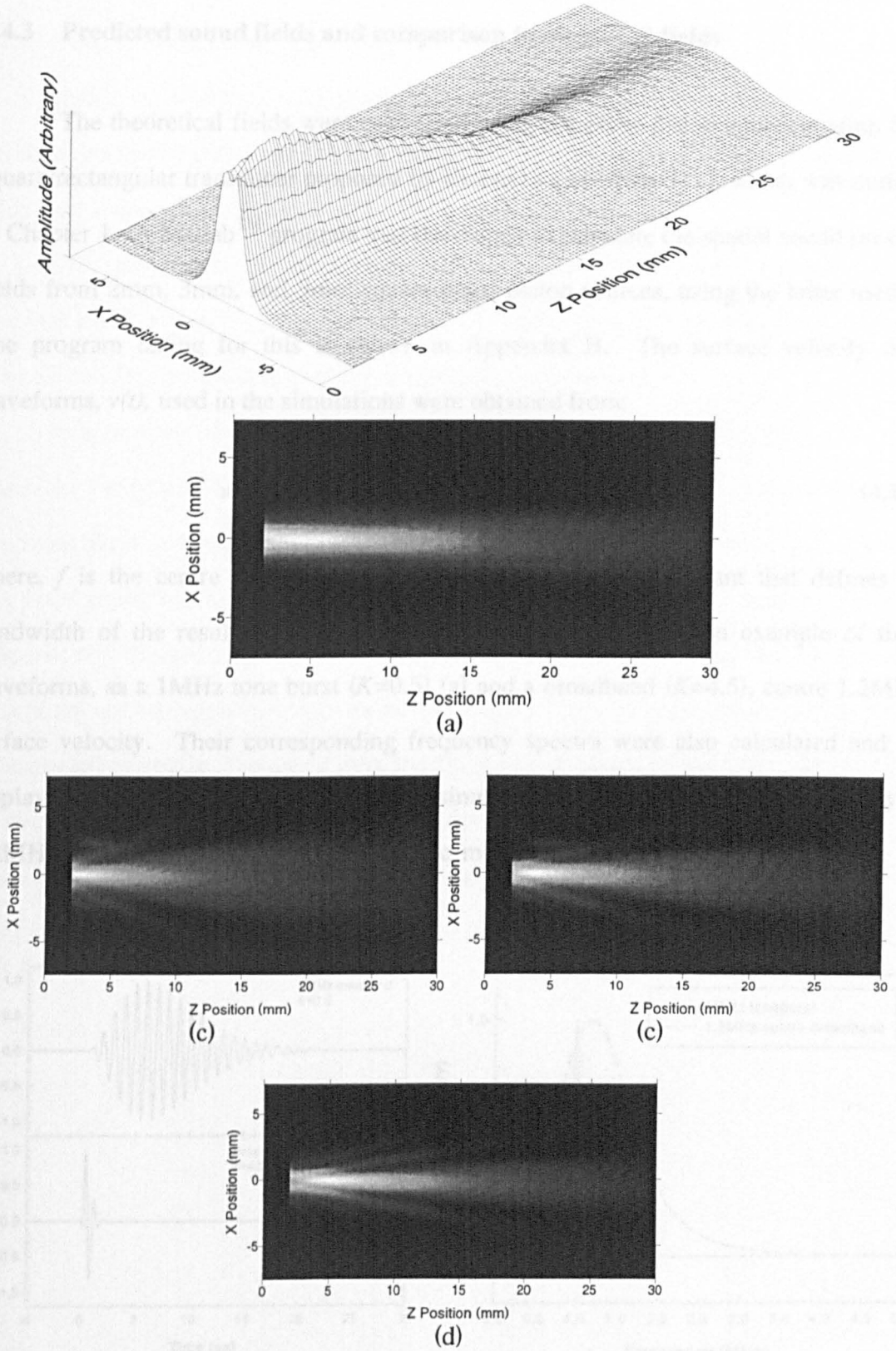

Figure 4.10: *Measured amplitude field plots for a 2mm micromachined source when driven with (a) broadband transient, (b) a 500kHz, (c) 1MHz, and (d) 1.5MHz tone bursts.*

4.4.3 Predicted sound fields and comparison to measured fields

The theoretical fields were calculated using the plane piston approximation for a square/rectangular transducer proposed by Emeterio and Ullate [11], which was outlined in Chapter 1. A Matlab™ program was developed to calculate the spatial sound pressure fields from 2mm, 3mm, and 5mm square plane piston sources, using the latter method. The program listing for this is shown in Appendix B. The surface velocity drive waveforms, *v(t)*, used in the simulations were obtained from:

$$v(t) = Ct^3 e^{-Kft} \cos(2\pi \cdot ft) \tag{4.1}$$

where, f is the centre frequency of oscillation, and K is a constant that defines the bandwidth of the resultant drive velocity. Figure 4.11(a) shows an example of these waveforms, as a 1MHz tone burst (K=0.5) (a) and a broadband (K=4.5), centre 1.2MHz, surface velocity. Their corresponding frequency spectra were also calculated and are displayed in (b). For broadband transient simulated waveform, the centre frequency of 1.2MHz was chosen, as the interferometric measurements performed above found the

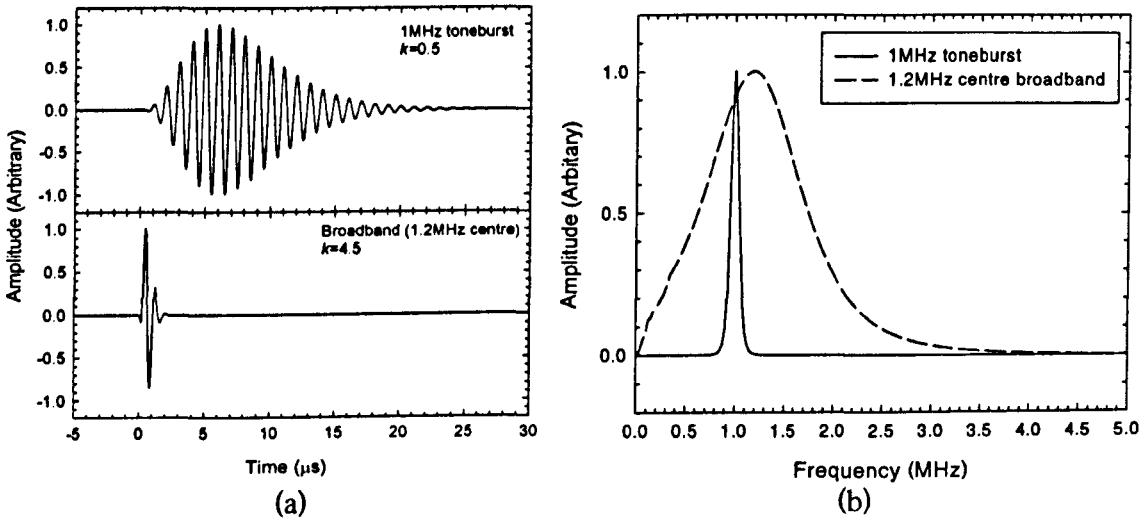

Figure 4.11: *(a) Example of the simulated drive velocity waveforms, and (b) their corresponding frequency spectra.*

surface velocity to exhibit this peak frequency with 20V applied bias. An approximation of the effect of atmospheric absorption was also included in the theoretical sound fields, by calculating the attenuation for the drive frequency used, at each *z* position in the field, and then multiplying these to the calculated field. This correction was done after the fields were calculated with the Matlab™ program.

The predicted sound pressure field plots for 5mm, 3mm, and 2mm square plane positions are shown in Figure 4.12 to Figure 4.14 respectively. They are displayed in the same way as the measured field plots to allow easy comparison.

Examination of the measured and theoretical plots show they agree well, with similar far field /near field boundaries and similar side lobe positions in the narrowband tone burst plots. Worth noting is the effect of atmospheric attenuation on the 1.5MHz tone burst plots, where the signal decay with distance can be easily seen in both the measured and theoretical plots. The variations within the nearfield regions (on the tone burst plots) are less apparent on the measured fields than the theoretical ones. This could be attributed to spatial averaging over the finite size of the miniature detector, and the directionality of the detector. In addition, the higher angle side lobes present in the predicted tone burst plots for the smaller devices, are absent in the measured fields. This could also be attributed to the directionality of the detector.

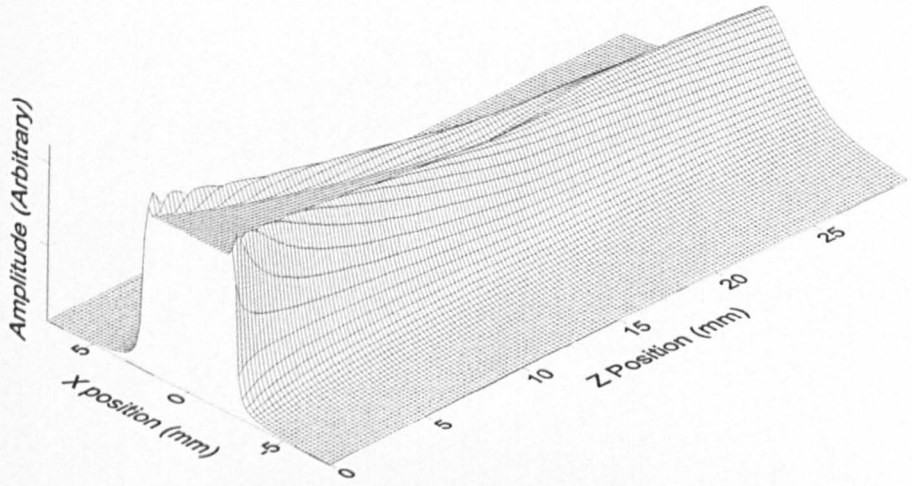

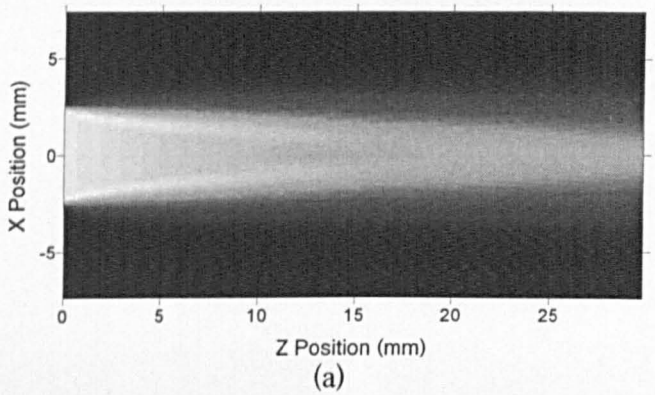

(a)

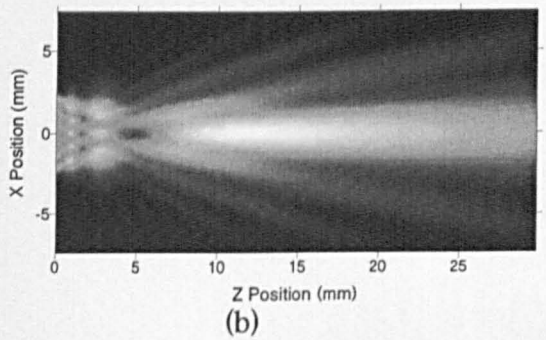

(b)

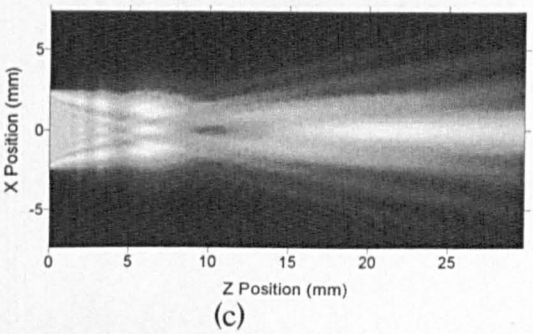

(c)

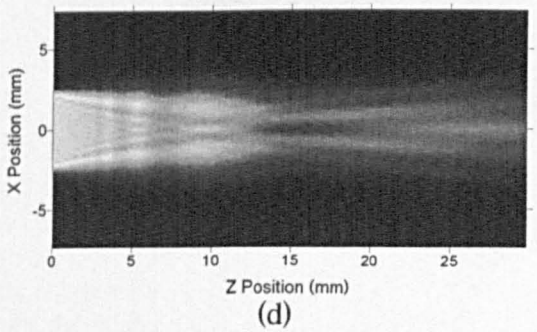

(d)

Figure 4.12: *Theoretical sound pressure field plots for a 5mm square plane piston source when driven with (a) simulated broadband surface velocity, (b) a 500kHz, (c) 1MHz, and (d) 1.5MHz simulated tone burst.*

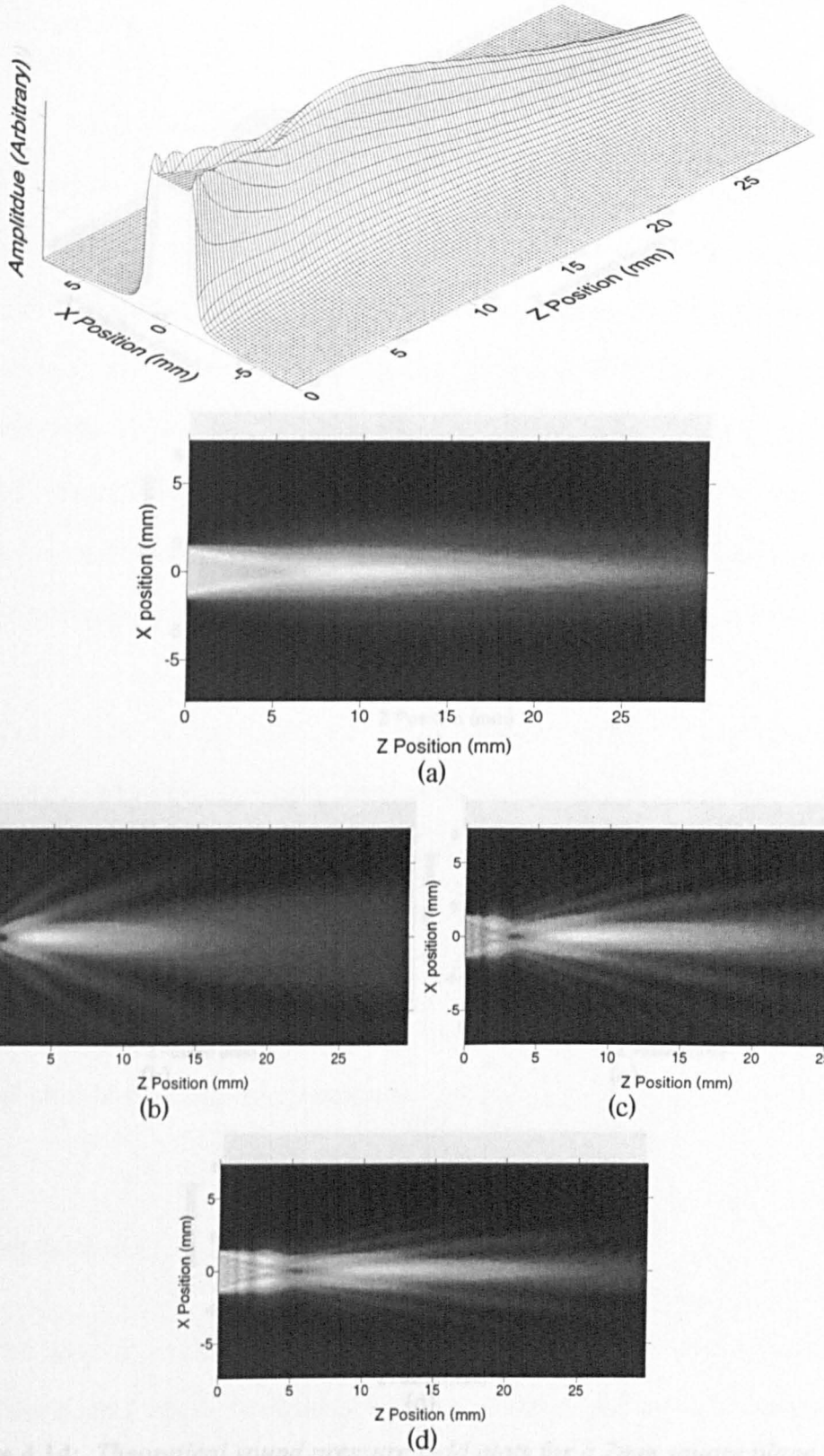

Figure 4.13: *Theoretical sound pressure field plots for a 3mm square plane piston source when driven with (a) simulated broadband surface velocity, (b) a 500kHz, (c) 1MHz, and (d) 1.5MHz simulated tone burst.*

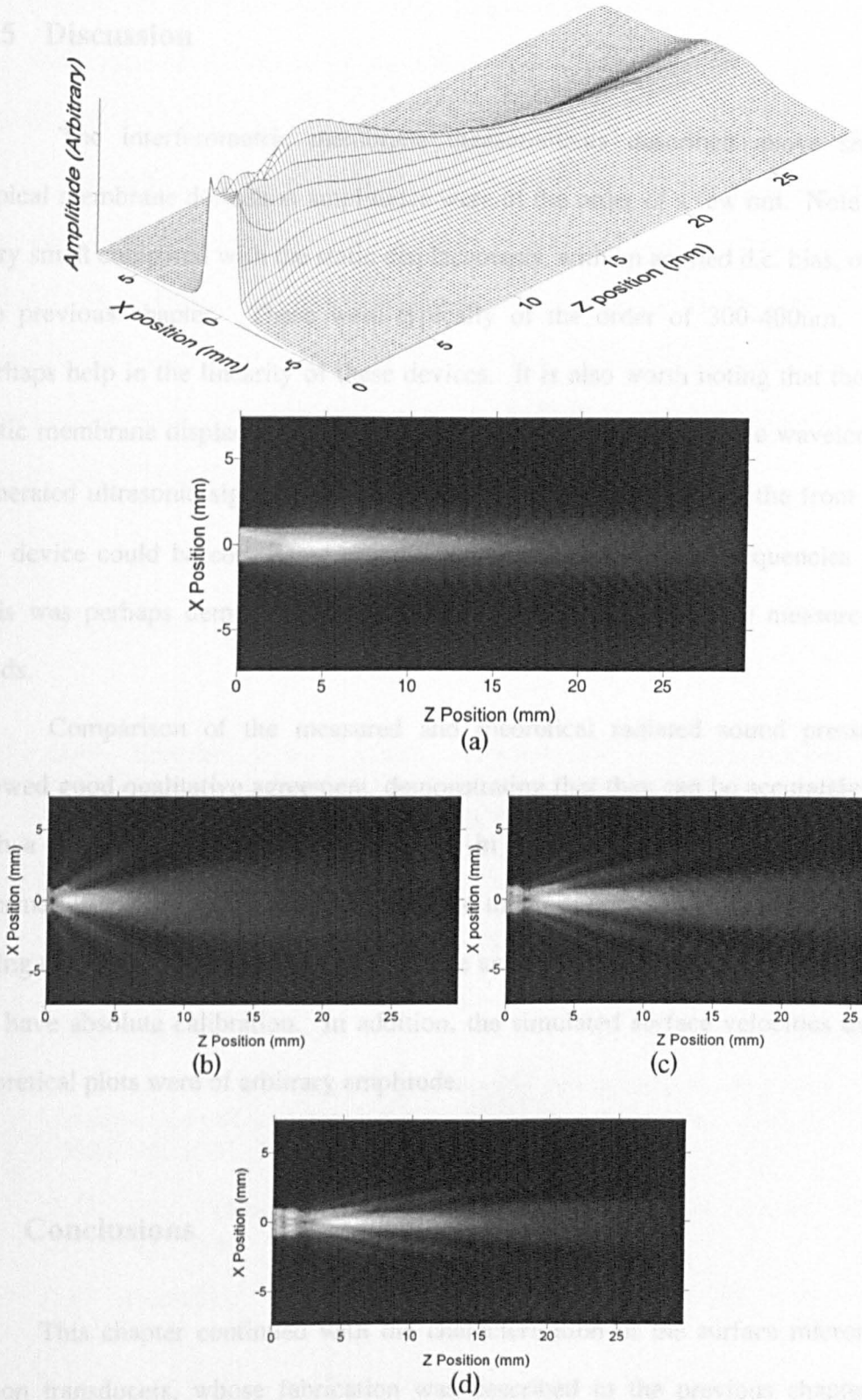

Figure 4.14: *Theoretical sound pressure field plots for a 2mm square plane piston source when driven with (a) simulated broadband surface velocity, (b) a 500kHz, (c) 1MHz, and (d) 1.5MHz simulated tone burst.*

4.5 Discussion

The interferometric membrane measurements described above showed that typical membrane deflection amplitudes were of the order of a few nm. Note that this is very small compared with the static displacements, with an applied d.c. bias, measured in the previous chapter. These were typically of the order of 300-400nm. This may perhaps help in the linearity of these devices. It is also worth noting that the measured static membrane displacements were also very small compared to the wavelength of the generated ultrasonic signal (typically ~0.3mm for 1.2MHz). Thus, the front surface of the device could be considered effectively flat at the ultrasonic frequencies generated. This was perhaps demonstrated by the well-behaved nature of the measured radiated fields.

Comparison of the measured and theoretical radiated sound pressure fields showed good qualitative agreement, demonstrating that they can be accurately modelled with a plane piston approximation. Thus, in an NDE system utilising these devices, information can be easily obtained from the medium under test. However, it is worth noting that only relative peak sound pressure amplitudes were plotted, as the detector did not have absolute calibration. In addition, the simulated surface velocities used in the theoretical plots were of arbitrary amplitude.

4.6 Conclusions

This chapter continued with the characterisation of the surface micromachined silicon transducers, whose fabrication was described in the previous chapter. Their dynamic membrane displacements were studied using a Michelson type interferometer. Typical measured displacements were of the order of a few nm when driven by a 75V 0.1μs transient voltage, with their frequency responses in good agreement with those

measured in the previous chapter using ultrasonic methods. This again confirmed that the peak frequency response of the transducers was in the MHz region, typically at 1.2MHz (@ 20V bias) for the transducers examined here.

The radiated fields from 2mm to 5mm square micromachined transducers were measured when driven with both broadband and narrowband tone burst excitation signals. They were found to exhibit well-behaved sound pressure fields. Theoretical pressure fields were calculated using a plane piston approximation and compared to the experimental fields, with good agreement found. Such knowledge is important for future applications of such devices.

4.7 References

[1] D.W. Schindel, D.A. Hutchins, "Applications of micromachined capacitive transducers in air-coupled ultrasonics and non-destructive evaluation", *IEEE Trans. Ultrason. Ferroelec. Freq. Control,* vol. 42, no. 1, pp. 51-58, 1995.

[2] S.P. Kelly, G. Hayward, R. Farlow, "Applications of through-air ultrasoiund for rapid scanning in the aircraft industry", *IEEE Trans. Ultrason. Ferroelec. Freq. Control,* vol. 43, no. 4, pp. 581-591,1996.

[3] A. Gachagan, G. Hayward, "Characterisation of Air-Coupled Transducers", *IEEE Trans. Ultrason. Ferroelec. Freq. Control,* vol. 43, no. 4, pp. 678-689, 1996.

[4] G. Benny, G. Hayward, "Beam profile measurements and simulations for ultrasonic transducers operating in air", *J. Acoust. Soc. Am.* , vol. 107, no. 4, pp. 2089-2100, 2000.

[5] W.H. Steel, "Interferometry", eds. A Herzenberg, J.M. Ziman, (Cambridge University Press, Cambridge), 1967.

[6] J.-P. Monchalin, "Optical detection of ultrasound", *IEEE Trans. Ultrason. Ferroelec. Freq Control.,* vol. 33, pp. 485-499, 1986.

[7] R.D. Huber, R.E. Green, "Non-contact acousto-ultrasonics using laser generation and laser interferometric detection", *Materials Eval.,* vol. 49, no.5, pp. 613-618, 1991.

[8] J.W. Wagner, "Optical detection of Ultrasound", *in Physical Acoustics – Principals and methods*, (Academic Press, New York), Vol. XIX, pp 201-266, 1990.

[9] Q. Shan, C.M. Chen, R.J. Dewhurst, "A conjugate optical confocal Fabry-Pérot interferometer for enhanced ultrasound detection", *Meas. Sci. Technol.,* vol. 6, pp. 921-928, 1995.

[10] A.G. Bashford, D.W. Schindel, D.A. Hutchins, W.M.D. Wright, "Field characterisation of an air-coupled micromachined ultrasonic capacitance transducer", *J. Acoust. Soc. Am.,* vol. 101, no. 6, pp. 315-322, 1997.

[11] L.G. Ullate, J.L.S Emeterio, "Diffraction impulse response of rectangular transducers", *Acout. Soc. Am.,* vol. 92, no. 2, pp. 651-662, 1992.

5 *Air-coupled line-focused transducers*

5.1 Summary

This chapter examines the development and characterisation of two variants of capacitive air-coupled line-focusing transducer. Focusing is achieved using shaped backplates, one being cylindrically concave, and the other conically shaped, to produce lines of focus. The design and construction of each of these transducers is described. Firstly, preliminary measurements are performed to examine the frequency characteristics of each transducer. Their sound pressure fields are then examined, by scanning with a miniature detector, and comparing to theoretical plane piston models. Further experiments are described to determine the resolution of the transducers. An application of surface imaging, using both devices for comparison is also studied.

5.2 Introduction

Over the last few years, there has been an ever-growing interest in the use of air-coupled ultrasound for non-destructive evaluation (NDE) [1]. Applications, such as rapid non-contact inspection of engineering materials and structures in the aircraft industry, have been shown to utilise air-coupled ultrasound well [2,3]. There are also many other application areas, continually being developed, where the use of non-contact air-coupled ultrasound is of advantage [4,5]. It is obvious that many of these would benefit from focused air-coupled transducers (as opposed to planar ones).

The focusing of ultrasound in air can provide relatively high resolutions at moderate frequencies when compared with that in solids or liquids. This is attributed to the relatively low velocity (~343.4 ms^{-1}) of sound in air resulting in smaller wavelengths. For example, a 700kHz ultrasonic signal in air would have a wavelength of approximately 0.49mm, compared with 2.14mm in water. In an ideal case, the resolution

of an ultrasonic imaging system is diffraction limited [6], and the width of the focal region of a spherical transducer is generally the order of a wavelength, λ. Hence, such systems could provide sub-millimetre resolution, adequate for a majority of applications.

As discussed in Chapter 2, there are predominately two main types of air-coupled transducer, the piezoelectric transducer, and the capacitive transducer. There have been a few reported derivatives of the former device, with a focusing configuration [7,8]. With this design, focused devices can be simply manufactured by forming the piezoelectric ceramic element into a spherical (or concave) shape. Conversely, a fully focusing capacitive transducer is difficult to build, due to the problems associated with forming a shaped membrane. As discussed in earlier chapters, the capacitive transducer, in air-coupled mode, exhibits inherent advantages over its piezoelectric counterpart, so there is a relevant need for a focused version.

Previous work [9,10] has shown that Fresnel zone plates can be used to focus ultrasound in water. Their use has since also been demonstrated in air by Schindel et al [11-13] who used them in the construction of a focusing capacitive transducer. This method of focusing proved successful, with a resolution of approximately 0.68mm being reported and applications of surface imaging demonstrated. However, there are a number of drawbacks. The first is due to the inherent operation of the zone plate, where a fixed frequency or tone-burst is required to give a fixed point of focus, so broadband operation is not possible. This results in the generation of side lobes, due to the use of these narrowband tone bursts, resulting in multiple phantom images being produced either side of the actual image. It has been demonstrated that these could be reduced with the addition of a suitable aperture. However, this is far from ideal.

This chapter describes the development of two variants of line focusing transducer. These devices, cylindrical and conical transducers respectively, utilise curved backplates to create lines of focus. Note that a third fully focusing device, using an off-axis parabolic mirror to reflect the ultrasound to a point of focus was also studied and is described in the next chapter. The cylindrically shaped backplate creates a line of

focus perpendicular to the axis of the transducer, while the conical backplate device creates a line of focus on axis with the transducer. These two backplate contours were chosen to allow unproblematic attachment of the membrane material. A spherically concave transducer was considered, but construction was deemed too difficult, mainly due to the inherent complications of forming a suitably shaped membrane, and successfully attaching this to the backplate without any creasing or trapped air pockets.

The layout of this chapter is as follows; firstly, a separate section is dedicated to each of the two designs of transducer, covering their construction, testing, and characterisation. These are then followed by an application section, examining the use of each of the transducers for surface imaging. The final section discusses the conclusions and areas where further work could be advantageous.

5.3 A cylindrical focusing transducer

5.3.1 Background

Focusing is achieved with this transducer by using a backplate cylindrically concave along its length. This configuration creates a line of focus parallel to the face of the transducer, approximately at the centre of the radius of curvature. There has been some reported work on similar line-focusing devices for immersion applications. One such device, developed by Xiang et al [14], utilised a cylindrically shaped PVDF active element and was used for the measurement of leaky surface and bulk waves in solid materials. Another similar device, constructed from a curved piezoelectric ceramic element, was developed for the manipulation of particles held in suspension [15]. However, no literature on such a device for use in air could be found.

5.3.2 Transducer design and fabrication

This transducer was based on the rigid fixed backplate / flexible membrane design, whose operation has been covered previously in Chapter 2. While designing the transducer, a number of considerations had to be made. Firstly, the choice of material for the backplate and its surface finish had to be determined. Referring back to the discussion in Chapter 2, about backplate surface topology, it was mentioned that micromachined backplates have been shown to improve bandwidth. However, for the prototype device it was decided to use a polished backplate, as opposed to one with a micromachined surface, for ease of manufacture. It was argued that such a device would produce sufficient bandwidth for the purpose of this investigation into focused devices. Brass was chosen as the backplate material as it could be easily machined and polished.

Another design consideration was the choice of radius of curvature of the backplate, and hence the position of the focal line. Referring back to the section on focusing ultrasound in Chapter 1, it was shown that for strongly focusing spherical radiators (i.e. radius of curvature << near field / far field boundary) the focal point is approximately at the geometric centre of radius. It was decided that the transducer would have an active area of approximately 20mm x 45mm. This would result in a near field / far field boundary position at approximately 147mm from the transducer (assuming a 500kHz (λ=0.68mm) centre frequency). Thus, a radius of curvature of 28mm was chosen, this being well within the near field, and would give sufficient working distance between the focal line and the transducer while not being too distant for atmospheric attenuation to become a limiting factor.

A cut-away schematic diagram of the device is shown in Figure 5.1 (membrane not shown for clarity). It consisted of a rectangular brass backplate, measuring 19.5mm wide by 45mm in length, which was polished by hand to give a mirror finish. An insulating nylon insert was utilised to retain this backplate within a machined aluminium casing. An electrical connection was made from the backplate to the centre pin of a

BNC connector mounted on the exterior of the device, with the case itself being grounded via the shield contact of this connector. Engineering drawings of the transducer can be found in Appendix C.

Final assembly involved fitting of the membrane, which was done after thorough cleaning by an air jet. A 3.5μm thick section of Mylar metallised film, large enough to cover the whole of the front of the device, was fixed in place by gluing around its edge. Electrically conducting silver paint was then used to connect the front metallised surface of the film to the case. This whole procedure was accomplished with an applied bias, to minimise trapped air between the membrane and backplate. A photograph of the fully assembled device is shown in Figure 5.2. Note there is obvious wrinkling of the membrane around the backplate area, while over the active area the majority of the air has been expelled from beneath it. This crinkling around the edges was found not to cause any unwanted effects, as will be seen later.

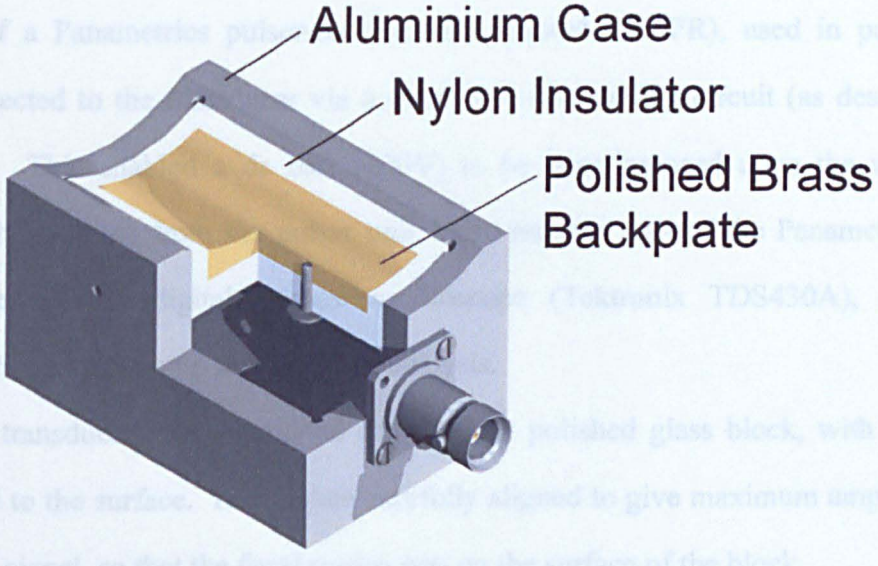

Figure 5.1: *A cut-away schematic drawing of the cylindrical line-focusing transducer.*

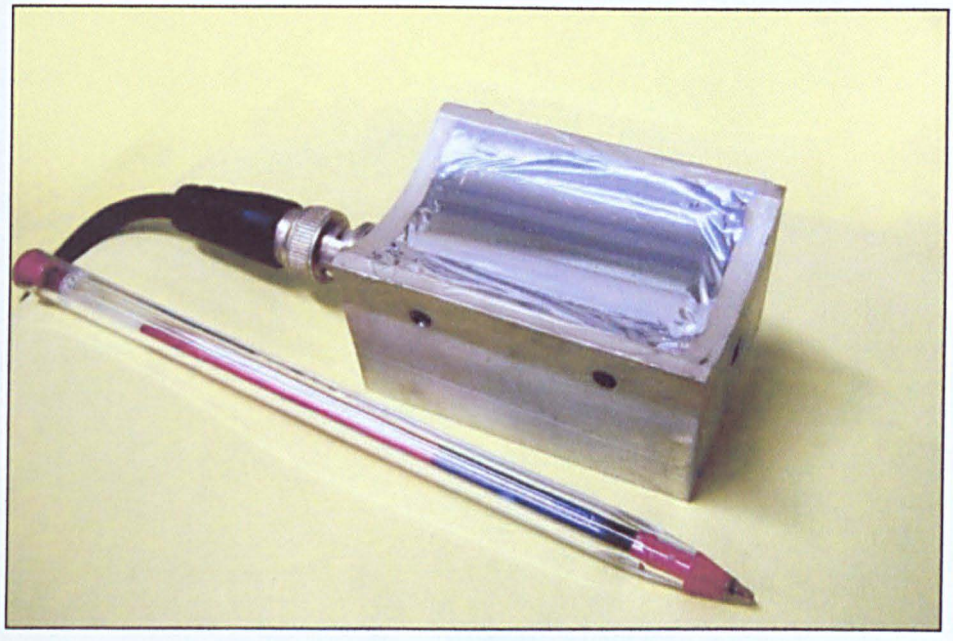

Figure 5.2: *A photograph of the fully assembled cylindrical line-focusing transducer.*

5.3.3 Transducer characterisation – Initial experiment

After construction of the transducer, a preliminary measurement was taken to examine its frequency response. The experimental set-up used is shown in Figure 5.3. It consisted of a Panametrics pulser-receiver unit (model 5055PR), used in pulse-echo mode, connected to the transducer via a capacitive de-coupling circuit (as described in Chapter 3). This enabled a dc bias (200V) to be superimposed upon the wideband transient drive voltage from the pulser unit. The receiver part of the Panametrics unit was connected to a digital storage oscilloscope (Tektronix TDS430A), allowing waveforms to be stored onto disk for later analysis.

The transducer was positioned above a flat polished glass block, with its front face parallel to the surface. It was then carefully aligned to give maximum amplitude of the received signal, so that the focal region was on the surface of the block.

Figure 5.4(a) shows the received waveform. It can be seen that a clean, well-damped signal has been produced. It can also be noted that the time of arrival

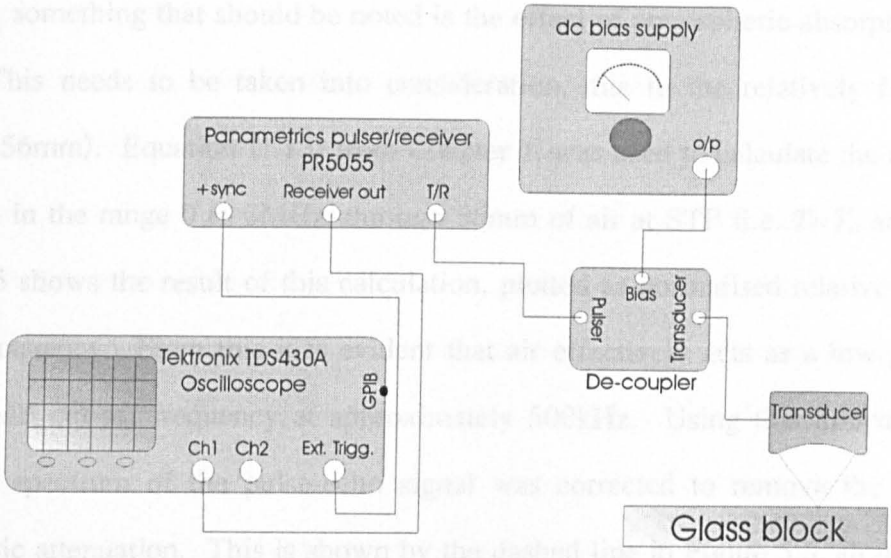

Figure 5.3: *Schematic diagram of the experimental apparatus for examination of device frequency response.*

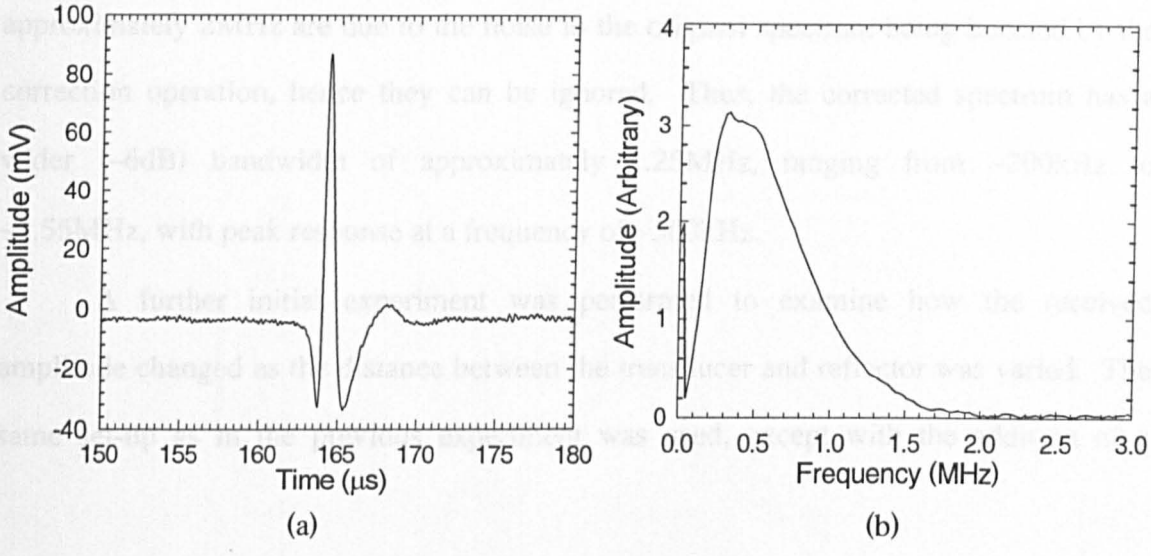

Figure 5.4: *(a) Typical received pulse-echo waveform from a flat glass block, and (b) corresponding frequency spectrum.*

of the reflected wave was approximately 163μs which corresponds to a distance of ~55.9mm in air (assuming a velocity of 343.4ms^{-1}), hence a distance of 27.95mm between the transducer and the surface of the block. This is consistent with the designed focal length of the transducer (28mm). The corresponding frequency spectrum of the waveform is shown in Figure 5.4(b). From this it is evident that the transducer has a (–6dB) bandwidth of approximately 700kHz, lower and upper frequency points of 150kHz and 850kHz respectively, and a peak centre frequency of approximately 400kHz. This response is typical for that of a polished backplate/thin polymer film device [16].

However, something that should be noted is the effect of atmospheric absorption on this result. This needs to be taken into consideration, due to the relatively long transit distance (56mm). Equation (1.13) from Chapter 1, was used to calculate the attenuation of signals in the range 0 to 3MHz, through 56mm of air at STP (i.e. $T=T_o$ and $P=P_o$). Figure 5.5 shows the result of this calculation, plotted as normalised relative amplitude against frequency. From this it is evident that air effectively acts as a low pass filter, with a –3dB cut-off frequency at approximately 500kHz. Using this information, the frequency spectrum of the pulse-echo signal was corrected to remove the effects of atmospheric attenuation. This is shown by the dashed line in Figure 5.5, along with the original frequency spectrum (solid line). Note that the peak(s) occurring at approximately 2MHz are due to the noise in the original spectrum being boosted by the correction operation, hence they can be ignored. Thus, the corrected spectrum has a wider (–6dB) bandwidth of approximately 1.25MHz, ranging from ~200kHz to ~1.55MHz, with peak response at a frequency of ~500kHz.

A further initial experiment was performed to examine how the received amplitude changed as the distance between the transducer and reflector was varied. The same set-up as in the previous experiment was used, except with the addition of a

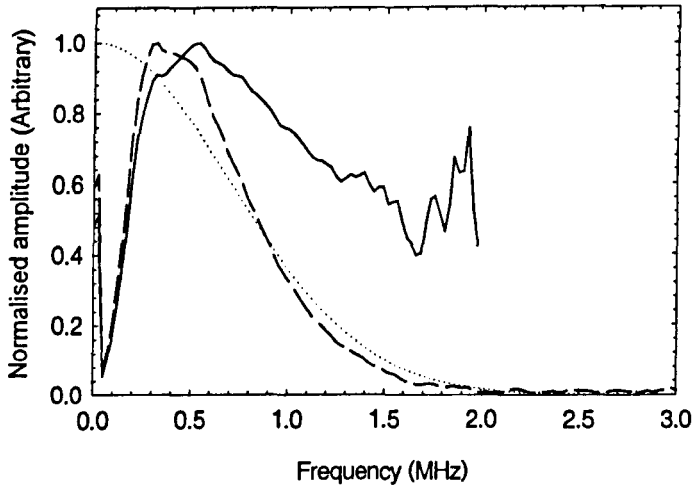

Figure 5.5: *Normalised attenuation of a wideband signal through 56mm of air at STP (dotted line). Original frequency spectra of received pulse-echo signal (dashed line), and corresponding frequency spectra corrected for attenuation in air (solid line)*

micrometer stage to allow accurate vertical movement of the transducer. The transducer-reflector distance was varied 15mm either side of the focal point (i.e. between 13mm and 43mm), with 0.5mm increments. Figure 5.6 shows the results obtained. Again, it is immediately clear that the point of maximum received signal is at a transducer-reflector distance of 28mm, the designed focal length. Also evident is that the area around the point of maximum amplitude is not symmetrical as might be expected. The reason for this was, again, thought to be due to atmospheric absorption of the signal. From Equation (1.13), the atmospheric attenuation of the signal from the focusing transducer can be calculated as $32.187 dBm^{-1}$, assuming a centre frequency of 450kHz, and atmospheric conditions at STP. The received signal amplitude corrected for atmospheric attenuation is also shown in Figure 5.6. This operation has resulted in a slightly more symmetric plot.

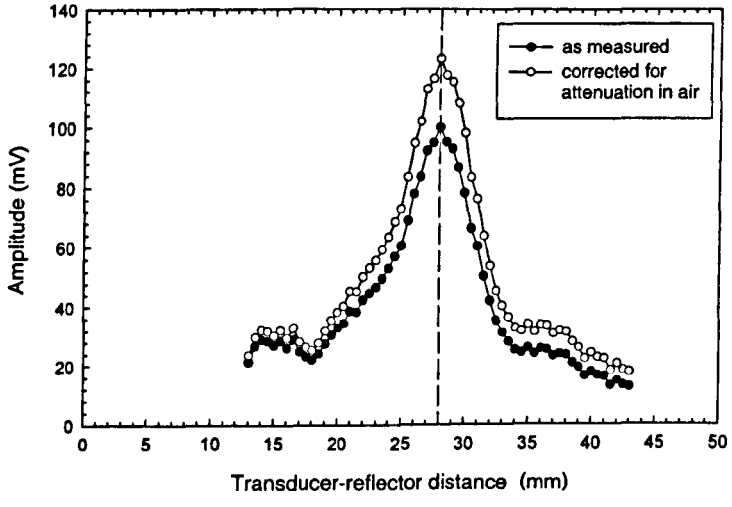

Figure 5.6: *Measured signal amplitude with increasing transducer-reflector separation. (Designed focal length of transducer shown as dashed vertical line)*

5.3.4 Measured sound pressure fields

Knowledge of the sound pressure field emanating from a transducer is important, as this can often be the limiting factor in an ultrasonic system. In this case, of a focusing transducer, the ability to characterise the pressure field is especially necessary. Thus, this section studies the radiated field from the cylindrical line-focusing transducer and examines how this compares to predicted theory.

The coordinate system employed in the following section is illustrated in Figure 5.7. The length and width of the active area is defined as $2a$ and $2b$ respectively, with the origin positioned at the centre of the front concave face of the transducer. Thus, for this transducer that has an active area of 19.5mm wide by 45mm in length, a=22.5mm and b=9.75mm.

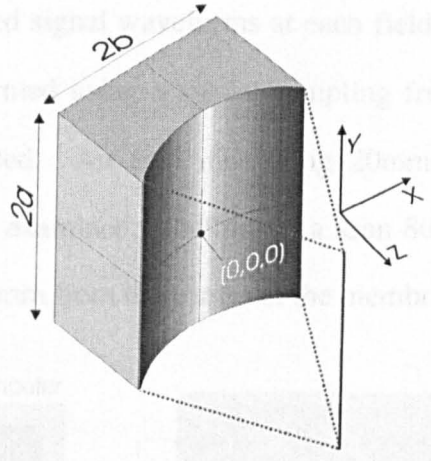

Figure 5.7: *Schematic diagram showing the coordinate system used.*

The pressure waveforms emanating from the focusing transducer were measured by scanning with a miniature detector. Ideally, this detector should be smaller in diameter than the acoustic wavelength being examined, to avoid spatial averaging and directional sensitivity errors. However, for high frequency operation (~1MHz), the receiver would need to be less than 0.34mm in diameter. This, in practice, would be impractical due to reduced sensitivity, and hence lower received signal amplitude. Thus, a 500μm square micromachined detector with a 1μm thick silicon nitride membrane, as previously described in Chapter 3 & 4, was utilised for this experiment. This resulted in a detector with a diameter of less than two wavelengths at the upper frequencies examined (1MHz), with suitable sensitivity and bandwidth.

A schematic diagram of the experimental arrangement used to scan the field is shown in Figure 5.8. It was scanned in a two dimensional horizontal plane (i.e. the x-z plane), with the source transducer positioned so that it radiated horizontally along the x-axis, and focused in the x-z plane. The scanned plane intersected with the y-axis at a position of y=0 (i.e. the centre of the focusing transducer). Scanning was achieved using

a PC, running the LabVIEW X-Y-Scan software, previously described in Chapter 4. This controlled a Tektronix TDS430A digital storage oscilloscope and a stepper motor controller, the latter driving a two-axis linear stage. The 500μm square detector was coupled to a Cooknell charge amplifier (CA6/C) with a gain of 250mV/pC, which also applied a bias of 30V to the detector. The signal from this amplifier was sent to the oscilloscope so that received signal waveforms at each field position were stored on the PC. All scans were performed using a spatial sampling frequency of 250μm (on both axis) unless otherwise stated. An area measuring 20mm by 35mm in the x and z directions respectively was examined, resulting in a scan 80 by 140 points in size. All scans were initiated at z=15mm from the centre of the membrane of the transducer.

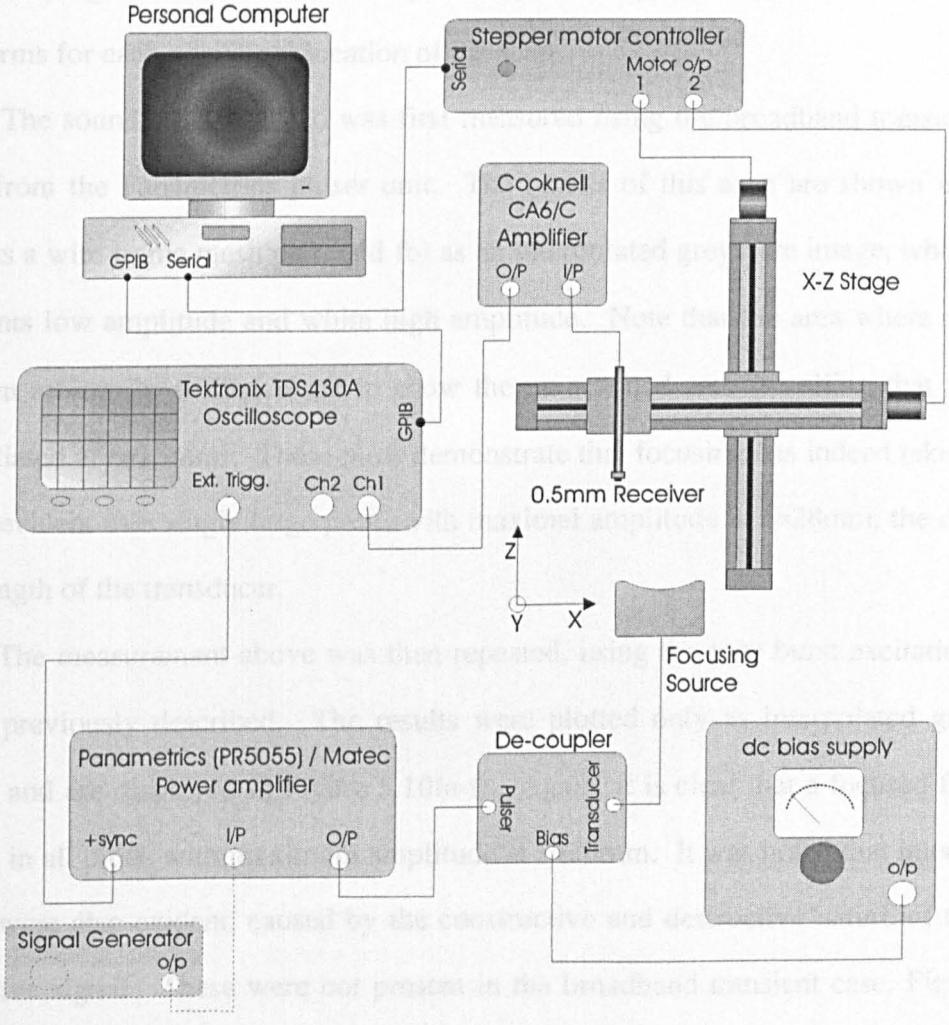

Figure 5.8: *Schematic diagram of the sound pressure field scanning system.*

Two types of excitation signal were applied to the source transducer during these experiments. The first was a pulsed voltage excitation provided by the same Panametrics (5055PR) pulser-receiver unit used in the previous experiment. This produced a wide bandwidth, 350V transient signal. The second type of drive signal consisted of a 200V pk-pk tone burst excitation, produced using a Matec R.F. gated power amplifier (model 515A) driven by a CW sine wave from a Wavetek signal generator (model 191). The frequency of the tone bursts used ranged from 500kHz to 1MHz in 100kHz increments. A gating period of 20μs was used; resulting in approximately 10 and 20 cycle bursts for the lower and upper drive frequencies respectively. A bias voltage of 200V was applied in all cases. The peak sound pressure variations were obtained using the LabVIEW™ PixieLab program to measure the peak-to-peak amplitude of each of the stored waveforms for each positional location of the scan.

The sound pressure field was first measured using the broadband transient drive signal from the Panametrics pulser unit. The results of this scan are shown in Figure 5.9(a) as a wire frame mesh plot, and (b) as an interpolated greyscale image, where black represents low amplitude and white high amplitude. Note that the area where z<15mm has been arbitrarily shaded black to show the un-scanned area (recalling that the scan was initiated at z=15mm). These plots demonstrate that focusing has indeed taken place. This is evident as a single large peak, with maximal amplitude at z=28mm, the designed focal length of the transducer.

The measurement above was then repeated, using the tone burst excitation drive signals previously described. The results were plotted only as interpolated greyscale images, and are displayed in Figure 5.10(a-f). Again, it is clear that a focused field has resulted in all plots, with maximum amplitude at z=28mm. It was noted that interference fringes were also evident, caused by the constructive and destructive nature of the tone burst drive signal. These were not present in the broadband transient case, Figure 5.9. The tone burst frequency plots, Figure 5.10(a-f), also show that the size of the focal region is a function of frequency, with it approximately halving at 1MHz compared to

that at 500kHz. To examine this further, cross sections of the sound field for the 500kHz, 1MHz and transient drive signals at z=28mm were extracted from the measured sound field data. These were then normalised and re-sampled using a linear interpolation operation to increase the spatial sampling period to 125μm, enabling the peaks to be aligned along the x-axis allowing an accurate comparison to be made. The resulting plots are shown in Figure 5.11. Again, the interference fringes are evident in the tone burst plots, as lobes either side of the main peak, while the broadband plot is relatively flat in these regions. Apart from these side-lobes, the 500kHz and broadband plots are similar, with main peaks of approximately the same width. This can be explained by

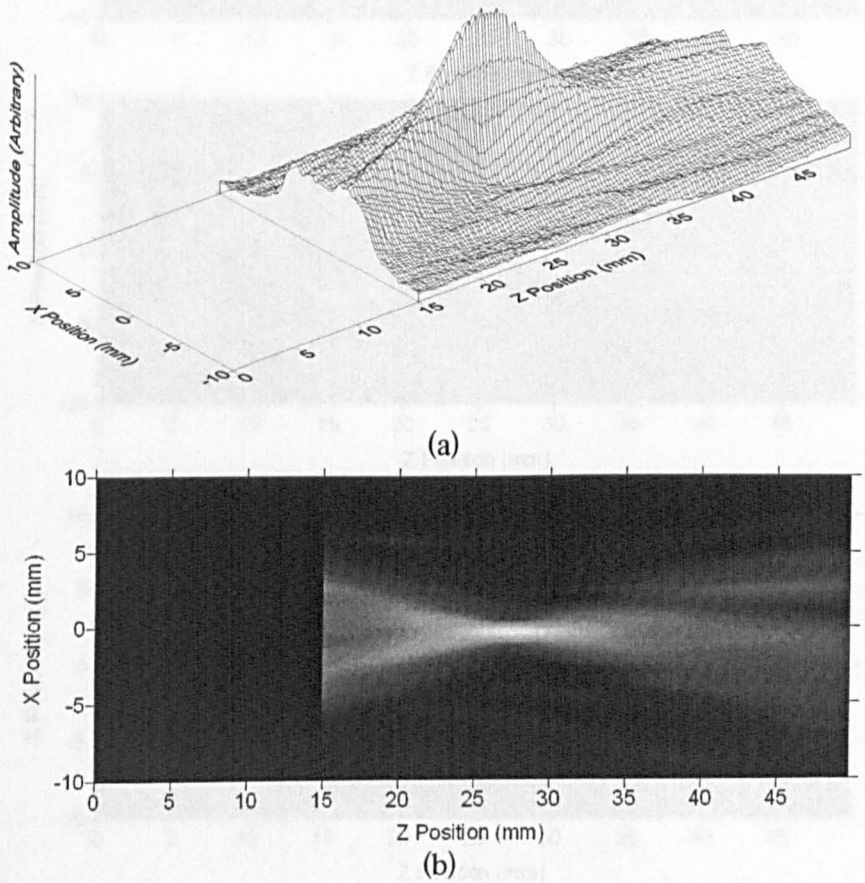

Figure 5.9: *Measured sound amplitude from the cylindrical focusing transducer, in the x-z plane (y=0), when driven by a transient broadband pulse. Plotted as (a) wire frame mesh plot, (b) interpolated greyscale image.*

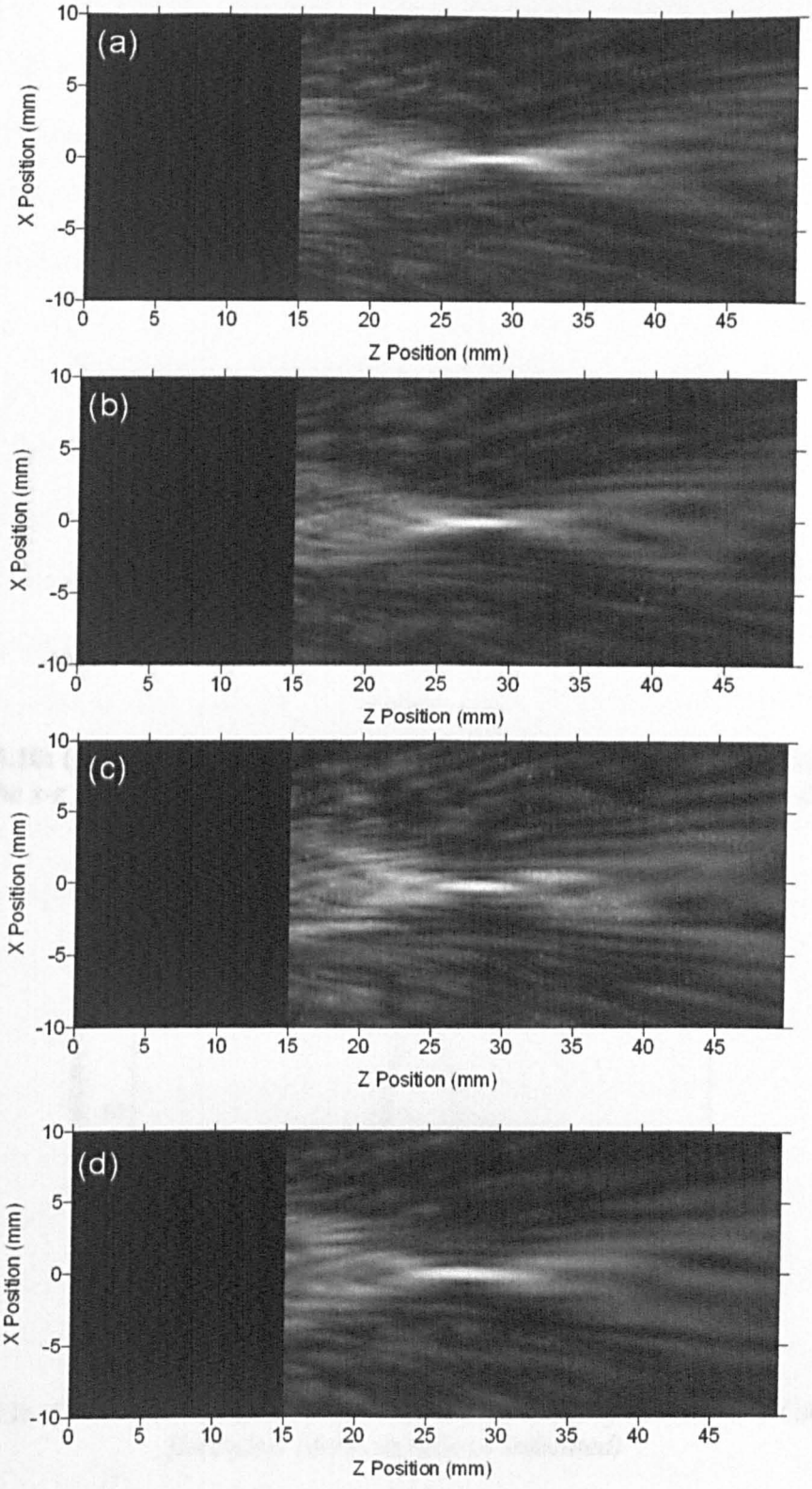

Figure 5.10: *Greyscale images of the measured sound amplitude field plots, in the x-z plane (y=0), from the cylindrical focusing transducer when driven by: (a) 1MHz, (b) 900kHz, (c) 800kHz (d) 700kHz tone burst signals.*

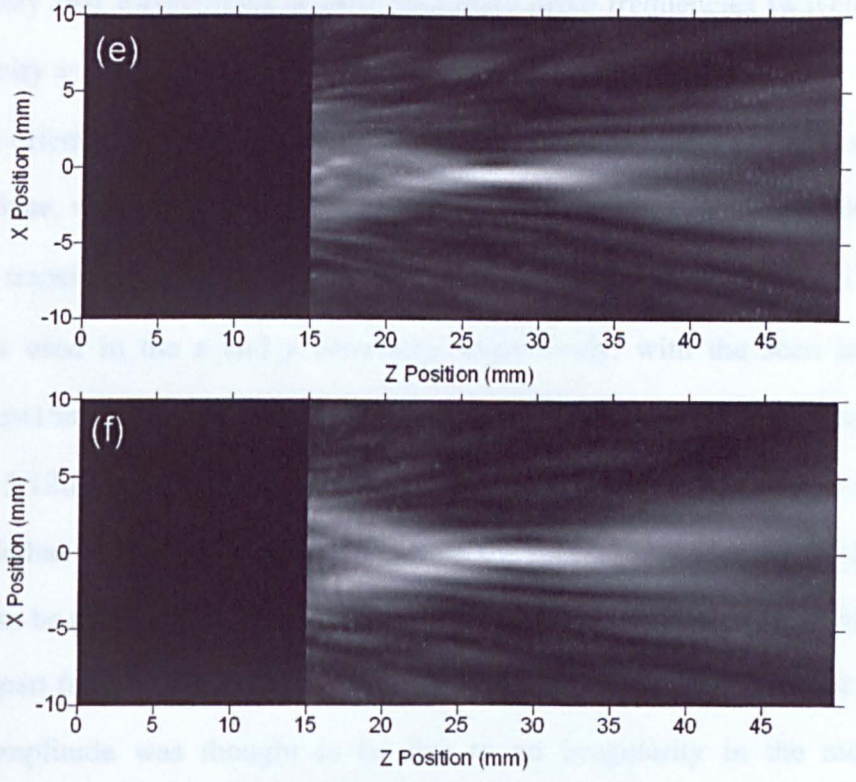

Figure 5.10: (Continued) *Greyscale images of the measured sound amplitude field plots, in the x-z plane (y=0), from the cylindrical focusing transducer when driven by:, (e) 600kHz, (f) 500kHz tone burst signals.*

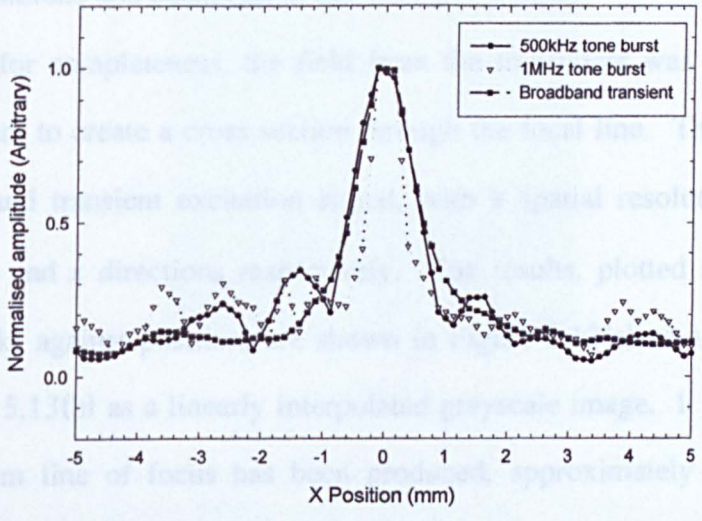

Figure 5.11: *Cross-sections of the focal region (z=28mm) of the measured amplitude field plots (drive signals as indicated)*

referring back to the previous section, where the peak frequency of the transducer (in broadband mode) was found to be approximately 400-500kHz (Figure 5.5). The full width at half magnitude (FWHM) of the main peak is ~0.7mm for the 1MHz case, and ~1.3mm for the broadband and 500kHz plot. Both these widths relating to

approximately two wavelengths at their respective drive frequencies (wavelength in air, where velocity = ~340ms^{-1}, at 500kHz=~0.68mm, 1MHz=~0.34mm).

The orientation of the transducer was now changed, so that the field was scanned in the y-z plane, with x=0. A scan was then performed, with the transducer driven by the broadband transient excitation signal. This time, a spatial resolution of 250μm by 500μm was used in the z and y directions respectively, with the scan initiated at a position of z=15mm. The results are shown in Figure 5.12(a) as a wire frame mesh plot, and Figure 5.12(b) as a linearly interpolated greyscale image. These again show that a focused field has resulted, with a line length (in the y direction) of approximately 45mm. It should also be noted that the amplitude of this focal region is reasonably uniform along its length, apart from the region highlighted in Figure 5.12(b). The reason for this area of increased amplitude was thought to be due to an irregularity in the membrane or backplate, such as membrane tension or particles of dust or dirt under the membrane. This was confirmed with an examination of the device that revealed a small air pocket between the membrane and backplate in this area (y=~18mm).

Finally, for completeness, the field from the transducer was scanned in its x-y plane, at z=28mm to create a cross section through the focal line. This was again done using a broadband transient excitation signal, with a spatial resolution of 500μm by 250μm in the y and x directions respectively. The results, plotted as received signal amplitude (pk-pk) against position, are shown in Figure 5.13(a) as a wire frame mesh plot, and Figure 5.13(b) as a linearly interpolated greyscale image. It can be seen that a relatively uniform line of focus has been produced, approximately 45mm in length. However, it was noted that slightly higher amplitude is evident in the region 18-20mm along the y-axis. This, again, (after an examination of the transducer) was found to be due to a small air pocket trapped under the membrane.

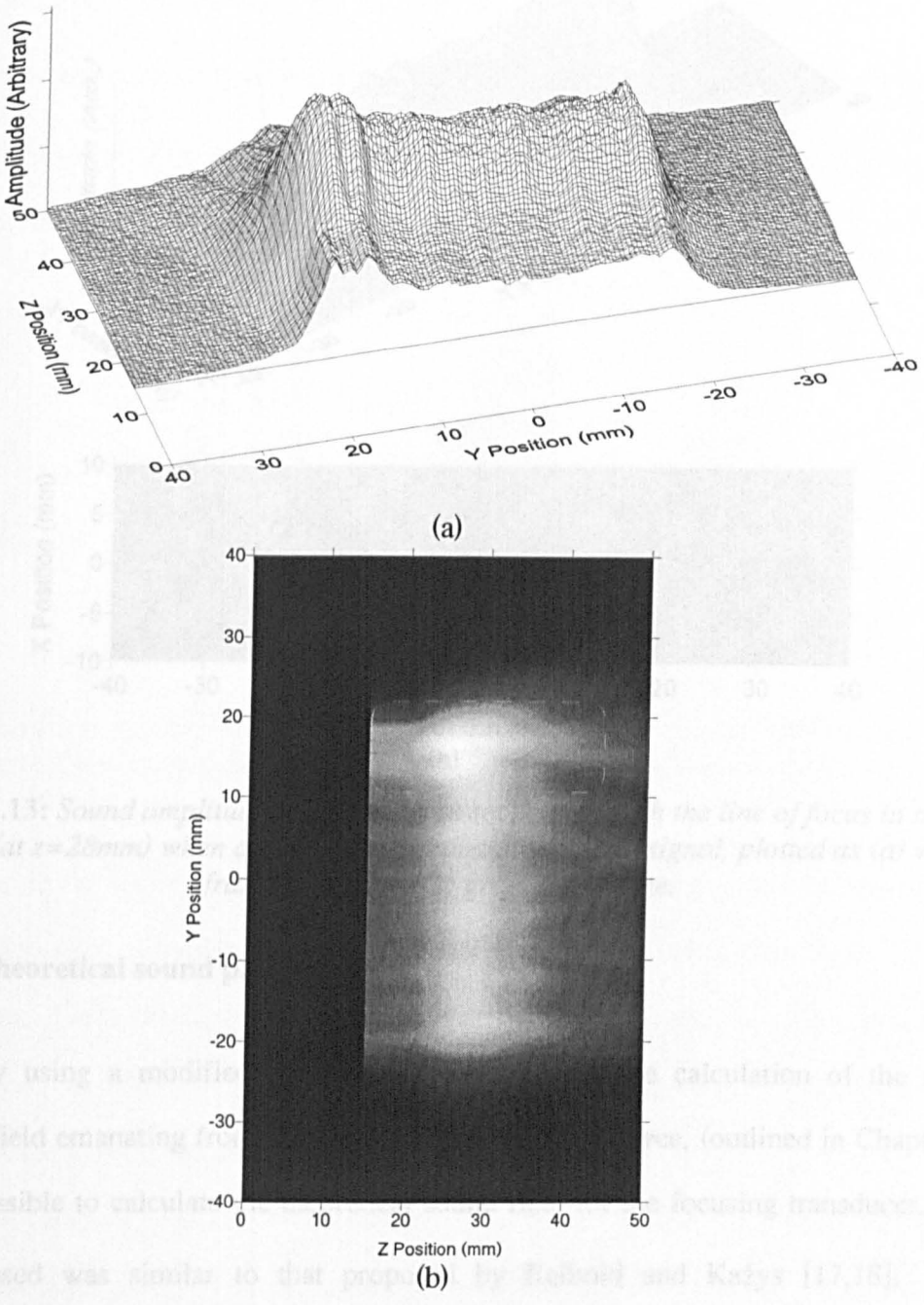

Figure 5.12: *Measured sound amplitude field from the cylindrical focusing transducer, in the y-z plane, when driven by a broadband transient. Displayed as (a) wire frame mesh plot, (b) greyscale image.*

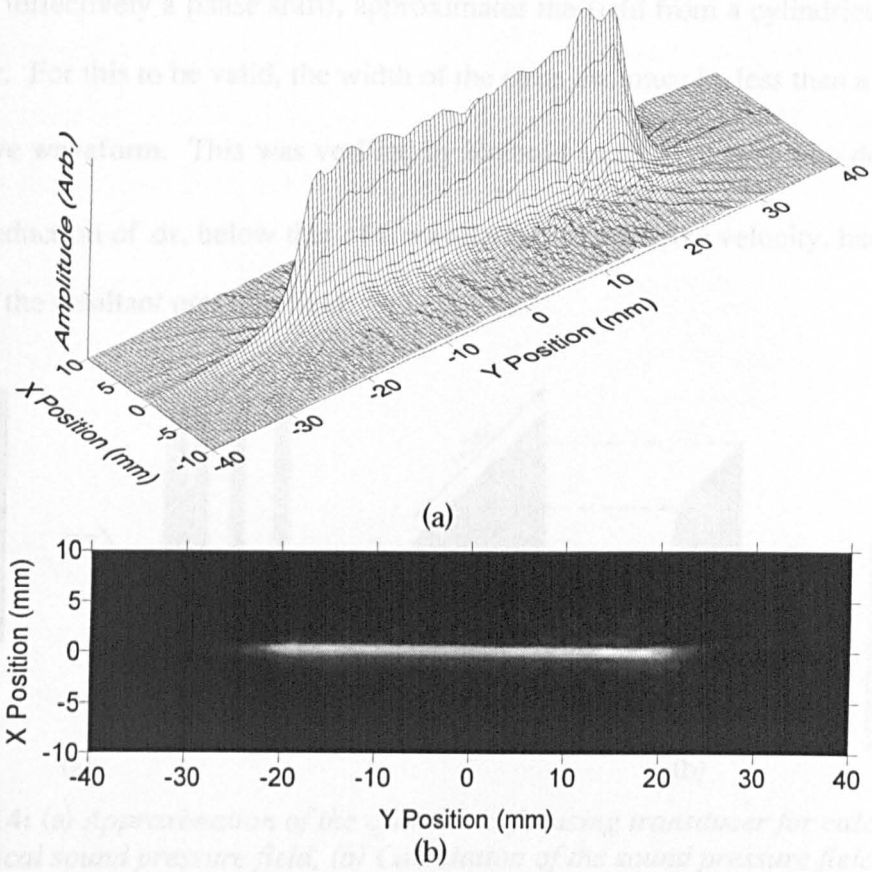

Figure 5.13: *Sound amplitude field plot cross section through the line of focus in the x-y plane (at z=28mm) when driven by a broadband transient signal, plotted as (a) wire frame mesh plot, (b) greyscale image.*

5.3.5 Theoretical sound pressure fields

By using a modified version of the theory for the calculation of the sound pressure field emanating from a plane piston rectangular source, (outlined in Chapter 1), it was possible to calculate the theoretical sound field for the focusing transducer. The method used was similar to that proposed by Reibold and Kažys [17,18]. This essentially subdivides the concave active front face of the transducer into N pairs of elementary strips, each of width Δx, along the x-axis, as illustrated in Figure 5.14(a). The resultant sound field from each a pair of strips, can then be calculated as the difference of the pressure fields from two overlapping rectangular sources, one smaller in width by $2\Delta x$, as demonstrated in Figure 5.14(b). Thus, the sum of the sound pressure fields from a number of these 'strip pairs', each with an appropriate added offset along

the z-axis (effectively a phase shift), approximates the field from a cylindrically concave transducer. For this to be valid, the width of the strip, Δx, must be less than a wavelength of the drive waveform. This was verified by Reibold and Kažys [17] who demonstrated that any reduction of Δx, below that of a wavelength of the drive velocity, had negligible change on the resultant pressure field.

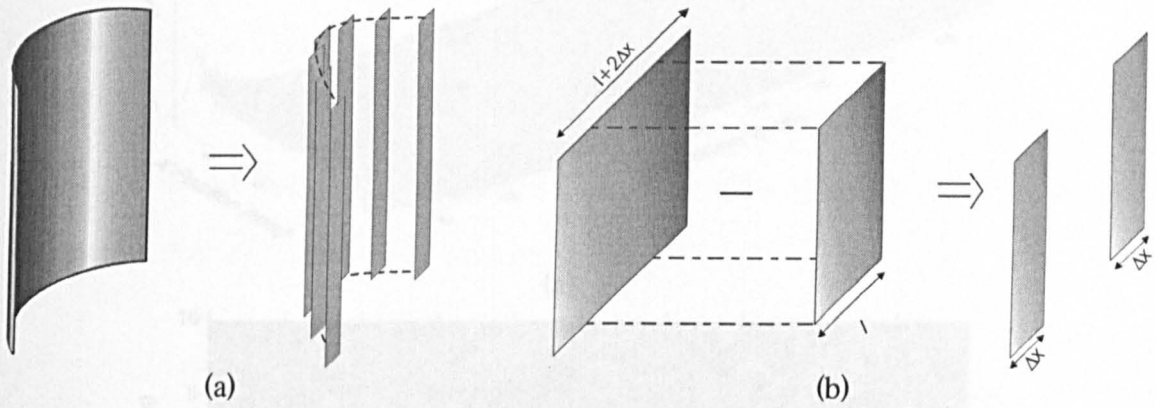

Figure 5.14: (a) *Approximation of the cylindrical focusing transducer for calculation of the theoretical sound pressure field, (b) Calculation of the sound pressure field for a pair of strip sources.*

Using the method described above, a Matlab™ program (listed in Appendix B) was developed to calculate the pressure field from the focusing transducer. For the simulations, it was decided to 'split' the transducer into 30 pairs of strips, hence each being 325μm in width. This was less than the wavelength of a 1MHz signal in air (~342μm), the highest frequency examined here.

The surface velocity waveforms, $v(t)$, used in the following theoretical calculations, were derived from the same equation used for field predictions in Chapter 4 (see equation (4.1)). It should be noted that these surface velocity waveforms were of arbitrary amplitude; hence, so were the resultant calculated pressure field plots.

Firstly, the theoretical sound pressure field was calculated for the broadband excitation case (500kHz centre frequency). The results were plotted as peak-to-peak pressure amplitude against position and are shown in Figure 5.15(a), as a wire frame mesh plot, and Figure 5.15(b), as a linearly interpolated greyscale image. These were

then compared to the previously measured sound amplitude field, when driven with a broadband transient excitation (Figure 5.9). Good agreement of form is evident, with the point of maximum pressure at z=28mm. It was also noted that no significant interference fringes were visible, as expected for a broadband signal.

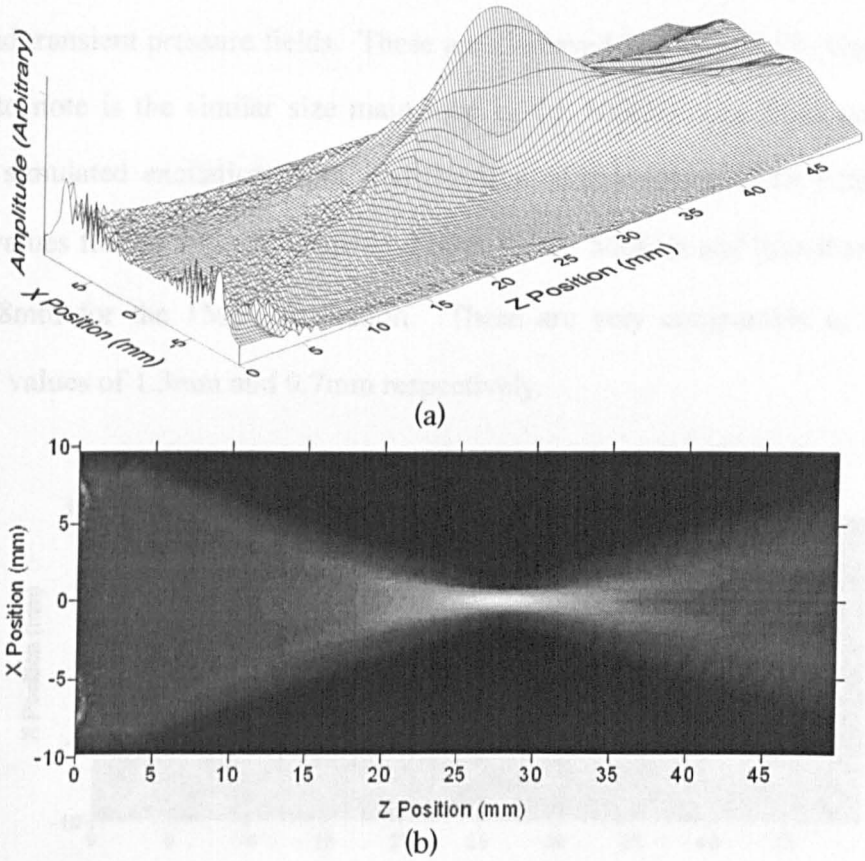

Figure 5.15: *Theoretical sound pressure field from the cylindrical focusing transducer, in the x-z plane (y=0), when driven by a broadband signal. Plotted as (a) wire frame mesh plot, (b) interpolated greyscale image.*

The sound pressure fields were then calculated for the simulated tone burst excitation cases, and plotted as linearly interpolated greyscale images. These are shown in Figure 5.16(a-f). A comparison to the previously measured sound amplitude field plots in Figure 5.10(a-f) was then made. Again, there was good agreement between them, with similar interference fringes clearly visible in both sets of plots, and the size of the focal regions were comparable. However, it was also noted that the measured amplitude plots suffered from noise, particularly with the higher frequency drive signals,

due to the lower response of the focusing transducer at these upper frequencies, and hence a lower amplitude of the transmitted signal.

As was done previously on the measured sound fields, the cross sections through the focal point (z=28mm) were plotted for the 500kHz tone burst, 1MHz tone burst, and broadband transient pressure fields. These are displayed in Figure 5.17. One of the main features to note is the similar size main lobe in the 500kHz tone burst and broadband transient simulated excitation plots, and the lack of side-lobes in the latter case. The FWHM values for the three plots are ~1.22mm for the 500kHz and broadband excitation, and ~0.68mm for the 1MHz excitation. These are very comparable to the previous measured values of 1.3mm and 0.7mm respectively.

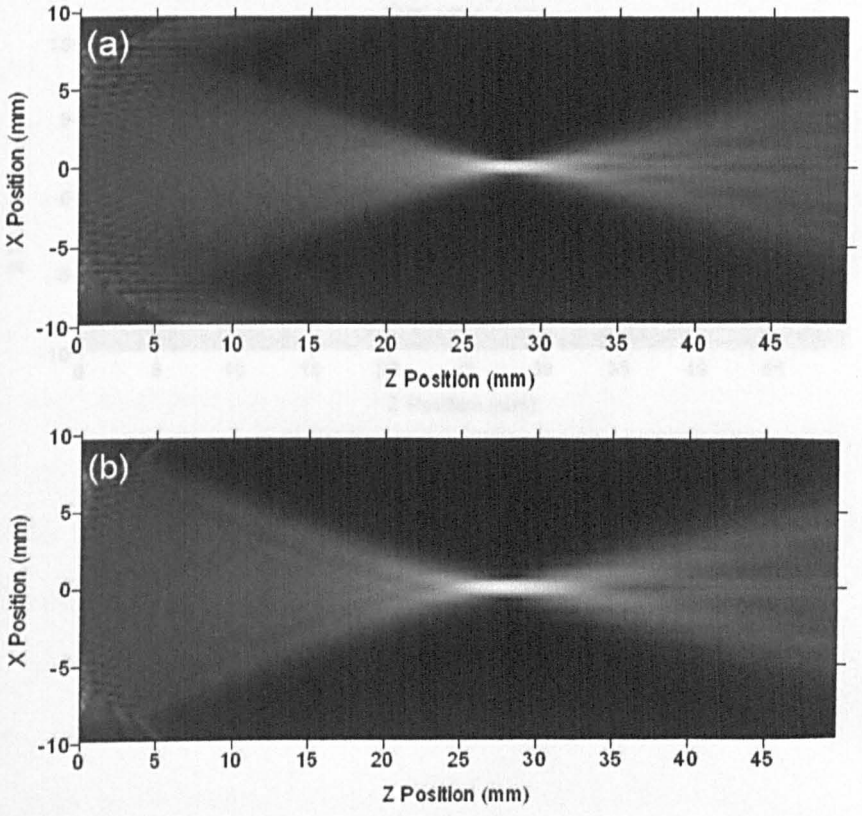

Figure 5.16: *Theoretical interpolated greyscale sound pressure field plots, in the x-z plane (y=0), when driven with a: (a) 1MHz, (b) 900kHz, simulated tone burst signal.*

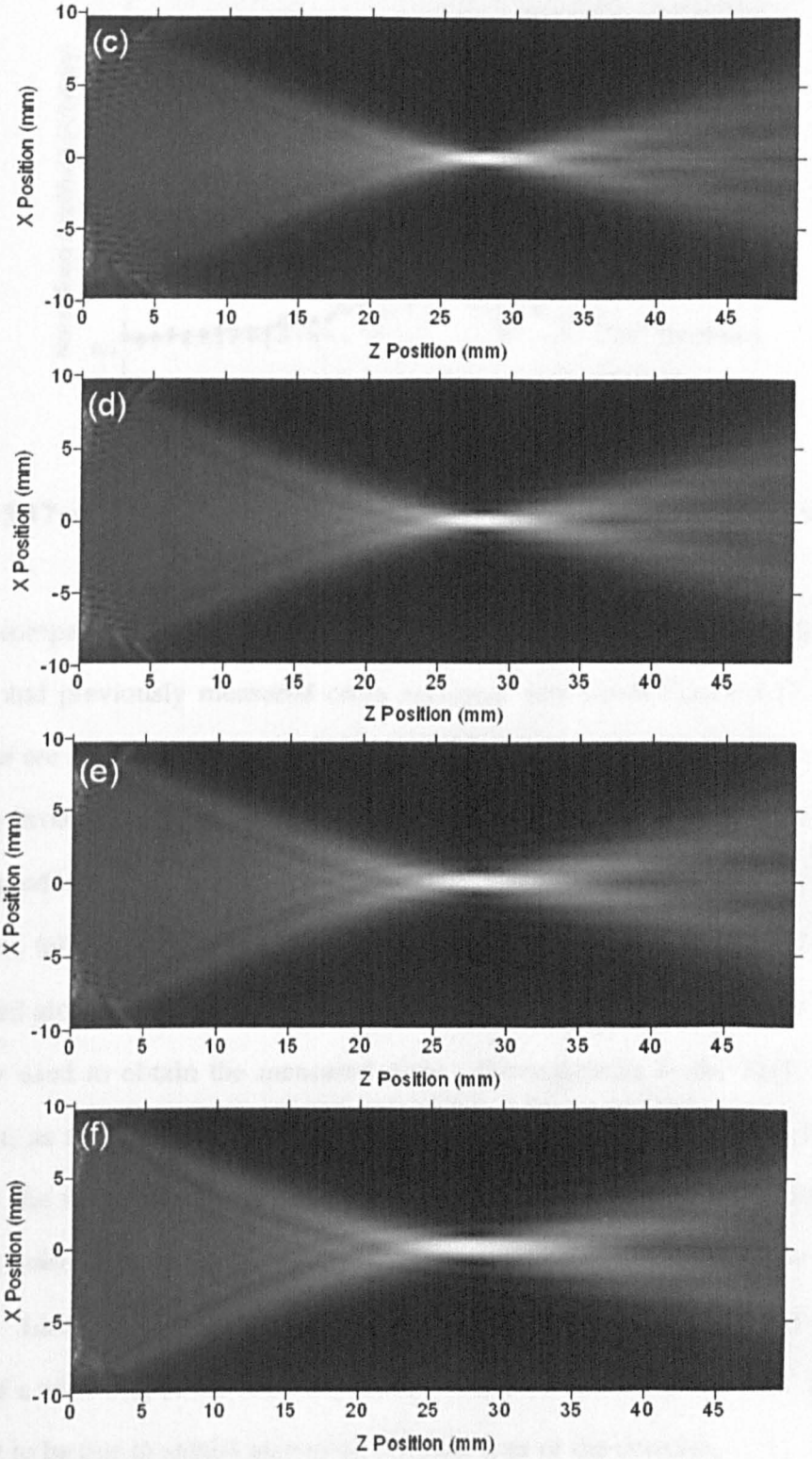

Figure 5.16: (Continued) *Theoretical interpolated greyscale sound pressure field plots, in the x-z plane (y=0), when driven with: (c) 800kHz, (d) 700kHz, (e) 600kHz, (f) 500kHz simulated tone burst signal.*

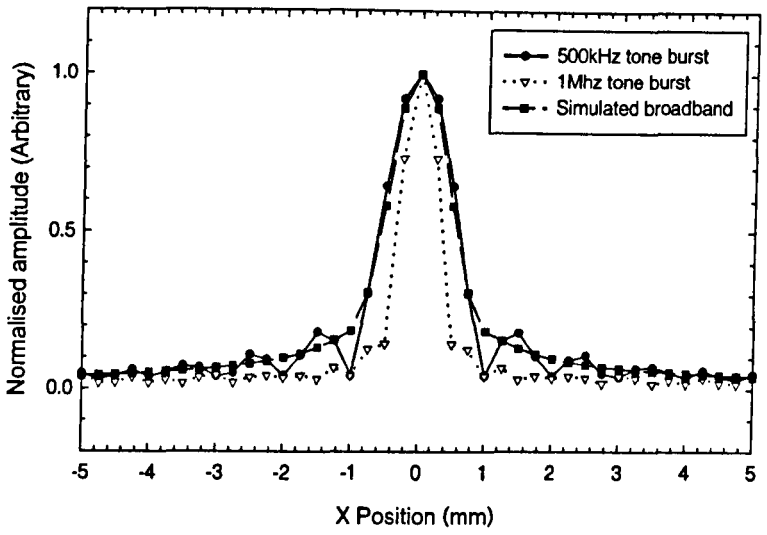

Figure 5.17: *Cross-sections of the focal region (z=28mm) of the theoretical sound pressure field plots (drive velocities as indicated).*

To compare these plots more closely, a series of three plots were created, with the theoretical and previously measured cross sectional data (from Figure 5.11) plotted on each. These are shown in Figure 5.18, where (a) is the 500kHz, (b) the 1MHz tone burst, and (c) the broadband drive/simulation excitation. It can be seen that they are all in relatively good agreement, although there are a few discrepancies. Starting with the 500kHz case, (a), it was noted that the minima either side of the main lobe were lower on the simulated plot. This was thought to be due to spatial averaging across the aperture of the detector used to obtain the measured plots. Discrepancies in the 1MHz plot were also evident, as differences either side of the main lobe, with the measured amplitude higher than the theoretical. However, in this case it was though to be mainly due to background noise, as well as the averaging effect of the detector (especially at this higher frequency). Lastly, the broadband signal plots are in quite good agreement, with the exception of a widening of the main lobe near its base for the measured plot. Again, this was thought to be due to spatial averaging over the area of the detector.

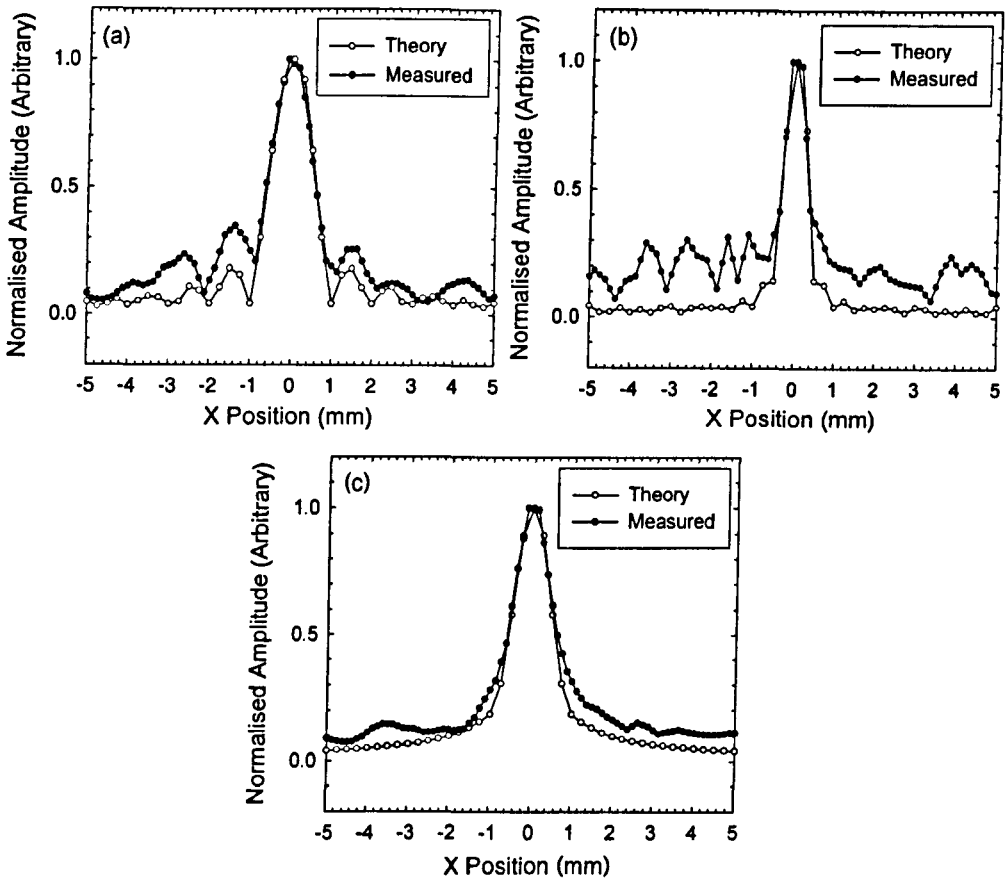

Figure 5.18: *Comparison of measured and theoretical cross sections of the focal region (z=28mm) of the sound pressure/amplitude field emanating from the cylindrical transducer, when driven by; (a) 500kHz tone burst, (b) 1MHz tone burst, and (c) broadband transient.*

5.3.6 Determination of transducer resolution

This section examines the focal resolution of the transducer, when used in pulse-echo mode, as it would be typically used in a measurement system. It is split into two sub-sections, with the first determining the lateral resolution of the transducer, and the second the vertical resolution.

Lateral Resolution

An experiment was devised to determine the lateral resolution (i.e. the width of the focal line) of the transducer when used in pulse echo mode. The method involved scanning the device across an 'infinite' step edge; to obtain its edge spread function

(ESF). The spatial derivative of this results in its line spread function (LSF), where the lateral resolution of the transducer can be measured [19]. The orientation of the transducer for the step edge scan is shown schematically in the diagram of Figure 5.19.

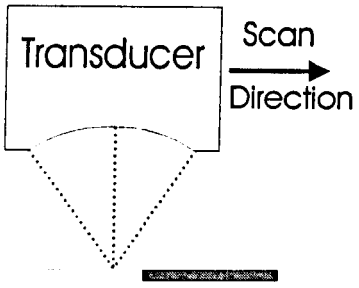

Figure 5.19: *Schematic diagram of the 'infinite step' edge scan method.*

The schematic diagram in Figure 5.20 illustrates the experimental arrangement used. This, again, utilised the computer controlled scanning system, to which the focusing transducer was attached, orientated so that it would scan in the x-z plane. The drive/receive equipment consisted of a Panametrics pulser/receiver unit (PR5055) used in pulse/echo mode. A 200V bias was applied throughout the experiment, via a de-coupling circuit. Note that this was the same drive/receive set-up as used previously to determine the frequency response of the transducer. The 'infinite' edge target consisted of a straight thin steel strip, positioned so that its edge was parallel to the line of focus of the transducer, with its upper surface at z=28mm (i.e. in the line of focus).

A high-resolution linear scan along the x-axis (i.e. across the edge) was then performed, using a spatial frequency period of 50μm. Figure 5.21(a) shows the results of this scan, plotted as received pk-pk signal amplitude (normalised) against x-position. Figure 5.21(b) shows its corresponding calculated first order spatial derivative, together with a fitted Gaussian function. The resulting plot is visibly noisy due to the differentiation operation. However, it is still possible to obtain the lateral resolution of the transducer from the FWHM of the peak. This was measured as approximately 0.67mm, or a wavelength at 500kHz (~0.68mm). Referring back to the previous section,

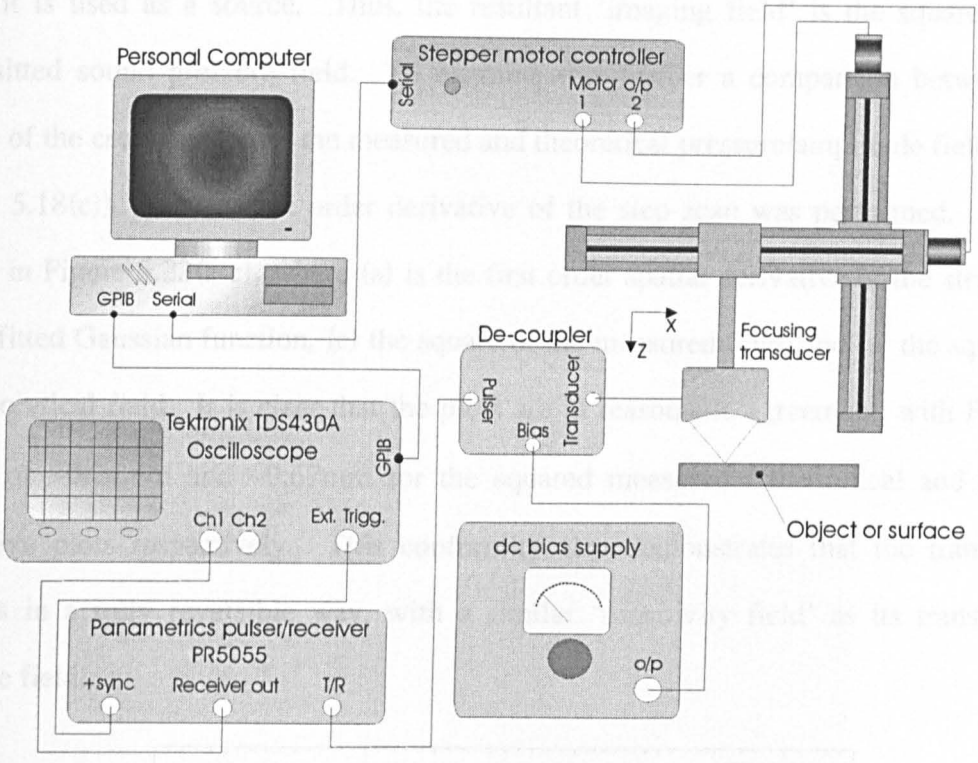

Figure 5.20: *Schematic diagram of the experimental set-up.*

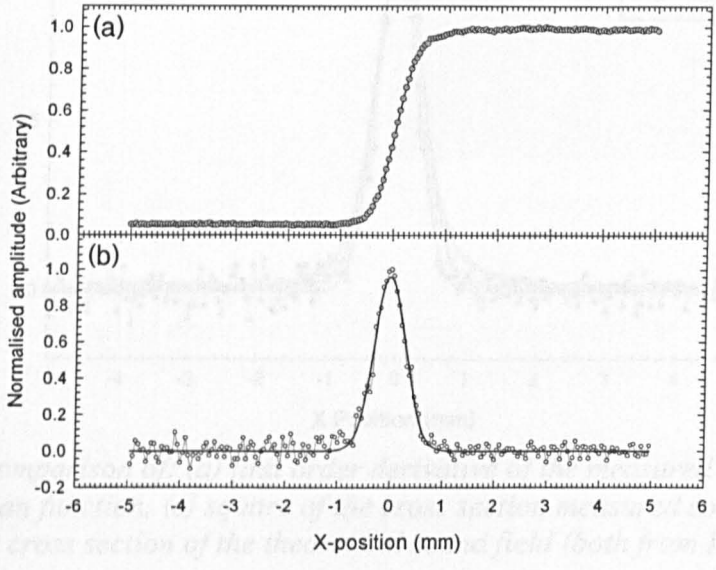

Figure 5.21: *'Infinite' step scan across edge at z=28mm (a) received amplitude, (b) first order spatial derivative, with fitted Gaussian function.*

the width of the focal line was found to be ~1.3mm, or double that than measured here. This discrepancy can be explained by the fact that in this first measurement, the transducer was only used as a source. However, it is now being used as a receiver too, whose sensitivity field (assuming a truly reversible transducer) is identical to that of

when it is used as a source. Thus, the resultant 'imaging field' is the square of the transmitted sound pressure field. To examine this further a comparison between the square of the cross section of the measured and theoretical pressure/amplitude field (from Figure 5.18(c)), and the first order derivative of the step scan was performed. This is shown in Figure 5.22(a-c), where (a) is the first order spatial derivative of the step scan, (b) its fitted Gaussian function, (c) the square of the measured field, and (c) the square of the theoretical field. It is clear that the plots are in reasonable agreement, with FWHM values of ~0.74mm and ~0.67mm for the squared measured / theoretical and spatial derivative plots respectively. This conformity also demonstrates that the transducer behaves in a truly reversible way, with a similar 'sensitivity field' as its transmitted pressure field.

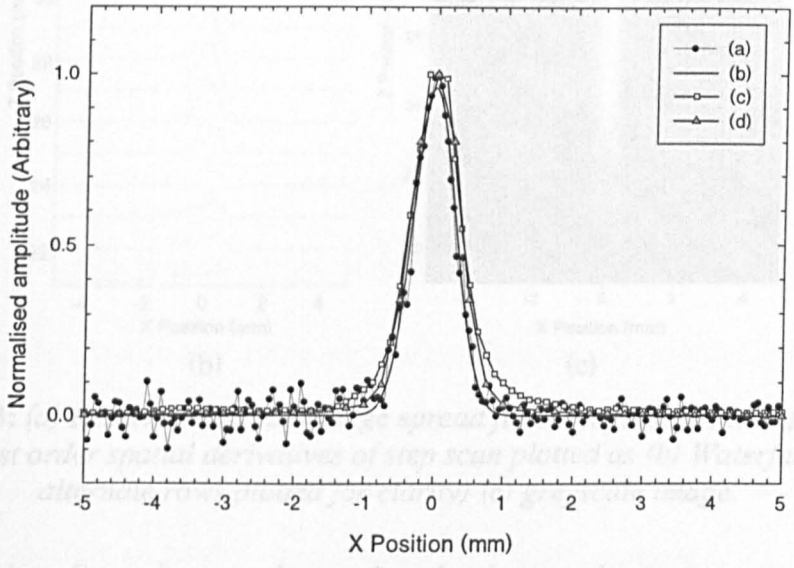

Figure 5.22: *Comparison of: (a) first order derivative of the measured step function, (b) its fitted Gaussian function, (c) square of the cross section measured sound field, and (d) square of the cross section of the theoretical sound field (both from Figure 5.18(c))*

This experiment described above was then repeated, this time also scanning in the z direction, to study the effect of defocusing the transducer/target. The scan was performed over the region of z=21mm to 36mm, with a spatial frequency period of 0.5mm. The results are shown in Figure 5.23(a), plotted as received peak-to-peak signal amplitude, against position. As expected, the signal with the largest amplitude was that

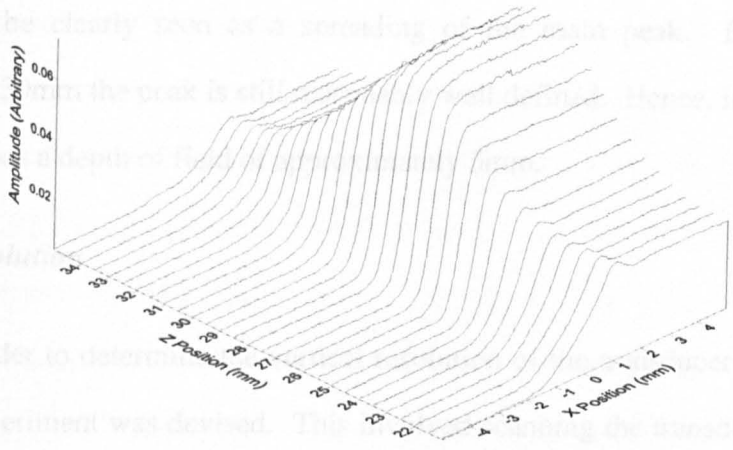

(a)

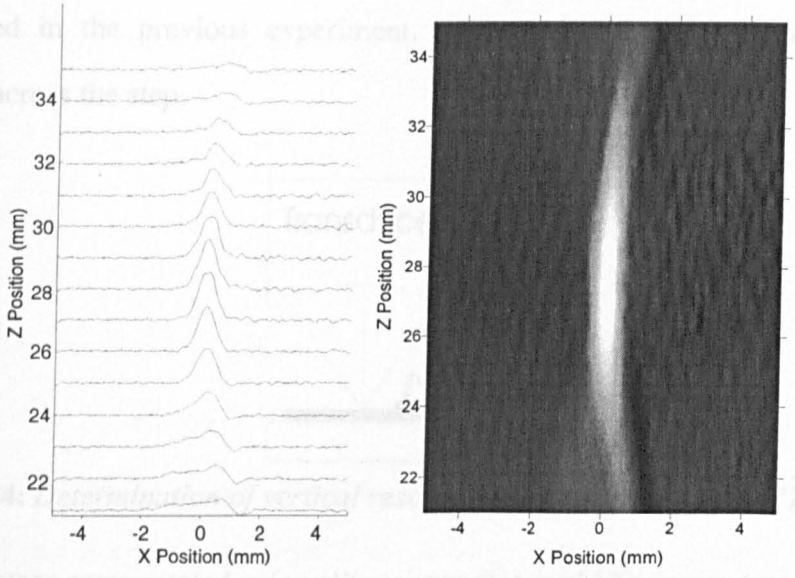

(b) (c)

Figure 5.23: *(a) Received amplitude edge spread function plots of the 'infinite edge' scan, and first order spatial derivatives of step scan plotted as (b) Waterfall plot (only alternate rows plotted for clarity) (c) greyscale image.*

at the focal point. It can be seen that as the edge is moved into then out of focus, the gradient of the ESF reduces, from a maximum at the focal point (z=28mm). The small peaks, or 'overshoot' on the edge profiles, visible in the out of focus plots, were though to be due to diffraction effects. The calculated first order spatial derivatives (LSF's), along the x-axis, are shown in Figure 5.23(b) as a set of line plots (only with every other line plotted for clarity) and in Figure 5.23(c) as a linearly interpolated greyscale image. These have both been smoothed (using a moving average function) to reduce the noise associated with this differential operation. The effect on the LSF's of defocusing the

device can be clearly seen as a spreading of the main peak. From approximately z=25mm to 30mm the peak is still reasonably well defined. Hence, it was concluded that this device has a depth of field of approximately 5mm.

Vertical resolution

In order to determine the vertical resolution of the transducer pulse echo system, a second experiment was devised. This involved scanning the transducer across steps of known height. This is illustrated in Figure 5.24. The experimental set-up was the same as that used in the previous experiment, with only the x-axis utilised to scan the transducer across the step.

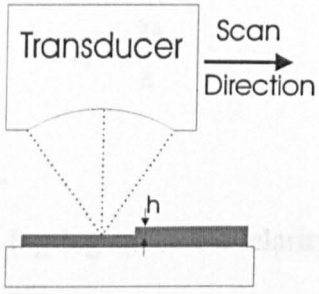

Figure 5.24: *Determination of vertical resolution, scan across a step of known height.*

The steps were created using slip gauges that could be wrung together to create a step profile of known height. These were placed onto an optically flat glass block. Firstly, two slip gauges, one of 1mm thickness, the other of 6mm thickness were placed side by side, abutting each other, to create a step of 5mm in height. This 'step' was then aligned so that it was parallel to the focal line of the transducer. The transducer was then moved vertically to focus onto the upper surface of the 1mm thick gauge (achieved by maximising the amplitude of the reflected signal). A linear scan was then performed across the step with a spatial frequency period of 0.05mm. This was then repeated for step heights of 2mm, 1mm, 0.5mm, 0.2mm, 0.1mm, 50μm, 20μm, 10μm, 5μm, and 2μm.

The data from these scans were then analysed, using the LabVIEW™ PixieLab program, to obtain the time of arrival of the maximum peak in the waveform for each x

position. These times were then adjusted so that t=0 related to the signal from the 1mm slip gauge (i.e. the lower part of the step). The results are shown in Figure 5.25(a-k). It is evident that there is a definite change in the time of arrival of the pulse in all cases except for the 2μm step. In this instance, a discontinuity can be observed at the point of the step, probably caused by the slight rounded edges of the gauges. However, there is no noticeable change in the time of arrival on either side of the step.

In Chapter 1, the velocity of sound in air at STP (20°C, 101.325 kPa) was shown to be approximately 343.4ms^{-1}. The predicted time of flight, t_s, for a step of height, h, (not forgetting the pulse-echo mode of operation) can be simply calculated from the following:

$$t_s = \frac{2h}{c} \tag{5.1}$$

where, c is the velocity of sound.

This was plotted (on a log-log scale for clarity), together with the measured change in the time of flights for each step (obtained from Figure 5.25, and also displayed in Table 5.1) and is shown in Figure 5.26. It can be seen that there is good agreement between the predicted and measured time of flights. The only discrepancy occurred with the 50μm (0.05mm) step, whose time of flight was shorter than expected. This may have been due to dust or dirt trapped under the lower (1mm) slip gauge, causing the overall step height to be less than 50μm. Hence, it was concluded that the vertical resolution of the system was in the region of 5μm. Note, however, that the transient pulse-echo method used here is not the best way in which to measure the time of arrival. A much more accurate way would be to utilise a tone burst signal and incorporate an accurate phase detection system into the receiver. Such a system if say, accurate to 0.1° could give a theoretical vertical resolution of approximately 0.1μm, using a 500kHz drive signal.

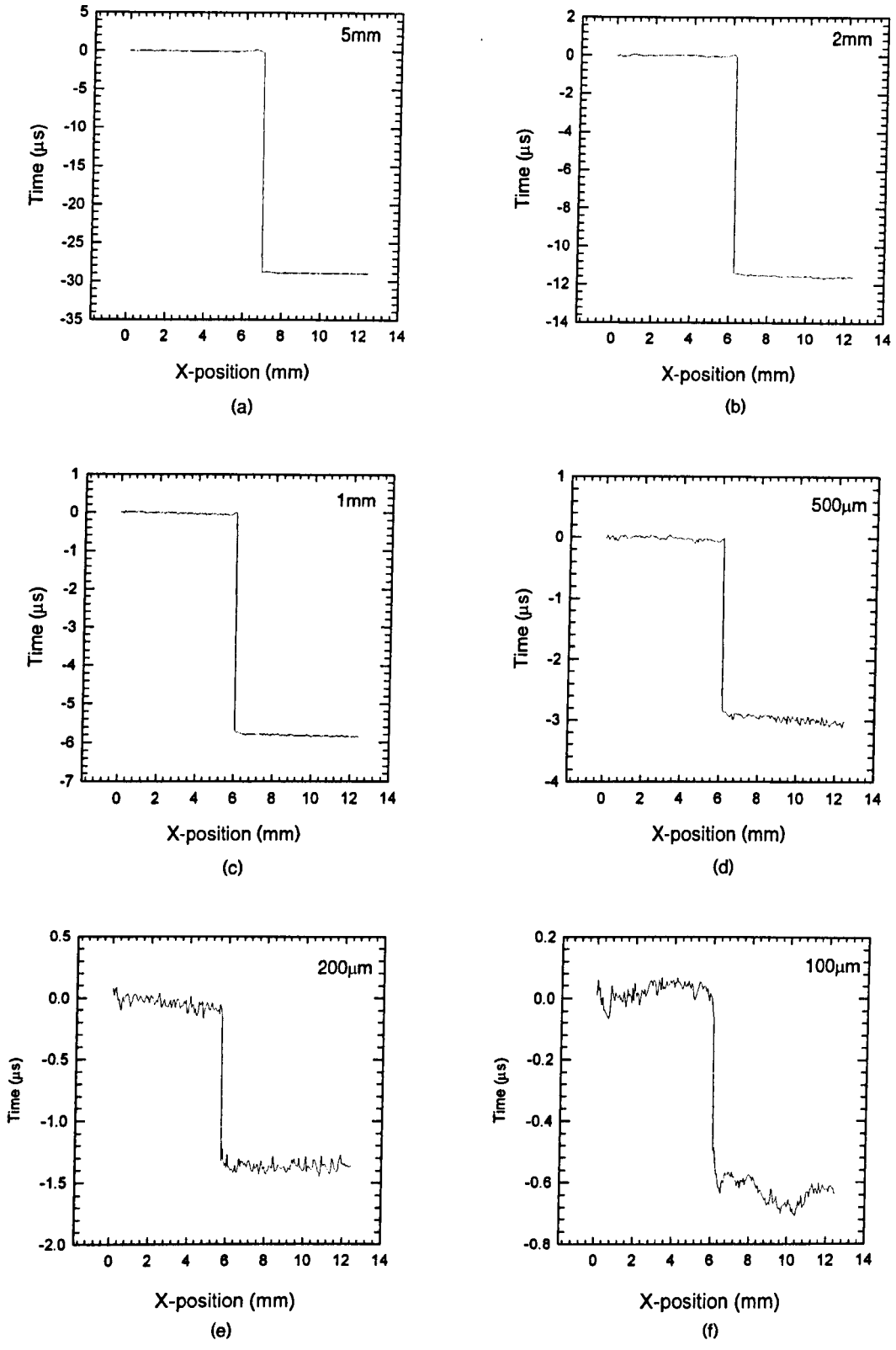

Figure 5.25: *Determination of the vertical resolution of the cylindrical line-focusing transducer; Time of arrival of the maximum peak in the received signal for a linear scan across steps of height shown.*

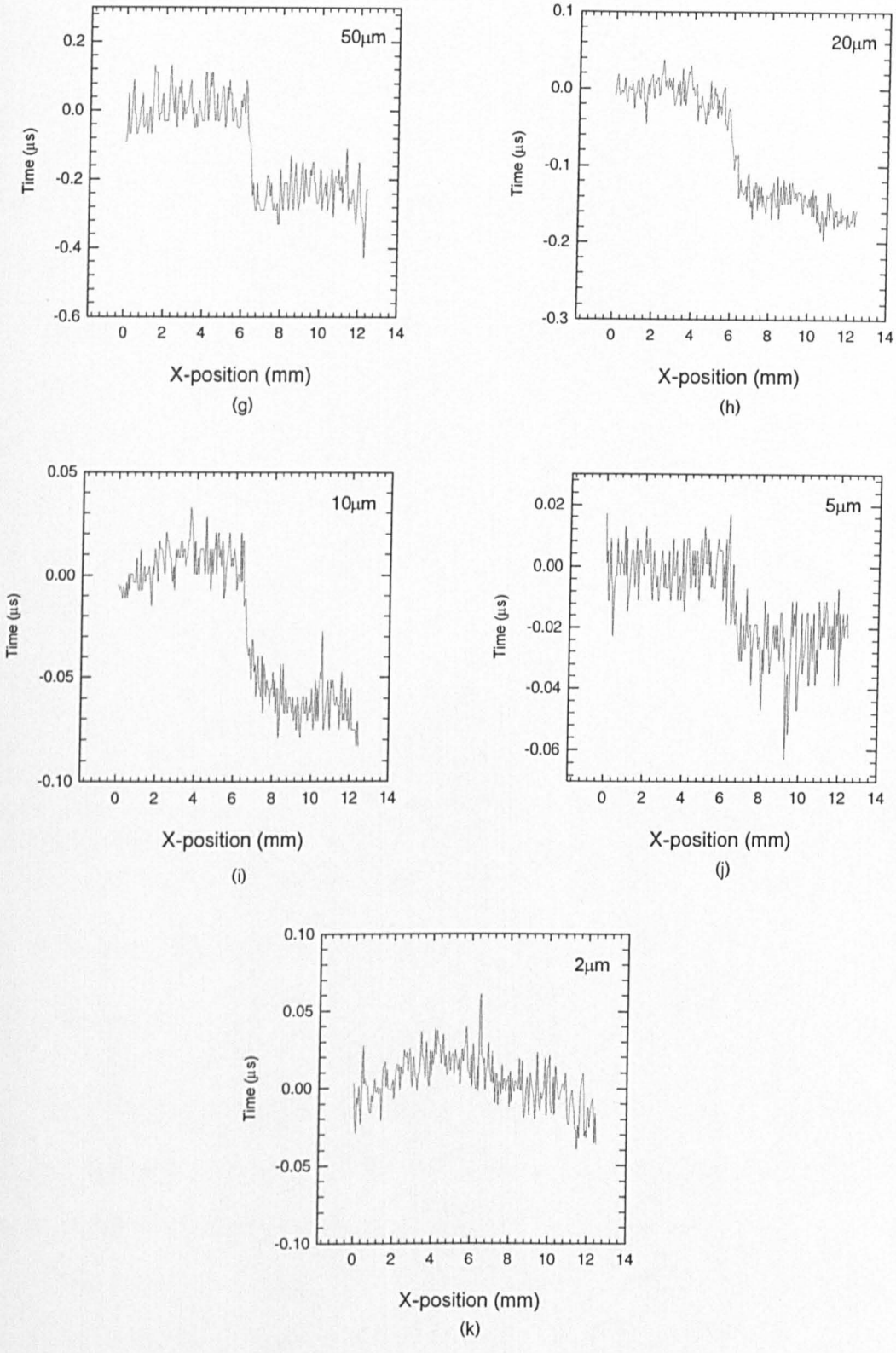

Figure 5.25: (Continued) *Determination of the vertical resolution of the cylindrical line-focusing transducer; Time of arrival of the maximum peak in the received signal for a linear scan across steps of height shown.*

Step Height (mm)	Change in Time of flight (μs)
5.00	29.00±1
2.00	11.80±0.5
1.00	5.80±0.3
0.50	3.00±0.2
0.20	1.30±0.05
0.10	0.60±0.05
0.05	0.21±0.04
0.02	0.12±0.04
0.01	0.06±0.02
0.005	0.03±0.02

Table 5.1: *Change in time of flight for step heights as shown (from Figure 5.25)*

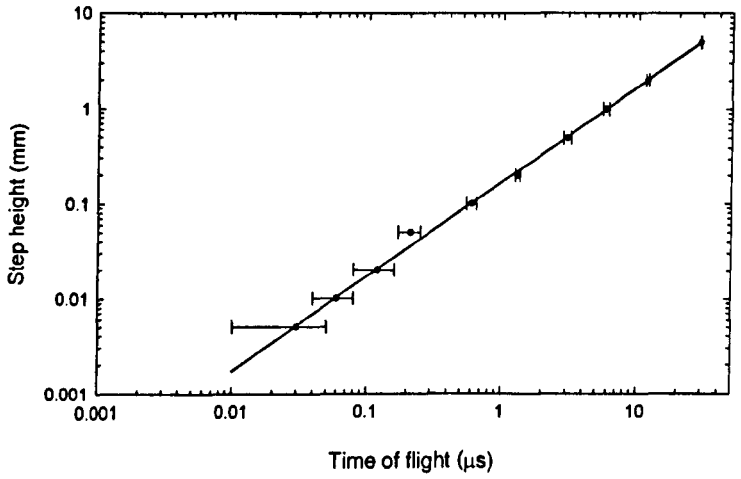

Figure 5.26: *Determination of vertical resolution; measured change in time of flight as the cylindrically focused transducer is scanned across steps of known height, plotted with predicted time of flight (solid line).*

5.4 A conical focusing transducer

5.4.1 Background

This section describes the design, construction, and characterisation of a conically shaped focusing transducer. This, like the cylindrically shaped transducer, described above, creates a line of focus, this time however, along the axis. Similar devices have been investigated for medical applications requiring large depths of focus. Such a device was described by Burckhardt et al [20]. This utilised a piezoelectric element, whose sound was focused by a Perspex lens onto a conical mirror. An alternative, described by Foster et al [21], utilised a conically shaped piezoelectric

transmitting element, and a planar receiver aimed along the axis of the cone to detect scattered ultrasound as a function of time. Both these devices were designed for immersion applications, and no references to similar air-coupled devices could be found; hence, it was decided interesting to study such a device.

The format of this section is essentially the same as the previous, consisting of a description of the construction of the device, preliminary testing, sound pressure field measurements, comparison to theoretical field predictions, and resolution measurements of the device. As the majority of the experiments performed on this transducer were identical to the previous section, the experimental methods will not be described again.

5.4.2 Transducer design and fabrication

The basic construction of this device was similar to that of the cylindrical transducer described above; consisting of a polished brass backplate, retained inside a machined aluminium casing with an insulating nylon insert. A cut-away schematic diagram of is shown in Figure 5.27. The internal active area of the backplate is in the shape of a truncated (45°) cone, with inner and outer radii of 13mm and 30mm respectively. This was designed to produce a line of focus 34mm in length, starting at a position of z=26mm from the extrapolated internal apex of the cone. These distances were again chosen to reduce the effect of atmospheric absorption. Engineering drawings of the device are shown in Appendix C.

After manufacture of the transducer, the backplate was carefully polished by hand. It was then fully disassembled, cleaned, and then reassembled. Finally, after rinsing with acetone and a thorough cleaning with an air jet, a 3.5μm thick Mylar metallised membrane was attached over the backplate. This was done in the presence of an applied bias voltage to reduce the amount of trapped air. Conducting silver paint was used to electrically connect the metallised front face of the film to the aluminium casing. A photograph of the fully assembled device is shown in Figure 5.28.

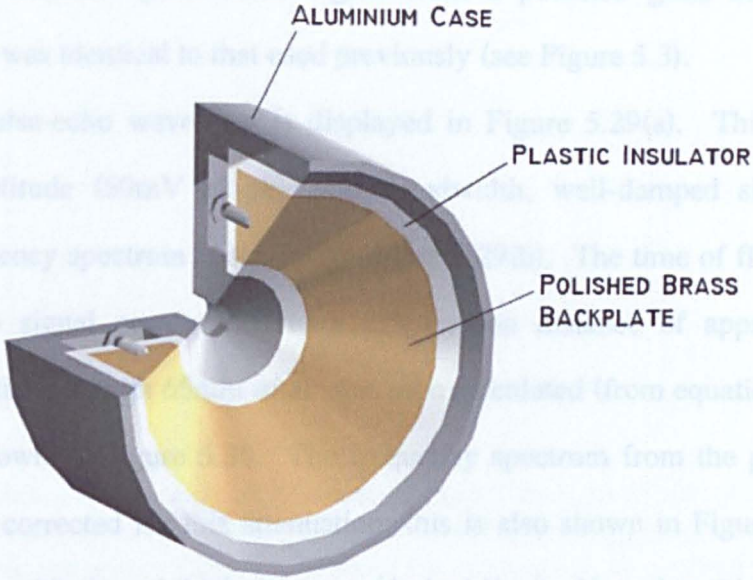

Figure 5.27: *Cut-away schematic diagram of the conical transducer (membrane not shown for clarity).*

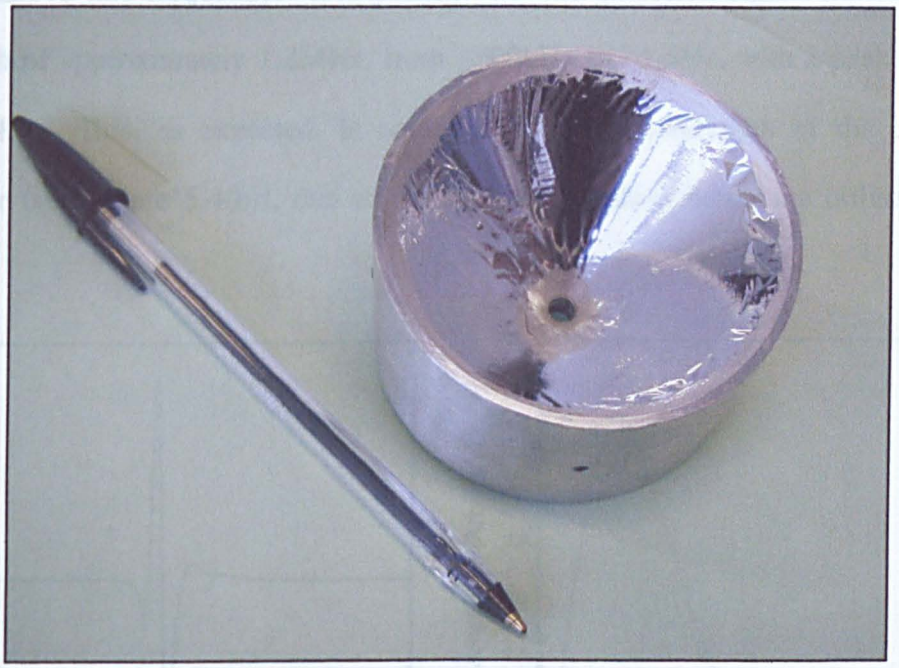

Figure 5.28: *Photograph of the assembled conical transducer.*

5.4.3 Transducer characterisation –Initial experiments

The initial experiments performed previously on the cylindrically focusing transducer were now repeated for the conical transducer. Recalling back from the previous section, the first initial experiment studied the frequency response of the device

by examining the reflected (pulse-echo) signal from a polished glass block. The experimental set-up was identical to that used previously (see Figure 5.3).

A typical pulse-echo waveform is displayed in Figure 5.29(a). This shows a relatively high-amplitude (50mV pk-pk), wide-bandwidth, well-damped signal. Its corresponding frequency spectrum is shown in Figure 5.29(b). The time of flight of the received pulse-echo signal corresponds to a propagation distance of approximately 65mm. The attenuation through 65mm of air was then calculated (from equation (1.13)). A plot of this is shown in Figure 5.30. The frequency spectrum from the pulse-echo waveform was then corrected for this attenuation; this is also shown in Figure 5.30 by the solid line, along with the original spectrum (dashed line). Note that this was only calculated up to 2MHz due to numerical inaccuracies of the large correction factor required above this frequency. It is evident that the corrected signal exhibits a –6dB bandwidth of approximately 1.2MHz, from ~300kHz to ~1.5Hz, with a peak frequency at ~800kHz. This, as expected, is comparable to the bandwidth of the cylindrical transducer (see Figure 5.4(b)), due to the similar backplate/membrane utilised in both devices.

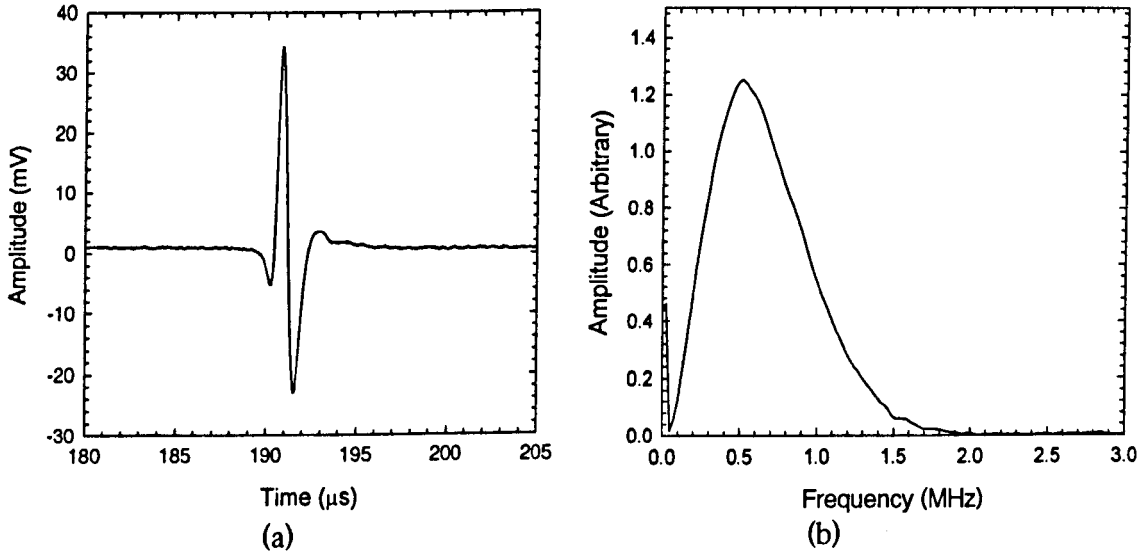

Figure 5.29: *(a) Typical received pulse-echo waveform, for the conical transducer, from a flat glass block (a), and corresponding frequency spectrum (b).*

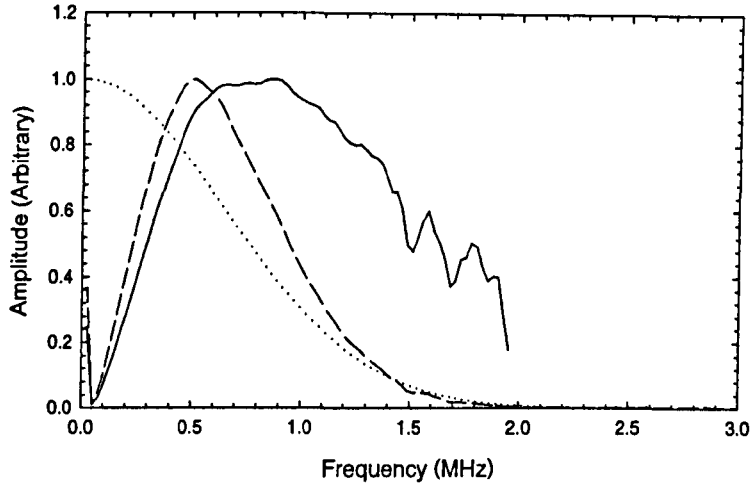

Figure 5.30: *Normalised attenuation of a wideband signal through 65mm of air at STP (dotted line). Original frequency spectra of received pulse-echo signal (dashed line), and corresponding frequency spectra corrected for attenuation in air (solid line).*

The second part of the initial testing involved measuring how the received amplitude changed as the transducer-reflector distance was varied. The device was first positioned with its front edge against the reflector block; in this position the transducer-reflector separation was 36mm from the extrapolated internal apex of the cone. The received amplitude (pk-pk) was then measured, and the transducer moved back by 0.5mm. This was repeated up to a separation distance of 75mm. The results of this are shown in Figure 5.31, along with the positions of the designed centre and end of the focal line. For completeness, as in the cylindrical transducer case, the signal amplitude

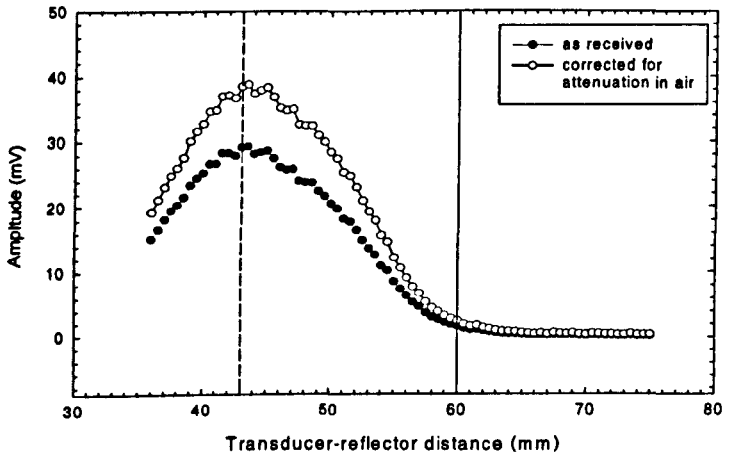

Figure 5.31: *Measured received signal amplitude (pk-pk) with increasing transducer-reflector separation. (Predicted central position of focal line shown as dashed line, predicted end position shown as solid line).*

corrected for air absorption has also been plotted, with the attenuation calculated from Equation (1.13), assuming a frequency of 500kHz, as 39.74dBm^{-1} (at STP). Little change in the overall shape of the plot can be observed.

The results show a broad peak in the region of the predicted position of the focal line. The centre of this peak is approximately at the centre of the predicted line of focus (z=43mm), with the amplitude reducing to background noise level at the end of the focal line (z=60mm). Note that the start of the focal line has not been plotted as this is actually within the front aperture of the device. If a comparison is made between this and the results from the cylindrical transducer (Figure 5.6), it is clear that a broader peak has resulted. Note that this peak is not rectangular in shape, as could perhaps be expected. This is due to the symmetry of the device, causing off-axis reflections with equal path lengths, as illustrated in Figure 5.32.

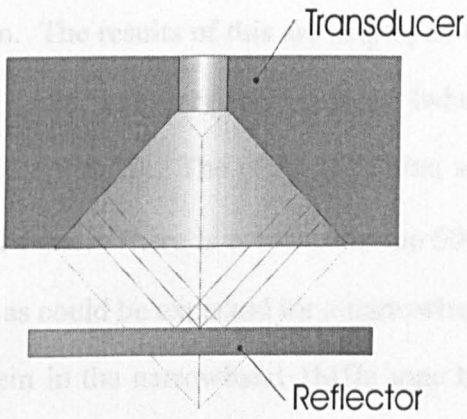

Figure 5.32: *Diagram illustrating the off-axis signal paths.*

5.4.4 Measured sound pressure fields

The sound pressure field was studied, by scanning with a 500μm square micromachined detector as described above. The coordinate system adopted for these and all subsequent scans is shown in Figure 5.33. The field was scanned in the x-z plane over an area measuring 50mm x 20mm with a spatial resolution of 250μm, and was initiated at a position of z=20mm (±1mm). Note that this was within the aperture of the transducer. Three scans were performed, the first using the transducer driven by a

broadband transient signal, from the Panametrics pulser unit, and the two subsequent scans using a tone burst drive of 500kHz and 1MHz, (200v pk-pk) from the Matec gated power amplifier. An applied bias of 200V was used throughout.

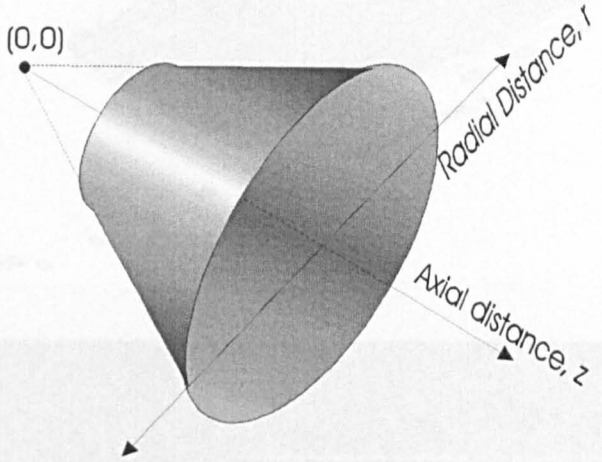

Figure 5.33: ***Coordinate system used for the conical transducer.***

The stored waveforms were then processed to calculate the peak-to-peak amplitudes at each position. The results of this are displayed in Figure 5.34(a-c), plotted as 3D wire frame mesh plots and greyscale images (where white represents high amplitude, and black low amplitude). The plots show that a line of focus $z \approx 25$mm to $z \approx 58$mm has resulted in all cases. There is evidence in the 500kHz plot of side lobes on each side of the focal line, as could be expected for a narrowband drive signal. However, there is no evidence of them in the narrowband 1MHz tone burst plot. This may have been due to spatial averaging over the detector, or the spatial sampling period used in the scan. To examine the focal region further, cross sections through it, at an axial position of z=35mm were taken. Figure 5.35(a-c) shows these for the 500kHz, and 1MHz tone bursts, and the broadband transient drive cases respectively. The FWHM values are approximately 0.75mm, 0.4mm, and 0.6mm respectively for the 500kHz, 1MHz and broadband drive cases.

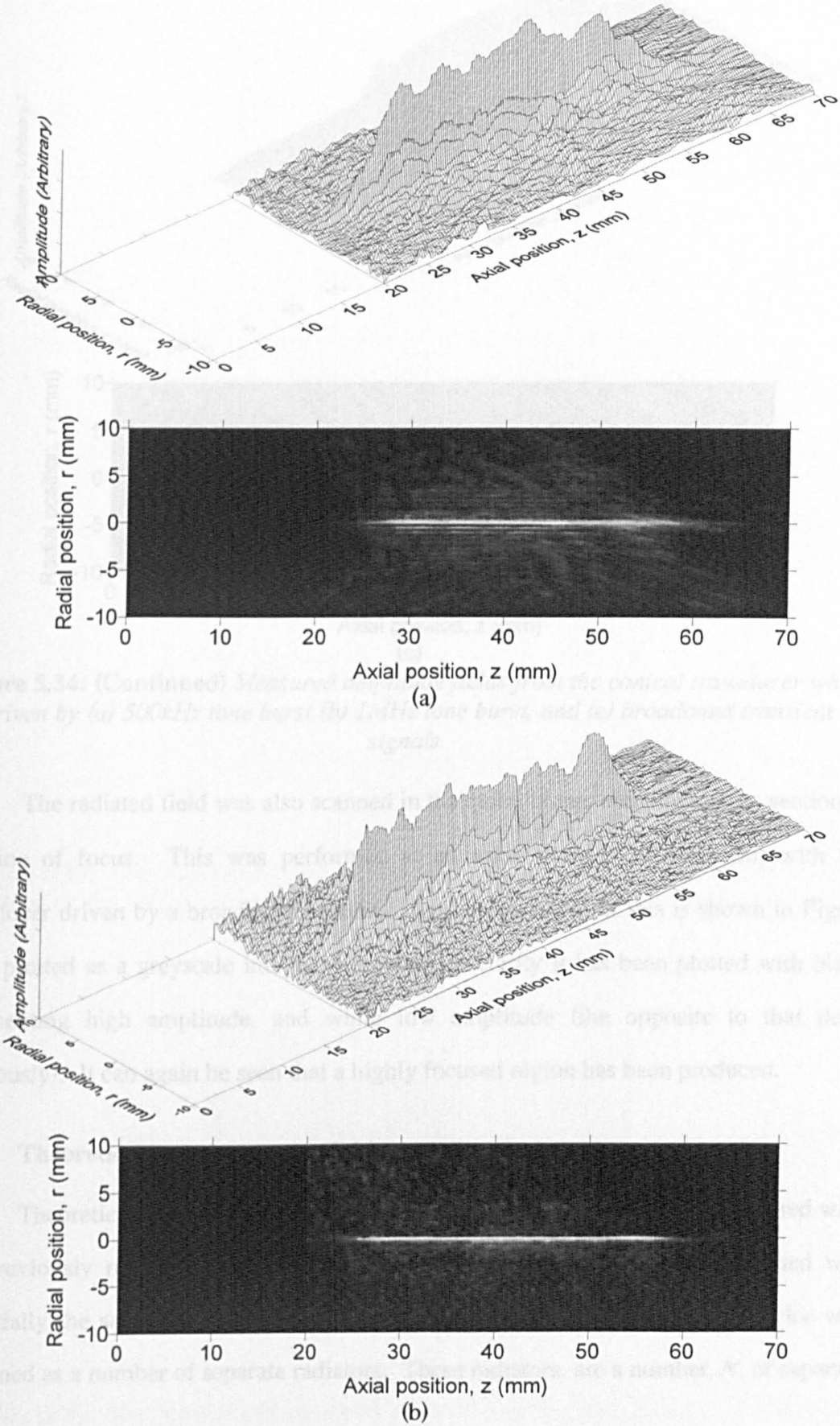

Figure 5.34: *Measured amplitude fields from the conical transducer when driven by (a) 500kHz tone burst (b) 1MHz tone burst, and (c) broadband transient signals.*

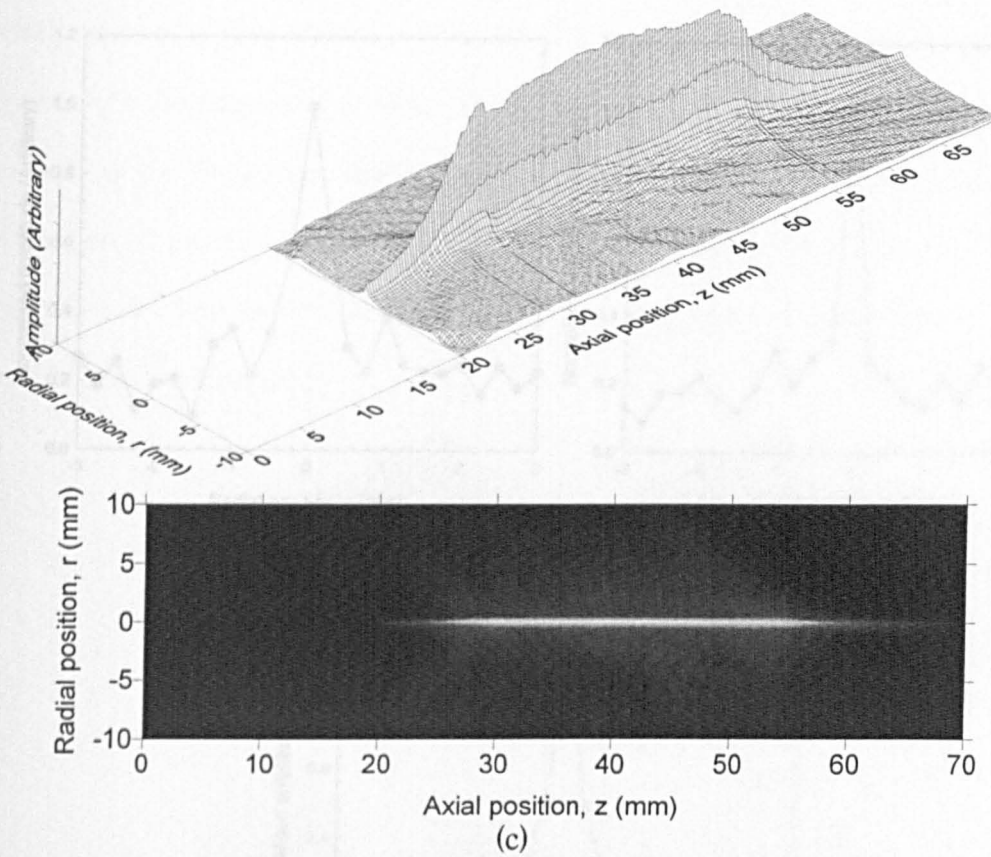

(c)

Figure 5.34: (Continued) *Measured amplitude fields from the conical transducer when driven by (a) 500kHz tone burst (b) 1MHz tone burst, and (c) broadband transient signals.*

The radiated field was also scanned in the radial plane, creating a cross section of the line of focus. This was performed at an axial position of z=35mm, with the transducer driven by a broadband transient signal. The result of this is shown in Figure 5.36, plotted as a greyscale image. Note that for clarity it has been plotted with black representing high amplitude, and white low amplitude (the opposite to that done previously). It can again be seen that a highly focused region has been produced.

5.4.5 Theoretical sound pressure fields

Theoretical field prediction plots were calculated so they could be compared with the previously measured sound amplitude fields. The calculation method used was essentially the same as for the cylindrically focusing transducer, where the device was imagined as a number of separate radiators. These radiators, are a number, N, of separate

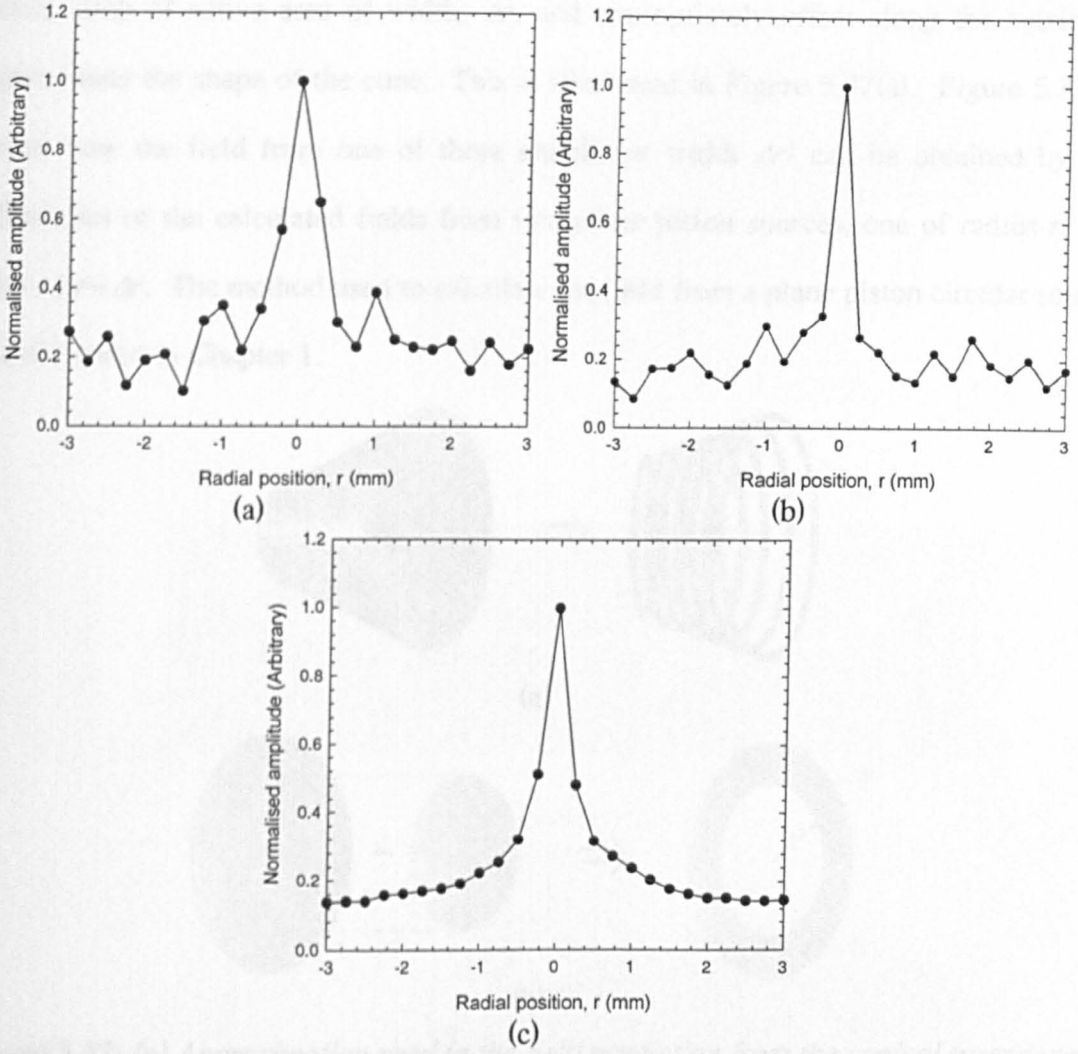

Figure 5.35: *Cross-sections of the focal region (at z=35mm), of the measured amplitude field plots for (a) 500kHz tone burst, (b) 1MHz tone burst and (c) broadband transient drive signals.*

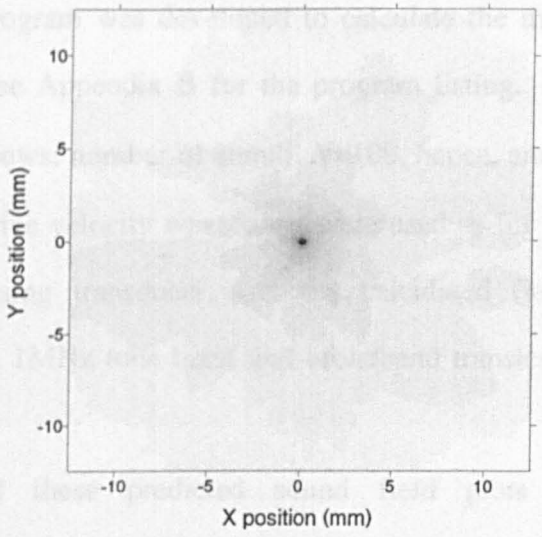

Figure 5.36: *Measured sound amplitude plots through the focal line (at z=35mm) when driven with a broadband transient. (Note black represents higher amplitude, white lower amplitude)*

annuli, each of active area of width, Δr, and appropriately offset along the z-axis, to approximate the shape of the cone. This is illustrated in Figure 5.37(a). Figure 5.37(b) shows how the field from one of these annuli (of width Δr) can be obtained by the subtraction of the calculated fields from two plane piston sources, one of radius r, the other of $r+\Delta r$. The method used to calculate the field from a plane piston circular source was discussed in Chapter 1.

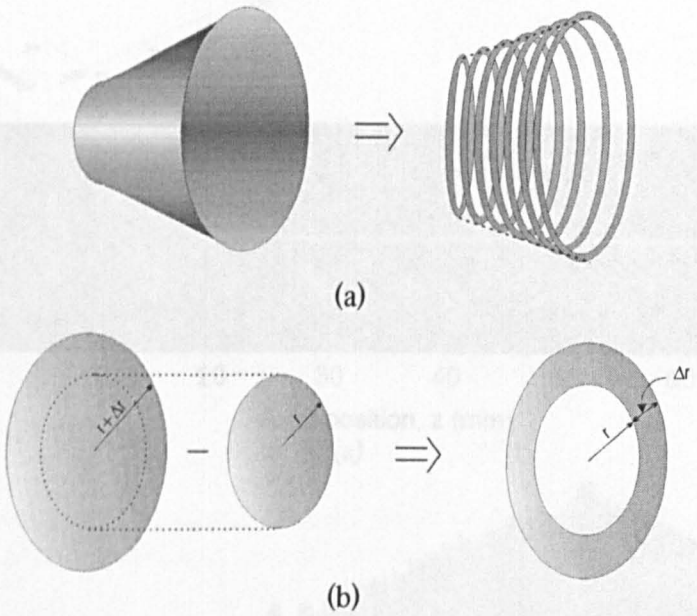

Figure 5.37: *(a) Approximation used in the field prediction from the conical transducer. (b) Subtraction of the fields from two overlapping circular transducers results in the predicted field from an annuli.*

A Matlab™ program was developed to calculate the theoretical field from the conical transducer. See Appendix B for the program listing. The parameters for the simulation were as follows; number of annuli, N=100, hence, annuli width, Δr=0.17mm. The same simulated drive velocity waveforms were used as for the field calculation for the cylindrically focusing transducer, and the calculated fields for drive velocity waveforms of 500kHz, 1MHz tone burst and broadband transient, are shown in Figure 5.38(a-c) respectively.

Comparison of these predicted sound field plots with those obtained experimentally shows agreement of form, with side lobes visible in the 500kHz case, and

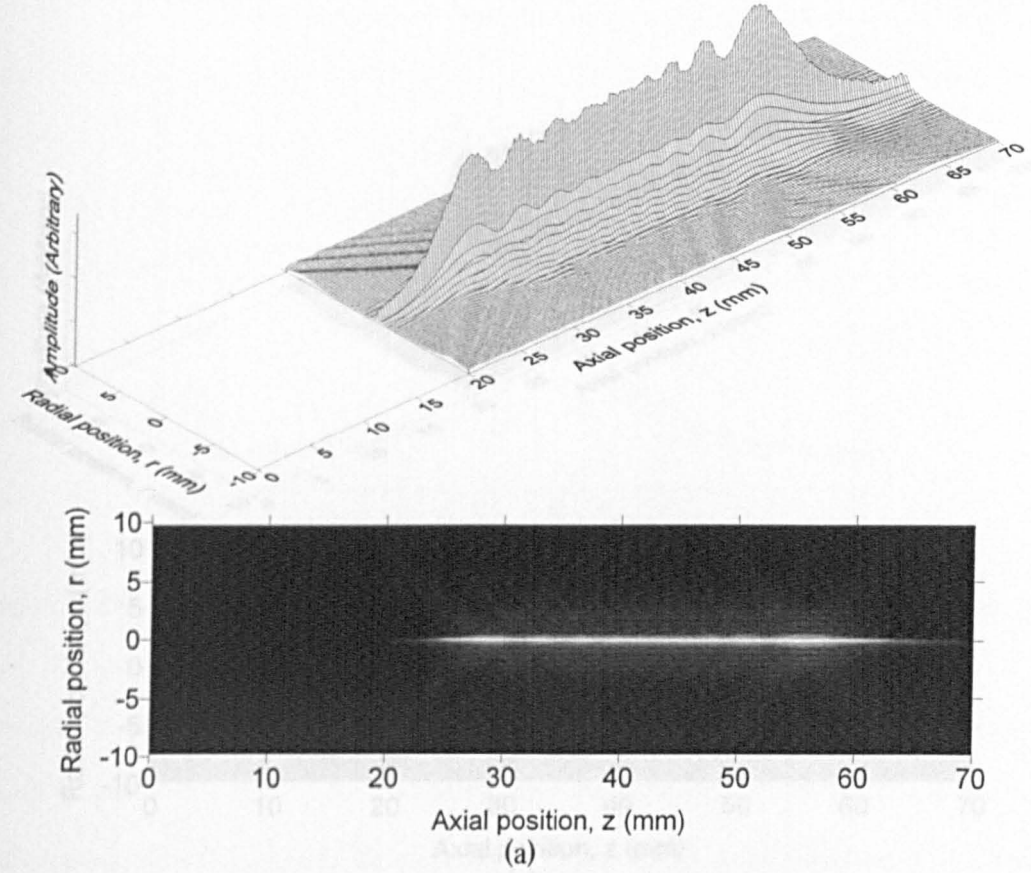

(a)

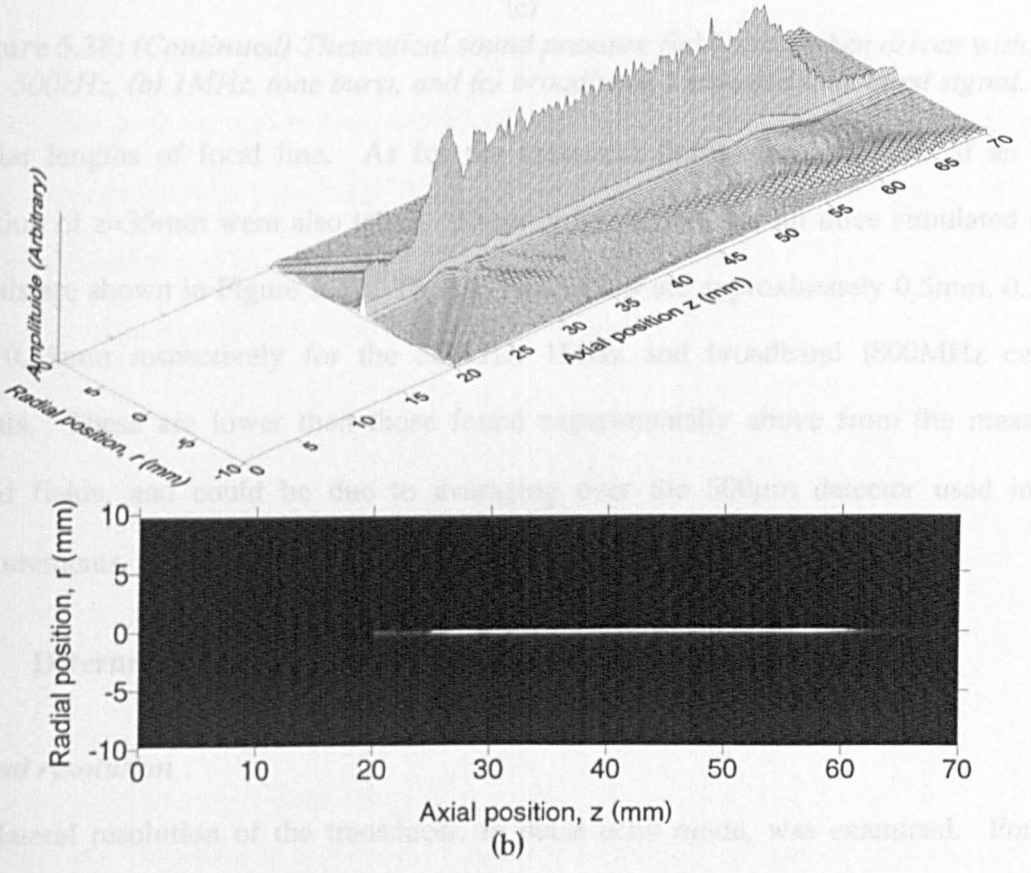

(b)

Figure 5.38: *Theoretical sound pressure field plots, when driven with: (a) 500kHz, (b) 1MHz, tone burst, and (c) broadband, simulated tone burst signal.*

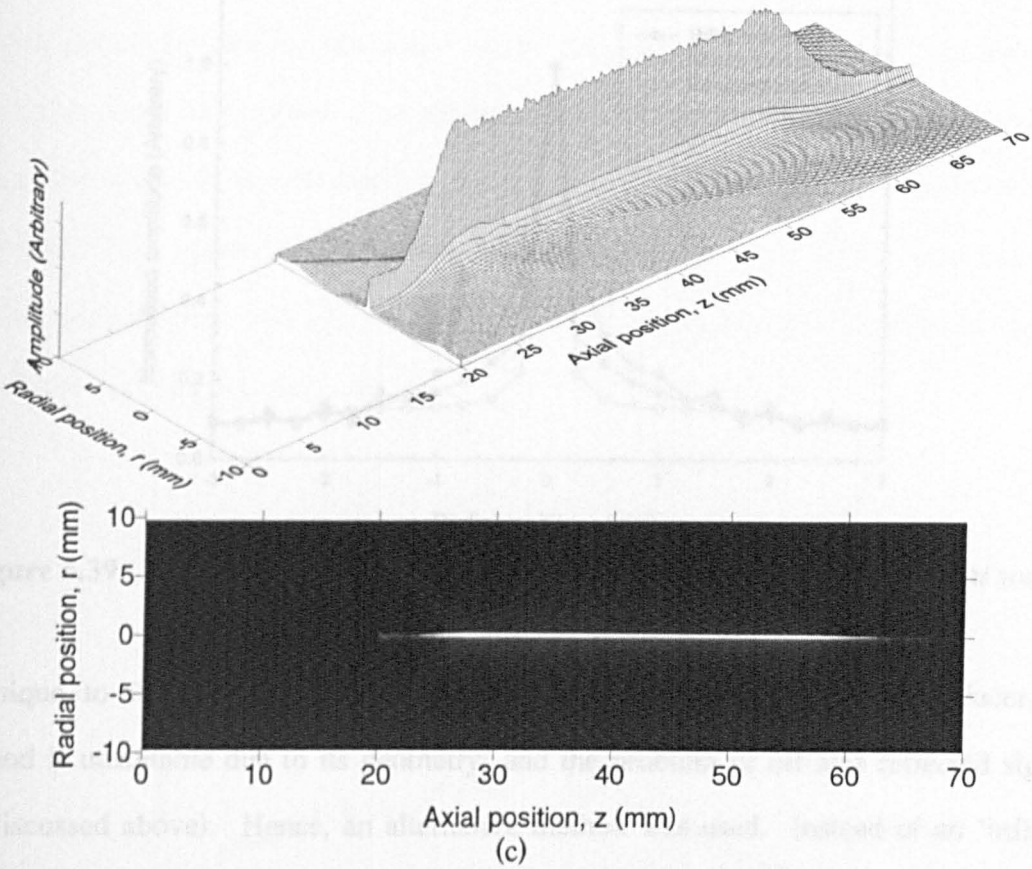

Figure 5.38: ***(Continued)*** *Theoretical sound pressure field plots, when driven with: (a) 500kHz, (b) 1MHz, tone burst, and (c) broadband, simulated tone burst signal.*

similar lengths of focal line. As for the measured fields, cross sections at an axial position of z=35mm were also taken. These cross-sections for all three simulated drive signals are shown in Figure 5.39. The FWHM values are approximately 0.5mm, 0.3mm and 0.35mm respectively for the 500kHz, 1MHz and broadband (800MHz centre) signals. These are lower than those found experimentally above from the measured sound fields, and could be due to averaging over the 500μm detector used in the measurements, effectively smoothing the observed peak of the focal region.

5.4.6 Determination of transducer resolution

Lateral resolution

The lateral resolution of the transducer, in pulse echo mode, was examined. For the cylindrical transducer, described above, this was achieved using an 'infinite' edge

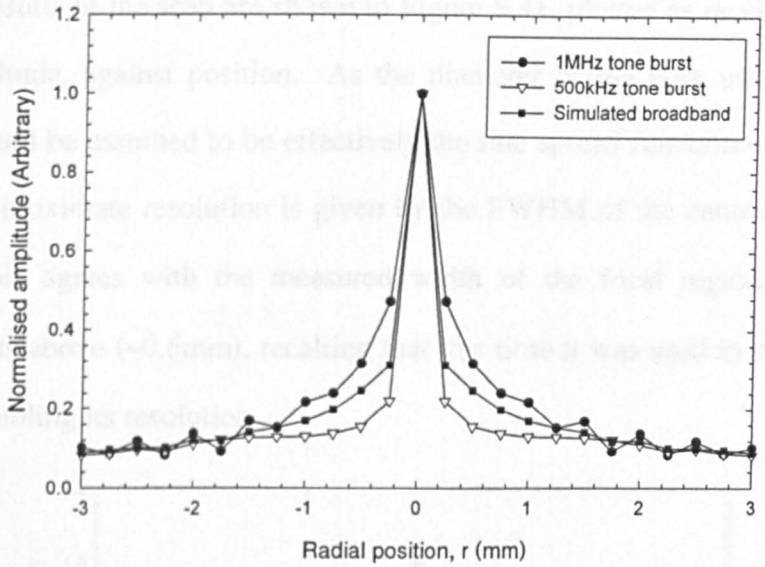

Figure 5.39: *Cross-sections through the focal line (z=35mm) of the theoretical sound pressure field plots (drive velocities as indicated).*

technique, to obtain an edge spread function. However, for the conical transducer, this method is unsuitable due to its geometry; and the problem of off-axis reflected signals (as discussed above). Hence, an alternative method was used. Instead of an 'infinite' edge, a thin (150μm) copper wire, stretched between two bench clamps, was used as a target. This is illustrated in Figure 5.40. A linear scan across this was then performed, using a spatial frequency period of 50μm. The equipment used was the same as that used to determine the resolution of the cylindrical transducer above (Figure 5.20), with the transducer used in pulse-echo and a 200V applied bias.

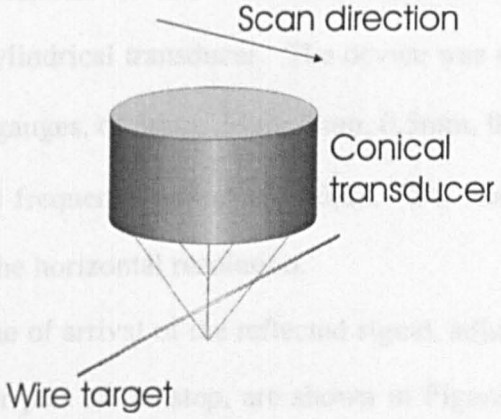

Figure 5.40: Determination of lateral resolution of the conical transducer; scan across a wire target.

The results of the scan are shown in Figure 5.41, plotted as received signal peak-to-peak amplitude, against position. As the diameter of the wire used was relatively small, this could be assumed to be effectively the line spread function of the transducer. Hence, the approximate resolution is given by the FWHM of the central peak, which is ~0.3mm. This agrees with the measured width of the focal region from the field amplitude plots above (~0.6mm), recalling that this time it was used in pulse-echo mode effectively doubling its resolution.

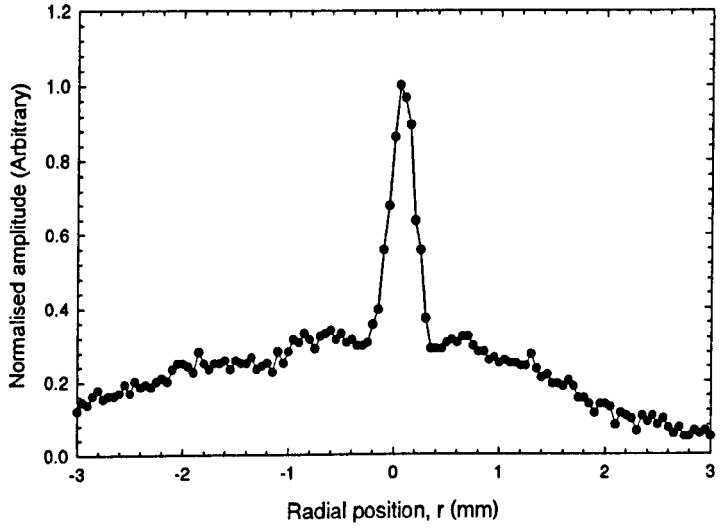

Figure 5.41: *Determination of lateral resolution of the conical transducer; measured signal amplitude of the scan across a wire target.*

Vertical resolution

The vertical resolution of the transducer was determined using the same technique used for the cylindrical transducer. The device was scanned across a series of steps, formed using slip gauges, of 5mm, 2mm, 1mm, 0.5mm, 0.2mm, 0.1mm, and 50μm in height, using a spatial frequency period of 100μm. The same equipment set-up was used as for determining the horizontal resolution.

The measured time of arrival of the reflected signal, adjusted so that t=0 relates to the signal from the lower part of the step, are shown in Figure 5.42(a-g). It is evident

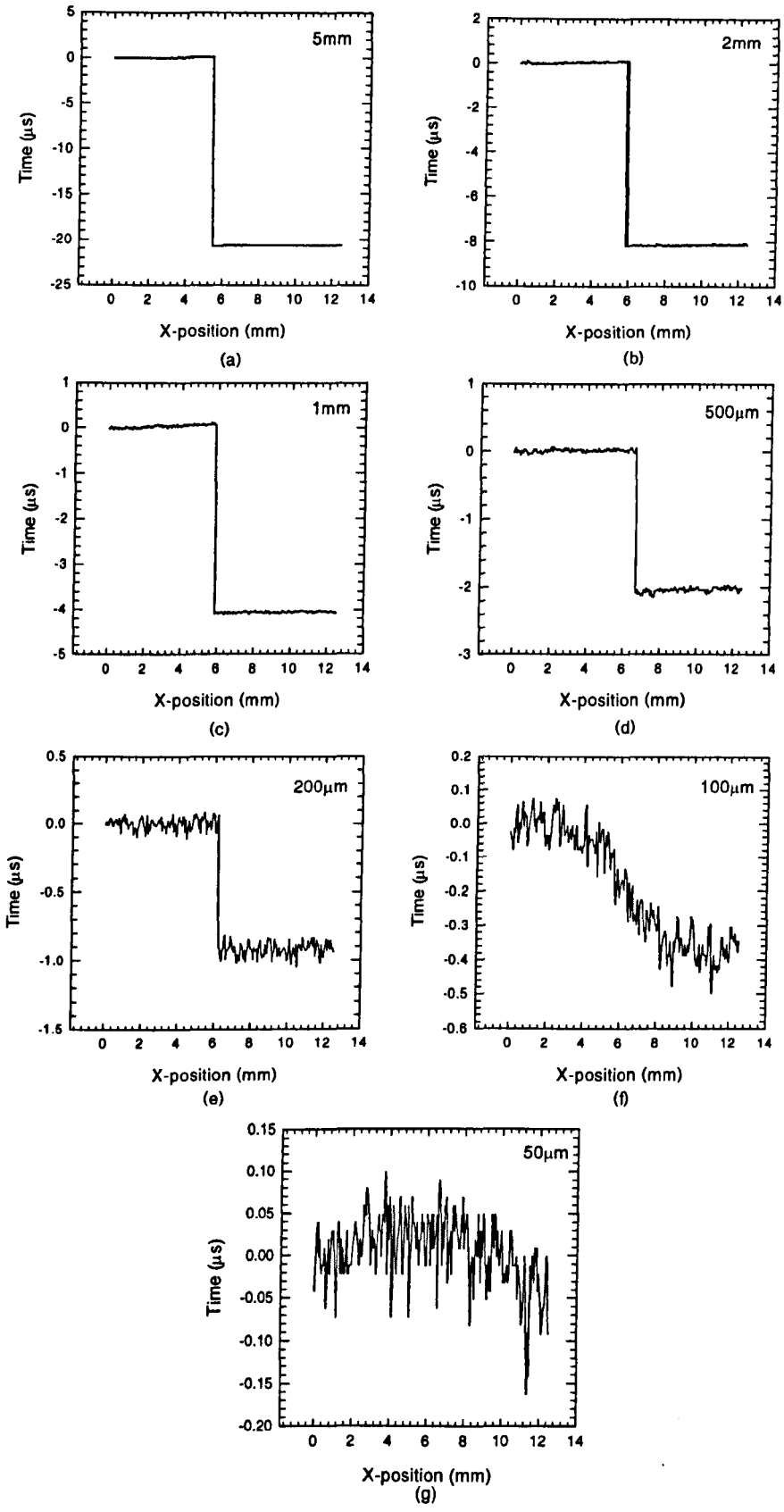

Figure 5.42: *Determination of the vertical resolution of the conical transducer; Time of arrival of the maximum peak in the received signal for a linear scan across steps of height shown.*

that for the steps down to (and including) 100μm, a definite change in the time of arrival either side of the step has occurred. The predicted time of arrival, t, can be calculated from the following:

$$t = \frac{2 \cdot h \cdot \sin\theta}{c} \tag{5.2}$$

where, θ is the angle of the cone, c the velocity of sound, and h is the height of the step. Hence, for this device, this becomes:

$$t = \frac{h\sqrt{2}}{343.4} \tag{5.3}$$

The change in the time of arrival for each of the steps, plotted against step height, are shown in Figure 5.43, along with the predicted time of arrival, calculated from Equation (5.3). Good agreement between the predicted and measured values can be seen. Hence, it was concluded that this transducer/ pulse echo system had a vertical resolution of approximately 100μm.

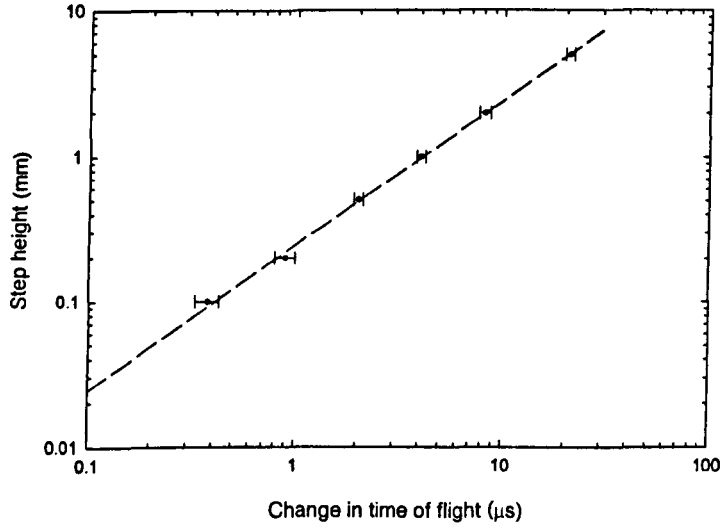

Figure 5.43: *Determination of vertical resolution; measured change in time of flight as the conical transducer is scanned across steps of known height, plotted with predicted time of flight (dashed line).*

5.5 Surface imaging

This section describes an experiment performed to image the surface features of a coin. Both of the transducer designs were tried in such an application so their performances could be compared.

The conical device was operated in pulse-echo mode. However, for the cylindrical transducer design, a pair of transducers were used in a pitch-catch orientation, where one device was used as a source, and the other as a detector to receive the reflected signal from the coins surface. They were positioned so that their lines of focus were at 90° to each other, and coincided on the surface of the coin. This method was used as it effectively allowed these line focusing devices to become 'point' focused; required for the surface imaging of a coin. This is illustrated in Figure 5.44.

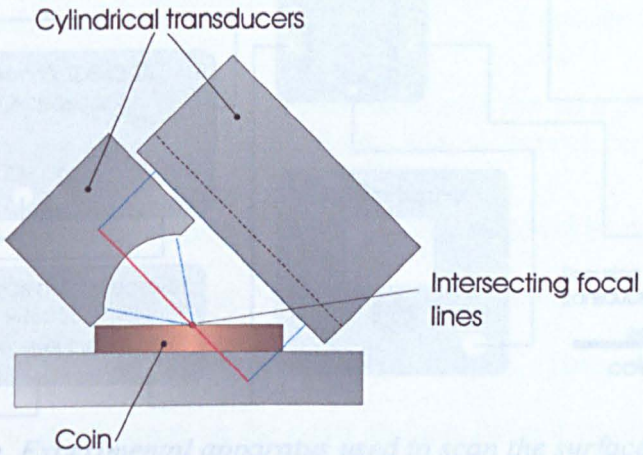

Figure 5.44: *Orientation of the cylindrical line focusing transducers used in pitch-catch mode, to image the surface features of a coin.*

A 2-axis *x-y* linear stage (same as used previously) was used to scan the transducer(s) in a 2-D plane across the surface of the rear side of a two pence coin. During the scan, received waveforms were stored as a function of position. The coin was placed onto a flat glass block, positioned so that the line, or point, of focus of the transducer(s) was on its surface. A spatial frequency period of 250μm was used, over an area measuring approximately 30mm by 30mm. The transducer was connected to a Panametrics (5055PR) pulser/receiver unit, via a capacitive de-coupling circuit to allow

the application of a 200V bias. A schematic diagram of the apparatus used (for pulse-echo operation using the conical transducer) is shown in Figure 5.45. The apparatus used for the surface scan using the pair of cylindrical transducers was similar to that just described, except that the pulser section of the Panametrics pulser/receiver unit was used to drive the source transducer, and a Cooknell charge amplifier was connected to the receiver transducer (with a 100V bias applied by the Cooknell amplifier). In this case the coin was also placed on top of a section of 'Vero' PCB matrix prototyping board.

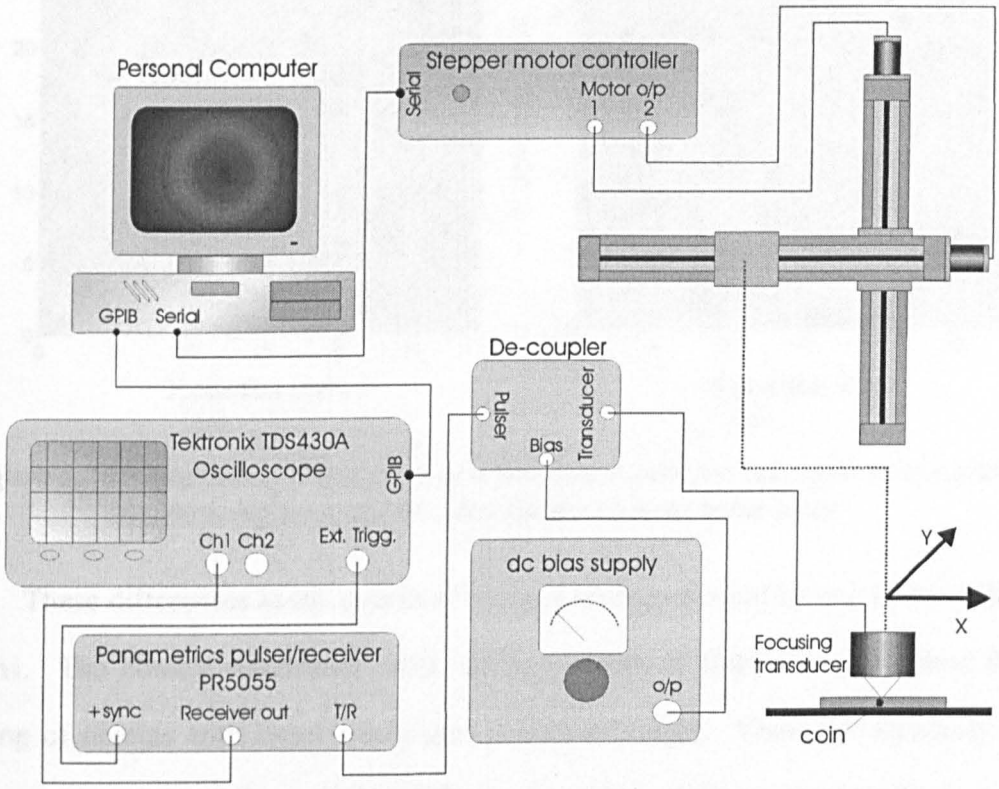

Figure 5.45: *Experimental apparatus used to scan the surface of a coin*

5.5.1 Results and discussion

Firstly, the captured waveforms were processed, using the PixieLab program, to calculate their peak-to-peak amplitude, and plotted as greyscale images, where lighter shading represents a higher amplitude signal. These are shown in Figure 5.46(a & b) for the cylindrical and conical devices respectively. It is evident that the coin outlines, and the majority of its surface features, are easily recognisable.

The image produced using the pair of cylindrical transducers (Figure 5.46(a)) is reasonably clear, with the head and facial features on the coin recognisable. However,

none of the lettering on the coin is legible. The copper tracks, and holes of the 'Vero' board PCB the coin was fixed to is also visible, as well as the glue holding the coin in position (lower centre of the image). Figure 5.46(b) shows the image produced using the conical transducer. The coin outline and head is recognisable, however no finer detail can be seen.

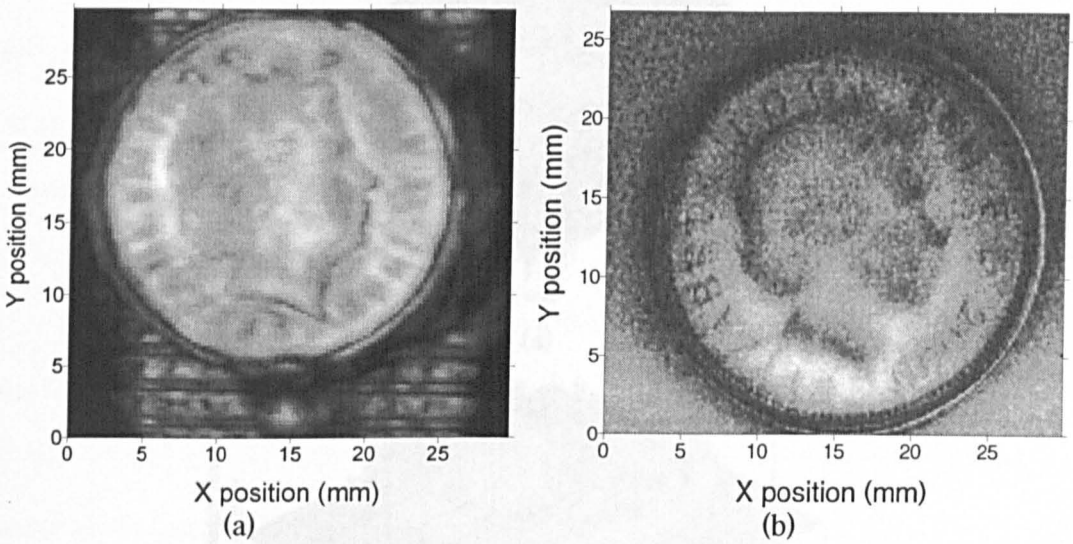

Figure 5.46: *Amplitude image plots of a two pence coin for (a) a pair of cylindrical focusing transducers, and (b) the conical transducer*

These differences in the quality of images produced could be due to the following reasons. The conical transducer, with its large depth of field, is more suited for the imaging of objects with larger variations in surface height. Thus, the relatively small differences in height of the features on the coins surface, did not significantly change the amplitude of the received signal. This is illustrated by the similar shading (hence received signal amplitude) on the surface of the coin and that of the glass block on which it was positioned. The observed changes in amplitude are entirely due to the scattering of the signal from the non-flat regions of the surface of the coin. The cylindrical transducer however, is more suited to this application, having much less depth of field; and hence having improved images over the conical device.

As well as the signal amplitude, the arrival time of the signal was also extracted from the stored waveforms, as a function of position. This was then used to calculate the

surface height at each position, enabling a 3D map of the coins surface to be produced. These images, for the two transducer designs are shown in Figure 5.47(a & b). They are plotted as 3D-wire frame mesh plots, with the signal amplitude data overlaid as shading. Again, a better quality image was produced with the cylindrical device.

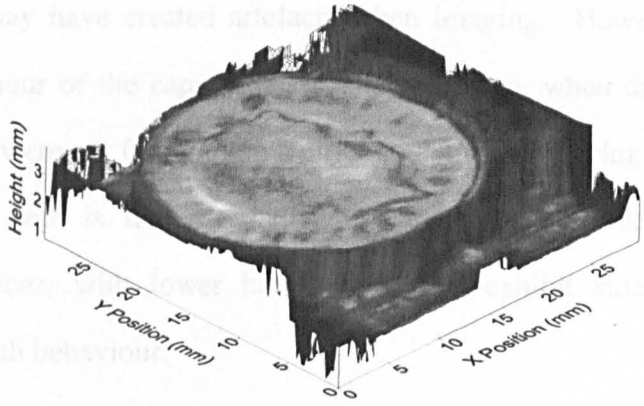

(a)

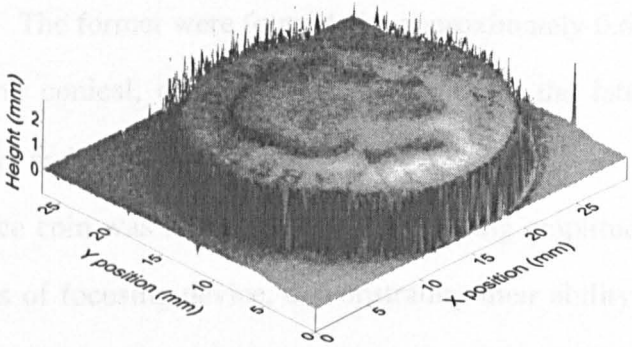

(b)

Figure 5.47: *3D images of the two pence coin. Plotted with height data (calculated from time of flight) and amplitude data overlaid (shading), for the (a) cylindrical transducers, and (b) conical transducer.*

5.6 Conclusions

Two new types of focusing air coupled capacitive transducer have been developed. Their design and construction has been discussed and their characteristics examined.

Firstly, their frequency characteristics were examined, with both devices demonstrating wide-bandwidth behaviour. They were both found to have similar bandwidths of approximately 1.2MHz, with centre frequencies of 500kHz and 800kHz respectively.

Their emitted sound pressure field was also measured, using a miniature detector scanning technique, for both narrowband tone burst and broadband drive signals. These results have been compared to theoretically computed pressure field plots, with good agreement of form. Generally, all the narrowband tone burst plots were found to exhibit side lobes that may have created artefacts when imaging. However, due to the wide bandwidth behaviour of the capacitive transducer design, when driven with a transient signal, side lobes were not found to be a problem, hence improving their imaging ability. Worthy of note here is that alternatives to the capacitive design, such as some piezoelectric devices, with lower bandwidths may exhibit side lobes due to their narrower bandwidth behaviour.

Experiments were also performed to determine the lateral and vertical resolution of the transducers. The former were found to be approximately 0.68mm, and 0.3mm, for the cylindrical, and conical, devices respectively, while the latter were found to be approximately 5μm, and 100μm.

A two pence coin was successfully imaged, using amplitude and time of arrival data, by both types of focusing device, demonstrating their ability to image surfaces in reflected signal mode. It is envisaged that further work could be conducted to examine their use in through transmission imaging of plate materials, allowing inspection of internal structure.

5.7 References

[1] W.A. Grandia, C. M. Fortunko, "NDE applications of air-coupled ultrasonic transducers", *Proc. IEEE. Ultrason. Symp.*, vol. 1., pp. 697-709, 1995.

[2] S.P. Kelly, R. Farlow, G. Hayward, "Applications of through-air ultrasound for rapid NDE scanning in the aerospace industry", *IEEE Trans. Utrason. Ferro. Freq. Contr.*, vol. 43, no. 4, pp. 581-591, 1996.

[3] D.W. Schindel, D. A. Hutchins, "Applications of micromachined capacitance transducers in air-coupled ultrasonics and non-destructive evaluation", *IEEE Trans. Ultra. Ferro. Freq. Contr.*, vol. 42, no. 1, pp. 51-58,1995.

[4] K. Lindström, L. Mauritzson, G. Benoni, P. Svedman, and S. Willner, "Application of air-borne ultrasound to biomedical measurements", *Med. & Biol. Eng. & Comput.*, vol.20, pp. 393-400, 1982.

[5] S.K. Yang, V.V. Varadan, V.K. Varadan, "Non-contact thickness measurement of wet/dry paint coating using an air-coupled transducer", *Mat. Eval.* , vol. 48, pp. 417-480, 1990.

[6] F.A. Jenkins, H.E. White, "Fundamentals of optics", McGraw-Hill Book Company Inc, Third Ed., 1957.

[7] T. Gudra, Z. Kojro, M. Schmachtl, et al. "Scanning acoustic air microscope", *Ultrasonics,* vol. 34, no.7, pp. 711-719, 1996.

[8] T. Yano, M. Tone, A. Fukumoto, "Range Finding and Surface Charaterization Using High-Frequency Air transducers", *IEEE Trans. Ultrason. Ferro. Freq. Contr.*, vol. 34, no. 2, pp. 232-236, 1987.

[9] M. Mortezaie, G. Wade, "Fresnel zone plate and Fresnel phase plate patterns for acoustic transducers", *Acoust. Imaging,* vol. 13, pp. 345-355, 1984.

[10] M.Z. Sleva, W.D. Hunt, R.D. Briggs, "Focusing performance of epoxy and air-backed polyvinylidene fluoride Fresnel zone plates", *J. Acoustic. Soc. Am.*, vol. 96, no. 3, pp. 1627-1633, 1994.

[11] D.W. Schindel, "Focussing of ultrasonic waves in air using a micromachined Fresnel zone-plate", *Ultrasonics,* Vol. 35, pp. 275-285, 1997.

[12] D.W. Schindel, "Ultrasonic imaging of solid surfaces using a focused air-coupled capacitance transducer", *Ultrasonics*, Vol. 35, pp. 587-594, 1998.

[13] D.W. Schindel, A.G. Bashford, D.A. Hutchins, "Chromatic Aberration of an Air-Coupled Ultrasonic Fresnel Zone-Plate", *IEEE Trans. Ultrason. Ferro. Freq. Contr.*, vol. 46, no. 1, pp. 242-246, 1999.

[14] D. Xiang, N.N. Hsu, G.V. Blessing, "A simplified ultrasonic immersion technique for materials evaluation", *Materials Evaluation,* Vol. 56, No. 7, pp. 854-859, 1998.

[15] T. Kozuka, T. Tuzuti, H. Mitome, T. Fukuda, "Control of a standing wave field using a line-focused transducer for two-dimensional manipulation of particles", *Jpn. J. Appl. Phys.*, Vol. 37, pp. 2974-2978, 1998.

[16] C. Wykes, "Advances in air-coupled ultrasonic transducers", *Nondestr. Test. Eval.*, Vol. 12, pp. 155-180, 1995.

[17] R. Reibold, R. Kažys, "Radiation of a rectangular strip-like focusing transducer, Part 1: harmonic excitation", *Ultrasonics*, vol. 30, no. 1, pp. 49-55, 1991.

[18] R. Reibold, R. Kažys, "Radiation of a rectangular strip-like focusing transducer, Part 2: transient excitation", *Ultrasonics*, vol. 30, no. 1, pp. 56-59, 1991.

[19] U.W. Lee and L.J. Bond, "Characterisation of ultrasonic imaging systems using transfer functions", *Ultrasonics,* Vol. 31, no. 6, pp. 405-415, 1993.

[20] C.B. Burckhardt, H. Hoffmann, P.-A. Grandchamp, "Ultrasound Axicon: a device for focusing over a large depth", *J. Acoust. Soc. Am.,* vol. 54, no. 6, pp. 1628-1630, 1973.

[21] F.S. Foster, M.S. Patterson, M. Anditi, J.W. Hunt, "The conical scanner: A two transducer ultrasound scatter imaging technique", *Ultrasonic Imaging,* vol. 3, pp. 62-82, 1981.

6 *An air-coupled fully focused transducer*

6.1 Summary

This chapter continues with the theme from the previous chapter, with the description of the design and characterisation of a fully focusing air-coupled transducer. This device differs to those described previously, as, here, focusing is achieved by reflection from an off-axis parabolic mirror. Initial measurements are performed to determine the devices frequency characteristics. Its radiated peak sound pressure field is also measured by scanning with a miniature detector. In addition, their lateral and vertical resolutions are determined. The work reported in this chapter has been the subject of a publication [1].

6.2 Introduction

The previous chapter described the development and characterisation of two line focussing air-coupled transducers. This chapter continues this investigation of focusing transducers with the study of another variant of focusing device. The focusing transducers described previously utilised curved backplates to create lines of focus. As mentioned in the last chapter, the design of a fully focusing (as opposed to line focused) capacitive transducer by shaping the backplate is difficult, due to the problems associated with forming and attaching a membrane to a surface curved in more than two dimensions. However, here, to avoid this problem a different approach was taken, as focusing is achieved by reflection from an off-axis parabolic mirror.

Very little published literature could be found on similar devices, except one described by Breeuwer [2]. This utilised a parabolic mirror for the focusing of air – coupled ultrasound. It used relatively low frequency air transducers (~70kHz), and

hence possessed a limited degree of focusing. However, this proved adequate for the imaging and recognition of returnable glass bottles with the device being used successfully in a number of commercial sorting machines.

The layout of this chapter is similar to the previous. The first section describes the design and fabrication of the device. This is followed with a description of the initial characterisation, using a pulse-echo method, to obtain the frequency response of the transducer. The sound pressure field is then studied, by measuring with a miniature detector. The lateral and vertical resolution of the device is then measured. Finally, the device is used to image the surface of a coin. Note that the experiments described here are similar to those in the previous chapter, so for brevity they will not be described in detail again.

6.3 Transducer design and fabrication

The focusing device was designed and constructed by Dr. D. Schindel (MicroAcoustic Instruments Inc., Ottawa, Ontario, Canada) in collaboration with the author. It consisted of a planar capacitive air transducer with a micromachined backplate [3]; the construction of which has been discussed previously in Chapter 2, and is shown in Figure 2.2. This polymer-filmed transducer had a 30mm diameter aperture, and was attached to an off-axis parabolic mirror via a machined aluminium housing. A schematic diagram of the transducer is shown in Figure 6.1. The focal point of the off-axis mirror was positioned 25.4mm from its central axis, at an angle of 12.8° to its normal. A photograph of the fully assembled device is shown in Figure 6.2.

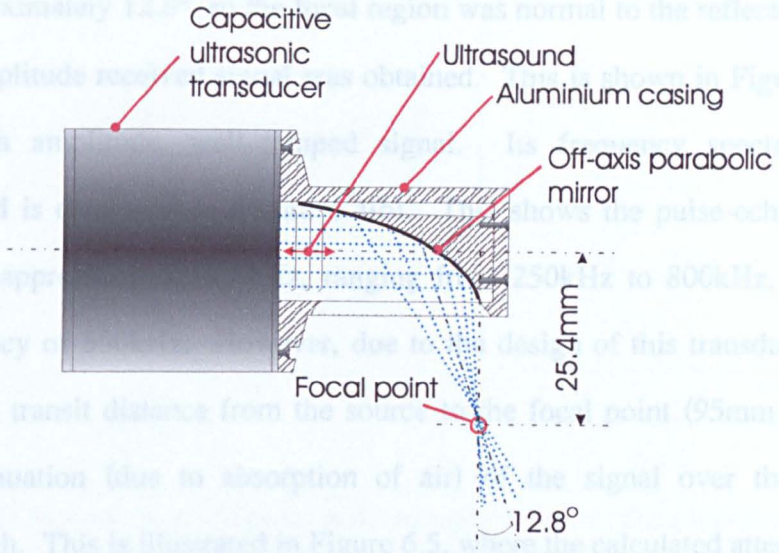

Figure 6.1: *Cut-away schematic diagram of the focusing off-axis parabolic mirror transducer.*

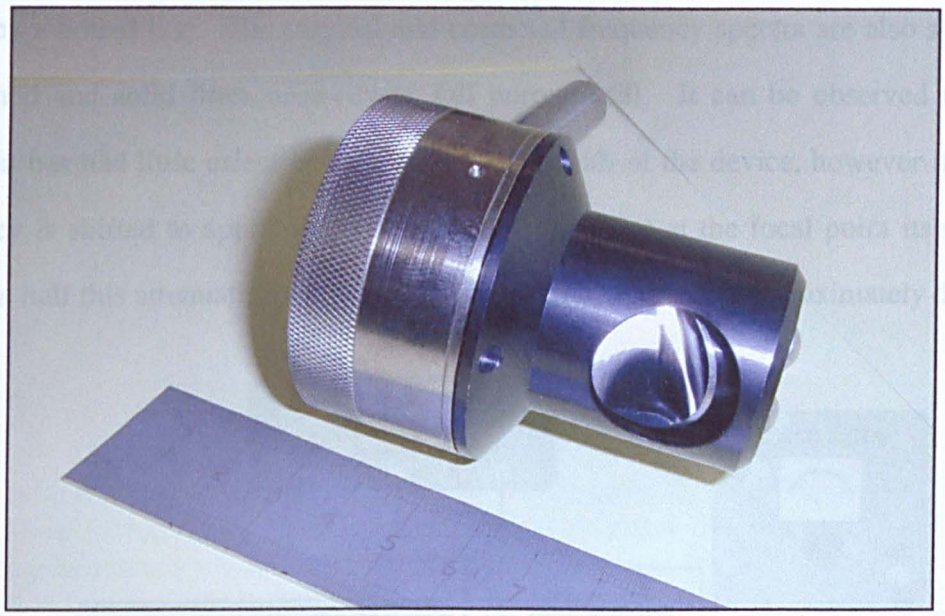

Figure 6.2: *Photograph of the parabolic mirror focusing transducer*

6.4 Transducer characterisation -Initial experiment

An initial pulse-echo measurement was performed to determine the bandwidth of the transducer. Figure 6.3 shows a schematic diagram of the pulse-echo apparatus. This consisted of a Panametrics pulser receiver unit coupled to the transducer via a capacitive decoupling box, to allow the application of a 200V bias voltage. The receiver output of the pulser/receiver unit was fed to a Tektronix TDS430A digital oscilloscope to allow the storage of waveforms. The transducer was carefully aligned above the glass block at an

angle of approximately 12.8°, so the focal region was normal to the reflector surface, and the largest amplitude received signal was obtained. This is shown in Figure 6.4(a), as a relatively high amplitude, well-damped signal. Its frequency spectrum was also calculated, and is displayed in Figure 6.4(b). This shows the pulse-echo signal has a bandwidth of approximately 550kHz, ranging from 250kHz to 800kHz, with a centre (peak) frequency of 550kHz. However, due to the design of this transducer, there is a relatively long transit distance from the source to the focal point (95mm in pulse echo mode). Attenuation (due to absorption of air) of the signal over this distance is moderately high. This is illustrated in Figure 6.5, where the calculated attenuation (using equation (1.13) from Chapter 1) of a wideband signal through 95mm of air at STP is shown by a dotted line. The original and corrected frequency spectra are also shown by the dashed and solid lines respectively (all normalised). It can be observed that this operation has had little effect on the overall bandwidth of the device, however its centre frequency is shifted to approximately 700kHz. Note that at the focal point itself, there would be half this attenuation, so the peak frequency would be at approximately 625kHz.

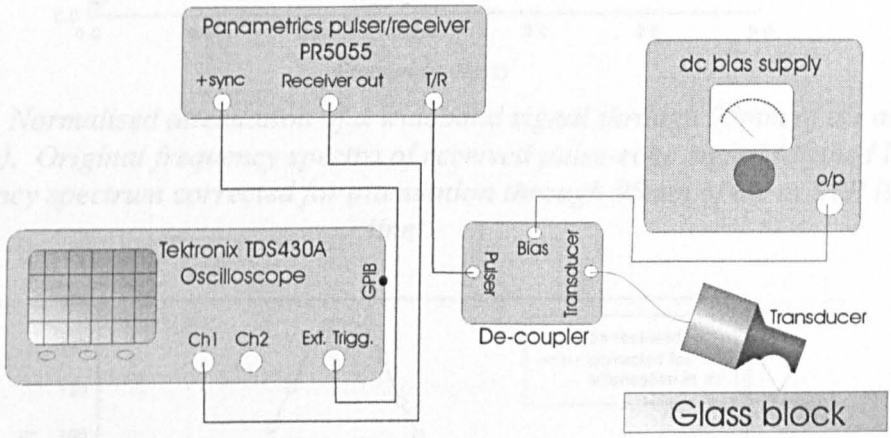

Figure 6.3: *Schematic diagram of the pulse-echo apparatus.*

The transducer-reflector distance was then varied while measuring the received signal amplitude. The results of this are shown in Figure 6.6. For completeness, they were also corrected for atmospheric absorption. It is evident that the peak received signal occurs at an axial position of approximately z=5mm, agreeing with the focal point of the parabolic mirror.

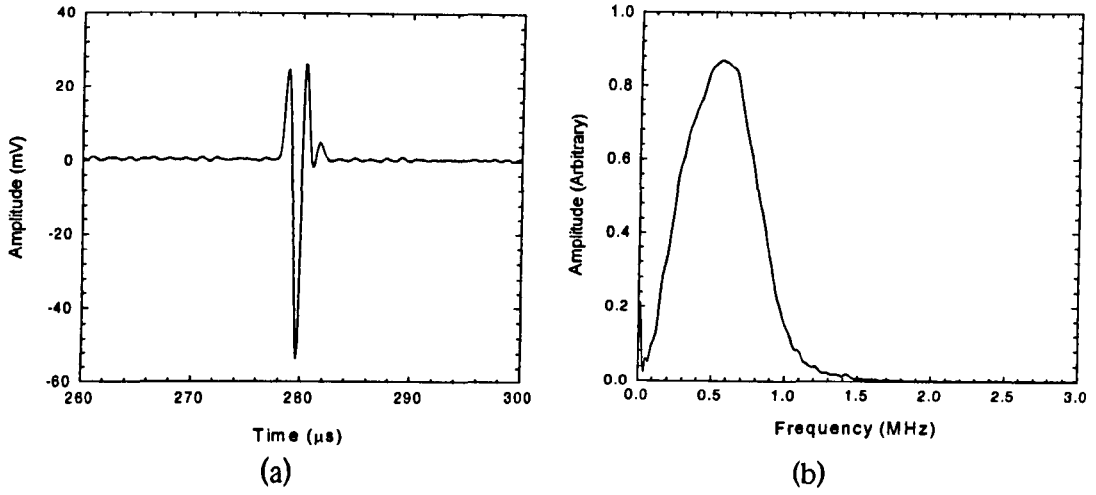

Figure 6.4: *(a) Typical received pulse echo waveform from a flat glass block positioned at the focal point, (b) corresponding frequency spectrum.*

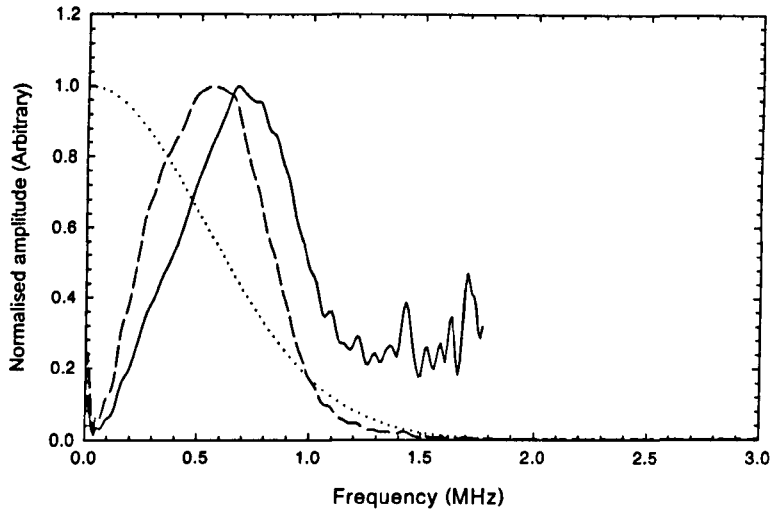

Figure 6.5: *Normalised attenuation of a wideband signal through 95mm of air at STP (dotted line). Original frequency spectra of received pulse-echo signal (dashed line), and frequency spectrum corrected for attenuation through 95mm of air at STP (solid line).*

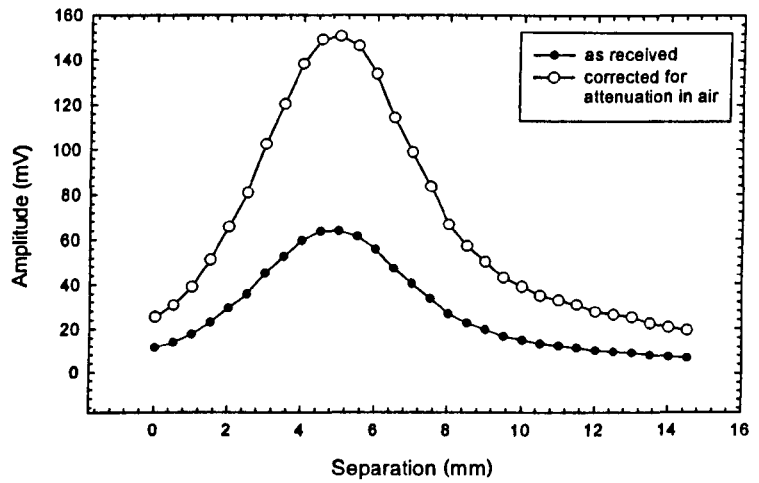

Figure 6.6: *Measured signal amplitude with increasing transducer reflector separation.*

6.5 Sound pressure field plots

The sound pressure field was examined by scanning with the 500μm square micromachined detector, firstly in the *x*-*z* plane. Figure 6.7 shows a diagram of the coordinate system adopted, where x=0 is in the centre of the focal region, and z=0 is level with the front aperture of the transducer. An area measuring approximately 20mm x 20mm was scanned, using a spatial resolution of 250μm, and initiated within the front aperture of the transducer at a position of z=-4mm. The scan was performed three times, the first with the transducer driven by a transient drive signal, supplied by a Panametrics pulser unit. The two subsequent scans were performed with tone burst excitation signals, of 500kHz and 1MHz respectively. A 200V bias was applied throughout the experiment.

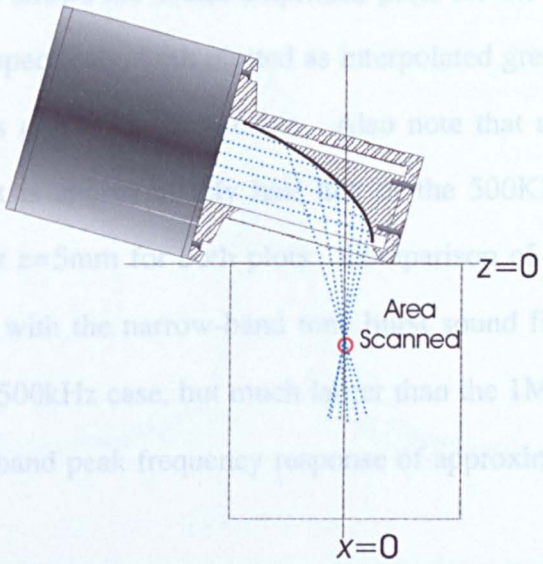

Figure 6.7: *Schematic diagram of the sound pressure field area scanned.*

Figure 6.8 shows the measured sound amplitude field for the broadband transient case, plotted as (a) a wire frame mesh, and (b) an interpolated greyscale image with brighter areas representing higher amplitude. It is evident that a focused field has resulted, with the point of highest amplitude at a position of approximately z=5mm. Note that a small amount of misalignment is evident, as the plot appears slightly tilted.

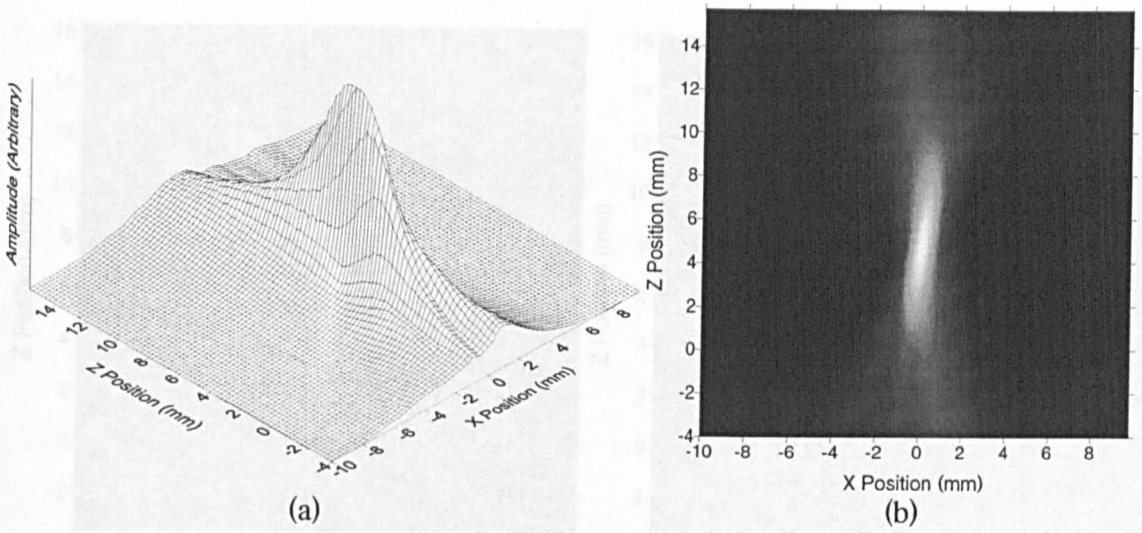

Figure 6.8: *Measured sound amplitude from the parabolic mirror transducer, in the x-z plane, when driven by a transient broadband pulse. Plotted as (a) wire frame mesh plot, and (b) interpolated greyscale image.*

Figure 6.9(a & b) shows the sound amplitude plots for the tone burst excitations of 500kHz and 1MHz respectively, both plotted as interpolated greyscale images. Slight evidence of side lobes is present in both cases. Also note that as expected, the focal region of the 1MHz plot is approximately half that of the 500KHz case, and that the centre of this region is at z=5mm for both plots. Comparison of the focal areas of the broadband transient plot with the narrow-band tone burst sound fields reveals that it is slightly smaller than the 500kHz case, but much larger than the 1MHz plot. This agrees with the measured broadband peak frequency response of approximately 625kHz (at the focal point).

Further examination of the focal region in all three cases was performed by studying their cross sections, at z=5mm. These are shown in Figure 6.10, plotted with normalised amplitude, against x-position. The FWHM values for each of the focal regions (measured from the plots) are as follows; 500kHz=1.2mm, 1MHz=0.6mm, broadband = 1.1mm. Note that these values relate to approximately 2λ for each case.

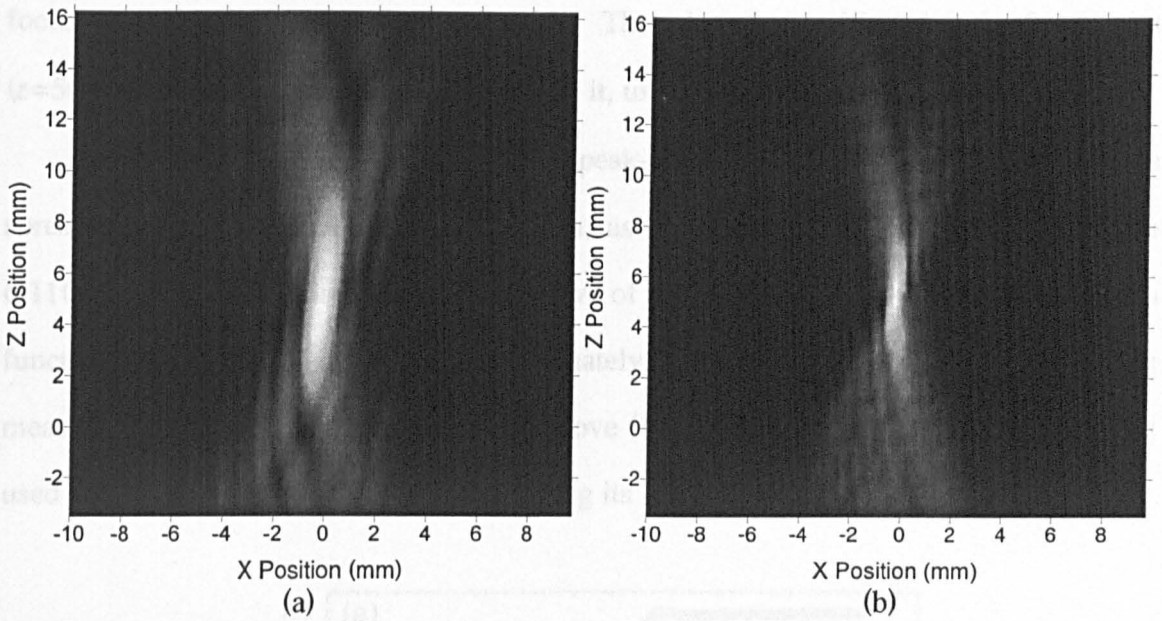

Figure 6.9: *Measured amplitude field plots for the parabolic mirror focusing transducer when driven with (a) 500kHz tone burst, and (b) 1MHz tone burst excitation signals.*

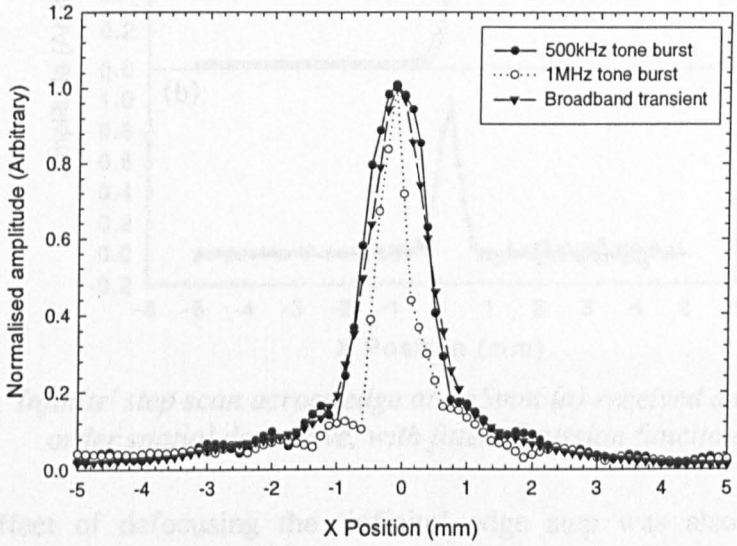

Figure 6.10: Normalised *cross-sections through the focal region (z=5mm) of the measured amplitude field plots (drive signals as indicated).*

6.6 Determination of transducer resolution

6.6.1 Lateral resolution

To determine the lateral resolution of the transducer, when used in pulse-echo operation, the scan across an 'infinite' step edge method, described in the previous chapter, was used. The experimental set up was identical to that used for the cylindrical

focusing device (see Figure 5.19 and 5.20). The edge was positioned at the focal point (z=5mm), and the transducer scanned across it, using a spatial resolution of 50μm.

Figure 6.11(a) shows the received peak-to-peak amplitude step function (edge spread function) of the received waveform, as a function of lateral position. Figure 6.11(b) shows the first order spatial derivative of the step, together with a fitted Gaussian function. The FWHM of this is approximately 0.5mm. This value, agrees with that measured from the field scans performed above (1.1mm), remembering it was now being used in pulse echo mode, effectively doubling its resolution.

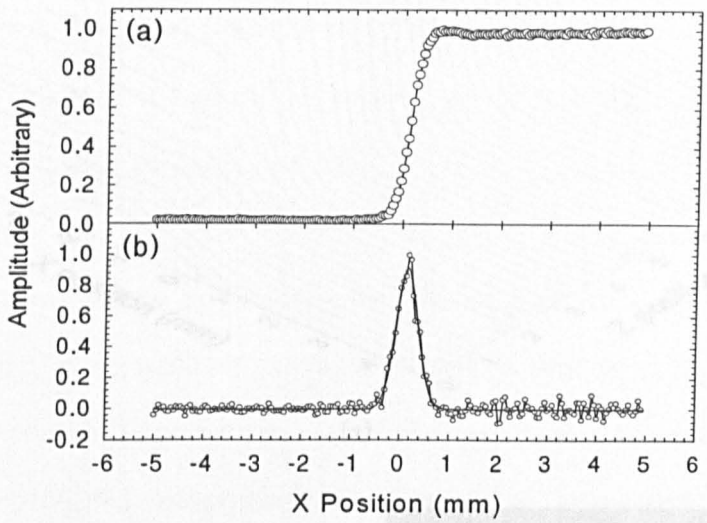

Figure 6.11: *'Infinite' step scan across edge at z=5mm (a) received amplitude, (b) first order spatial derivative, with fitted Gaussian function*

The effect of defocusing the 'infinite' edge step was also investigated, by performing the above experiment again, while also scanning in the z direction. An area 5mm either side of the focal point was examined, using a spatial frequency period of 0.5mm in the z direction. Figure 6.12(a) shows the pk-pk amplitude edge-spread functions, plotted against z position. It is evident that the highest amplitude, and gradient, is obtained at the focal point, with both these reducing as the edge is moved out of focus. Their first order spatial derivatives (LSF's) were also calculated and are shown in Figure 6.12(b & c), as a set of line plots (with only alternate ones shown for clarity), and an interpolated greyscale image plot respectively. Note that these have been smoothed to remove the noise associated with the numerical derivative operation. It is

evident that the effect of defocusing can be seen as the spreading of the main peak. In the region of z=4mm to 7mm the peak is well defined, hence it was concluded that the device exhibited a depth of field of approximately 3mm. It is also worth noting the similarity of the greyscale image of the LSF's with the measured broadband field plot (Figure 6.8(b)).

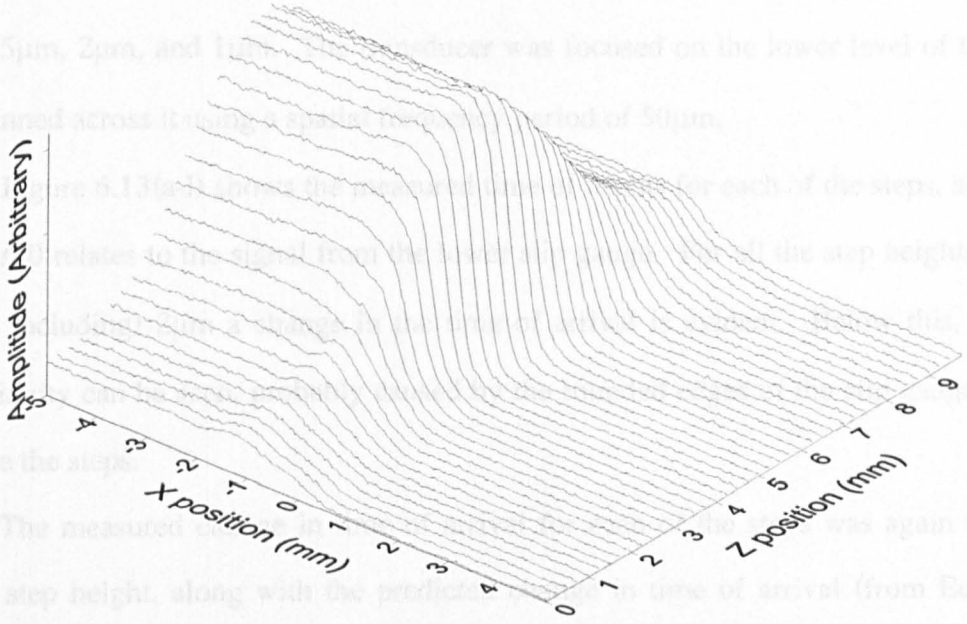

(a)

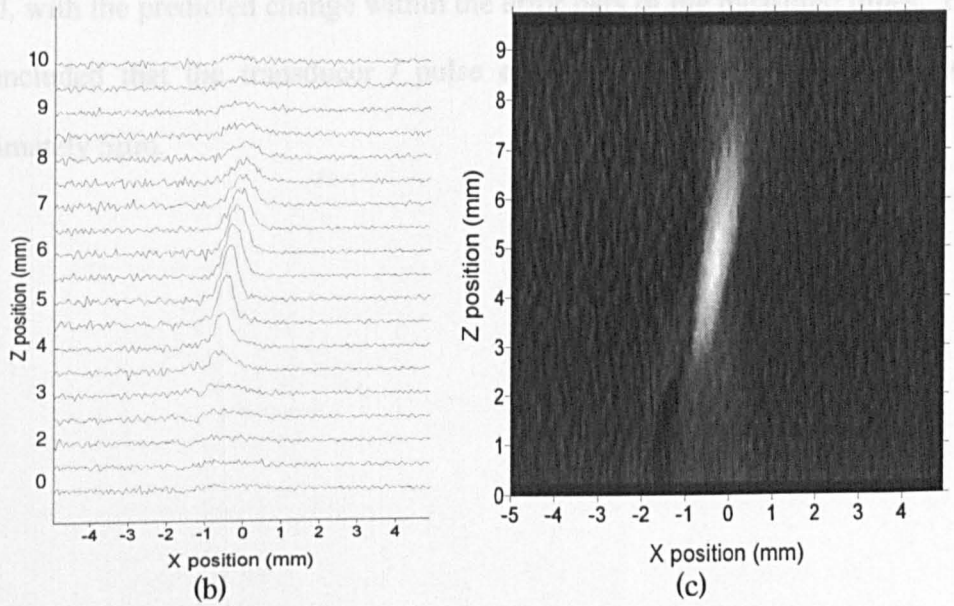

(b) (c)

Figure 6.12: *(a) Received amplitude edge spread function plots of the 'infinite edge' scan, and first order spatial derivatives of step scan plotted as (b) Waterfall plot (only alternate rows plotted for clarity) (c) greyscale image, where white is higher/black lower amplitude.*

6.6.2 Vertical resolution

The vertical resolution of the transducer was determined by scanning across a series of steps with known height, the same method used in the previous chapter for the conical and cylindrical transducers. Steps were formed with slip gauges of different thickness with heights of 5mm, 2mm, 1mm, 0.5mm, 0.2mm, 0.1mm, 50μm, 20μm, 10μm, 5μm, 2μm, and 1μm. The transducer was focused on the lower level of the step and scanned across it using a spatial frequency period of 50μm.

Figure 6.13(a-l) shows the measured time of flights for each of the steps, adjusted so that t=0 relates to the signal from the lower slip gauge. For all the step heights down to (and including) 2μm a change in the time of arrival is evident. Below this, only a discontinuity can be seen, probably caused by the rounded edges of the slip gauges used to create the steps.

The measured change in time of arrival for each of the steps was again plotted against step height, along with the predicted change in time of arrival (from Equation 5.1). This is shown in Figure 6.14. It can be seen that reasonable agreement has resulted, with the predicted change within the error bars of the measured times. Hence, it was concluded that the transducer / pulse echo system had a vertical resolution of approximately 5μm.

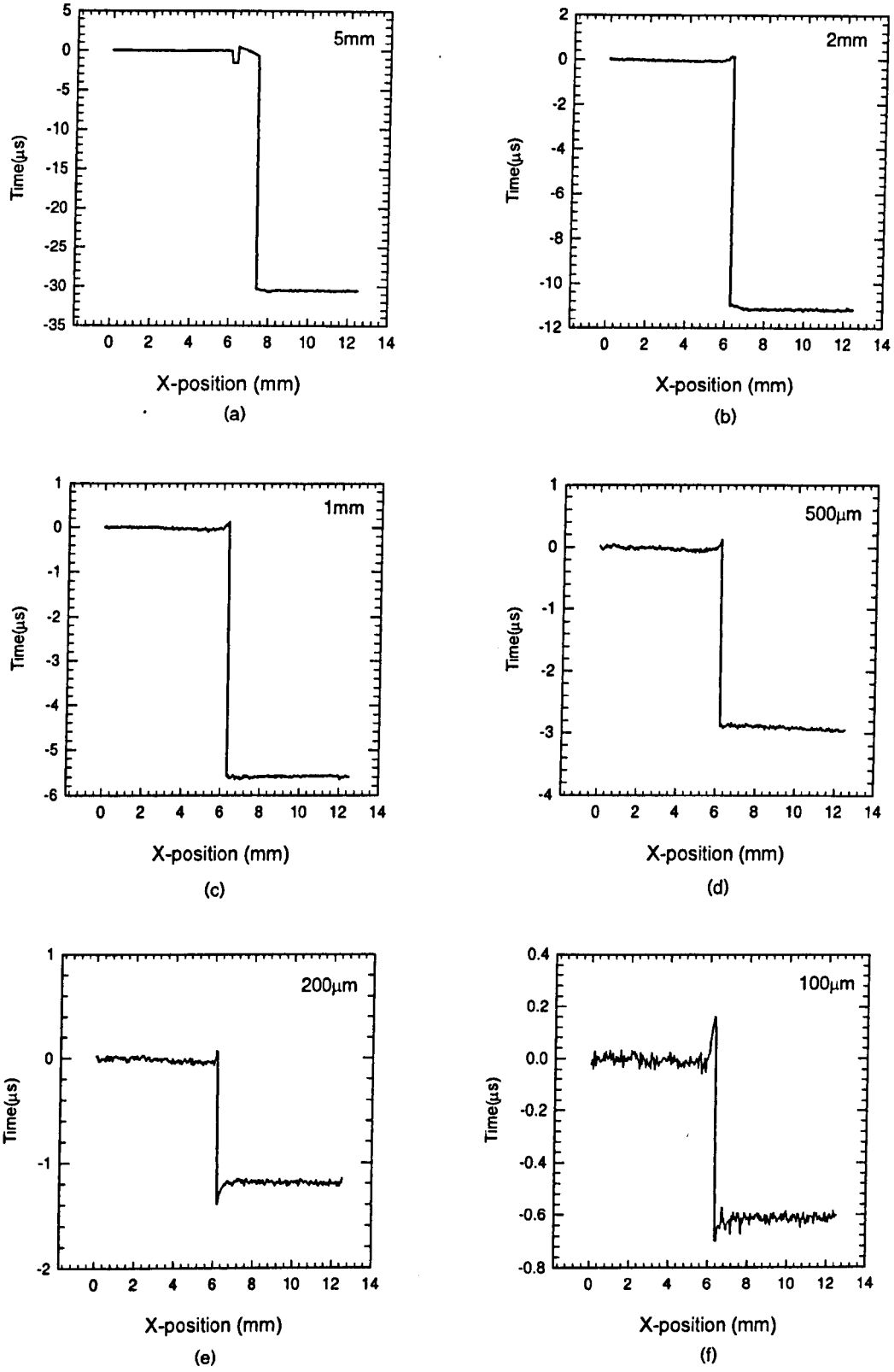

Figure 6.13: *Determination of the vertical resolution of the parabolic mirror transducer; Time of arrival of the maximum peak in the received signal for a linear scan across steps of height shown.*

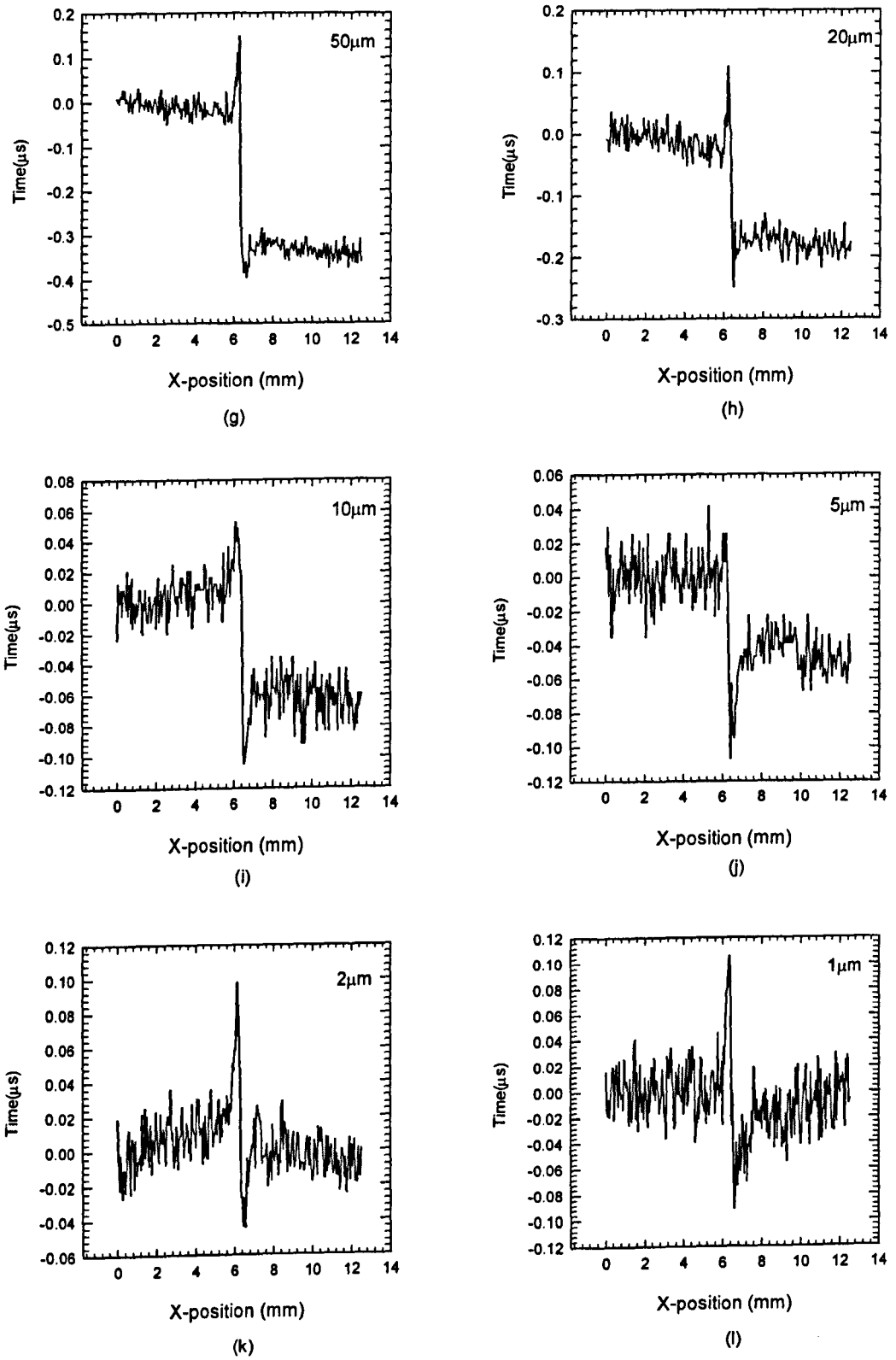

Figure 6.13: (Continued) *Determination of the vertical resolution of the parabolic mirror transducer; Time of arrival of the maximum peak in the received signal for a linear scan across steps of height shown.*

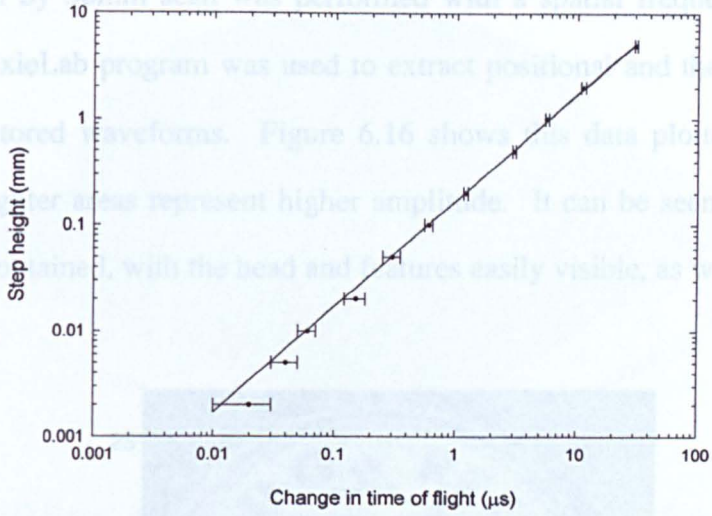

Figure 6.14: *Determination of vertical resolution; measured change in time of flight as the parabolic mirror transducer is scanned across steps of known height, plotted with predicted time of flight (solid line).*

6.7 Surface imaging

In the previous chapter, the line-focusing transducers were used to image the surface of a two pence coin. Here, this experiment is repeated again using the fully focusing parabolic mirror device. Figure 6.15 shows the method used to scan the coins surface. The apparatus used was the same as that described previously in Chapter 5 (see Figure 5.45). The transducer was operated in pulse-echo mode, and positioned so that its focal region was on and normal to the surface of the coin (i.e. the coin was at z=5mm).

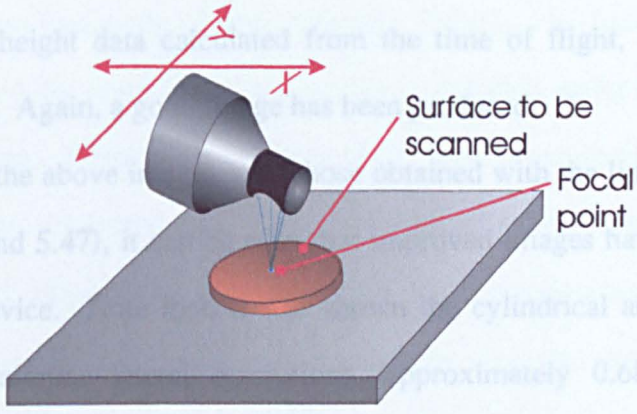

Figure 6.15: *Method used to scan the surface of the coin.*

A 30mm by 30mm scan was performed with a spatial frequency resolution of 250μm. The PixieLab program was used to extract positional and the pk-pk amplitude data from the stored waveforms. Figure 6.16 shows this data plotted as a greyscale image, where lighter areas represent higher amplitude. It can be seen that a very clear image has been obtained, with the head and features easily visible, as well as the lettering around the edge.

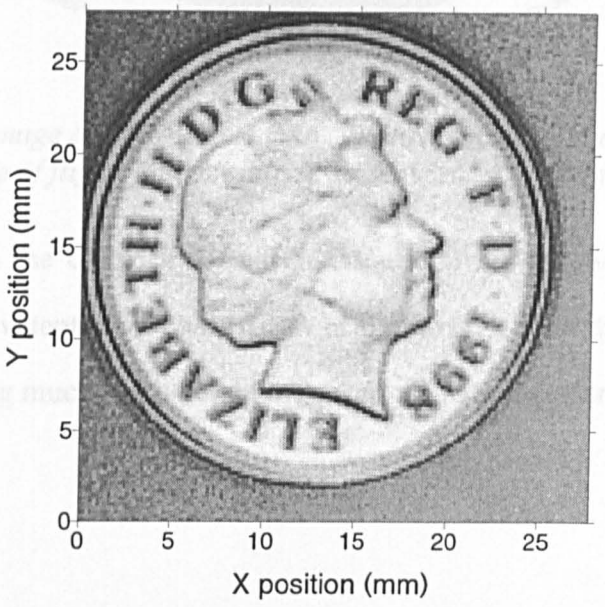

Figure 6.16: *Greyscale amplitude image plot of a two pence coin (darker areas lower amplitude)*

The PixieLab program was also used to extract the time of flight data from the waveforms. This was used to create a 3-D image of the coin. This is shown in Figure 6.17, plotted with height data calculated from the time of flight, and amplitude data overlaid as shading. Again, a good image has been produced.

Comparing the above images with those obtained with the line-focussing devices (see Figures 5.46 and 5.47), it can be seen that improved images have resulted with the parabolic mirror device. Note that, it was shown the cylindrical and parabolic mirror devices exhibited similar lateral resolutions (approximately 0.68mm and 0.55mm respectively), when used in pulse echo mode. However, the pitch catch method used to

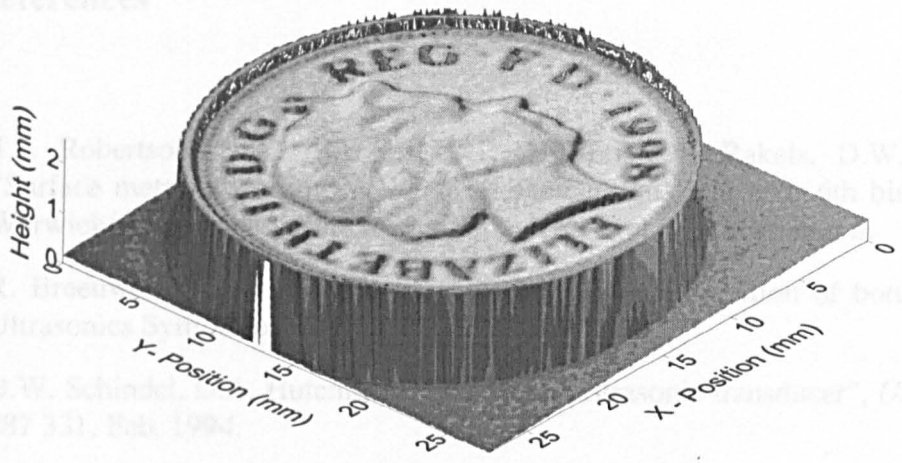

Figure 6.17: *3-D image of a two pence coin. Plotted with height data calculated from time of flight, and amplitude data overlaid as shading.*

image the coin with the cylindrical transducers effectively halved the systems lateral resolution. This is evident from comparison of the images, with the one created by the parabolic mirror being much sharper than that from the cylindrical transducer.

6.8 Conclusion

The design and characterisation of a novel fully focusing air-coupled transducer has been discussed. Initial experiments were performed to study the frequency response of the transducer, using a pulse-echo method. The device was found to exhibit a bandwidth and centre frequency of approximately 700kHz. Its radiated sound pressure fields were examined, by scanning with a miniature detector, using both broadband and tone burst excitations. These were found to show peak pressure at the expected focal position. In addition, its lateral and vertical resolutions were measured, by scanning a series of steps and edges, and were found to be approximately 0.5mm and 5μm respectively. Surface imaging of a two pence coin was also performed, with good images obtained, using both amplitude and time of flight data.

6.9 References

[1] T.J. Robertson, D.A. Hutchins, D.R. Billson, J.H. Rakels, D.W. Schindel, "Surface metrology using reflected ultrasonic signals in air", 6th biennial joint Warwick/ Tokyo nanotechnology symposium. Sept. 2000, (in press).

[2] R. Breeuwer, "Ultrasonic scanning, imaging and recognition of bottles", IEEE Ultrasonics Symposium, vol. 1, pp. 635-638, 1989.

[3] D.W. Schindel, D.A. Hutchins, "Air-coupled ultrasonic transducer", *US Patent*, 5 287 331, Feb. 1994.

7 *Capacitive Immersion Transducers*

7.1 Summary

This chapter describes the development and characterisation of a capacitive transducer for use in immersion. Firstly, the design and construction of the transducer is described. This is followed by a preliminary experiment to compare the characteristics of the device when used in air and in immersion. The effects of backplate topography are also examined, firstly using manufactured random metallic backplates, then with machined backplates produced by a photolithography process. The effect of applied bias on transducer characteristics is also studied. Radiated sound pressure fields are measured and compared to theoretical plane piston predictions. An alternative membrane material, mica, is also investigated. Finally, the device operation is demonstrated in a pulse-echo defect detection system, where artificially induced defects on the rear of Perspex and aluminium plates were imaged using a C-scan pulse-echo method.

7.2 Introduction

Immersion transducers are widely used in industrial and medical applications [1]. The use of water as the coupling medium is advantageous due to its similar acoustic impedance to that of the material(s) under test, enabling the majority of the ultrasound to be transmitted into (and out of) the sample. Generally, for immersion work, piezoelectric transducers are commonly used. The typical construction of one of these devices is shown in Figure 7.1. They generally consist of a piezoceramic disc, usually of lead zirconium titanate (PZT), with a sintered metallised electrode on each face [2]. The rear face of the disc is attached to a backing layer; typically a highly attenuating tungsten

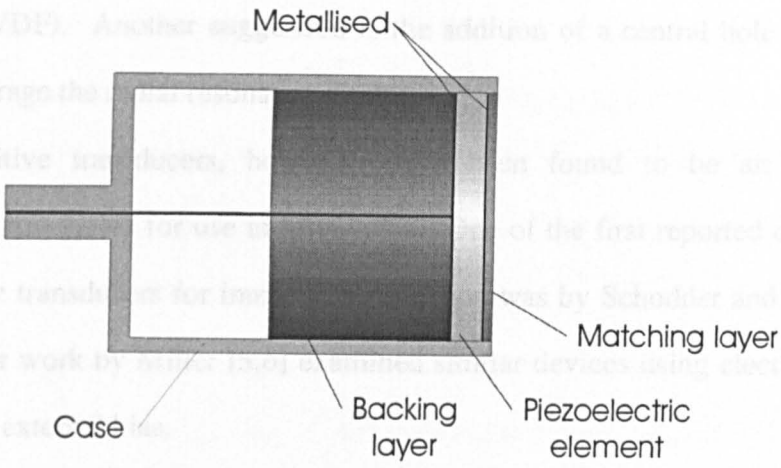

Figure 7.1: *Schematic diagram of a piezoelectric immersion transducer*

loaded epoxy, with an acoustic impedance similar to that of the piezoceramic. The purpose of this is to absorb the energy radiated backwards and damp out any reverberations, and reduce the subsequent ringing of the device, hence increasing its bandwidth. The front of the disc is usually covered with a ¼ wavelength matching layer, generally an epoxy or polymer, to improve coupling into the water. As discussed in Chapter 2, this matching layer also tends to reduce the overall bandwidth of the device, due to its thickness dependence on wavelength. Referring back to Table 2.1, which illustrated the acoustic properties of some common piezoelectric materials with their transmission coefficients into air and water, it can be seen that the transmission losses, in water, are relatively small compared with that for air. Hence, piezoelectric devices are much more suited to immersion applications. However, they have a number of disadvantages. Firstly, the backing layer is only mainly useful in damping the thickness resonance of the piezoceramic, although, radial resonances, especially with PZT, which has a high cross-coupling from thickness to radial modes [3], exist. These generally degrade the performance of such transducers due to non-uniform surface displacements, making prediction of the radiated sound field difficult. A number of methods of reducing these resonances have been tried. Using an alternative piezoelectric material having lower coupling to radial modes is one way, for instance polyvinylindene

difluoride (PVDF). Another suggestion is the addition of a central hole in the ceramic disc to discourage the radial resonance modes.

Capacitive transducers, however, have been found to be an alternative to piezoelectric transducers for use in immersion. One of the first reported demonstrations of electrostatic transducers for immersion operation was by Schodder and Wiekhorst [4] in 1957. Later work by Miller [5,6] examined similar devices using electrets to remove the need of an external bias.

Another device, described by Cantrell et al [7,8], consisted of a 10μm thick tensioned alloy membrane positioned 10μm from a back electrode. The membrane-electrode gap was kept constant with the use of a pneumatic system to adjust the air pressure within the device. A schematic diagram of this electrostatic acoustic transducer, or ESTAT, is shown in Figure 7.2. It was shown to operate over a flat frequency range of 200kHz to 15MHz. However, a disadvantage with the design was that compensation for atmospheric and/or water pressure was required to keep the membrane-electrode gap constant.

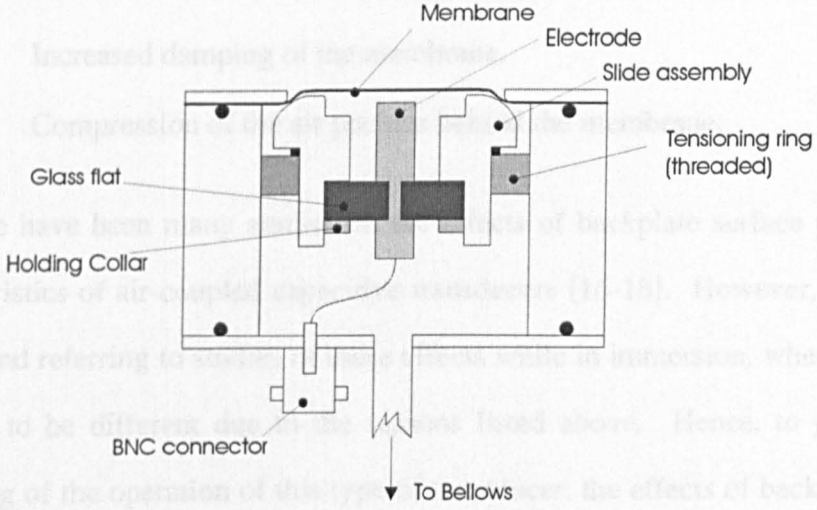

Figure 7.2: *Schematic diagram of the ESTAT transducer (from [7]).*

An alternative capacitive immersion device to those described above was an acoustically transparent capacitance immersion hydrophone described by Clark [9]. This differed to other devices in that they all used air as the compliant medium, whereas this

utilised a 25μm thick solid polymer dielectric (Mylar) between two plates to create an ultrasonic detector. Its sensitivity was found to be independent of frequency.

Preliminary work by Schindel et al [10,11], and Bashford et al [12], demonstrated that capacitive transducers, primarily designed for use in air, could also operate in liquids with extended bandwidth and sensitivity. These devices were of the polymer film / ridged conducting backplate design, described in Chapter 2, and of the type studied in this chapter. More recently, use of fully micromachined silicon based devices in immersion has been reported [13-15]. These devices, constructed with either thin silicon nitride or polysilicon membranes have generally been found to operate in fluids with bandwidths greater than those in air, with up to 20MHz being reported.

The reason for these observed increases in bandwidth is though to be due to the following reasons:

- Improved matching of the membrane to the water (due to similar acoustic impedances).
- Reduced attenuation of the higher frequencies in water.
- Increased damping of the membrane.
- Compression of the air pockets behind the membrane.

There have been many studies on the effects of backplate surface properties on the characteristics of air-coupled capacitive transducers [16-18]. However, no literature could be found referring to studies of these effects while in immersion, where they could be expected to be different due to the reasons listed above. Hence, to gain a better understanding of the operation of this type of transducer, the effects of backplate surface properties on its characteristics are one aspect that is examined in this chapter.

7.3 Transducer design and construction

The design of the transducer was based on previous air-coupled capacitive devices, with the addition of a number of rubber O-ring seals. The transducer(s) were required to be watertight, and provide even clamping of the membrane material. They also needed to be designed to allow easy changing of the membrane. A pair of transducers were constructed, each consisting of a machined aluminium casing, housing a polished aluminium backplate. The backplate being insulated from the case with a nylon inset and internally connected to the centre pin of a waterproof 'N' type RF connecter, positioned on the rear cover of the transducer. The insert/backplate assembly was designed to slide within the housing, thus enabling the backplate to be correctly positioned and then retained by the tightening of a grub screw. The front cover, or aperture, contained one of two O-ring seals used in the device, with the other recessed into the front of the main casing. A threaded hole was also positioned in the main casing, to allow attachment of an optical rod mount. Figure 7.3 shows a cut away schematic diagram of the device. Engineering drawings of the transducer are shown in Appendix C.

After the manufacture of the device, all parts were washed in acetone, and cleaned with compressed air to remove any remaining dirt/dust particles. They were then assembled; firstly, with the backplate/insulator components then the rear cover and RF connector were screwed in place, using a silicone-based sealant to ensure water tightness. The O-rings were lightly covered with silicone grease, and placed into their respective housings. A dc bias (~50 V) was then applied, and a 3.5μm thick metallised Mylar membrane was placed onto the polished backplate. The front aperture was then screwed

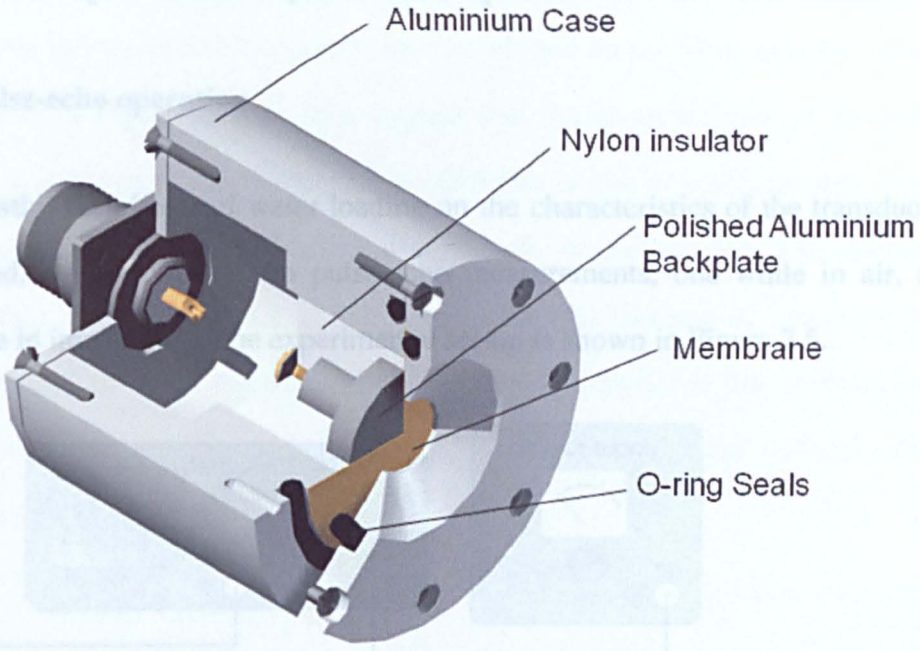

Figure 7.3: *Cut-away schematic diagram of the capacitive immersion transducer.*

into place. The application of the dc bias during assembly ensured that no (large) air bubbles were trapped between the membrane and backplate. The transducer was then ready for use. Figure 7.4 shows a photograph of the fully assembled device (with an optical rod fitted).

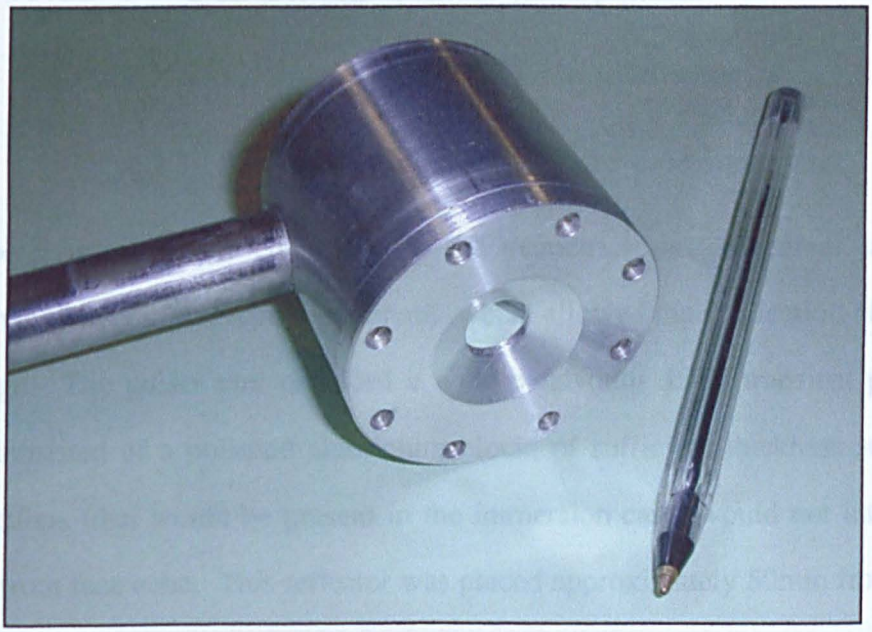

Figure 7.4: *Photograph of the fully assembled immersion transducer.*

7.4 Initial experiments – pulse echo operation in air and water.

7.4.1 Pulse-echo operation

Firstly, the effects of water loading on the characteristics of the transducer were investigated, by performing two pulse-echo measurements, one while in air, and the other while in immersion. The experimental set-up is shown in Figure 7.5.

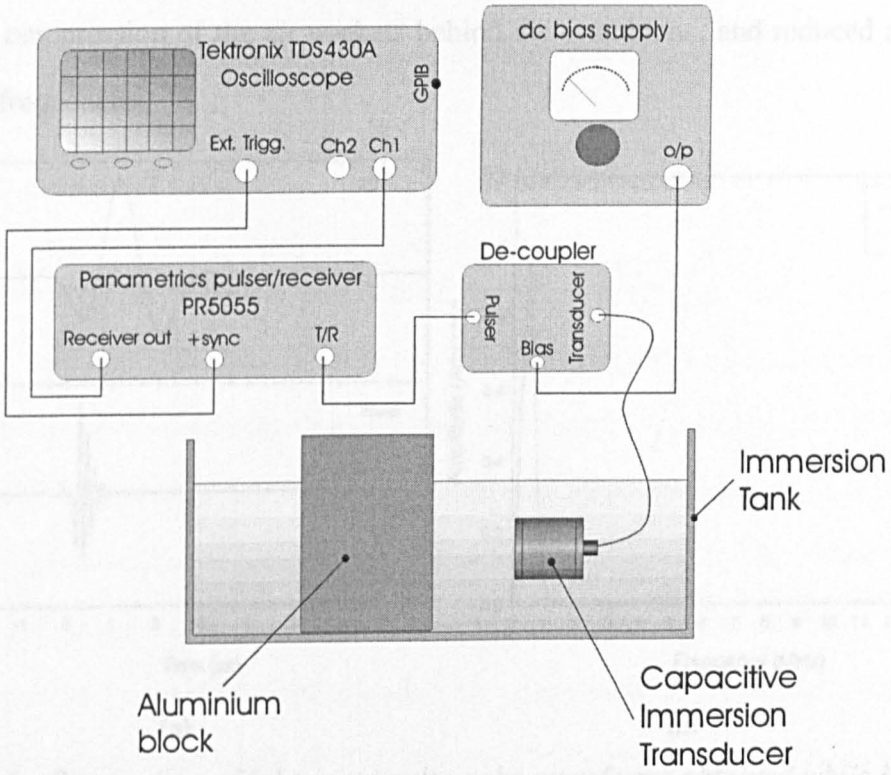

Figure 7.5: *Schematic diagram of the pulse-echo apparatus.*

The transducer was connected to a Panametrics pulser/receiver unit (model 5055PR), via a capacitive decoupling circuit, which allowed the application of a 100V dc bias voltage. The pulser unit provided a wide bandwidth 350V transient pulse. The reflector consisted of a polished aluminium block, of sufficient thickness so that back wall reflections (that would be present in the immersion case) would not interfere with the initial front face echo. This reflector was placed approximately 50mm from the front face of the transducer, and carefully aligned to give the largest amplitude received signal.

Figure 7.6(a) shows typical pulse-echo waveforms obtained while in air and water. Their corresponding frequency spectra, plotted on the same axis for comparison, are displayed in Figure 7.6(b). It is evident that the characteristics of the pulse-echo system have changed appreciably, with a –6dB bandwidth of approximately 800kHz in air, compared to >2MHz in immersion. Peak frequency has also shifted from approximately 500kHz to 6MHz. The reasons for this increase in frequency response can be attributed to better matching of the membrane material to the medium, increased damping, compression of the air pockets behind the membrane, and reduced attenuation of higher frequencies.

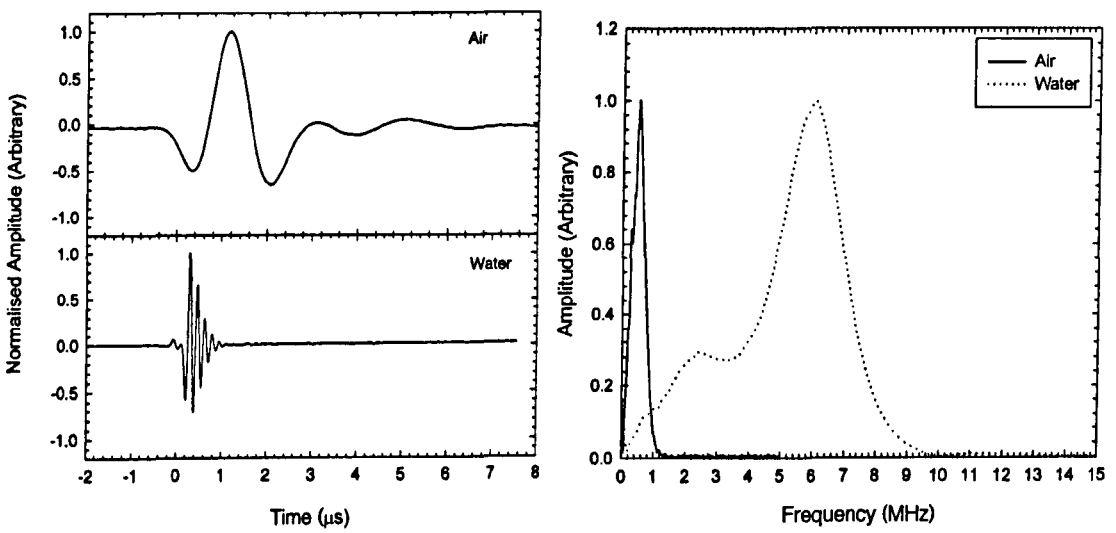

Figure 7.6: *Comparison of (a) typical pulse-echo waveforms obtained while in air and water, and (b) their corresponding frequency spectra.*

7.5 The effects of backplate surface properties: Random metallic backplates.

7.5.1 Background

As stated in the introduction, there have been many studies conducted examining the effect of backplate surface topology on the characteristics of capacitive transducers

while air-loaded. However, no such studies could be found for capacitive transducers when used in immersion, where differences due to the effects of water loading may occur. Therefore, it was decided that such an investigation was merited in this area.

This section investigates the relationship (if any) between the bandwidth / sensitivity of the immersion transducer, and its backplate surface properties. For this study, a number of backplates with different surface roughness' were manufactured. These were then fitted in the immersion transducer, which was then characterised as a source and detector. Comparisons of the results were then made.

7.5.2 Transducer modification.

To perform the study of the effect of backplate surface properties, the transducer required a small modification so that the backplate could be changed easily. The roughened backplates (described below) were fabricated from brass scanning electron microscope (SEM) sample holders. These were a 12.5mm diameter by 3mm thick brass disc with a 2.5mm diameter, 10mm long pin extending from its centre on one side. The original polished backplate was drilled with a central hole to allow the 'pin' of the SEM sample holder to be inserted, thus allowing easy replacement of the backplate without having to disassemble the whole device. Figure 7.7 illustrates the modification made to one of the immersion transducers.

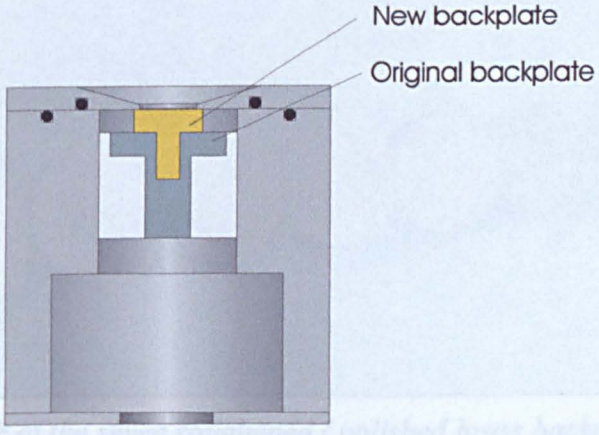

Figure 7.7: *Modification made to the immersion transducer.*

7.5.3 Manufacture of random metallic backplates

To create a variety of backplates with different surface characteristics, a range of grades of silicon carbide (SiC) paper were used to grind/polish the surface of the SEM sample holders. In total seven backplates were produced. Firstly, all the backplates were ground flat, using a Metaserv 2000 universal grinding/polishing machine fitted with a #400 SiC paper disc (the coarsest available on the machine). Three of these backplates were then put to one side, while the remaining four were then ground using a finer #600 SiC paper disc. Of these four, one was removed, and the remaining three were then ground with #1200 paper. Again, one was kept back and the remaining two were polished using #4000 SiC paper. Finally, one of these was then polished with 0.04μm OP-U polishing paste. With exception of the OP-U polishing stage, water was used throughout as a lubricant. To make backplates with a coarser finish than that was available on the grinding/polishing machine, two of the three backplates previously put to one side after the initial #400 stage, were ground (by hand) using #80 and #150 grade SiC paper, using a glass block to ensure flatness. All seven backplates were then placed into a heated ultrasonic bath for 10 minutes to remove any debris. They were then washed with acetone and dried with a compressed air jet. Figure 7.8 shows a photograph of the completed backplates.

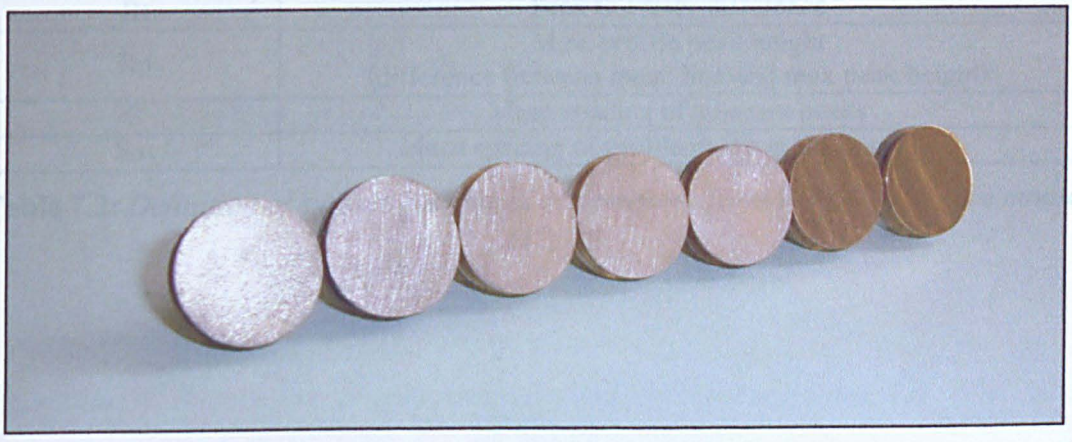

Figure 7.8: *Photograph of the seven roughened / polished brass backplates (#80 left through to #0.04 furthest right).*

The surface properties of the backplates were then measured using a Wyko optical surface profiler. Table 7.1 shows a summary of the main surface properties, with definitions of each of these outlined in Table 7.2. The Wyko surface profiler images of the backplates (2.4mm x 1.8mm section) are shown in Figure 7.9 as greyscale images, together with their corresponding scales.

Backplate	Ra (nm)	Rq (nm)	Rt (μm)	Rp (μm)	S (μm)	Sm (μm)
#80	1034.0	1179.0	7.84	3.58	22.3	64.9
#150	510.4	674.7	4.57	1.85	19.6	47.6
#400	254.4	325.2	2.02	0.855	17.3	36.5
#600	158.3	203.2	1.32	0.560	16.4	31.5
#1200	131.5	177.6	1.19	0.530	15.8	25.3
#4000	27.2	36.5	0.268	0.108	18.5	27.3
#0.04	21.6	32.9	0.243	0.0620	20.8	53.9

Table 7.1: *Surface properties of manufactured random backplates.*

Surface parameter	Definition
Ra	Average roughness
Rq	RMS roughness
Rt	Peek to valley difference
Rp	Max. profile peak height (difference between mean line and max peak height)
S	Mean spacing of adjacent peaks
Sm	Mean spacing of profile peaks at the mean line

Table 7.2: *Definition of surface roughness parameters (from WYKO reference manual [19])*

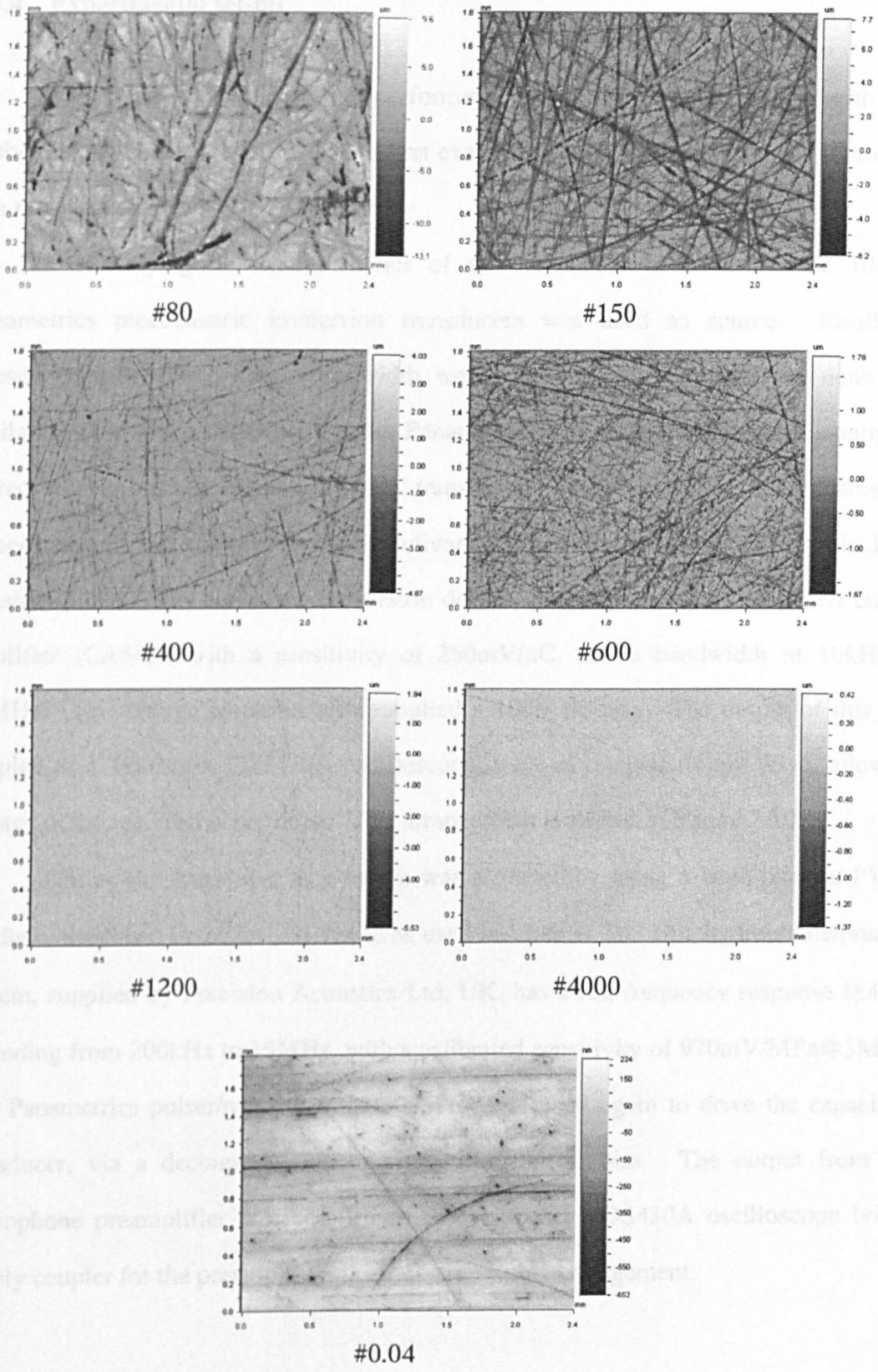

Figure 7.9: *WYKO surface profiler images of the random backplates (SiC paper grade as shown)*

7.5.4 Experimental set-up

Two main experiments were performed to characterise the transducer with each of the different backplates fitted. The first examined the characteristics of the transducer as a receiver, and the second as a source.

For studying the characteristics of the transducer as a detector, a 10MHz Panametrics piezoelectric immersion transducers was used as source. Ideally, a transducer with a very large bandwidth would have been used, however none was available so it was decided to use the Panametrics immersion sources and attempt to correct for its response later. These transducers were driven by the Panametrics pulser/receiver unit (5055PR), which delivers a short duration wide bandwidth 350V transient pulse. The capacitive immersion device was connected to a Cooknell charge amplifier (CA6/C), with a sensitivity of 250mV/pC, and a bandwidth of 10kHz to 10MHz. This charge amplifier also supplied a 100V dc bias. The output of this was coupled to a Tektronix TDS430A oscilloscope, with an integral floppy drive, allowing storage of the received waveforms. This arrangement is shown in Figure 7.10.

Testing the transducer as a source was achieved by using a 1mm circular PVDF needle hydrophone detector [20] (same as used in Chapter 3). This hydrophone/preamp system, supplied by Precision Acoustics Ltd, UK, has a flat frequency response (±4dB) extending from 200kHz to 15MHz, with a calibrated sensitivity of 970mV/MPa@3MHz. The Panametrics pulser/receiver unit (5055PR) was used again to drive the capacitive transducer, via a decoupling box to apply a 100V dc bias. The output from the hydrophone preamplifier was coupled to the Tektronix TDS430A oscilloscope (via a supply coupler for the preamp). Figure 7.11 shows this arrangement.

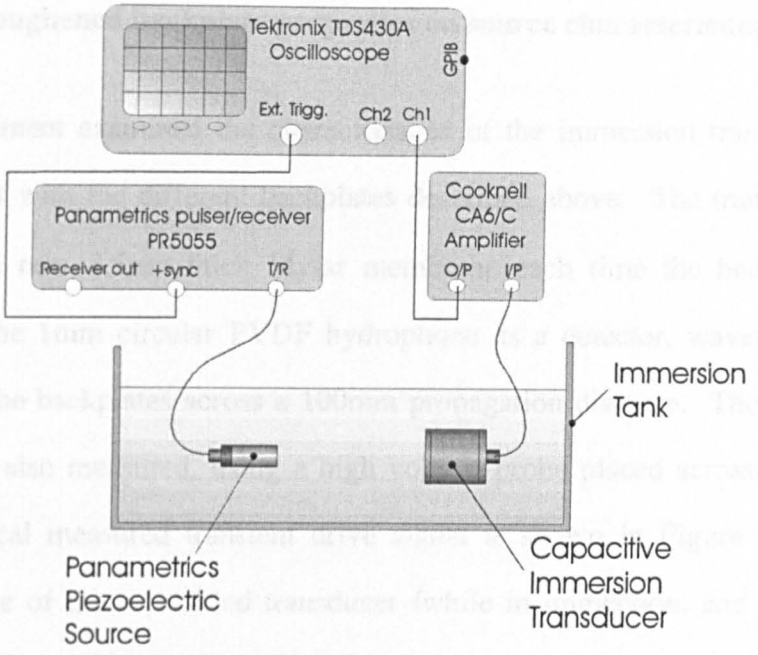

Figure 7.10: *Immersion transducer receiver experiment; schematic diagram of the experimental apparatus*

The separation of the transducers used in both the experiments above was 100mm (±1mm), ensuring that the receiver was positioned in the far field region of the source transducer. They were also carefully aligned to give a maximum amplitude / frequency of the received signal.

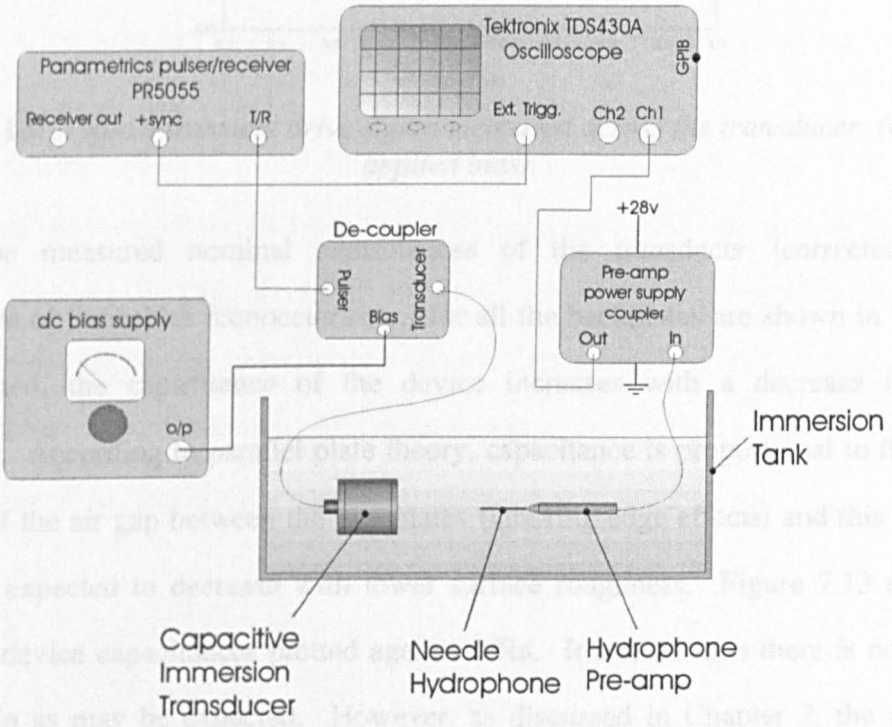

Figure 7.11: *Immersion transducer source experiment; schematic diagram of the apparatus.*

7.5.5 Effect of roughened backplate properties on source characteristics

This experiment examined the characteristics of the immersion transducer as a source, when fitted with the different backplates described above. The transducer was assembled using a new 3.5μm thick Mylar membrane each time the backplate was changed. Using the 1mm circular PVDF hydrophone as a detector, waveforms were taken for each of the backplates across a 100mm propagation distance. The transducer drive signals were also measured, using a high voltage probe placed across the device terminals. A typical measured transient drive signal is shown in Figure 7.12. The nominal capacitance of the assembled transducer (while in immersion, and without an applied bias) was also measured using a Wavetek capacitance meter (model CM-20A).

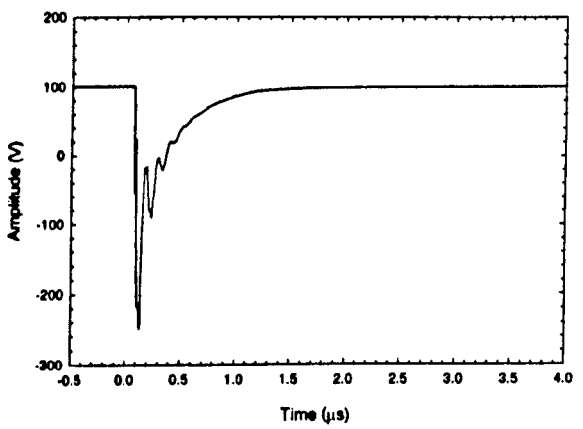

Figure 7.12: *Typical transient drive signal measured across the transducer. (with 100V applied bias)*

The measured nominal capacitances of the transducer (corrected for the capacitance of the cables /connectors etc.) for all the backplates are shown in Table 7.3. As expected, the capacitance of the device increases with a decrease in surface roughness. According to parallel plate theory, capacitance is proportional to the inverse distance of the air gap between the two plates (ignoring edge effects) and this mean gap would be expected to decrease with lower surface roughness. Figure 7.13 shows the measured device capacitances plotted against 1/Ra. It can be seen there is not a linear relationship as may be expected. However, as discussed in Chapter 2, the capacitive transducer with a roughened backplate is far more complex, and does not possess an

accurately defined air gap. A further literature search on this problem revealed that no simple linear relationship exists between the backplate surface properties and the device capacitance.

Backplate	Capacitance (pF ±10pF)
#80	171.0
#150	238.0
#400	280.0
#600	299.0
#1200	322.0
#4000	414.0
#0.04	495.0

Table 7.3: *Measured nominal device capacitances.*

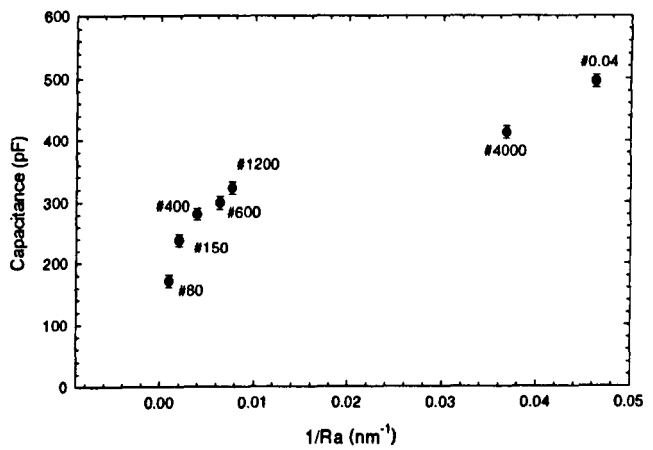

Figure 7.13: *Measured nominal capacitance of device fitted with the backplates as shown, plotted against 1/Ra.*

A typical received waveform from the transducer when fitted with the #0.04 backplate is shown in Figure 7.14(a). This shows a reasonably damped signal has been produced. Figure 7.14(b) shows a waveform where the capacitive transducer was replaced by a 10MHz Panametrics piezoelectric immersion source. Comparison of the two waveforms reveals they have comparable signal amplitudes, hence similar acoustic pressures have been produced.

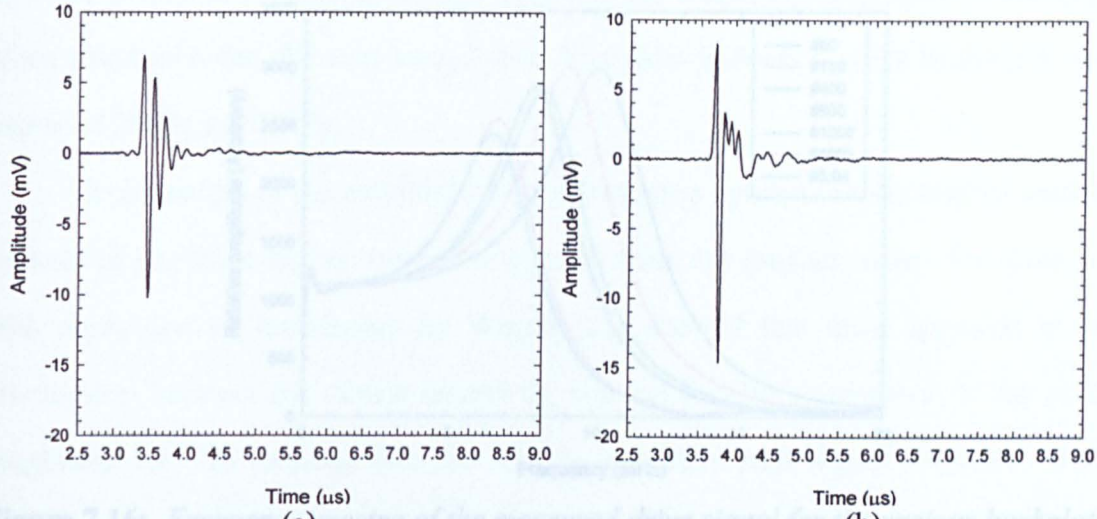

Figure 7.14: *Typical received waveforms from the 1mm circular PVDF hydrophone when positioned 100mm from (a) the capacitive immersion source fitted with the #0.04 backplate and a 3.5μm Mylar membrane, and (b) 10MHz Panametrics piezoelectric immersion transducer.*

Figure 7.15 shows a comparison of the frequency spectra from all the backplates. Note that the waveforms themselves are not shown, as they are all very alike. Examination of the frequency spectra reveals that there appears to be some relationship between the amplitude and peak frequencies, and the backplate properties, with smoother backplates producing a lower peak frequency and higher amplitude. However, inspection of the measured drive signals, whose frequency spectra are shown in Figure 7.16, reveals that their characteristics are also different for the different backplates. This

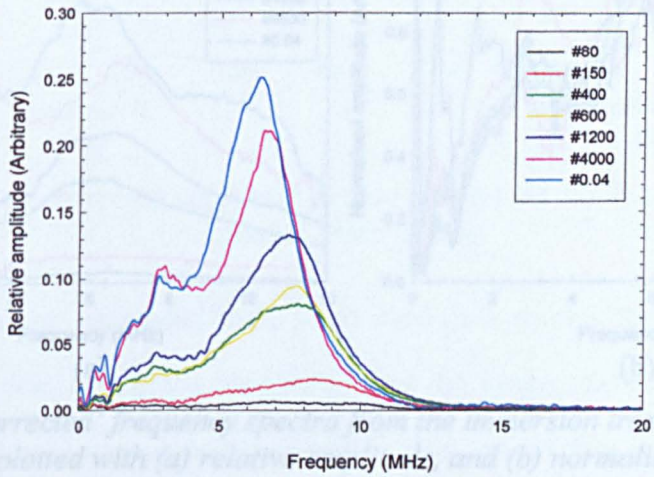

Figure 7.15: *Comparison of the frequency spectra of the waveforms from the immersion transducer fitted with the various backplates.*

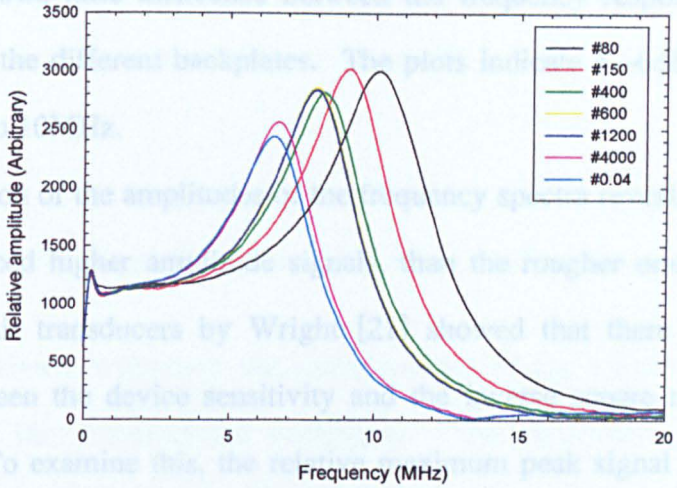

Figure 7.16: *Frequency spectra of the measured drive signal for the various backplates.*

was thought to be due to the variations of capacitance of the devices changing the load impedance on the pulser unit. In an attempt to remove this effect, the frequency spectra of the received waveforms were each 'normalised' by their respective drive signal frequency spectra. The results of these 'corrected' frequency spectra are shown in Figure 7.17, plotted with relative amplitude (a), and normalized amplitude (b). Note that these were only plotted up to 12MHz, due to numerical errors arising from the correction operation above this frequency. They are also visibly very noisy. However, examination

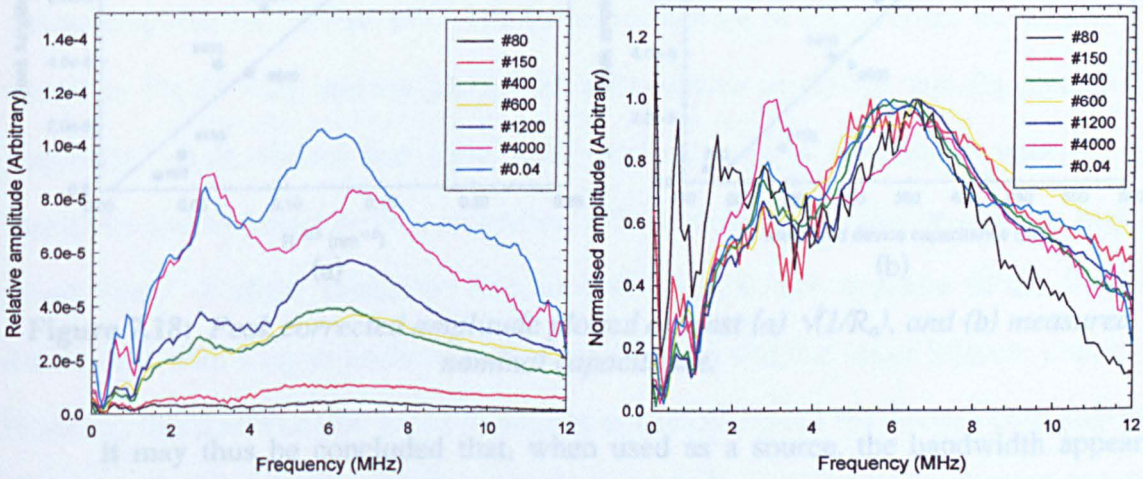

Figure 7.17: *'Corrected' frequency spectra from the immersion transducer (when used as a source) plotted with (a) relative amplitude, and (b) normalised amplitude.*

of these plots shows little difference between the frequency responses of the system when fitted with the different backplates. The plots indicate a –6dB bandwidth in the region of 2MHz to 10MHz.

Examination of the amplitudes of the frequency spectra reveals that the smoother backplates produced higher amplitude signals, than the rougher ones. Previous work with capacitive air transducers by Wright [21] showed that there appeared to be a relationship between the device sensitivity and the inverse square root of the surface roughness, Ra. To examine this, the relative maximum peak signal amplitude of each backplate, from Figure 7.17(a), were plotted against $1/\sqrt{R_a}$. They were also plotted against the nominal device capacitance for comparison. These are shown in Figure 7.18(a & b). There would appear to be a linear relationship in both plots, with a slightly better fit in the plot against capacitance. This is revealed by examination of the least squares best fits coefficients of determination, R^2 of 0.942 and 0.964 for the $1/\sqrt{R_a}$ and capacitance plots respectively.

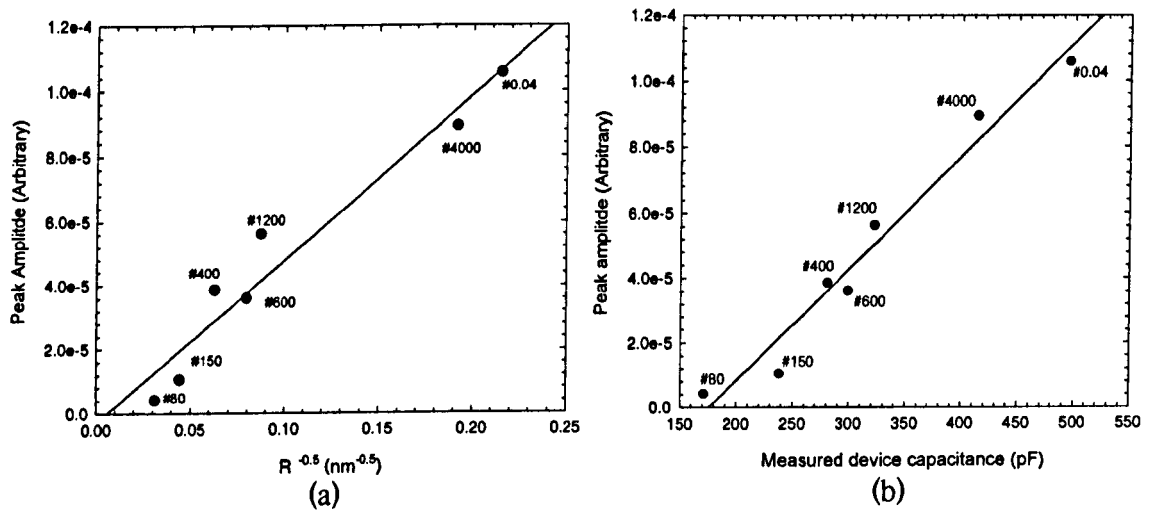

Figure 7.18: *Peak corrected amplitude plotted against (a) $\sqrt{(1/R_a)}$, and (b) measured nominal capacitance.*

It may thus be concluded that, when used as a source, the bandwidth appears relatively independent of surface roughness over the range studied, but that smoother surfaces result in larger transmitted amplitudes. The latter effect is probably due to the smaller gap between the electrodes. The bandwidth observation differs from those

reported in air [21, 22], and is thought to be due to the water loading, which dampens the membrane response and becomes the dominant effect. This will be discussed further below.

7.5.6 Effect of backplate surface properties when used as a receiver

This experiment examined the characteristics of the transducer as a receiver, when fitted with the manufactured backplates. The experimental set-up has been described previously (Figure 7.10). Firstly, the capacitive transducer as assembled with the #80 backplate, and a 3.5μm Mylar membrane. It was then connected to the Cooknell charge amplifier (sensitivity 250mV/pC, bandwidth 10Hz to 10MHz), and a 100V bias was applied. The transducers were positioned 100mm (±1mm) apart. Waveforms were then taken of the signal received by the immersion transducer for both sources. This was repeated for each of the backplates, again renewing the membrane each time.

A typical waveform from the transducer when fitted with the #0.04 backplate and positioned 100mm from the 10MHz piezoelectric source is shown in Figure 7.19. This shows a high amplitude, well-damped signal. Note that this was taken without signal averaging, demonstrating the high signal to noise ratio (typical noise from the Cooknell charge amplifier ~1.1mV pk-pk). The frequency spectra of the received waveforms are shown in Figure 7.20, and are plotted (a) with relative amplitude, and (b) normalised amplitude. It is evident that there again appears to be a relationship between the sensitivity and backplate surface properties, with smoother backplates resulting in higher sensitivities. A slight change in frequency response is also apparent in the 10MHz source case, with rougher backplates appearing to have a higher upper frequency cut-off. However, this could be due to the variations in capacitance of the devices changing the upper cut-off frequency (specified as 10MHz) of the charge amplifier, indicating that the upper frequency limit is restricted by the amplifier itself, and not by the transducer.

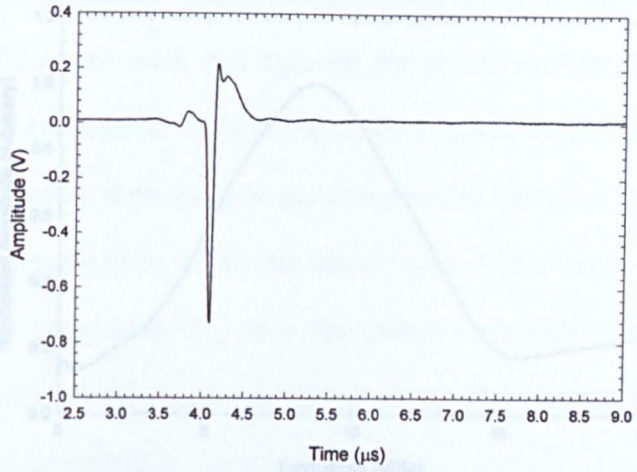

Figure 7.19: *Typical waveform received by the capacitive immersion transducer, fitted with the #0.04 backplate positioned 100mm from a 10MHz Panametrics piezoelectric transducer.*

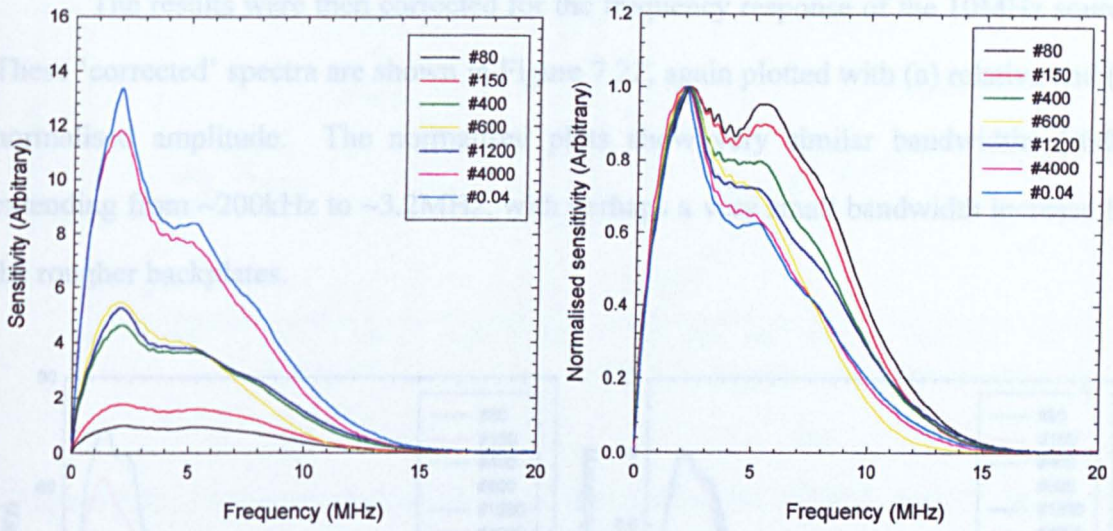

Figure 7.20: *Comparison of frequency spectra of the waveforms received by the immersion transducer when fitted with different backplates. (10MHz Panametrics piezoelectric immersion source). Plotted with (a) relative sensitivity, and (b) normalised sensitivities.*

The pulse-echo waveform from the 10MHz Panametrics immersion transducer was also taken during the experiment. This was so that its characteristics could be corrected, in an attempt to resolve the true receiver characteristics of the capacitive immersion transducer. As this waveform was the pulse-echo response, the square root of its corresponding frequency spectrum was calculated. This, assuming a truly reversible transducer, results in the 'one-way' frequency response of the device. This is shown in Figure 7.21.

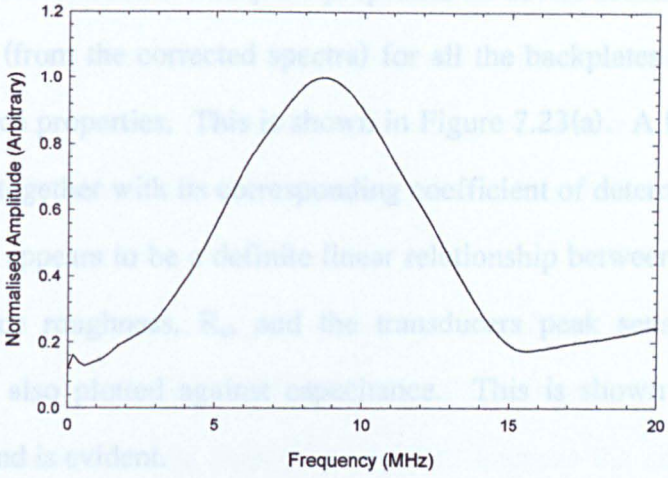

Figure 7.21: *Normalised square root of the frequency spectra of the measured pulse-echo waveform from the 10MHz, Panametrics piezoelectric immersion transducer.*

The results were then corrected for the frequency response of the 10MHz source. These 'corrected' spectra are shown in Figure 7.22, again plotted with (a) relative and (b) normalised amplitude. The normalised plots show very similar bandwidths (-6dB) extending from ~200kHz to ~3.2MHz, with perhaps a very small bandwidth increase for the rougher backplates.

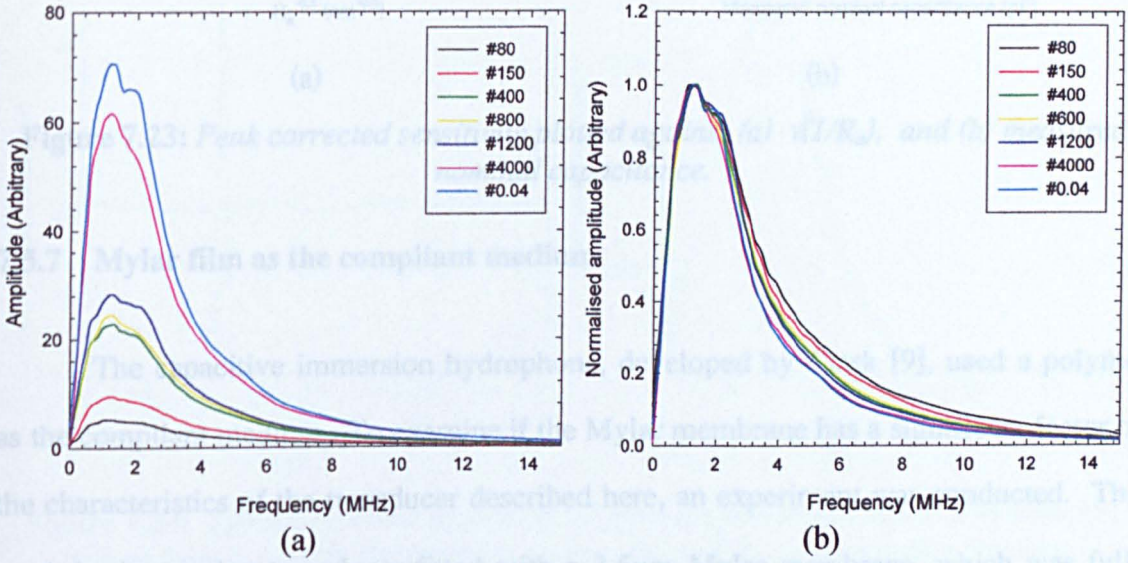

Figure 7.22: *Comparison of the 'corrected' received frequency spectra from the immersion transducer when fitted with different backplates. Plotted with (a) relative sensitivity and (b) normalised sensitivity.*

To examine the effect of backplate properties on device sensitivity, the maximum peak sensitivities (from the corrected spectra) for all the backplates were plotted firstly against their surface properties. This is shown in Figure 7.23(a). A line of least squares best fit is shown, together with its corresponding coefficient of determination, R^2. It can be seen that there appears to be a definite linear relationship between the inverse square root of the surface roughness, R_a, and the transducers peak sensitivity. The peak sensitivities were also plotted against capacitance. This is shown in Figure 7.23(b). Again, a linear trend is evident.

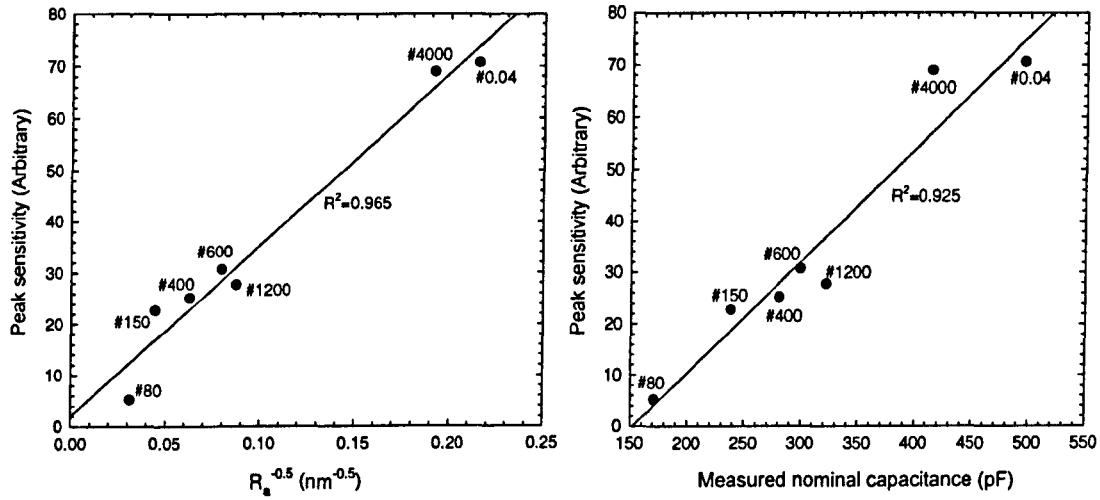

Figure 7.23: *Peak corrected sensitivity plotted against (a) $\sqrt{(1/R_a)}$, and (b) measured nominal capacitance.*

7.5.7 Mylar film as the compliant medium

The capacitive immersion hydrophone, developed by Clark [9], used a polymer as the compliant medium. To examine if the Mylar membrane has a significant factor on the characteristics of the transducer described here, an experiment was conducted. This used the immersion transducer fitted with a 3.5μm Mylar membrane, which was fully metallised on its front surface, and also partly on the rear, over the area where the backplate would normally contact. This effectively shorted out the effect of the backplate, and any signal was due to the effects within the membrane.

Firstly, the transducer was tried as a source (using the experimental set-up described above). However, this proved unsuccessful with no measurable signal being produced. It was then tested as a detector, again using the experimental set-up described previously. A 100V bias was applied, and the 10MHz Panametrics piezoelectric transducer was used as a source.

Figure 7.24 displays a typical received waveform and its corresponding frequency spectra. The waveform shows a highly damped signal. Note, however, that it has very low amplitude and was highly averaged to improve the signal to noise ratio. This low amplitude indicates that the contribution of the compression of the Mylar film is insignificant when compared to the amplitudes of the signals received with air (and the membrane) as the compliant medium (see above). The frequency spectra shows a wide bandwidth response, similar to that of the calculated one-way response of the 10MHz piezoelectric source (Figure 7.21(b)), implying it has greater bandwidth than this.

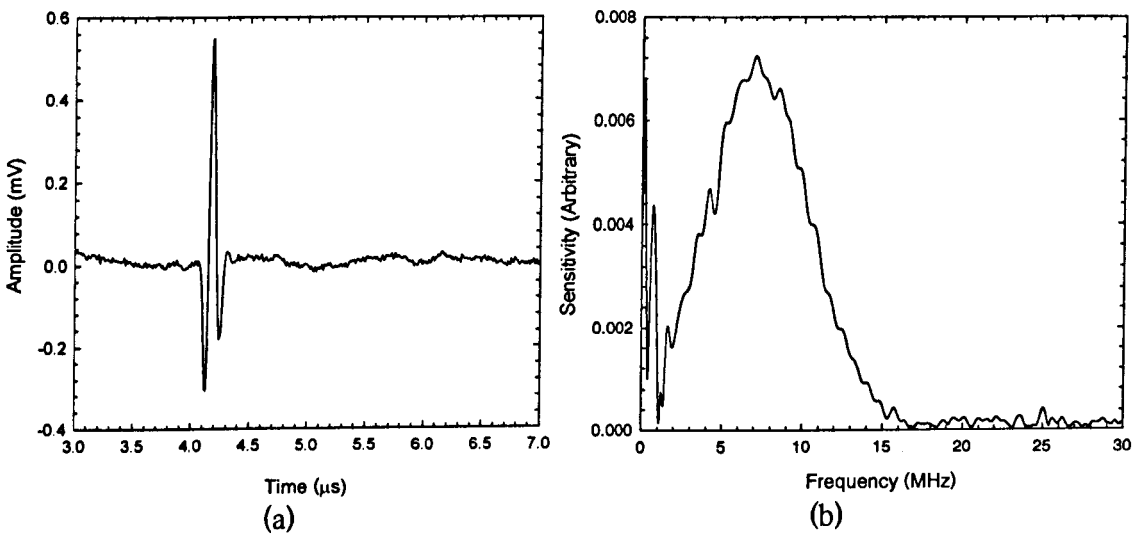

Figure 7.24: *Typical received waveform (a) from the metallised Mylar film detector, 100mm from a 10MHz Panametrics source, (b) and its corresponding frequency spectrum.*

7.5.8 Effects of applied bias

This experiment examined the effect of applied bias on the characteristics of the transducer. The device was fitted with the #1200 backplate and a 3.5μm thick Mylar film. It was used as a source, with the 1mm circular PVDF hydrophone as a receiver. A variable dc power supply with a maximum output of 1kV was used to supply the bias voltage, via the capacitive de-coupling circuit.

Waveforms were taken as the bias voltage was ramped up in 50V steps. At approximately 700V arcing of the membrane occurred so the experiment was halted. It was then repeated again, after replacement the membrane with a thicker 5μm Mylar film. Arcing again occurred, this time at approximately 800V.

Figure 7.25 shows the peak-peak amplitude of the received signals from the 3.5μm, and the 5μm membrane, plotted as a function of bias voltage. It is evident that there appears to be a maximum amplitude for both membranes, with, as expected, greater signal amplitude from the thinner 3.5μm filmed device. A slight drop in the amplitude for the 5μm film at 50V bias can also be seen. This was assumed to be due to residual charge on the membrane, caused by polarisation. The slight decrease in amplitude as the bias is increased in excess of 300V could also be attributed to the film polarising during the experiment. Figure 7.26 displays a comparison of the frequency spectra from the received waveforms for a selection of applied bias voltages, plotted with relative amplitudes. There appears to be a slight shift in the peak frequencies, being lower for the higher bias voltages. However, examination of the drive signal spectra (Figure 7.27) shows that this frequency shift is again partly due to changes in the drive signal. The spectra were then corrected for their corresponding drive signal. The resultant spectra are displayed in Figure 7.28. Note that above approximately 15MHz errors arise due to the correction operation. From these corrected spectra, there appears to be little change in the frequency response of the device for all of the applied bias voltages. The effect of water loading would again appear to be a dominant feature of the response.

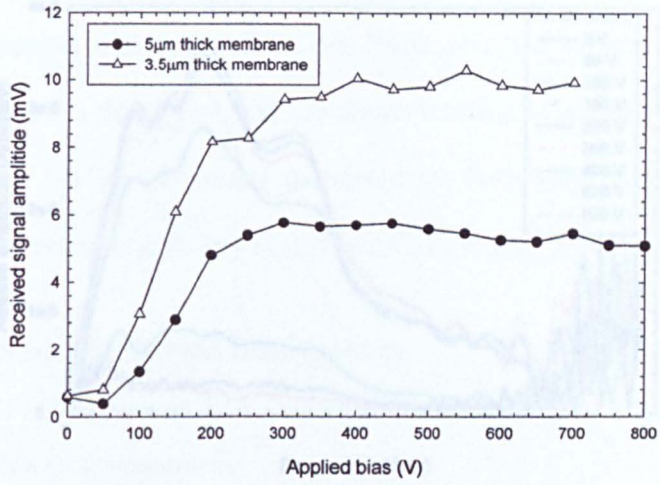

Figure 7.25: *Received signal amplitude (pk-pk) as a function of applied bias voltage, when fitted with a #1200 backplate. Membrane thickness as shown.*

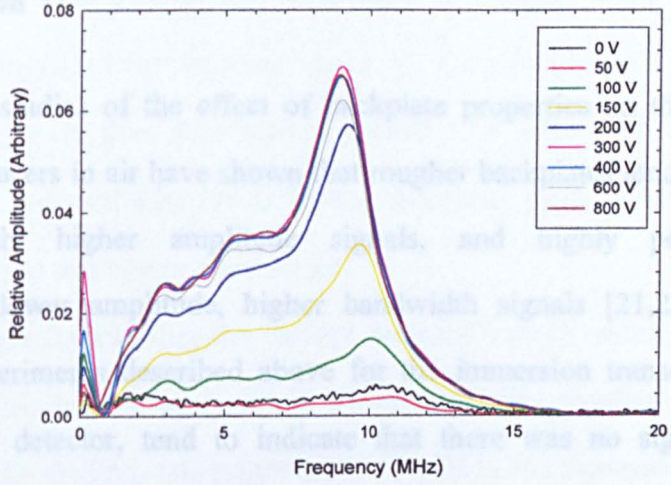

Figure 7.26: *Frequency spectra of the received signals from a capacitive immersion source fitted with a #1200 backplate and a 5μm Mylar film. Applied bias as shown.*

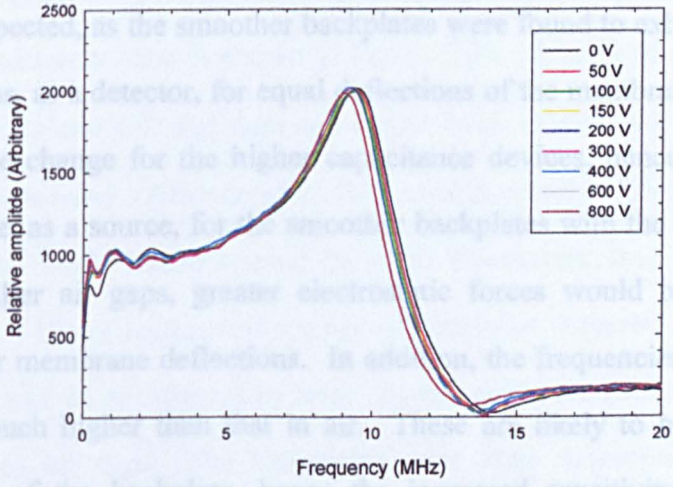

Figure 7.27: *Frequency spectra of measured transient pulse across the transducer, from the Panametrics pulser/receiver unit (5055PR) for the applied bias as shown.*

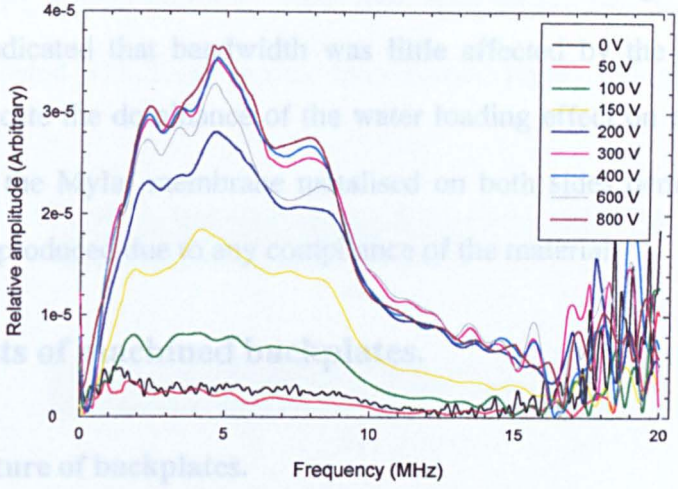

Figure 7.28: *Comparison of the frequency spectra corrected for their corresponding drive signal. Applied bias as shown.*

7.5.9 Discussion

Previous studies of the effect of backplate properties on the characteristics of capacitive transducers in air have shown that rougher backplates tend to produce/receive lower bandwidth, higher amplitude signals, and highly polished backplates produce/receive lower amplitude, higher bandwidth signals [21,22]. However, the results from experiments described above for the immersion transducer, operating as both source and detector, tend to indicate that there was no significant change in frequency response for the different backplates. Conversely, the experiments demonstrated significant amplitude/sensitivity increases for the smoother backplates. This could be expected, as the smoother backplates were found to exhibit higher nominal capacitance. Thus, as a detector, for equal deflections of the membrane there would be a larger capacitance change for the higher capacitance devices, hence producing greater signals. Likewise, as a source, for the smoother backplates with the higher capacitance, thus with a smaller air gaps, greater electrostatic forces would be produced, hence resulting in larger membrane deflections. In addition, the frequencies observed in water immersion are much higher than that in air. These are likely to be generated by the 'flatter' sections of the backplate, hence the increased sensitivity observed for the smoother backplates.

The results of the study on the effect of bias voltage on the transducer characteristics indicated that bandwidth was little affected by the applied bias. This would again indicate the dominance of the water loading effect on the membrane. The experiment with the Mylar membrane metalised on both sides demonstrated that little effects would be produced due to any compliance of the material.

7.6 The effects of machined backplates.

7.6.1 Manufacture of backplates.

These backplates were again manufactured using SEM sample holders. Firstly, all the backplates were ground flat with #400 SiC paper, using the Metaserv 2000 universal polishing/grinding machine used to manufacture the random roughness backplates. They were then successively ground with finer grades of SiC paper until they were finally polished with OP-U 0.04μm polishing paste. They were then washed in acetone, and dried in a compressed air jet.

The process for creating the surface features was by using a photoresist layer, where a pit or hole was defined simply by exposing the required area to a UV light source and then developing, this removing the resist in the exposed area. The depth of the hole was hence controlled by the thickness of the photo resist layer. To make the surface conducting, the last process step was an evaporation of a gold layer.

The fabrication process is shown in Figure 7.29. A layer of photoresist was first spun onto the backplates (a), and then soft-baked in an oven at 90°C for 5 minutes (to drive off the solvent base). After cooling, they were exposed to UV light, for 6 seconds, through an optical mask (manufactured by PPM Photomask Inc., Canada) (b). This contained 10mm x 10mm sections of a range of size holes, squares, lines etc. For these experiments, a range of circular holes were chosen, with one backplate left unexposed for comparison to the rest. The backplates were then developed by immersing in developer for 20 seconds, and then washed in distilled water (c). A hard bake was then

performed at 180°C for 20 minutes. They were then loaded into an Edwards Auto 306 evaporator and coated with 20nm chrome (an adhesion layer), followed by 80nm of gold (d).

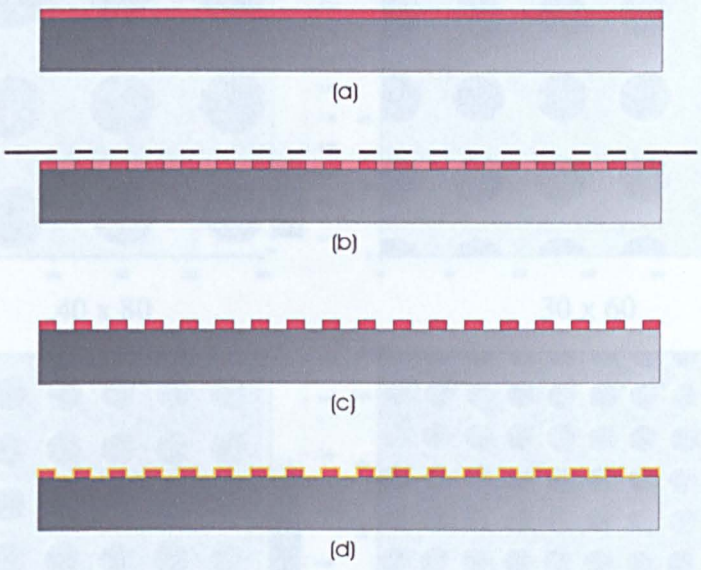

Figure 7.29: *Fabrication process of machined photo resist backplates.*

A total of six backplates were produced, one without any etched pits, the others using masks with holes of 40μm x 80μm (diameter x pitch), 30μm x 60μm, 20μm x 40μm, 15μm x 30μm, and 10μm x 20μm.

Figure 7.30 shows Wyko surface profiler images of sections of the backplates. It can be seen that holes with well-defined edges have been produced for all the mask sizes. Table 7.4 shows the measured sizes of the hole diameter, spacing, and depth for each of the backplates, together with the calculated hole area, hole volume, total flat area, and total hole volume. It is evident that the holes are slightly larger than that defined by the masks. This may be due to diffraction of the UV light through the mask, or slight overexposure of the photo resist. The hole spacing however agrees with that of the mask used.

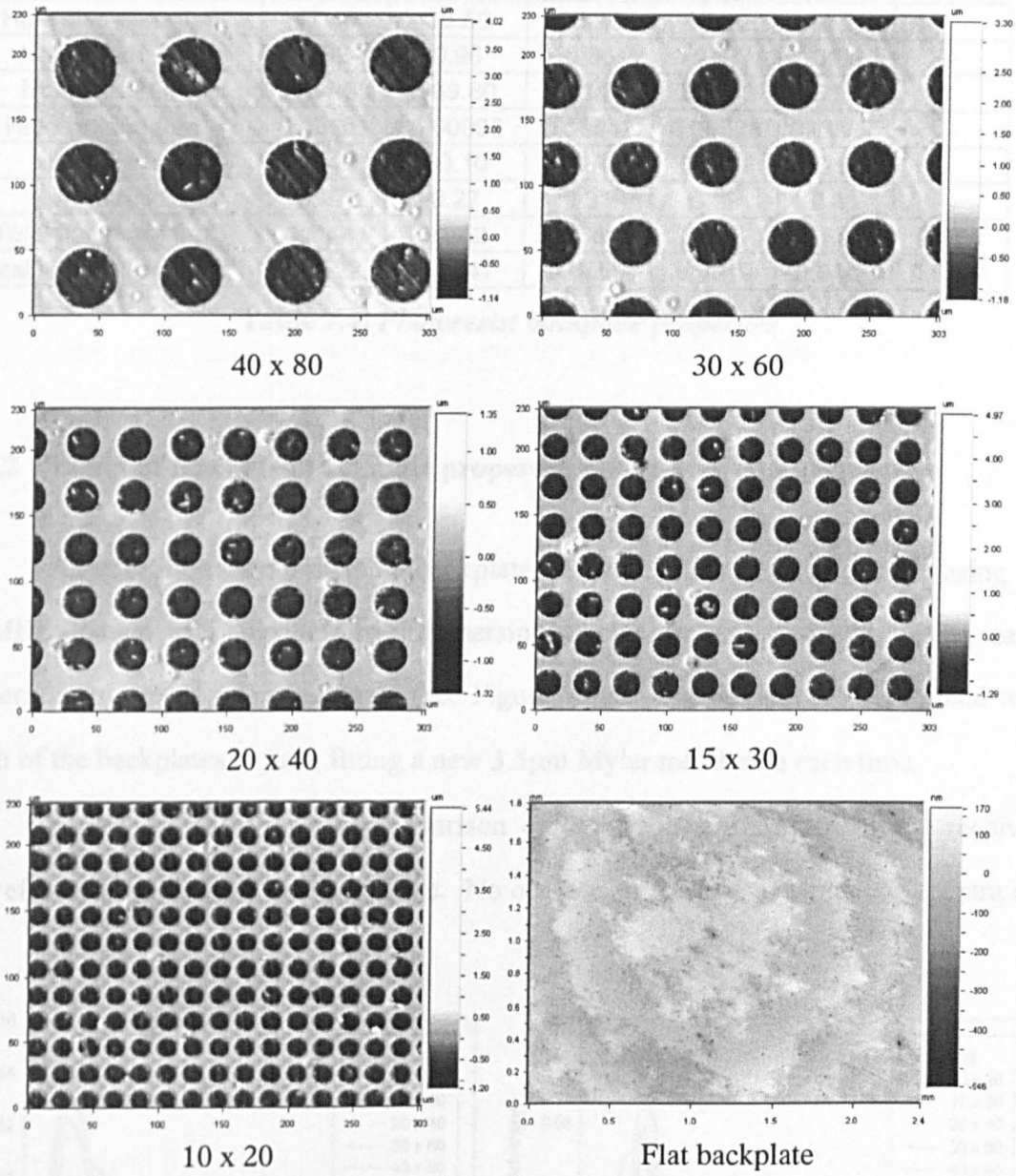

Figure 7.30: *WYKO surface profiler images of all the photoresist backplates.*

Measurement	Device					
	40x80	30x60	20x40	15x30	10x20	Flat
Hole diameter (μm)	47.40	35.50	25.20	19.20	14.10	-
Hole depth (μm)	0.92	0.96	0.85	0.97	0.95	-
Hole area (nm^2)	1764.60	989.80	498.76	289.53	156.14	
Hole volume (μm^3)	0.00161	0.00095	0.00042	0.00028	0.00015	-
Hole spacing	80.40	60.10	39.90	30.20	19.60	-
Area ratio	0.27	0.27	0.31	0.32	0.41	-
Total flat area (mm^2)	21.44	21.52	24.61	24.93	31.92	78.54
Total hole volume (μm^3)	0.0522	0.0547	0.0459	0.0519	0.0441	0.0000

Table 7.4: *Photoresist backplate properties*

7.6.2 Effect of machined backplate properties on receiver characteristics

As with the random metallic backplates, they were tested as a receiver using the 10MHz Panametrics piezoelectric immersion transducer as a source. The same experimental set-up was used again (see Figure 7.10). The device was assembled with each of the backplates in turn, fitting a new 3.5μm Mylar membrane each time.

Figure 7.31(a) shows a comparison of the frequency spectra of the received waveforms from each of the backplates. No obvious differences between the spectra are

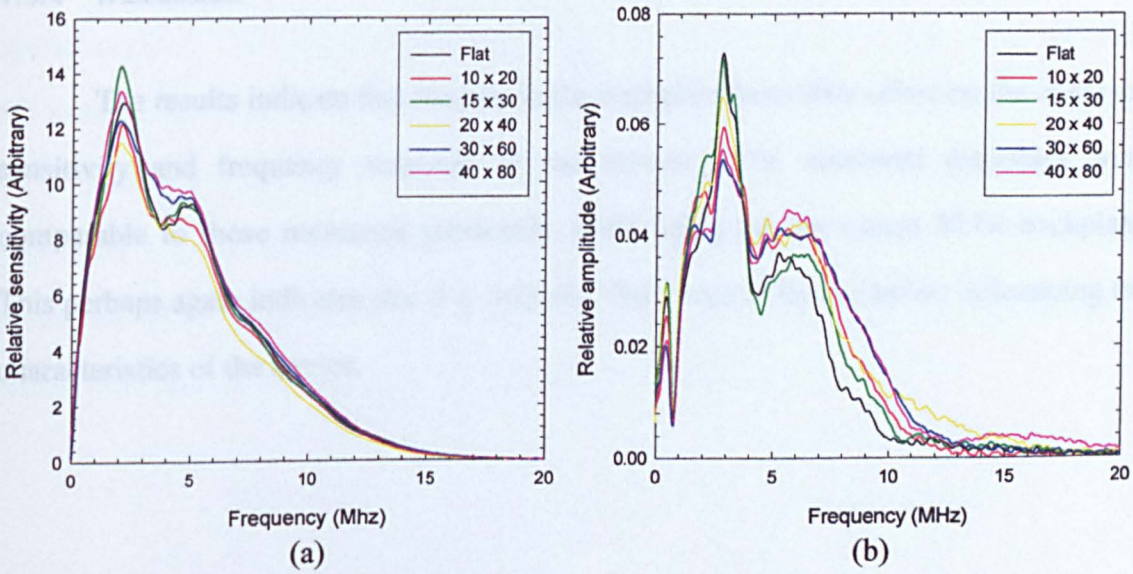

Figure 7.31: *Comparison of relative frequency spectra from the machined backplates used (a) as a source, (b) a receiver.*

apparent; either in terms of magnitude or form. The plots are, however, in good agreement with those obtained for the polished (#0.04) random metallic backplate (see Figure 7.20(a & b)).

7.6.3 Effect of machined backplate properties on source characteristics

The source characteristics of the photoresist backplates were also examined. The experimental set-up was identical to that used previously, with the 1mm circular PVDF hydrophone as a detector, and the immersion transducer driven by a Panametrics pulser/receiver unit (PR5055X); note that this was a slightly different model to that used previously. A 3.5μm Mylar membrane was again fitted to the device, and renewed after changing the backplate.

Figure 7.31(b) shows a comparison of the frequency spectra from the received waveforms for each of the backplates. Slight differences are evident, with perhaps the 30x60 and 40x80 backplates showing slightly higher bandwidth than the flat and 15x30 devices. However, no conclusive trends can be seen, and these differences could be due to slight changes in transducer alignment, and/or the membrane replacement process.

7.6.4 Discussion

The results indicate that the pits in the backplate have little effect on the observed sensitivity and frequency response of the device. The measured responses were comparable to those measured previously while using the smoothest #0.04 backplate. This perhaps again indicates that it is only the 'flat' areas of the backplate influencing the characteristics of the device.

7.7 Radiated sound pressure fields

7.7.1 Background

Examination of the sound pressure field emanating from a device is another method that can also be used to characterise immersion transducers [23]. As discussed in the introduction to this chapter, traditional PZT based immersion transducers can suffer from a high coupling between radial and thickness modes of resonance. This can lead to non-uniform displacements across the front face of the transducer, hence producing unpredictable sound fields.

The air-coupled capacitive transducer, however, has been shown to behave more predictably, and its emitted field can be modelled accurately using a piston in a planar baffle model [24]. This section examines this by measuring the radiated pressure fields from the capacitive immersion transducer, and comparing this to the theoretical predicted fields.

7.7.2 Experimental set-up

The fields were obtained by scanning along the radial and axial axis of the transducer, with the 1mm diameter PVDF hydrophone, and storing a waveform at each spatial position. The experimental apparatus is shown in Figure 7.32, this is essentially the same as the scanning system previously described in Chapter 4. The 1mm diameter PVDF needle hydrophone was attached to the scanning stage. The immersion transducer was fitted with the #0.04 backplate, and a new 3.5μm Mylar membrane, and positioned at one end of the immersion tank, so its sound field was radiating horizontally, along the z-axis. The photograph in Figure 7.33 shows this arrangement.

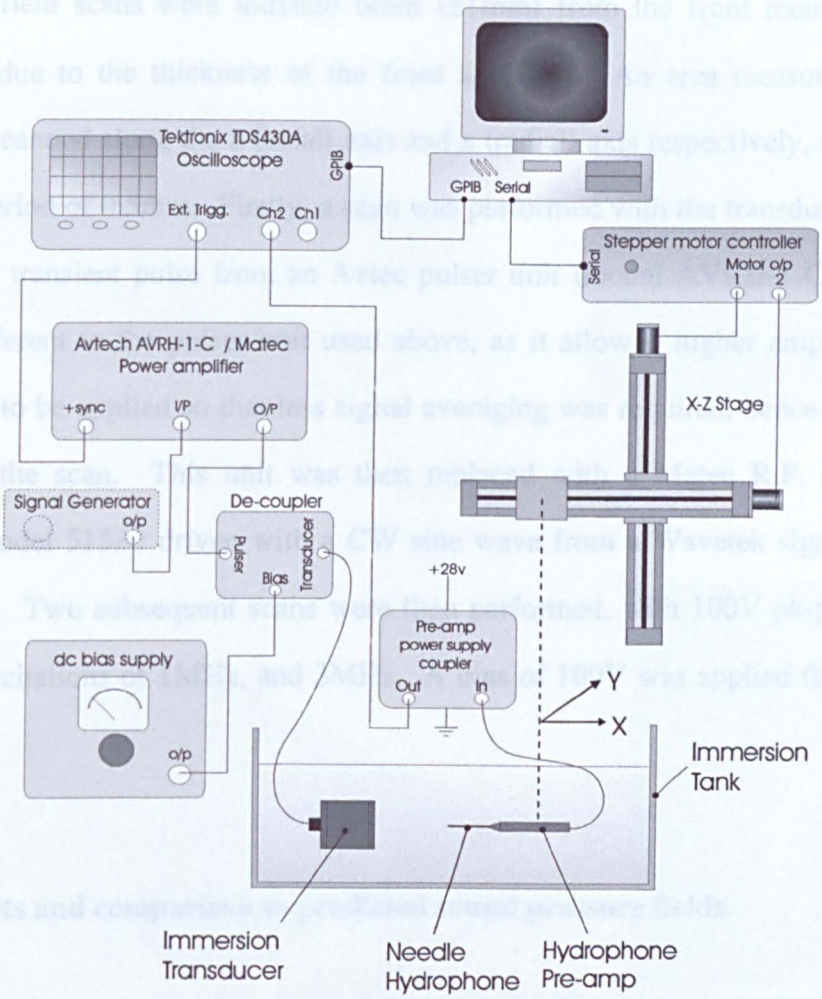

Figure 7.32: *Schematic diagram of the experimental set-up for scanning of the radiated sound pressure field.*

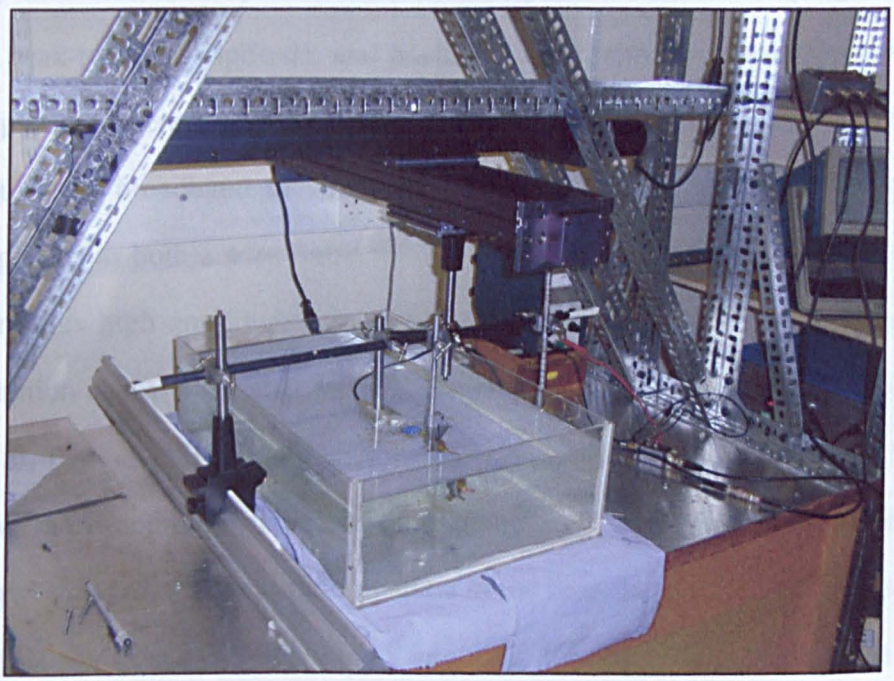

Figure 7.33: *Photograph of the field scanning rig (with the hydrophone and immersion transducer visible).*

The field scans were initiated 6mm (±1mm) from the front membrane of the transducer (due to the thickness of the front aperture). An area measuring 45mm x 40mm was scanned along the z (axial) axis and x (radial) axis respectively, with a spatial frequency period of 0.5mm. Firstly, a scan was performed with the transducer driven by a broadband transient pulse from an Avtec pulser unit (model AVRH-1-C). Note that this was different to the pulser unit used above, as it allowed higher amplitude (up to 1kV) pulses to be applied so that less signal averaging was required, hence reducing the duration of the scan. This unit was then replaced with a Matec R.F. gated power amplifier (model 515A) driven with a CW sine wave from a Wavetek signal generator (model 191). Two subsequent scans were then performed, with 100V pk-pk, 20 cycle, tone burst excitations of 1MHz, and 3MHz. A bias of 100V was applied throughout all the scans.

7.7.3 Results and comparison to predicted sound pressure fields.

Analysis of the waveforms was performed the PixieLab LabVIEW™ program, previously described in Chapter 4. For the scans performed here, the program was used to extract peak-to-peak amplitude, and positional data from the stored waveforms. This was then plotted, to create 3-D maps of the peak sound pressure fields from the device. The result of the broadband transient drive signal scan, are shown in Figure 7.34(a). They are plotted as both a wire frame mesh plot and as a greyscale intensity plot, where white represents high amplitude, and black low amplitude. The results from the tone burst excitation scans were also plotted in the same way and are displayed in Figure 7.34(b & c), for the 1MHz and 3MHz cases respectively. As expected, the tone burst plots show more complex variations within the near field than the broadband plot. Interestingly, the far field / near field maxima in the broadband and 3MHz tone burst plot are in similar positions ($z \approx$ 50mm), implying the broadband signal has a centre frequency of approximately 3MHz.

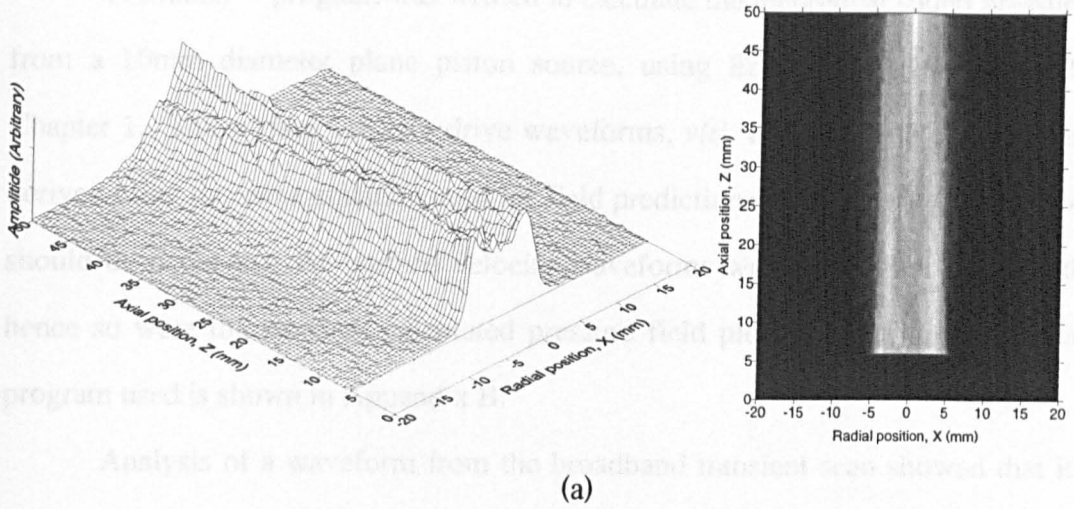

(a)

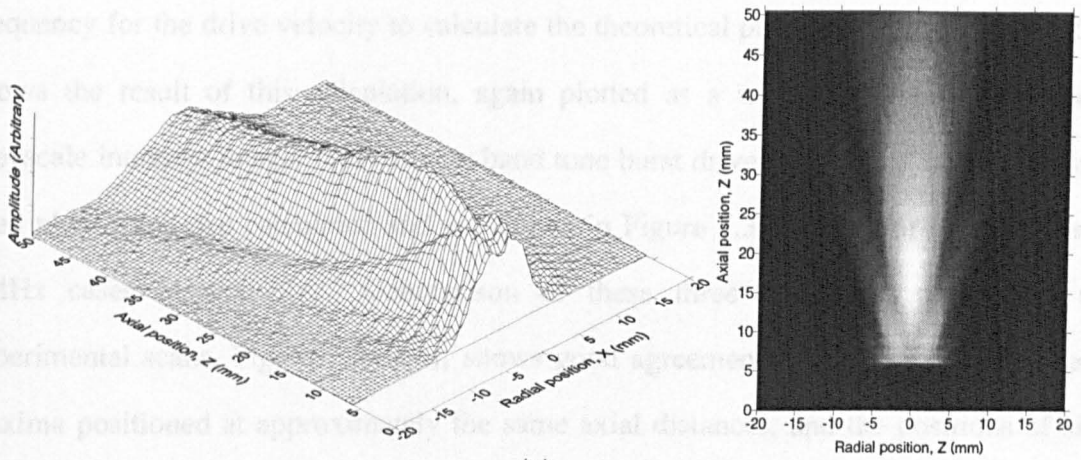

(b)

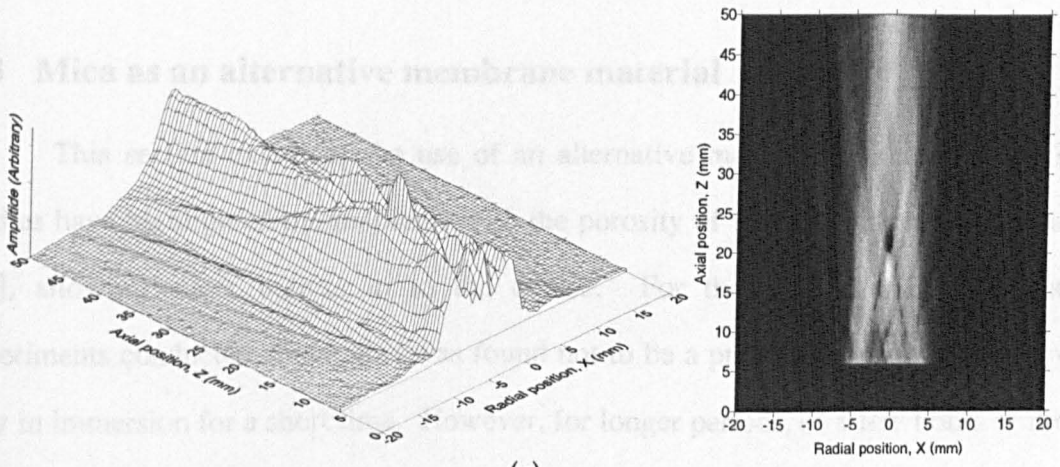

(c)

Figure 7.34: *Measured pk-pk amplitude of the sound fields from the capacitive immersion transducer when driven by (a) a broadband transient (b) 1MHz tone burst, and (c) a 3MHz tone burst signal.*

A Matlab™ program was written to calculate the theoretical sound pressure fields from a 10mm diameter plane piston source, using Equations (1.19) to (1.22) from Chapter 1. The surface velocity drive waveforms, *v(t)*, used in these calculations, were derived using the same equation used for field predictions in Chapter 4 (Equation 4.1). It should be noted that the surface velocity waveforms were of arbitrary amplitude; and hence so were the resultant calculated pressure field plots. A listing of the Matlab™ program used is shown in Appendix B.

Analysis of a waveform from the broadband transient scan showed that it had a centre frequency of approximately 3MHz. Hence, this value was used as the centre frequency for the drive velocity to calculate the theoretical pressure field. Figure 7.35(a) shows the result of this calculation, again plotted as a wire frame mesh plot and a greyscale intensity image. The narrow band tone burst driven theoretical sound pressure filed plots were also calculated and are shown in Figure 7.35(b & c) for the 1MHz and 3MHz cases respectively. Comparison of these three theoretical plots with the experimental scans, Figure 7.34(a-c), shows good agreement, with on axis minima and maxima positioned at approximately the same axial distances, and the positions of side lobes, present in the tone burst plots, also agreeing well.

7.8 Mica as an alternative membrane material

This section examines the use of an alternative membrane material. Previous studies have highlighted the problems with the porosity of the thin polymer membranes [12], allowing water ingress in to the device. For the backplate characterisation experiments conducted above, this was found not to be a problem as the transducer was only in immersion for a short time. However, for longer periods, of a few hours or more, (i.e. during the pressure field scans) the performance of the transducer was found to degrade with time until it ceased to work. This was assumed to be due to water ingress through/into the membrane. One solution is to coat the membrane with a waterproof or

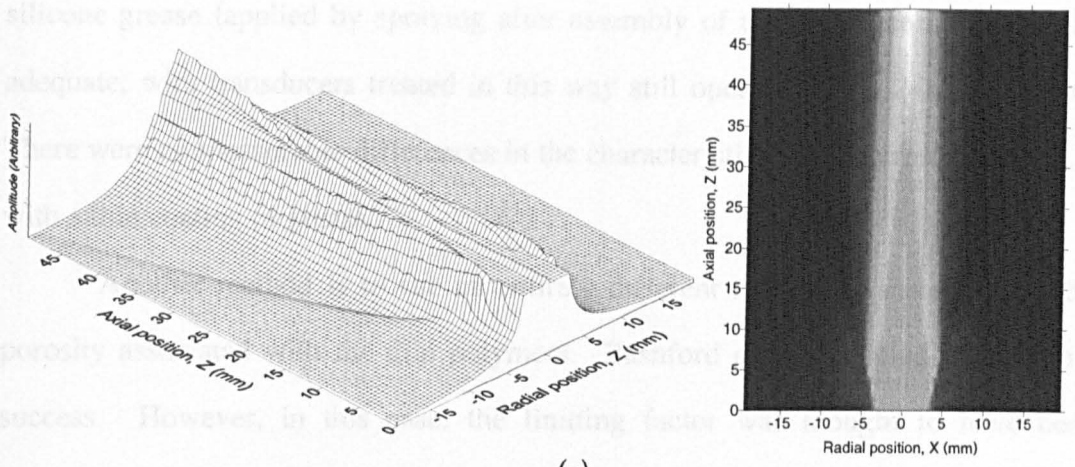

(a)

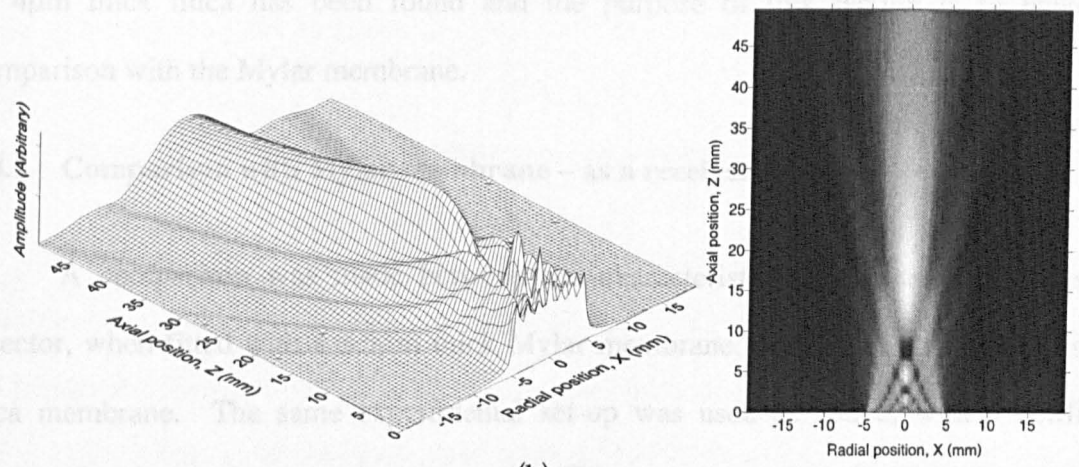

(b)

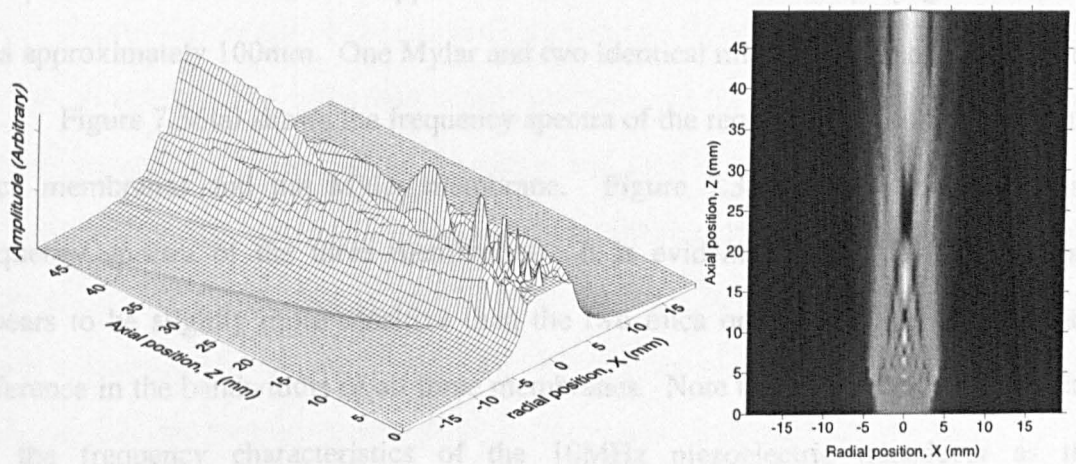

(c)

Figure 7.35: *Theoretical sound pressure field plot for a 10mm diameter plane piston transducer, when driven by (a) a broadband signal (centre 3 MHz), (b) a 1MHz tone burst and (c) a 3MHz tone burst simulated surface velocity.*

hydrophobic film, such as Teflon. During the field scan study above, a thin layer of silicone grease (applied by spraying after assembly of the transducer) was found to be adequate; with transducers treated in this way still operating after 24hrs of immersion. There were no measurable differences in the characteristics of an untreated device, to one with a thin coating of grease.

Another method is to use an entirely different membrane material, without the porosity associated with the thin polymers. Bashford et al [12] tried mica with some success. However, in this case, the limiting factor was thought to have been the thickness, where the thinnest available at that time was approximately 20μm. A source of 4μm thick mica has been found and the purpose of this section is to make a comparison with the Mylar membrane.

7.8.1 Comparison with Mylar membrane – as a receiver

A comparison was made between the characteristics of the transducer, as a detector, when fitted with a 3.5μm thick Mylar membrane, and a 4μm thick metallised mica membrane. The same experimental set-up was used as above, with a 10MHz Panametrics immersion transducer source. The transducer was fitted with a #1200 backplate, and a 100V bias was applied for all the membranes. The propagation distance was approximately 100mm. One Mylar and two identical mica membranes were tested.

Figure 7.36(a) shows the frequency spectra of the received waveforms for the two mica membranes and the Mylar membrane. Figure 7.36(b) shows the normalised frequency spectra of the three membranes. It is evident that the Mylar membrane appears to be slightly more sensitive than the two mica ones. However there is little difference in the bandwidths of all three membranes. Note that these were not corrected for the frequency characteristics of the 10MHz piezoelectric transducer as this experiment was just a comparison between the two types of membrane.

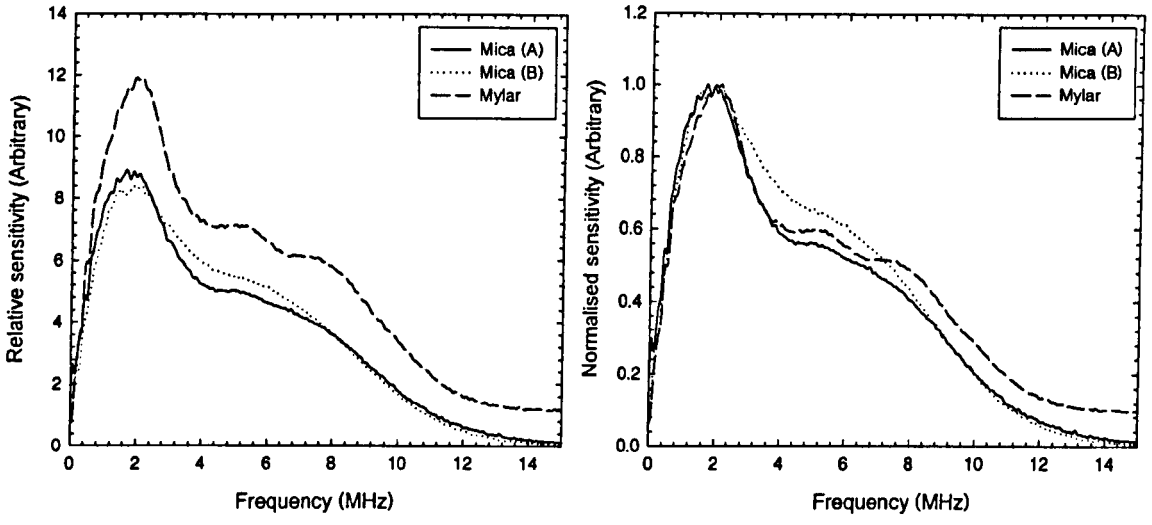

(a) (b)

Figure 7.36: *Relative amplitude frequency spectra (a) and normalised frequency spectra (b) of the signals from two mica (A and B) and one Mylar membraned receiver fitted with a #1200 backplate, 100mm from a 10MHz piezoelectric source.*

7.8.2 Comparison with Mylar membrane – as a source

The mica was also characterised as a source and compared to the Mylar membrane material. The 1mm circular PVDF hydrophone was used as a receiver, and the Panametrics pulser unit was used to drive the immersion device. The transducer was again fitted with a #1200 backplate, and a 100V bias was applied for all the measurements.

Figure 7.37(a) shows the received waveforms. It can be see that the amplitudes of the waveforms for both membrane materials are similar. However, the mica waveforms appear to be of lower frequency and more highly damped than the Mylar waveform. This also confirmed by examination of their corresponding frequency spectra (Figure 7.37(b)). This shows the mica membranes to have a peak frequency of approximately 2MHz, and the Mylar approximately one of 5MHz. Note that these have not been corrected for their drive signals, but examination showed they were very similar for the two membrane materials.

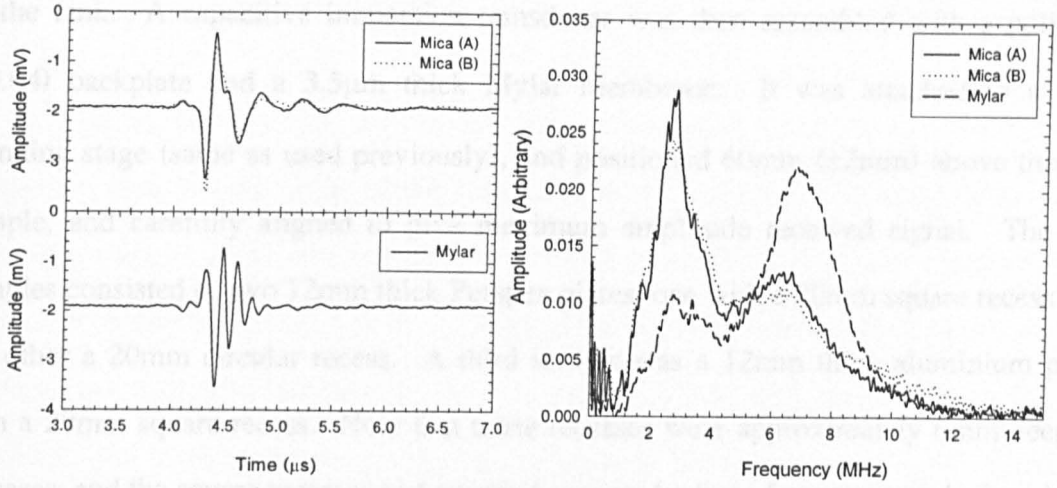

Figure 7.37: *Waveforms (a) and corresponding frequency spectra from two mica (A and B) and one Mylar membraned source (#1200 backplate).*

7.9 Application – Defect detection in Perspex and aluminium plates using a capacitive immersion transducer

7.9.1 Apparatus and experiment

To investigate an application of the capacitive immersion transducer, and demonstrate its use in a practical defect detection system, an experiment was performed to attempt to image artificially induced defects in Perspex and aluminium plates. A C-scan arrangement was used, with the immersion transducer operating in pulse-echo mode.

The schematic diagram in Figure 7.38 illustrates the experimental set-up used. The transducer was connected to the Panametrics (5055PR) pulse-receiver unit, via a capacitive de-coupling box to allow the application of a 200V dc bias (a higher bias than used previously to improve signal amplitude). The receiver output of the Panametrics pulser was connected to a Tektronix TDS430A oscilloscope, which, in turn, was connected to a PC via a GPIB bus. The test specimen (plate) was positioned horizontally at the bottom of the immersion tank, with the 'defect' on its underside. It was supported at both ends with spacers to ensure that its lower side was not in contact with the bottom

of the tank. A capacitive immersion transducer was then assembled with a polished (#0.04) backplate and a 3.5μm thick Mylar membrane. It was attached to a X-Y scanning stage (same as used previously), and positioned 60mm (±2mm) above the test sample, and carefully aligned to give maximum amplitude received signal. The test samples consisted of two 12mm thick Perspex plates, one with a 20mm square recess and the other a 20mm circular recess. A third sample was a 12mm thick aluminium plate with a 20mm square recess. Note that these recesses were approximately 6mm deep in all cases, and the square recesses had rounded corners (radius of approximately 3mm).

A scan of the test samples was then performed, using a spatial frequency period of 1mm, over an area of 50mm x 50mm. The received waveforms at each scan position were stored for later analysis.

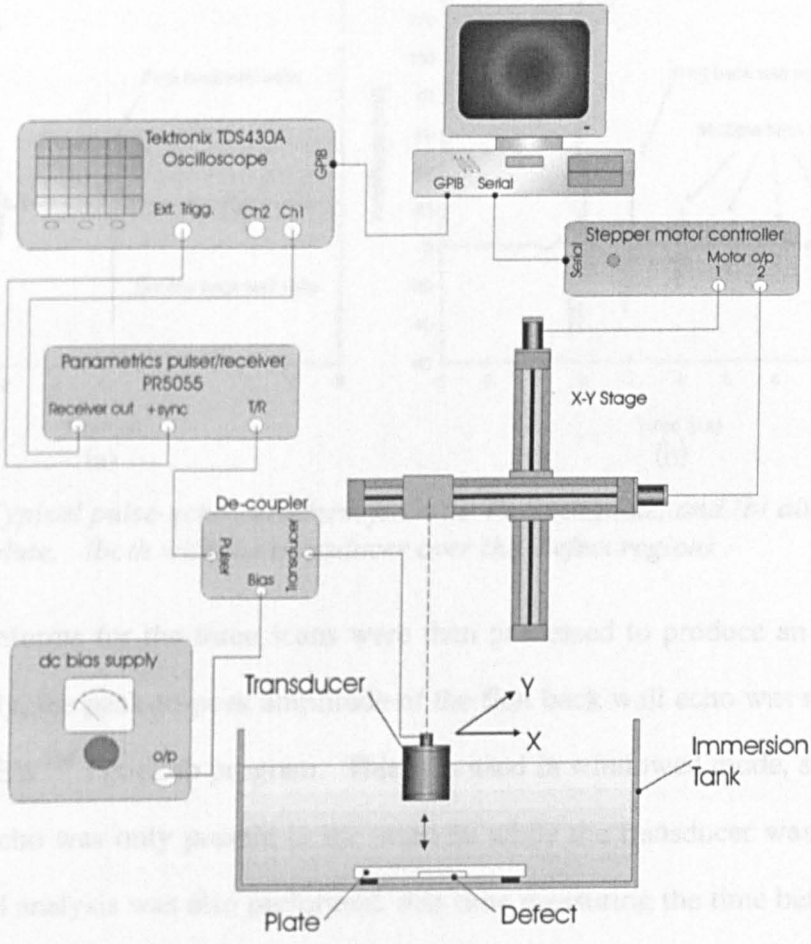

Figure 7.38: *Schematic diagram of the experimental pulse echo C-scan apparatus.*

7.9.2 Results and discussion

Typical waveforms received over the defect area in both the Perspex and aluminium plate are shown in Figure 7.39. The front face echo, first, and multiple back wall echoes are easily visible in both cases, with their phase inversions as expected. It is also worth noting the difference in the ratio of the amplitude of the front face signal to the first back wall echo (and also between the subsequent echoes) are different in the two materials, due to their differing acoustic impedances (Perspex (Acrylic) ≈ 3.1 MRayl, Aluminium ≈ 17 MRayl). The time between the main front face echo and the back wall echo is consistent with approximately 6mm of material in both cases.

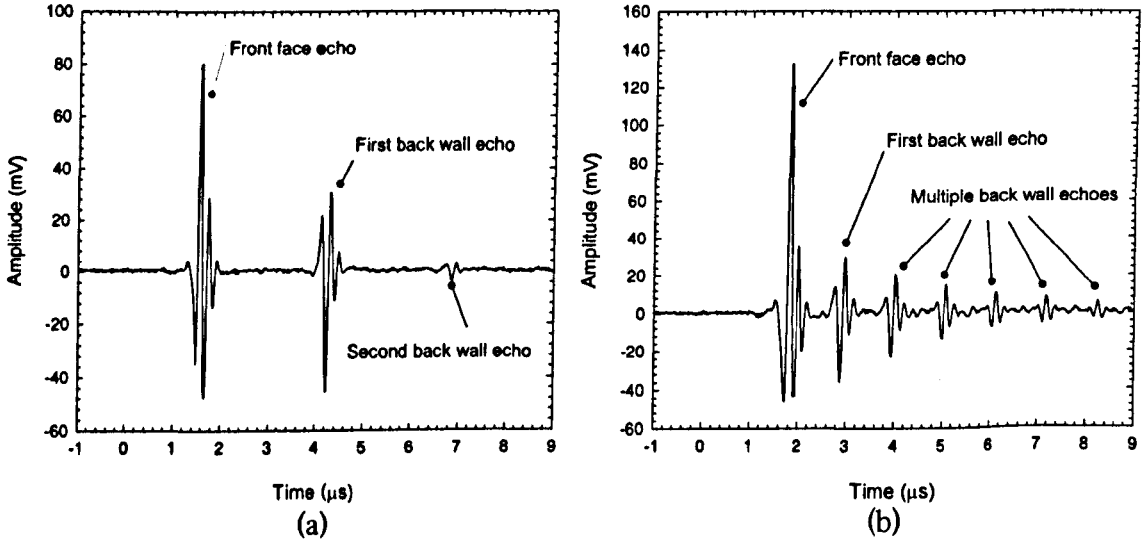

Figure 7.39: *Typical pulse-echo waveform from (a) Perspex plate, and (b) aluminium plate. (both with the transducer over the defect region).*

The waveforms for the three scans were then processed to produce an image of the defect. Firstly, the peak-to-peak amplitude of the first back wall echo was measured, using the LabVIEW™ PixieLab program. This was used in windowed mode, so that the first back wall echo was only present in the window while the transducer was over the defect. A second analysis was also performed, this time measuring the time between the front face echo and the back wall echo. Figure 7.40 to Figure 7.42 show the greyscale images obtained using these methods, with the defect shown by the dashed lines, for the Perspex plate with the square and circular defects, and the aluminium plate with the

square defect, respectively. Note that darker areas represent high amplitude/value and the lighter areas lower amplitude/value. It is clear that an accurate representation of the defect in all cases has been obtained. The discrepancy between the sizes of the actual and measured defect is due to the finite size of the ultrasonic beam. Referring back to Figure 7.34, which shows the measured sound pressure field when driven by a transient excitation, it can be seen that at z=50mm the width of the beam (-6db width) is approximately 5mm. This resolution agrees with that observed on the images of the defect, where the blurred region of the edges (in the amplitude plots) are also approximately 5mm ±1mm in width. It should also be noted that there is little noticeable difference between the image of the square defect in the Perspex plate (Figure 7.41) and that of the aluminium plate (Figure 7.42), even though the acoustic impedance of the latter is greater by a factor of approximately five. Thus, this experiment illustrated that a capacitive immersion transducer is easily capable of imaging such defects in plates.

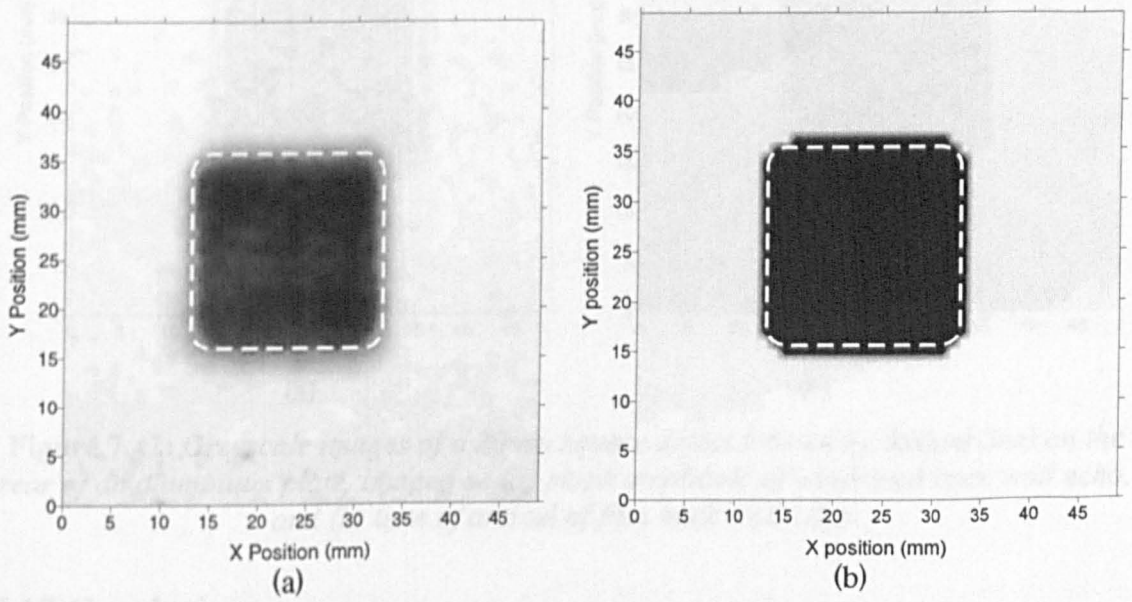

Figure 7.40: *Greyscale images of a 20mm square defect (shown by dashed line) on the rear of a Perspex plate, imaged as (a) pk-pk amplitude of windowed back wall echo, and (b) time of arrival of first back wall echo.*

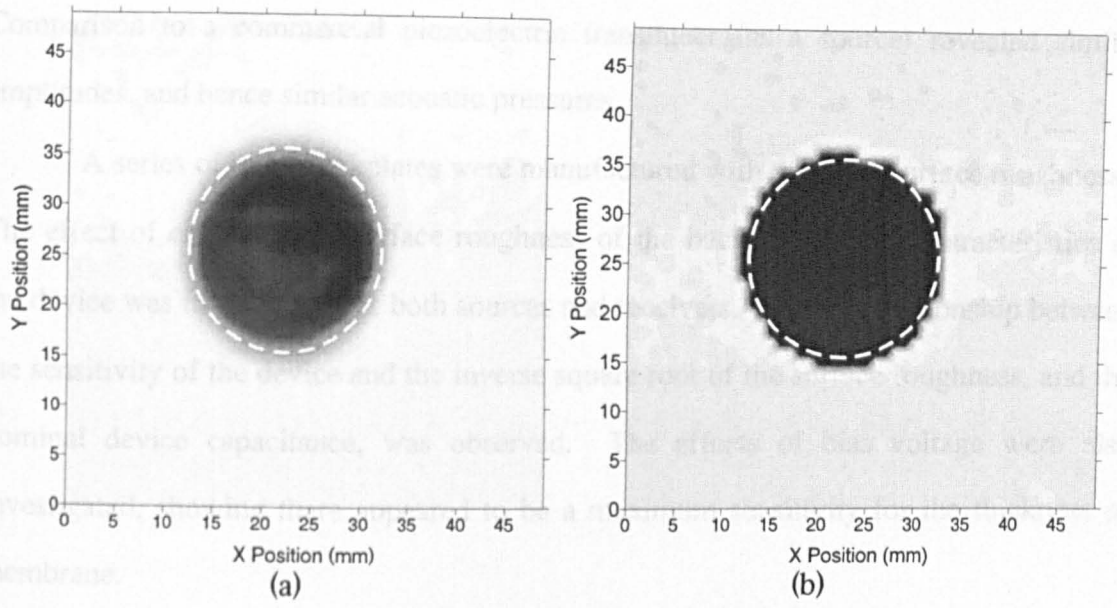

Figure 7.41: *Greyscale images of a 20mm circular defect (shown by dashed line) on the rear of a Perspex plate, imaged as, (a) pk-pk amplitude of windowed back wall echo, and (b) time of arrival of first back wall echo.*

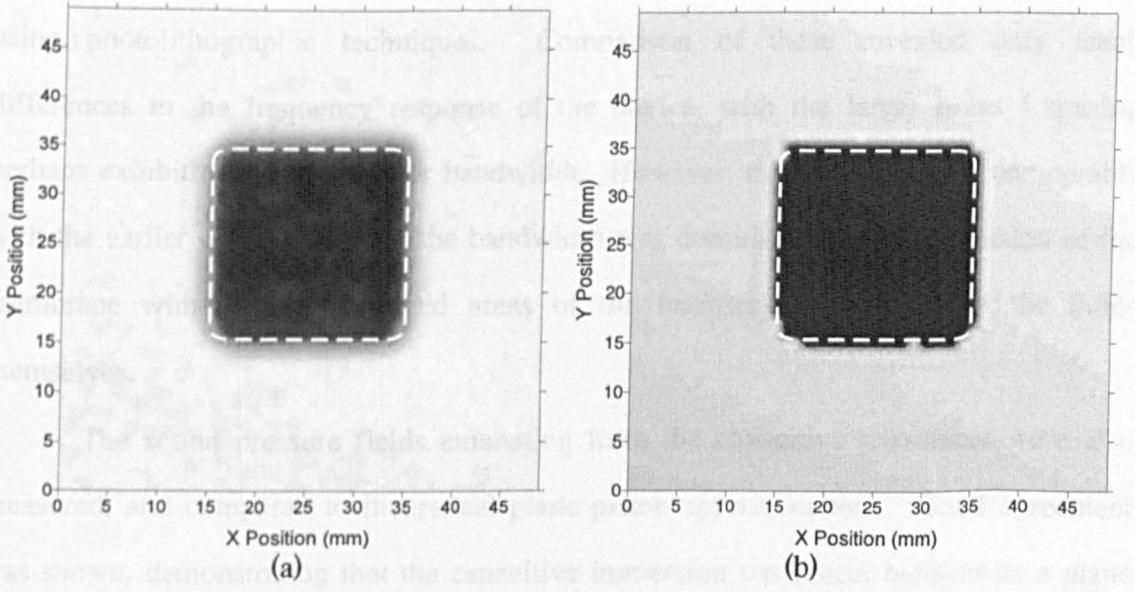

Figure 7.42: *Greyscale images of a 20mm square defect (shown by dashed line) on the rear of an aluminium plate, imaged as (a) pk-pk amplitude of windowed back wall echo, and (b) time of arrival of first back wall echo.*

7.10 Conclusions

The work presented in this chapter examined the development and characterisation of a capacitive immersion transducer.

The transducer was shown to exhibit different characteristics when operated in air and in immersion, with a higher frequency response / bandwidth in the latter case.

Comparison to a commercial piezoelectric transducer (as a source) revealed similar amplitudes, and hence similar acoustic pressures.

A series of brass backplates were manufactured with different surface roughness'. The effect of changing the surface roughness of the backplate on the characteristics of the device was investigated, as both sources and receivers. A linear relationship between the sensitivity of the device and the inverse square root of the surface roughness, and the nominal device capacitance, was observed. The effects of bias voltage were also investigated, showing there appeared to be a maximum sensitivity for the thickness of membrane.

A set of backplates with arrays of holes ranging in size from 10μm to 40μm, and spacing from 20μm to 80μm, and approximately 1μm in depth have been manufactured using photolithographic techniques. Comparison of these revealed only small differences in the frequency response of the device, with the larger holes / spacing perhaps exhibiting slightly higher bandwidth. However, these results were comparable with the earlier observation that the bandwidth was dominated by the interaction of the membrane with the flat polished areas of the backplate, and not with the holes themselves.

The sound pressure fields emanating from the capacitive transducer were also measured, and compared to theoretical plane piston approximations. Good agreement was shown, demonstrating that the capacitive immersion transducer behaves as a plane piston radiator with uniform particle velocity across its face.

Mica was examined as an alternative membrane material as the porosity of polymer films is known to be a problem with immersion devices. It was found to exhibit similar sensitivities to the Mylar membranes. Its frequency response as a receiver was also found to be similar. However, as a source, it was found to exhibit a lower frequency response than that of a similar Mylar membrane.

The transducer was used to demonstrate the imaging of defects in Perspex an aluminium plates using a pulse-echo C-scan method. Good images of the defects were obtained.

7.11 References

[1] D.M. Makow, D.L. McRae, "Symmetrical scanning of the head with ultrasound using water coupling", *J. Acoust. Soc. Am.,* vol. 44, no. 5, pp. 1346-1352, 1968.

[2] J. Krautkrämer, H. Krautkrämer, "Ultrasonic testing of materials", 4th edition, Springer-Verlag, New York 1990.

[3] D.A. Hutchins, H.D. Mair, P.A. Puhcah, A.J. Osei, "Continuous-wave pressure fields of ultrasonic transducers", *J. Acoust. Soc. Am,* Vol. 80, no. 1, pp. 1-11, 1986.

[4] G.R. Schodder, F. Wiekhorst, "Electrostatic transducers with solid dielectric for waterborne sound", *Acoustica,* vol. 7, pp. 38-45, 1957.

[5] G. K. Miller, "Flexible electret transducers", *J. Acoust. Soc. Am.,* vol. 60, no. 47, 1976.

[6] G. K. Miller, "Electret coaxial cable hydrophone performance", *J. Acoust. Soc. Am.,* vol. 57, no. 44, 1976.

[7] J.H. Cantrell, J.S. Heyman, W.T. Yost, M.A. Torbett, M.A. Breazeale "Broardband electrostatic acoustic transducer for ultrasonic measurements in liquids", *Rev. Sci. Instrum.,* vol. 50, no. 1, pp. 31-33, 1979.

[8] J.H. Cantrell, W.T. Yost, "Liquid-membrane coupling response of submersible electrostatic acoustic transducer", *Rev. Sci. Instru.,* vol. 60, no. 3, pp. 487-488, 1989.

[9] J.A. Clark, "A matched impedance, electrostatic approach to hydrophone design", *J. of Sound and Vibration*, vol. 77, no. 1, pp.51-59, 1981.

[10] D.W. Schindel, D.A. Hutchins "Capacitance devices for the controlled generation of ultrasonic fields in liquids", *Proc. IEEE Ultrasonics Symposium,* vol. 1, pp. 301-304, 1991.

[11] D.W. Schndel, D.A. Hutchins, L. Zou and M. Sayer, "Capacitance Transducers for Generating Ultrasonic Fields in Liquids and Gases", *Proc. IEE Conf. On 'Acoustic Sensing and Imaging",* pp. 7-12. #369, London, UK., 1993.

[12] A.G. Bashford, D.W. Schindel, D.A. Hutchins, "Micromachined Ultrasonic Capacitance Transducers for Immersion Applications", *IEEE Trans. Ferroelec. Freq. Control.,* vol. 45,no. 2, pp. 367-375, 1998.

[13] X.C. Jin, I. Ladabaum, F.L. Degertekin, S. Calmes, "Fabrication and characterisation of surface micromachined capacitive ultrasonic immersion transducers", *J. Microelectromech. Sys.*, vol. 8, no. 1, pp. 100-114, 1999.

[14] P.-C. Eccardt, K. Niederer, "Micromachined ultrasonic transducers with improved coupling factors from a CMOS compatible process", *Ultrasonics,* vol. 38, pp. 774-780, 2000.

[15] R.A. Noble, A.D.R. Jones, T.J. Robertson, D.A. Hutchins, D.R. Billson, "Novel wide-bandwidth micromachined ultrasonic transducers", *IEEE Trans. Ultrason. Ferroelec. Freq Control.,* (accepted for publication, in press), 2001.

[16] J. Hietanen, P. Mattila, J. Stor-Pellin, F. Tsuzuki, H. Väätäjä, K. Sasaki, M. Luukkala, "Factors affecting the sensitivity of electrostatic ultrasonic transducers", *Measur. Sci. & Tech.,* vol. 4, pp 1138-1142, 1993.

[17] M. Rafiq, C. Wykes, "The performance of capacitive ultrasonic transducers using v-grooved backplates", *Meas. Sci. Technol.,* vol. 2, pp. 168-174, 1991.

[18] P. Mattila, J. Hietanen, "Bandwidth control of an electrostatic ultrasonic transducer", *Sensors Actuators A,* vol. 45, pp. 203-208, 1994.

[19] S. Lippold, J. Podlensy, "WYKO Surface Profilers Technical Reference Manual", WYKO Corporation, Tucson, AZ, USA, 1996.

[20] M. Platte, "A polyvinylidene fluoride needle hydrophone for ultrasonic applications", *Ultrasonics,* vol. 23, no. 3, pp. 113-118, 1985.

[21] W.M.D Wright, "Air-Coupled Ultrasonic Testing of Materials", *Ph.D. Thesis,* University of Warwick. 1996.

[22] H. Carr, C. Wykes, "Diagnostic measurements in capacitive transducers", *Ultrasonics,* vol. 31, pp. 13-20. 1993.

[23] W. Sachse, N.N. Hsu, "Ultrasonic transducers for materials testing and characterisation", *Physical Acoustics,* Vol. XIV, Academic Press, New York. 1979.

[24] A.G. Bashford, D.W. Schindel, D.A. Hutchins, W.M.D. Wright, "Field characterisation of an air-coupled micromachined ultrasonic capacitance transducer", *J. Acoust. Soc. Am.,* vol. 101, no. 6, pp. 315-322, 1997.

8 *Conclusions*

8.1 Conclusions and further work

The research work described in this thesis has been concerned with the development and characterisation of a number of new novel types of ultrasonic capacitive transducer.

The first chapter introduced ultrasound, with a brief synopsis of its history, and how its usefulness in NDE applications were realised. The basic properties of ultrasound, such as propagation through a medium, transmission, and radiated field patterns were also described.

Chapter 2 presented a review of capacitive transducer technology, describing the development of capacitive transducers, from the basic metallic backplate types, through to the most recent fully micromachined silicon devices. Basic device operation was also described, and alternatives to the capacitive design were examined, the most predominant being the piezoelectric based transducers, the merits and deficiencies of each were discussed.

In Chapter 3, the fabrication and initial characterisation of new novel surface micromachined capacitive silicon transducers were discribed. These devices differed to others cited in the literature as they had a large lateral dimensioned silicon nitride membrane, whereas the former generally consist of a large number of individual cells, each of approximately 50μm in diameter. Their static membrane deflections were measured, with a snap down effect observed in one batch of devices. The transducers were characterised in air using a variety of techniques, and were found to be reversible, exhibiting frequency responses in the MHz region, with (-6dB) bandwidths of approximately 75%. Further experiments were performed to examine the effect of membrane thickness and lateral

dimensions on the transducer characteristics. Observed trends demonstrated that thinner membranes increased bandwidth, sensitivity, and centre frequency response. Little change in the frequency response was observed in devices of different lateral dimensions (1mm to 5mm square), indicating that this was relatively independent of the size of transducer. The effect of applied bias voltage was also studied, with observed trends indicating increases in bias voltage resulted in increases in centre frequency response, with bandwidth remaining approximately constant. Finally, an initial experiment was performed with the transducers in immersion, with increased bandwidth and frequency responses observed. It was noted that the inherent operation of these devices is very complex and further work, using finite element analysis tools, such as MEMCAD, would be required to accurately model their operation. In the future work with arrays of such devices is envisaged; with studies on the problems of cross talk between elements, and incorporation of on-chip drive/receive electronics.

Chapter 4 continued with the characterisation of the surface micromachined devices, with first an examination of their dynamic membrane displacements when driven with a broadband transient excitation signals, using optical interferometry. Typical measured displacements were of the order of a few nm, with the observed frequency response agreeing with measurements made in Chapter 3. The radiated fields from a selection of devices were also measured, using both broadband transient and narrowband tone burst excitations, and compared to theoretical plain piston approximations. Good agreement was found, demonstrating that they produced well-behaved sound pressure fields.

In Chapter 5, the design and characterisation of two variants of line focusing transducer was described. One utilised a cylindrically shaped backplate, to produce a line of focus normal to its axis, and the other a conically shaped device, to produce a line of focus along its axis. Their frequency characteristics were studied, using a pulse-echo technique. The transducers, both utilising

polished brass backplates, were found to exhibit similar bandwidths of approximately 1.2MHz, with centre frequencies of ~500kHz and ~800kHz respectively. Their radiated sound fields were measured using both broadband and tone burst excitations, and compared to theoretical plane piston approximations with good agreement being found. Experiments were also performed to study their resolutions, using broadband transient excitations. Lateral resolutions of 0.68mm and 0.3mm, for the cylindrical, and conical, devices respectively were measured. In addition, their vertical resolutions were found to be approximately 5μm and 100μm correspondingly. Imaging of a two pence coin was performed using both devices. Both amplitude and time data were used to construct 3-D surface images, demonstrating their ability to image surfaces in reflected signal mode. Further work with these devices could examine additional applications, such as through transmission imaging systems, which would allow the examination of the internal structure of a material.

In Chapter 6, another air-coupled focusing transducer utilising an off-axis parabolic mirror was described. Its frequency characteristics were examined, and it was found to exhibit a bandwidth and centre frequency of approximately 700kHz. Its horizontal and vertical resolutions were determined using similar methods used for the shaped backplate devices described in Chapter 5. These were 0.5mm and 5μm respectively. It was used to successfully image a two pence coin, using both amplitude and time of arrival data.

In Chapter 7, the design, construction, and characterisation of a capacitive transducer for use in immersion were described. Experiments demonstrated that improved performance resulted when it was in immersion (as opposed to operation in air) with increases in bandwidth and centre frequency response. Several roughened and polished brass backplates were manufactured and were used to study the effect of surface properties on the characteristics of the device, as both sources and receivers. A linear relationship between the sensitivity and the inverse

square root of the surface roughness of the backplate, and its capacitance was observed. The high frequency operation observed in immersion was thought to be produced by the flatter parts of the backplate, hence higher sensitivity was observed with the smoother backplates. Another selection of backplates was manufactured using a photolithography process. These contained a series of pits ranging from 10μm to 40μm in diameter, and 1μm deep. Comparison of the characteristics of the device when fitted with these backplates revealed little differences between them. These results were compatible with those observed for the roughened/polished backplates, where the frequency response was dominated by the interaction of the membrane with the flatter parts of the membrane. The effects of bias voltage were also investigated, showing there appeared to be a maximum sensitivity for the thickness of membrane. Their radiated sound pressure fields were measured, using both broadband transient and narrowband tone burst excitation signals. These were compared to theoretical plane piston approximations, with good agreement being found. Mica was also investigated as an alternative membrane material and was found to exhibit similar sensitivities to Mylar membranes. Its frequency response as a receiver was also found to be similar. However, as a source it was found to exhibit a lower one than that of a similar Mylar membrane. Finally, the transducer was also demonstrated in a pulse-echo application, where defects were imaged in Perspex and aluminium plates. Good results were obtained, demonstrating that these transducers could perform the same application as traditional piezoelectric transducers.

It is felt that the work covered in this thesis has increased knowledge in the area of capacitive transducers, with the development and characterisation of a number of new novel transducers. It is hoped that these will be useful for use in future NDE and measurement systems.

Bibliography

'Guide to Examinations for Higher Degrees by Research", The University of Warwick Graduate School, October 1999.

Publications arising from this thesis

[1] R.A.Noble, R.J.Bozeat, T. J. Robertson, D. R. Billson and D. A. Hutchins, "Novel silicon nitride micromachined wide bandwidth ultrasonic transducers", 1998 IEEE Ultrasonics Symposium - Proceedings, Vol. 2, pp.1081-1084, 1998

[2] R. A. Noble, A. R. D. Jones, T. J. Robertson, D. A. Hutchins and D. R. Billson, "Novel Wide-Bandwidth Micromachined Ultrasonic Transducers", *IEEE Trans. Ultrason. Ferroelec. Freq.Control,* (accepted for publication in IEEE Trans. UFFC, in press).

[3] T.J. Robertson, D. A. Hutchins and D. R. Billson, "An Air-Coupled Line-Focused Capacitive Ultrasonic Transducer", *IEEE Ultrasonics symposium proceedings*, San Juan, Puerto Rico, vol. 2, pp. 1061-1064, 2000

[4] R. A. Noble, T.J. Robertson, J.S. McIntosh, D. A. Hutchins, D. R. Billson, "Miniature Silicon Micromachined Ultrasonic Point Detectors for Measurement of airborne Radiated Fields", *IEEE Ultrasonics symposium proceedings*, San Juan, Puerto Rico, vol. 1, 955-958, 2000.

[5] T.J. Robertson, D.A. Hutchins, D.R. Billson, J.H. Rakels, D.W. Schindel, "Surface metrology using reflected ultrasonic signals in air", 6th biennial joint Warwick/ Tokyo nanotechnology symposium. Sept. 2000, (in press).

Appendix A - Equipment Specifications

Panametrics 5055PR Pulser-Receiver

Pulser

Maximum pulse amplitude	-250V into 50Ω -350V into 250Ω
Pulse repetition rate (internal)	100-2000Hz
Damping range	10-250Ω
Minimum rise time	10ns
Available pulse energy	18-110μJ in 4 steps

Receiver

Voltage gain	40dB (x100) or 60dB (x1000) selectable
Input Impedance	500Ω
Output Impedance	50Ω
Noise Levels	50μV pk-pk referred to the input
Bandwidth	10kHz-10MHz

Cooknell CA6/C charge amplifier

Input impedance	100Ω above 10kHz
Sensitivity	250mV/pC
Series noise voltage generator	0.6nV//Hz typical
Parallel noise current generator	$4x10^{-14}$A//Hz typical
Bandwidth	<10kHz to > 10Mhz
Max output level	1V rms into 50Ω

Avtech AVR1-C-1 Pulser unit

Output	0-1000V positive square pulse
Pulse width	0.1μs to 5μs
Delay	0.1μs to 5μs
Repetition rate (internal)	1Hz to 10kHz

Computer controlled scanning stages

Two Thomson liner stages: Fitted with synchronous stepper motors

Motor steps per revolution	400
Motor steps per mm	80

Maximum stroke	526mm
Accuracy	0.023mm per 300mm of travel
Repeatability	0.005mm

Precision Acoustics 1mm circular hydrophone and submersible preamp

Probe frequency response	Class A (±2dB)	3 to 12MHz
	Class B (±4dB)	200kHz to 15MHz
Preamp frequency response	10kHz to 50MHz (-3dB)	
	5kHz to 100MHz (-6dB)	
Combined sensitivity	970mV/Mpa @ 3MHz	
Sensor material	28μm PVdF	
Preamp		

Brüel & Kjær piston phone sound pressure calibrator (type 4231)

Sound pressure level	94.00dB ±0.2dB (re 20μPa at reference conditions)	
Level step	20dB ±0.1dB	
Frequency	1000Hz ±0.1%	
Distortion	<1% THD	
Reference conditions	Temperature	20°C
	Pressure	1013hPa
	Humidity	65% RH

Brüel & Kjær 1/8" microphone (type 4138) and 2670 preamp

Combined sensitivity	-66.18 dB re 1V/Pa	
	0.49 mV/Pa	
Microphone Capacitance	3.4pF	
Calibration conditions	Polarisation voltage	200V
	Frequency	251.2Hz
	Pressure	101.3 kPa
	Temperature	23°C
	Humidity	50% RH

Matec Gating modulator (model 5100) and RF Gated Amplifier (515A HP)

Frequency Range	500kHz to 20MHz, 6 ranges, final stage continuously tuneable.
Pulse widths	<0.5μs to 1000μs
Peak RF voltage	550V

Appendix B - Matlab™ program listings

Rectangular transducer field calculation program listing (used to predict fields from the micromachined transducers. Calls rectangular impulse response function recimpulse.m listed below)

recfield.m

```
% Calculates sound pressure field from a rectangular plane piston source.
% Written by T.J. Robertson 10/5/99

%************************
%** Transducer variables*
%************************

%Width (m)
width=5e-3;

%Length (m)
length=5e-3;

%*****************************
%***Grid size and step set-up*
%*****************************

%Number of points on the x axis (half scan)
xmax=38;

%X step size (m)
xstep=0.2e-3;

%Number of points on the z axis
zmax=150;

%Z step size (m)
zstep=0.2e-3;

%Y position for field calculation (usually 0 i.e. centre of transducer)
y=0

%Initalise arrays
amp=zeros(xmax*zmax,1);


%******************
%*Medium constants*
%******************

%Speed of sound in medium (m/s)
c=343.4

%Density of medium
density=1.2;


%*******************************
%**Input waveform initialisation*
%*******************************

%Frequency of excitation (Hz)
f=500e3;

%Constant for wave equation
K=0.5;

%Time interval used in calculation
delta_t=2e-8;


%calc drive velocity waveform (v(t)) and differential of drive velocity (V(t)=dv(t)/dt))
for T=1:2000
   t=(T-1)*delta_t;
   tm(T)=t;
   thta=2*pi*f*t;
   V(T)=3*c*t^2*exp(-K*f*t)*cos(thta)-c*t^3*K*f*exp(-K*f*t)*cos(thta)-2*c*t^3*exp(-K*f*t)*sin(thta)*pi*f;
   v(T)=c*t^3*exp(-K*f*t)*cos(thta);
end

V_fft=fft(V,2048);

for Z=1:zmax
   Z
   z=(Z)*zstep;
   for X=1:xmax

      x=(X-1)*xstep;

      %Call impulse response recimpulse.m function.

      h=recimpulse(width, length, x, y, z, 2000, delta_t, z/c-50e-7);
```

```
      h_fft=fft(h,2048);
      con=ifft(h_fft.*V_fft);

      p=(real(con)*delta_t*density);
      amp((Z-1)*xmax+X)=max(p)-min(p);

   end
end

%Mirror field and create amplitude map

amp=reshape(amp,xmax,zmax);
amp2=amp(2:xmax,:);
amp2=flipud(amp2);
ampt=[amp2; amp];

%Calculate Grid

z=meshgrid(0:zstep*1e3:((zmax-1)*zstep*1e3),1);
x=meshgrid(-(xmax-1)*xstep*1e3:xstep*1e3:(xmax-1)*xstep*1e3,1);

%Plot result
mesh(z,x,ampt);
```

Rectangular impulse response function

recimpulse.m

```
%Function returns impulse response, at position x,y,z
%for a rectangular transducer of size width by length
%at position 0,0,0.  Impulse response calculation from
%"Diffraction impulse response of rectangular transducers"
%J. Luis, S. Emeterio, L.G. Ullate J. Acoust. Soc. Am Vol. 92,
%No. 2, Pt. 1., 1992
%
%Written by T.J. Robertson 8/5/99

%Function arguments are as follows:
%
%width - width of rectangular transducer (in m)
%length - length of rectangular transducer (in m)
%x,y,z - coordinates at which to calculate impulse response (in m)
%tmax - end time (no. of steps)
%tstep - time increment (delta t)
%tstart - offset time (in s)

function out=recimpulse(width, length, x, y, z, tmax, tstep, tstart)

A=width/2;
B=length/2;

c=343.4;

%reserve array memory
d=zeros(1,4);
alpha=zeros(1,4);
Ts=zeros(1,4);

ivp=zeros(1,tmax);


d(1)=x-A;
d(2)=y-B;
d(3)=x+A;
d(4)=y+B;

%Define time intervals

Ta=(sqrt(d(1)^2+d(2)^2+z^2)/c);
Tb=(sqrt(d(2)^2+d(3)^2+z^2)/c);
Tc=(sqrt(d(1)^2+d(4)^2+z^2)/c);
Td=(sqrt(d(3)^2+d(4)^2+z^2)/c);

Tm=min(Tb,Tc);
TM=max(Tb,Tc);
T0=z/c;

for i=1:4
  Ts(i)=(sqrt(d(i)^2+z^2)/c);
end

%Determine current geometrical region

if (x>=A & y>=B)
     region=1;
elseif (x<=A & y>=B)
   region=2;
elseif (x>=A & y<=B)
   region=3;
elseif (x<=A & y<=B)
   region=4;
end


%Calculate impulse response depending on region and current time interval.
```

```
for T=1:tmax
   t=(T-1)*tstep+tstart;

   sigma=sqrt(c^2*t^2-z^2)+eps;

       for i=1:4
      a(i)=asin(d(i)/sigma);
      ab(i)=sign(d(i))*asin(min((abs(d(i))/sigma),1));
   end

   %Test to see if within first time period
   if (0<t & t<Ta)
      switch region
      case 2
         if (Ts(2)<t)
            ivp(T)=pi-(2*a(2));
         end
      case 3
         if (Ts(1) < t)
            ivp(T)=2*ab(3)-2*a(1);
         end

      case 4
         if (T0<t)
            ivp(T)=-2*pi-2*ab(1)-2*ab(2)+2*ab(3)+2*ab(4);
         end

      end

   %Test to see if within second time period
   elseif(Ta<=t & t<=Tm)
      switch region
      case 1
         ivp(T)=pi/2-a(1)-a(2);
      case 2
         ivp(T)=pi/2-a(1)-a(2);
      case 3
         ivp(T)=-pi/2-a(1)-a(2)+2*ab(3);
      case 4
         ivp(T)=-((3*pi)/2)-a(1)-a(2)+2*ab(3)+2*ab(4);
      end

   %Test to see if within third time period
   elseif(Tm<=t & t<=TM & Tb<=Tc)
      switch region
      case 1
         ivp(T)=-a(1)+a(3);
      case 2
         ivp(T)=-pi-a(1)+a(3)+2*ab(4);
      case 3
         ivp(T)=-a(1)+a(3);
      case 4
         ivp(T)=-pi-a(1)+a(3)+2*ab(4);
      end

       elseif(Tm<=t & t<=TM & Tc<=Tb)
      switch region
      case 1
         ivp(T)=-a(2)+a(4);
      case 3
         ivp(T)=-pi-a(2)+2*ab(3)+a(4);
      case 4
         ivp(T)=-pi-a(2)+2*ab(3)+a(4);
      end

   %Test to see if in fourth time period
   elseif(TM<=t & t<=Td)
        ivp(T)=-pi/2+a(3)+a(4);
   end

end

%Complete impulse response calculation
h=ivp./(2*pi/c);

%Return impulse responce
out=h;
```

Cylindrically focusing transducer – radiated sound pressure field prediction program listing (calls rectangular impulse response function recimpulse.m listed above)

cylindfield.m

```
%Program cylindfield.m
%This program calculates the sound pressure field
%from a cylindrically concave focusing transducer.
%Written by T.J. Robertson 21/7/99

%clear varable space
clear all

%************************
%** Transducer variables*
%************************

%Radius of curvature of transducer (m)
R=28e-3;

%Width of transducer (m)
trans_width=19.5e-3;

%Length of transducer (m)
trans_length=43e-3;

%******************
%*Medium constants*
%******************

%Velocity of sound in medium (m/s)
c=343.4

%Density of medium
density=1.2;

%*****************************
%***Grid size and step set-up*
%*****************************

%Number of points on the x axis (half scan)
xmax=40;

%X step size (m)
xstep=0.25e-3;

%Y position for field calculation (usually 0 i.e. centre of transducer)
y=0

%Number of points on the z axis
zmax=200;

%Z step size (m)
zstep=0.25e-3;

%Number of pairs of strips to use in approximation
N=30;

%Window pre-trig delay (s)

pre_delay=200e-7;

%*******************************
%**Input waveform initialisation*
%*******************************

%Waveform constant
K=0.5;

%Frequency of pulse (Hz)
f=1000e3;

%Delta t (s)
delta_t=4e-8;

%Initalise storage matricies
p_amp=zeros(xmax*zmax,1);
h_strip=zeros(N,2000);
h_1=zeros(1,2000);
h_s=zeros(1,2000);


%Calculate time input waveform  v(t) and V(t)=dv(t)/dt
for T=1:2000
   t=(T-1)*delta_t;

   thta=2*pi*f*t;
   V(T)=3*c*t^2*exp(-K*f*t)*cos(thta)-c*t^3*K*f*exp(-K*f*t)*cos(thta)-2*c*t^3*exp(-K*f*t)*sin(thta)*pi*f;
   v(T)=c*t^3*exp(-K*f*t)*cos(thta);
end

%Calculate fft of V(t)
V_fft=fft(V,2048);

%Start field calculation
```

```
%Step through each field position
for Z=1:zmax
   disp(sprintf('Processing row: %d out of %d.....\n\n',Z,zmax))
   z=(Z-1)*zstep;
   for X=1:xmax

      x=(X-1)*xstep;


      %Calculate impulse response of strip(s) i at point x, y, z.
      delta_x=trans_width/(2*N);
      for i=1:N
         x_i=delta_x*i;
         width=2*x_i;

         %Calc z-mod (difference to shift strip position from z=0 )
         z_mod=R-sqrt(R^2-(x_i-(delta_x/2))^2);

         %Call recimpulse function to calculate impulse response due to strip pairs at current position
         %Note that first strip is single strip not strip pair
         if i == 1
            h_strip(1,:)=recimpulse(width, trans_length, x, y, z, 2000, delta_t, (sqrt(z^2+x^2)/c)-pre_delay);

         else
            h_l=recimpulse(width, trans_length, x, y, (z-z_mod), 2000, delta_t, (sqrt(z^2+x^2)/c)-pre_delay);
          h_s=recimpulse((width - (2*delta_x)), trans_length, x, y, (z-z_mod), 2000, delta_t, (sqrt(z^2+x^2)/c)-
pre_delay);
          h_strip(i,:)=h_l-h_s;
         end

      end

      %Calc impulse response due to strips by the summing of all the strip impulse responses:
      h_imp=zeros(1,2000);

      for i=1:N
               h_imp=h_imp + h_strip(i,:);
      end

      %Calc pressure field: by convoluting impulse response with V(t)
      %Note that this is achieved by multiplying fft's then performing an inverse fft

      imp_fft=fft(h_imp,2048);

      p=density*real(ifft(imp_fft.*V_fft))*delta_t;

      %Calcluate pk-pk pressure amplitude from pressure waveform

      p_amp(((Z-1)*xmax+X))=max(p)-min(p);

   end
end

%Reshape array and mirror for -ve x values.

amp=reshape(p_amp,xmax,zmax);
amp2=amp(2:xmax,:);
amp2=flipud(amp2);
ampt=[amp2; amp];
z=meshgrid(0:zstep*1e3:((zmax-1)*zstep*1e3),1);
x=meshgrid(-(xmax-1)*xstep*1e3:xstep*1e3:(xmax-1)*xstep*1e3,1);
save 500khz_10nw_b ampt z x

%Plot pressure field

mesh(z,x,ampt);
```

Conically focusing transducer – radiated sound pressure field prediction program listing (calls circular impulse response function circularimp.m listed below)

conicfield.m

```
%This program calculates the sound pressure field
%from a cylindrically concave focusing transducer.
%Written by T.J. Robertson 3/8/99

%Clear workspace
clear all

%*****************************
%***Grid size and step set-up*
%*****************************

xmax=40
zmax=320

xstep=0.25e-3;
zstep=0.25e-3;

%************************
%** Transducer variables*
%************************

inner_dia=26e-3;
outer_dia=60e-3;
angle=45;

%calc angle in radians

theta=(angle/180)*pi;

%******************
%*Medium constants*
%******************

%Velocity of sound in medium (m/s)
c=343.4;

% Number of annuli
N=100;

% Density of the medium

density=1.2;

% Sampling period used in calculation
delta_t=1.5e-8;

%Setup arrays
p_amp=zeros(xmax*zmax,1);
trans=ones(xmax*zmax,1);
imp_ann=zeros(N,4000);

%*****************************
%**Input waveform initialisation*
%*****************************

% Frequency of toneburst (Hz)
f=500e3;

% Waveform constant
K=0.5;

%Calculate time input waveform  v(t) and V(t)=dv(t)/dt
for T=1:4000
   t=(T-1)*delta_t;
   tm(T)=t;
   thta=2*pi*f*t;
   V(T)=3*c*t^2*exp(-K*f*t)*cos(thta)-c*t^3*K*f*exp(-K*f*t)*cos(thta)-2*c*t^3*exp(-K*f*t)*sin(thta)*pi*f;
   v(T)=c*t^3*exp(-K*f*t)*cos(thta);

end

% Calculate the fft of the impulse response.
V_fft=fft(V,4096);

delta_r=(outer_dia-inner_dia)/(2*(N-1))

delta_z=delta_r/tan(theta)
z_min=inner_dia/(2*tan(theta))
z_max=outer_dia/(2*tan(theta))

%Start field calculation
%Step through each field position
for X=1:xmax
   disp(sprintf('Processing row: %d out of %d.....\n\n',X,xmax))
   x=(X-1)*xstep;
   for Z=12:zmax
      z=(Z-1)*zstep;
      for i=1:N
          a=((i-1)*(delta_r))+(inner_dia/2)-(delta_r/2);
        z_mod=z_min+(delta_z*(i-1));

        %Calc z-mod (difference to shift annuli position from z=0 )
        if (z <= z_mod) & ( (z+zstep) > z_mod) & (x <= a) & ((x+xstep) > a)
```

```
            trans((X-1)*zmax+Z)=0;
        end

        %Calculate impulse responces of large and small circular sources and subtract for impulse
        %responce from annuli.
            imp_l=circularimp(x,(z-z_mod),a,c,delta_t,4000,(sqrt((z-z_min)^2+x^2)/c)-10e-7);
        imp_s=circularimp(x,(z-z_mod),(a-delta_r),c,delta_t,4000,(sqrt((z-z_min)^2+x^2)/c)-10e-7);
        imp_ann(i,:)=imp_l-imp_s;
    end

    imp=zeros(1,4000);

    %Calc impulse response due to annuli by the summing all the impulse responses:
    for i=1:N
            imp=imp + imp_ann(i,:);
    end

    %Calc pressure field: by convoluting impulse response with V(t)
    %Note that this is achieved by multiplying fft's then performing an inverse fft

    imp_fft=fft(imp,4096);
        con=ifft(imp_fft.*V_fft);
    p=density*real(con(1:2000))*delta_t;

    %Calcluate pk-pk pressure amplitude from pressure waveform
    p_amp((X-1)*zmax+Z)=max(p)-min(p);

  end
end

%Transform pressure field to make complete and add scales.
p_amp=p_amp.*trans;
p_amp=reshape(p_amp,zmax,xmax);
p_amp2=p_amp(:,2:xmax);
p_amp2=fliplr(p_amp2);
amp=[p_amp2 p_amp];

z=meshgrid(0:zstep*1e3:((zmax-1)*zstep*1e3),1);
x=meshgrid(-(xmax-1)*xstep*1e3:xstep*1e3:(xmax-1)*xstep*1e3,1);

%Display field
mesh(x,z,amp);
```

Circular impulse response calculation function

circularimp.m

```
%Function returns impulse response, at position x,y,z
%for a circular transducer.  Impulse response calculation from
%J.C. Lockwood, J.G. Willette, "High-speed method for computing
%the exact solution for the pressure variations in the nearfield
%of a baffled piston", J. Acoust. Soc. Am., vol. 53, no. 3, pp.
%735-741. 1973.
%Written by T.J. Robertson 3/5/99

%Function arguments are as follows:
%
%a - radius of transducer (in m)
%x,y,z - coordinates at which to calculate impulse response (in m)
%tmax - end time (no. of steps)
%tint - time increment (delta t)
%tstart - offset time (in s)

function out=circularimp(x,z,a,c,tint,tmax,tstart);

% Calculate time intervals
t1=z/c;
t2=(sqrt(z^2+(x-a)^2))/c;
t3=(sqrt(z^2+(x+a)^2))/c;

%Reserve array memory
imp=zeros(1,tmax);

%Calculate impulse response depending on region and current time interval.
for T=1:tmax
   t=(T-1)*tint+tstart;

   %for all instances where time between t1 and t2 then:
   if  t1<t & t<t2
      % If radial position less than radius of transducer then
      if x<a
         imp(T)=1;
      % if radial position equal to radius of transducer then
      elseif x==a
         imp(T)=0.5;
      %if radial position x greater than radius of transducer then:
      elseif x>a
         imp(T)=0;
      end
   %for all instances where time is between t2 and t3 then:
   elseif (t2<t & t<t3)
      imp(T)=(1/pi)*acos((c^2*t^2-z^2+x^2-a^2)/(2*x*sqrt(c^2*t^2-z^2)));
   end
end

%Finally calculate impulse response by multiplying by c.
out=c*imp;
```

Circular transducer field calculation program listing (used to predict fields from the immersion transducer). Calls circular impulse response function circularimp.m listed above.

circfield.m

```
%This program calculates the sound pressure field
%from a circular plane piston source.
%Written by T.J. Robertson 2/5/99

%Clear environment space
clear all

%*****************************
%***Grid size and step set-up*
%*****************************

%Number of points on the x axis (radial axis) (half scan)
xmax=40

%Number of points on the z axis (axial axis)
zmax=100

%X step size (m)
xstep=0.5e-3;

%Z step size (m)
zstep=0.5e-3;

%Initalise arrays
p_amp=zeros(xmax*zmax,1);

%************************
%** Transducer variables*
%************************

%Radius (m)
a=5e-3;

%******************
%*Medium constants*
%******************

%Velocity of sound in medium (m/s)
c=1484;

%Density of medium
density=1000;

%*******************************
%**Input waveform initialisation*
%*******************************

%Frequency of excitation (Hz)
f=3000000;

%Constant for wave equation
K=0.5;

%Time interval used in calculation
delta_t=1e-8;

%Calculate time input waveform  v(t) and V(t)=dv(t)/dt
for T=1:4000
   t=(T-1)*delta_t;
   tm(T)=t;
   thta=2*pi*f*t;
   V(T)=3*c*t^2*exp(-K*f*t)*cos(thta)-c*t^3*K*f*exp(-K*f*t)*cos(thta)-2*c*t^3*exp(-K*f*t)*sin(thta)*pi*f;
   v(T)=c*t^3*exp(-K*f*t)*cos(thta);
end

%Calculate FFT of V(t)
V_fft=fft(V,4096);

%Start field calculation
%Step through each field position
for X=1:xmax
   disp(sprintf('Processing row: %d out of %d.....\n\n',X,xmax))
   x=(X-1)*xstep;
   for Z=1:zmax
      z=(Z-1)*zstep;

      %Call circular impulse response function to calc impulse
      %response at position x,y
      imp=circularimp(x,z,a,c,delta_t,4000,(sqrt(z^2+x^2)/c)-10e-7);

      %Calc pressure field: by convoluting impulse response with V(t)
      %Note that this is achieved by multiplying fft's then performing an inverse fft
      imp_fft=fft(imp,4096);
      con=ifft(imp_fft.*V_fft);
      p=density*real(con(1:4000))*delta_t;

      %Get peak presure
      p_amp((X-1)*zmax+Z)=max(p)-min(p);
   end
```

```
end

%Reshape array and mirror for -ve x values
p_amp=reshape(p_amp,zmax,xmax);
p_amp2=p_amp(:,2:xmax);
p_amp2=fliplr(p_amp2);
amp=[p_amp2 p_amp];

%Calculate x and z coordinates
z=meshgrid(0:zstep*1e3:((zmax-1)*zstep*1e3),1);
x=meshgrid(-(xmax-1)*xstep*1e3:xstep*1e3:(xmax-1)*xstep*1e3,1);

%Plot pressure field
mesh(x,z,amp);
```

Appendix C - Transducer Designs

Cylindrically focusing transducer designs

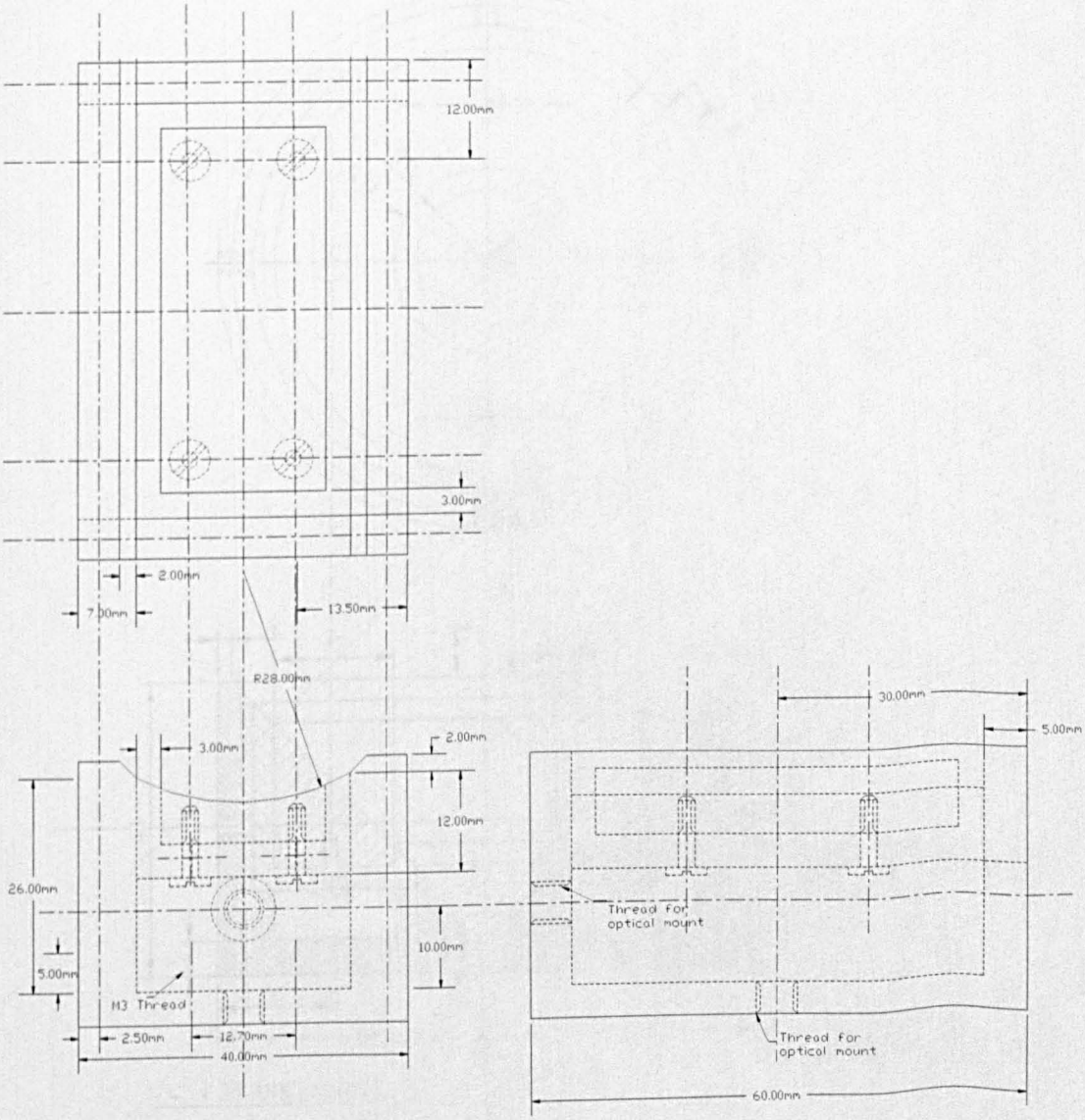

Conically focusing transducer design

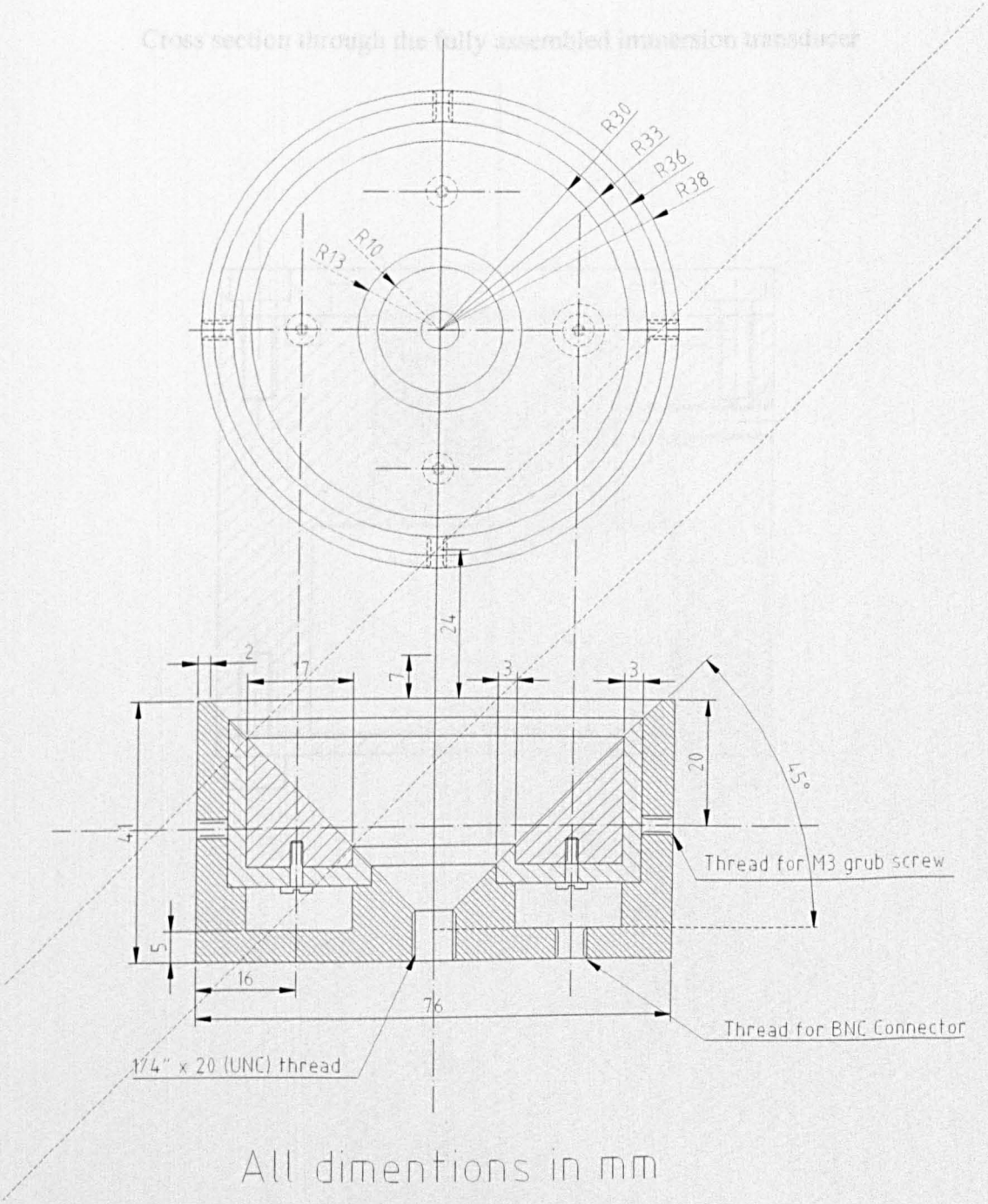

Immersion Transducer Designs

Cross section through the fully assembled immersion transducer

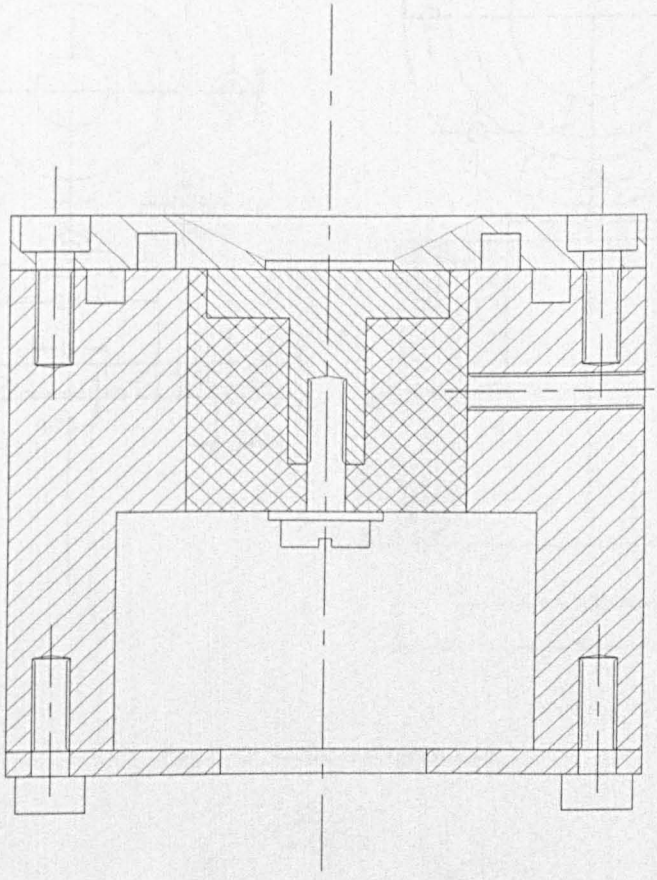

Part A: Aluminium Aperture

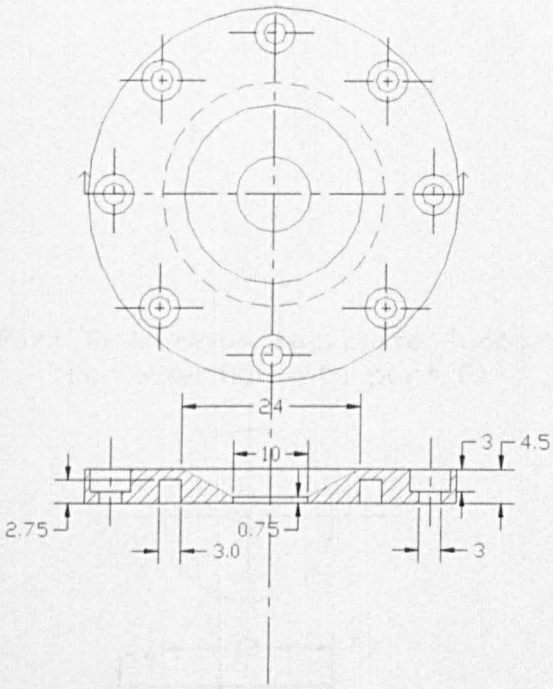

Part B: Aluminium Housing
(All Threads M3)

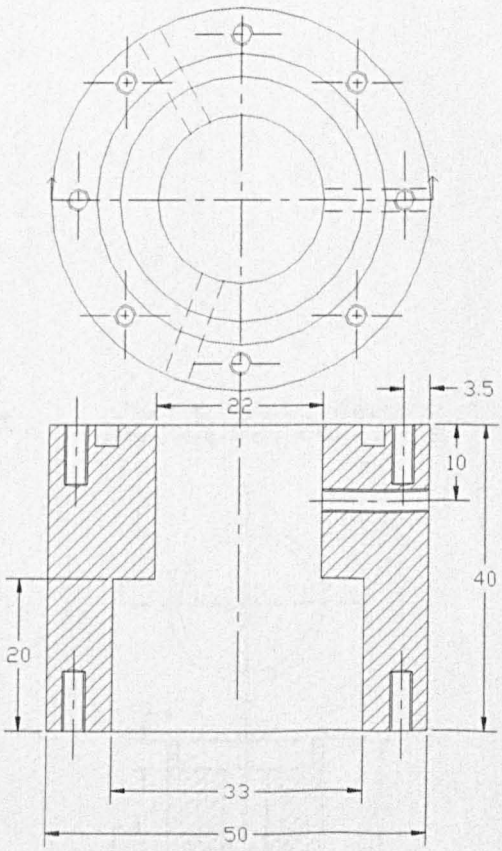

Part C: Aluminium end Cap

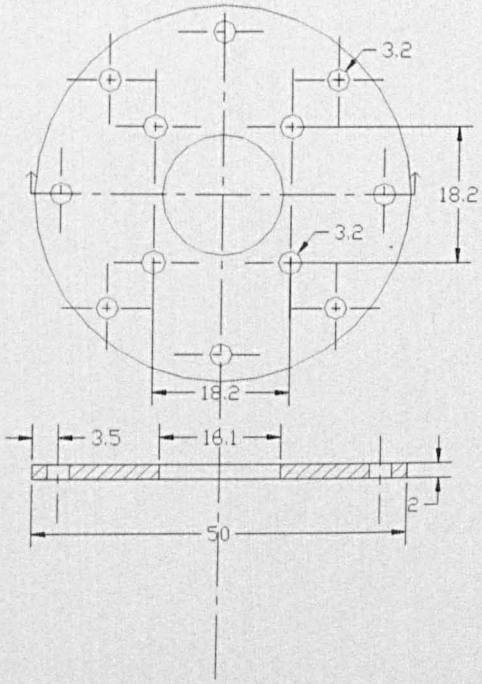

Part D: Aluminium Backplate Support
(for insertion into part E)

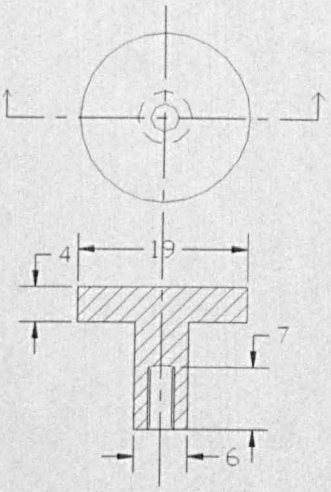

Part E: Nylon Insulator
(For insertion into part B)